



Xuhui Lee

Fundamentals of Boundary- Layer Meteorology

Springer Atmospheric Sciences

More information about this series at <http://www.springer.com/series/10176>

Xuhui Lee

Fundamentals of Boundary-Layer Meteorology



Springer

Xuhui Lee
School of Forestry and Environmental Studies
Yale University
New Haven, Connecticut, USA

ISSN 2194-5217
Springer Atmospheric Sciences
ISBN 978-3-319-60851-8
DOI 10.1007/978-3-319-60853-2

ISSN 2194-5225 (electronic)
ISBN 978-3-319-60853-2 (eBook)

Library of Congress Control Number: 2017948647

© Springer International Publishing AG 2018

This work is subject to copyright. All rights are reserved by the Publisher, whether the whole or part of the material is concerned, specifically the rights of translation, reprinting, reuse of illustrations, recitation, broadcasting, reproduction on microfilms or in any other physical way, and transmission or information storage and retrieval, electronic adaptation, computer software, or by similar or dissimilar methodology now known or hereafter developed.

The use of general descriptive names, registered names, trademarks, service marks, etc. in this publication does not imply, even in the absence of a specific statement, that such names are exempt from the relevant protective laws and regulations and therefore free for general use.

The publisher, the authors and the editors are safe to assume that the advice and information in this book are believed to be true and accurate at the date of publication. Neither the publisher nor the authors or the editors give a warranty, express or implied, with respect to the material contained herein or for any errors or omissions that may have been made. The publisher remains neutral with regard to jurisdictional claims in published maps and institutional affiliations.

Printed on acid-free paper

This Springer imprint is published by Springer Nature
The registered company is Springer International Publishing AG
The registered company address is: Gewerbestrasse 11, 6330 Cham, Switzerland

Acknowledgments

I wish to thank the following colleagues for their review of the manuscript: Brian Amiro (Chap. 4), Don Aylor (Chap. 5), Dennis Baldocchi (Chap. 8), Rob Clement (Chap. 3), Tim Griffis (Chaps. 1, 2, 10 and 11), Bill Massman (Chaps. 2 and 9), HaPe Schmid (Chap. 7), Natalie Schultz (Chaps. 1, 7 and 10), Jielun Sun (Chap. 6), and Lei Zhao (Chap. 10). Thanks also go to Chang Cao, Cheng Hu, Cheng Liu, and Zhen Zhang for their beta-testing of the problem sets.

Yale University
December 2016

Xuhui Lee

Contents

1	Introduction	1
1.1	Boundary-Layer Meteorology	1
1.2	Application Topics	4
1.3	Structure of This Book	8
1.4	How to Use This Book	9
2	Fundamental Equations	11
2.1	Coordinate Systems	11
2.2	Principle of Momentum Conservation	12
2.3	Conservation of Mass	15
2.4	Conservation of Energy	18
2.5	The Ideal Gas Law	20
2.6	The Surface Energy Balance	22
2.7	Problems	25
References		27
3	Governing Equations for Mean Quantities	29
3.1	Reynolds Decomposition	29
3.2	Flow Incompressibility	33
3.3	The Mean Equations for Velocity, Mixing Ratio, and Potential Temperature	35
3.4	Simplified One-Dimensional Equations	37
3.5	The Closure Problem	40
3.6	Quantifying Eddy Fluxes	45
3.7	Problems	51
References		56
4	Generation and Maintenance of Atmospheric Turbulence	57
4.1	Energy Pools and Energy Transfers	57
4.2	Budget of the Mean Flow Kinetic Energy	60
4.3	Budget of the Turbulent Kinetic Energy	64

4.4	Air Stability	68
4.5	Problems	75
	References	79
5	Flow in Plant Canopies	81
5.1	Canopy Morphology	81
5.2	Canopy Volume Averaging	82
5.3	The Mean Momentum Equations	85
5.4	Analytical Wind Profiles in the Canopy	87
5.5	Budgets of Mean Flow and Turbulent Kinetic Energy	89
5.6	Shear Instability and Transition to Turbulence	91
5.7	Problems	97
	References	100
6	Balance of Forces in the Atmospheric Boundary Layer	101
6.1	Atmospheric Layers	101
6.2	Balance of Forces in Neutral and Convective Conditions	107
6.3	Balance of Forces in Stable Conditions	110
6.4	Problems	116
	References	119
7	Tracer Diffusion in the Lower Boundary Layer	121
7.1	Basic Constraints	121
7.2	Point-Source Diffusion in Homogeneous Turbulence	124
7.3	Gaussian Plume Model for Elevated Sources in the Boundary Layer	129
7.4	Diffusion from Ground-Level Sources	132
7.5	Diffusion in Plant Canopies	136
7.6	Footprint Theory	138
7.7	Problems	145
	References	148
8	Principle of Eddy Covariance	149
8.1	Introduction	149
8.2	The Canopy Source Term	150
8.3	The Concept of Net Ecosystem Exchange	153
8.4	The Chamber Method	154
8.5	The Eddy Covariance Control Volume	156
8.6	Eddy Covariance in Advection-Free Conditions	160
8.7	Vertical Advection	161
8.8	Horizontal Advection	166
8.9	Practical Considerations	168
8.10	Problems	169
	References	173

9 Density Effects on Flux Measurements	175
9.1 Density Effects	175
9.2 Density Corrections to Eddy Covariance Fluxes.....	176
9.3 Density Effects on Flux-Gradient Relation	181
9.4 Density Corrections to Chamber Fluxes	184
9.5 Problems	186
References.....	189
10 Energy Balance, Evaporation, and Surface Temperature	191
10.1 Resistance Analogy for Leaf-Scale Fluxes.....	191
10.2 Canopy Energy Balance and the Big-Leaf Model	195
10.3 One-Source Model in Remote Sensing Applications.....	198
10.4 Two-Source Model of Evaporation	200
10.5 Improved Representations of Surface-Air Exchange	203
10.6 One-Source Model of Surface Temperature	205
10.7 Problems	210
References.....	213
11 Budgets of Heat, Water Vapor, and Trace Gases in the Atmospheric Boundary Layer	215
11.1 Introduction.....	215
11.2 The Slab Approximation of the Convective Boundary Layer	216
11.3 Boundary-Layer Growth and Entrainment	219
11.4 Heat Budget in the Convective Boundary Layer.....	227
11.5 Carbon Dioxide Budget in the Convective Boundary Layer	229
11.6 Water Vapor Budget in the Convective Boundary Layer	232
11.7 Trace Gases in the Nighttime Stable Boundary Layer.....	233
11.8 The Equilibrium Boundary Layer	235
11.9 Problems	238
References.....	242
Symbols and Constants	243
Index	251

Chapter 1

Introduction

1.1 Boundary-Layer Meteorology

Boundary-layer meteorology, a subdiscipline of meteorology, is concerned with the state of and processes in the air layer in immediate contact with the Earth's surface. This air layer, about 1 km in thickness and termed the atmospheric boundary layer (Fig. 1.1), is the interface between the free atmosphere and the Earth's surface, which can be land ecosystems, lakes, ice fields, or the oceans. From the atmospheric perspective, the boundary layer is the lower boundary of large-scale atmospheric flows. From the biospheric perspective, conditions in the boundary layer impose a top-down influence on ecosystem functions.

The boundary layer's physical state is described with variables such as temperature, humidity, pressure, and wind, and its chemical state with variables that measure the abundance of trace gases such as carbon dioxide and air pollutants. The physical state variables are tightly related to the dynamic aspects (level of turbulence, diffusion efficiency, and air stability) of the boundary layer, whereas the chemical state variables, except aerosols, are passive scalars that have no direct dynamic consequences. Changes in boundary-layer state are controlled by processes that transfer momentum, energy, and materials within the boundary layer and between the boundary layer and the surface below or the free atmosphere aloft. Flux variables are used to quantify the rate of these transfer processes. An important goal of boundary-layer meteorology is to study the relationships between the state and the process variables.

Radiation energy exchange with the surface is a key process that regulates the physical and chemical state of the boundary layer. In cloud-free conditions, the boundary layer is basically transparent to solar radiation. Absorption, reflection, and emission of the radiation energy occur only at the surface. Absorption of solar radiation by the Earth's surface in daylight hours warms the boundary layer, and loss of longwave radiation at night cools it. Solar radiation supplies energy for evapotranspiration, the process in which liquid water is lost to the atmosphere

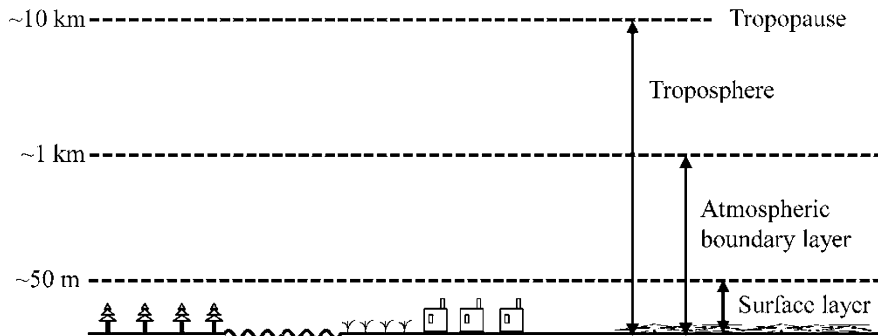


Fig. 1.1 Division of the lower atmosphere. The vertical dimension is not drawn to scale

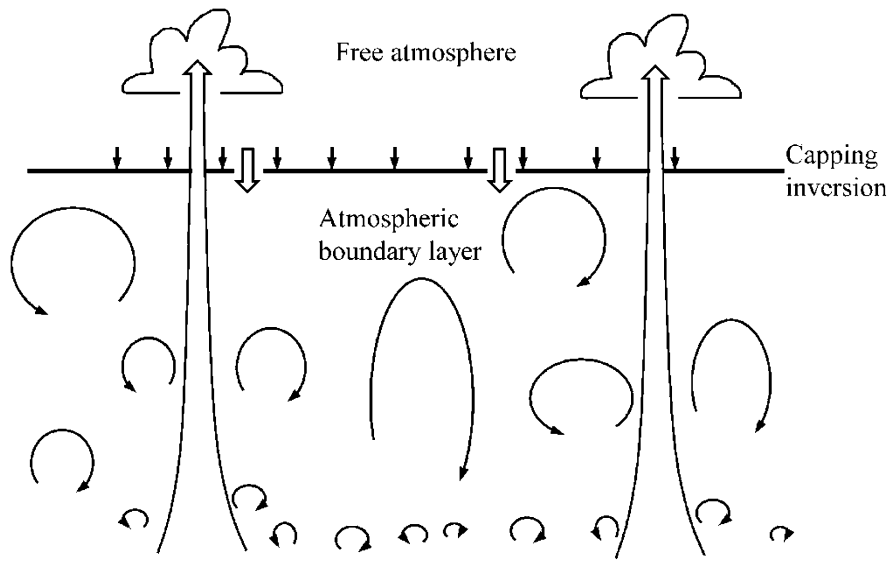


Fig. 1.2 Illustration of eddy motion in a convective boundary layer

via vaporization. In land ecosystems, evapotranspiration occurs primarily in the daytime, causing the moisture level in the air to rise, and is weak or absent at night. Plant photosynthesis and respiration activities are regulated by this daylight and night cycle, generating variations in concentrations of carbon dioxide and other biologically active gas species. The boundary layer is characterized by large diurnal variations, or variations through the 24-h cycle, of its physical and chemical conditions. In contrast, diurnal variations are absent in the free atmosphere.

Another important character of the boundary layer is that air motion is generally turbulent. In a convective boundary layer (Fig. 1.2), turbulent eddies are generated by wind shear, or variation of the velocity with height, and by buoyancy associated

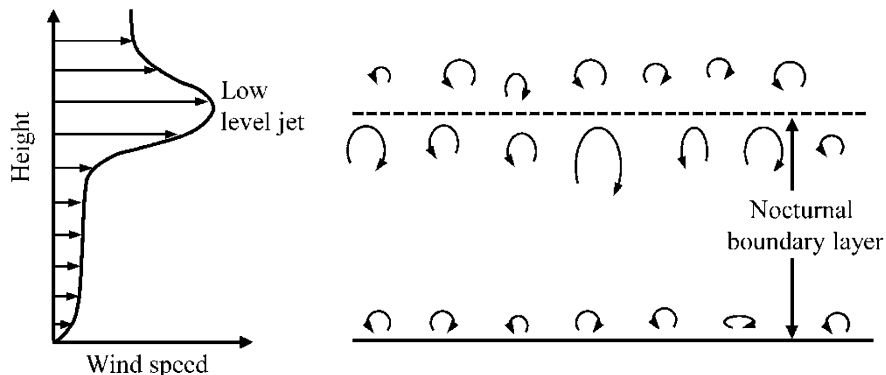


Fig. 1.3 Illustration of a nocturnal low level jet (*left*) and eddy motion generated by wind shear near the jet layer and near the surface (*right*)

with surface heating. Some of the large eddies can penetrate into the free atmosphere, generating convective clouds. At night, shear generation is the only source of turbulence, which occurs near the surface and occasionally at the top of the nocturnal boundary layer if a low-level jet is formed there (Fig. 1.3).

The turbulent nature of the flow allows energy and materials to diffuse in the boundary layer and to the upper atmosphere at much higher efficiencies than molecular processes allow. Turbulence also generates a frictional force on larger-scale air motion. It is because of this retarding force that wind velocity in the boundary layer is lower than in the free atmosphere; without this force, wind would be intolerably high to humans and to many other living things on Earth. Air above the boundary layer can move freely without being hindered by the surface friction.

Turbulent motion is inherently chaotic. A question that arises naturally is whether the motion is so chaotic to the extent that boundary layer processes basically defy any useful and predictive treatment. The answer is no. Orderly patterns often emerge out of the seemingly random motion structures, if one follows a set of established principles of energy, mass, and momentum conservation. Paradoxically, the more intense the turbulence is, the easier it is to quantify the mean state of the boundary layer. How to properly apply these principles constitutes an essential task of boundary-layer meteorology.

The influences of larger-scale atmospheric state on boundary-layer processes are prescribed by a set of known parameters. For example, the pressure gradient associated with synoptic weather patterns is considered as a known parameter, and the task of a boundary-layer meteorologist is to determine from the known pressure gradient the surface frictional force, the intensity of turbulence, the wind directional shear in the boundary layer, and so forth. Another known parameter is solar radiation above the boundary layer. The intensity of solar radiation varies in a more predictable way in cloud-free conditions than in the presence of clouds. Prediction of clouds, except for those formed in the boundary layer due to convective

and radiative cooling, is beyond the scope of boundary-layer meteorology. Whether the sky is overcast or clear is prescribed either from weather observation or from a weather forecast model, and from these prescribed conditions, calculations are made on how various forms of energy flux balance each other at the surface.

Embedded in the atmospheric boundary layer is the surface layer which spans a few meters to a few tens of meters of space above the surface (Fig. 1.1). This is the air layer where the surface influences are the strongest and where most micrometeorological phenomena occur. Sometimes a plant or an urban canopy occupies the lower portion of this layer. At other times the surface is free of plants and other roughness elements. Of special interest are vertical profiles of wind, temperature, humidity, and gaseous concentrations, as they control the efficiency of exchanges of momentum, energy, water, and trace gases between the atmosphere and the surface. Some trace gases, such as sulfur dioxide, ozone, and volatile organic compounds, are air pollutants. Others are long-lived greenhouse gases related to biological activities, such as carbon dioxide and methane. Methods established by micrometeorologists for quantifying the fluxes of these gases have found a wide range of applications. The theoretical foundations of these methods are discussed in this book.

1.2 Application Topics

Boundary-layer meteorology is the basis for many application topics in earth and environmental sciences. The following examples illustrate its connection to related disciplines, including dynamic meteorology, terrestrial ecology, hydrology, and air pollution meteorology. This book does not treat these topics in equal depth. However, the materials covered should equip the reader with adequate preparation for further literature exploration. The multidisciplinary linkages motivate the need for a good understanding of boundary-layer phenomena and supply new questions for boundary-layer meteorologists.

Parameterization of Surface Fluxes

The flux of a certain quantity is the net amount of flow of this quantity across a reference plane of a unit surface area over a unit time. A radiation energy flux of 200 W m^{-2} indicates that 200 J of energy moves across a surface of area 1 m^2 in 1 s . A water vapor flux of $0.1 \text{ g m}^{-2} \text{ s}^{-1}$ indicates that 0.1 g of water vapor flows across a surface area of 1 m^2 in 1 s . If the reference plane is leveled and is located just above the Earth's surface, the flux is equivalent to the rate of exchange between the surface and the atmosphere. Surface fluxes of radiation energy, sensible heat, momentum,

and water vapor constitute the lower flux boundary conditions for weather and climate prediction models. In the models, these fluxes are represented by a set of mathematical formulae called parameterizations. The relationships between the flux and surface morphology, surface optical properties, and ecological attributes of vegetation are described with a set of known parameters. In online mode in which these parameterizations are coupled with other model codes to make forecasts, the actual flux calculations require forcing variables predicted at every time step by the atmospheric model, at its first grid height. A typical set of forcing variables consists of incoming solar radiation, incoming longwave radiation, air temperature, air humidity, wind speed, and precipitation. In offline mode, flux parameterizations are forced by observed values of these variables. Offline calculations are one way with which experimentalists interpret field data. A robust parameterization must be firmly grounded on sound principles of atmospheric transport processes. Boundary-layer meteorological studies are essential for this endeavor.

Ecosystem Metabolism

The metabolic processes of an ecosystem involve constant flow of energy and materials between the system and its surroundings. In daylight hours, carbon dioxide is taken up from the atmosphere for photosynthesis. Coupled to the carbon capture is loss of water via transpiration, which prevents the plants from overheating and helps their roots absorb nutrients from the soil. At night, carbon dioxide is released back to the atmosphere by respiration. These processes are highly dynamic, changing by the hour owing to weather fluctuations. The exchanges of carbon dioxide and water vapor take place in the atmospheric surface layer, making this layer of air an excellent environment to observe these processes. In comparison, it is virtually impossible to obtain information on ecosystem functions from observations made in the upper atmosphere. The ecosystem's imprints on the surface layer make it possible to infer the ecosystem exchanges of these two gases from atmospheric measurements. The techniques that accomplish this task are at the appropriate scale that matches the size of a typical ecosystem. These micrometeorological techniques are widely used, largely because they do not require destructive sampling of individual plants or alteration of their growth environment. With these advantages, however, come methodological challenges. The theoretical foundation underlying these techniques is the principle of mass conservation. In reality, only an incomplete number of terms in the mass conservation equation can be measured, and we are forced to approximate the true net ecosystem exchange with these measurable quantities. Knowledge about meteorological and site conditions under which this approximation may break down is essential for proper design of a measurement campaign and the subsequent data analysis.

Pathways of Biological Agents

Biological agents in the atmosphere fall into two size groups. Plant seeds that rely on wind for dispersal are in the large size group, their size ranging from several millimeters to several centimeters. In the small size group (0.5–100 μm) are pollen grains and spores. The life cycle of these agents consists of production, release, dispersion, and deposition. All of these stages are impacted by atmospheric conditions in the boundary layer. Their movement through the atmosphere is especially sensitive to wind patterns and the structure of air turbulence. Having large settling velocity, plant seeds rarely escape the surface layer. The majority of the seeds have a dispersion distance on the order of tens of meters from the parent plant. Their exact travel path is controlled by wind speed at the plant height, wind direction, and directional shear inside the plant canopy. The smaller biotic particles (pollen and spore) can travel over longer distances, with the majority deposited within a distance of several kilometers from the source. Caught in large convective eddies, a small fraction of these particles can escape the surface layer to the upper boundary layer and the free atmosphere and undergo long-distance transport. Long-distance transport of spores is the main mechanism by which plant diseases spread over large areas. Similarly, long-distance transport of pollen can cause genetic contamination, a concern for plant breeders. Determination of the escape fraction is made on the basis of the particle's morphological characteristics, production timing, as well as the structure of turbulence in the atmospheric boundary layer.

Dispersion of Air Pollutants

The severity of air pollution downwind of a pollution source is controlled by the rate of pollution emission, source configuration, and local meteorology. For inert pollutants, the dependence on emission rate is linear: a doubling of emission results in a doubling of the pollution concentration. The dependence on meteorological conditions is much more complex. The same source may be in compliance with air quality standards in one day but become noncompliant the next day as the state of the atmosphere changes. The atmospheric power to disperse air pollutants increases with wind speed, turbulence intensity, static instability, and the height of the boundary layer. Taking these dispersion conditions into account and utilizing conservation of mass, an air quality model aims to predict the concentration of the pollutant near an emission source. These predictions are made for existing sources to inform local residents about air quality in their neighborhood. In regulatory applications, air quality models are used to determine if construction of a new source may cause new violation of air quality standards. The rate of deposition of air pollution to the ground is proportional to pollution concentration in the surface layer, so predicting ground-level concentrations is helpful for assessment of air pollution impact on ecosystem health.

Prediction of Evapotranspiration

Water is a vital resource for plant growth. The amount of water incorporated into plant biomass is, however, negligible, and a large quantity is lost via evapotranspiration to the atmosphere. The rate of evapotranspiration is controlled primarily by available radiation energy and soil moisture, and to a lesser extent by air temperature, air humidity, and wind speed in the surface layer. Predictions of evapotranspiration flux from these state variables are useful to farmers in their scheduling of irrigation timing and amount. More generally, the ability to quantify evapotranspiration helps to determine plant growth in ecosystem models. The surface water vapor flux, or the rate of evapotranspiration, is bounded by conservation of energy and conservation of mass, expressed in the form of the surface energy balance equation and water balance equation, respectively. No equivalent constraints from the first principles exist for the carbon dioxide flux. However, water use efficiency, that is, the ratio of carbon dioxide flux to water vapor flux, is a biological trait that is known to vary within a narrow range among plants that share the same photosynthetic mode (e.g., C₃ or C₄). Modelers take advantage of the conserved behavior of water use efficiency in their calculation of ecosystem productivity.

Urban Heat Islands

The urban heat island refers to the phenomenon of higher surface and air temperature in urban areas than in the surrounding rural land. Even though urban heat islands are localized hot spots in the landscape, they have a profound impact on the lives of urban residents, who comprise more than half of the world's population. They increase energy demand for air conditioning and aggravate heat stress on human health. There are growing efforts to mitigate urban heat. The scientific foundation underlying these efforts is the principle of surface energy balance. Replacement of a natural landscape with man-made structures disrupts this balance in several ways. Reduction of evaporative cooling is an important factor contributing to urban warming. Anthropogenic heat release is an added energy input to the energy balance and increases the surface temperature. Energy input by solar radiation also increases if albedo is reduced in the process of land conversion. Buildings and other artificial materials store more radiation energy in the daytime than do natural vegetation and soil; release of the stored energy at night contributes to nighttime warming. Energy redistribution through convection between the surface and the atmospheric boundary layer either increases or reduces the intensity of the urban heat island, depending on whether the efficiency of convection over urban land is suppressed or enhanced relative to that over the adjacent rural land. These concepts have been known for some time. To aid urban heat island mitigation efforts, it is important to quantify how their roles vary through the course of the day and the year, among individual neighborhoods of a city, and among cities across different climate zones.

Connection to Large-Scale Atmospheric Flows

Ekman pumping is one well-recognized mechanism that connects the flow in the boundary layer with larger-scale atmospheric dynamics. Owing to the balance between the pressure gradient force and the Coriolis force, air above the boundary layer moves counterclockwise in a low-pressure system and clockwise in a high-pressure system in the Northern Hemisphere. The horizontal extent of these synoptic weather systems is on the order of several hundreds of kilometers. In the boundary layer, the presence of surface friction deflects the flow inward in the low-pressure system resulting in flow convergence, and outward in the high-pressure system resulting in flow divergence. Ekman pumping refers to the phenomenon whereby flow convergence in the low-pressure system causes upward motion at the top of the boundary layer, bringing moisture from the surface to upper levels to sustain clouds. The rising motion is compensated by sinking motion in the (neighboring) high-pressure system, thus forming a secondary circulation that interacts with the counterclockwise and clockwise rotations. Successful predictions of cloud and precipitation require accurate formulation of the Ekman pumping mechanism.

Transport Phenomena

Aside from the above issues, investigation on diffusion in the lower atmosphere can help scientists refine theory of turbulent transport. Transport phenomena in the atmospheric boundary layer take place under conditions that would not be possible in controlled environments, thus pushing established theories beyond their conventional parameter space. For example, Prandtl's theory on turbulent diffusion, established for boundary layer flows in pipes and in wind tunnels, works reasonably well in the atmospheric surface layer but does a poor job in the upper boundary layer and in a plant canopy where diffusion is dominated by large turbulent eddies whose length scale is much greater than Prandtl's mixing length. Another case in point is the exchange of energy and materials at the interface between the free atmosphere and the boundary layer. Here the transport of heat and water vapor is best described by a mass movement of the diffusion media itself rather than by a pure diffusion process linked to temperature and gaseous concentration gradients.

1.3 Structure of This Book

The materials presented in this book are organized around a set of fundamental governing equations: conservation of momentum, conservation of mass (dry air, water vapor, and trace gases), conservation of energy (applied to both the moving air and the Earth's surface), and the ideal gas law. Insights and consequences are explained via logical deduction by manipulating these equations for various situations.

The basic equations are introduced in Chap. 2. Chapter 3 applies the Reynolds decomposition rules to these equations. The result is a set of governing equations that express the relations between time-averaged state variables and flux variables.

The next three chapters (Chaps. 4, 5 and 6) are applications of the momentum conservation principle. In Chap. 4, the mean momentum equations are manipulated further to gain insights on generation and maintenance of turbulent kinetic energy in the atmospheric boundary layer. Chapter 5 is an application of momentum conservation to the airspace in plant canopies, where an additional volume-averaging operation is used to handle the interaction between plant elements and the moving air. In Chap. 6, the boundary layer is divided into several sublayers, and the balance of forces after omitting small terms leads to simplified analytical solutions for the mean velocities.

Chapters 7 and 8 are applications of the mass conservation principle. Chapter 7 deals with diffusion processes involving a tracer released in the boundary layer. In Chap. 8, a volume-averaging operation is applied to the Reynolds mean mass conservation equations to establish the connection between plant carbon dioxide, water vapor and heat sources, and process variables in the atmosphere. This connection forms the basis of the eddy covariance technique for flux measurements.

Chapter 9 examines the interferences caused by dry air density variations on our ability to measure gaseous fluxes in the boundary layer. Here, the ideal gas law is used extensively to constrain the interdependence between temperature, humidity, trace gas concentration, and atmospheric pressure.

Chapter 10 develops mathematical models of evaporation and surface temperature. The theoretical basis for these applications is the surface energy balance, or the principle of energy conservation applied to a surface (a leaf surface, a canopy, and the ground surface).

In the final chapter (Chap. 11), the energy and mass conservation principles are used to establish a predictive understanding of the transport of energy, water, and trace gases between the whole boundary layer, the Earth's surface, and the free atmosphere.

1.4 How to Use This Book

This book is intended primarily as a text for an upper-level undergraduate or a graduate-level course on boundary-layer meteorology and micrometeorology. The content is slightly more than the amount needed for a three-credit course. In the author's university, a three-credit course consists of 3-h lectures per week for 12 weeks. A course that emphasizes measurement techniques can skip the modeling chapter (Chap. 10) and a majority of Chap. 7 but retain the section on flux footprint. Likewise, a course devoted to modeling of boundary-layer phenomena can omit two measurement chapters (Chaps. 8 and 9).

A research reference book typically presents materials in a historical sequence to show how concepts and theories have evolved over time. This is not the strategy used

here. Instead, the content is organized by a structure deemed most logical, without regard to when it was published. A short list of citations is provided at the end of each chapter, so an interested reader can reconstruct the historical development of a particular topic or pursue further literature exploration.

Users of this book are expected to have working knowledge of multivariable calculus. Prior preparation in fluid mechanics and thermodynamics is helpful but is not required. Students majoring in atmospheric sciences may find materials presented in Chap. 2 repetitive to what they may have already encountered in other atmospheric courses, but still it is helpful to review these fundamental principles before moving onto more specialized topics in later parts of the book. While derivation of equations is presented wherever appropriate, it is more important for the reader to grasp the physical meaning of the equations and the conditions under which simplifications are made than to perform the mathematical derivation itself.

An emphasis is on theories and concepts that have universal appeal. Obviously, this is simply a matter of presentation style and does not diminish the importance of observational studies in boundary-layer meteorology. Some empirical results published by the author and by other scientists are incorporated into the problem set at the end of each chapter. Users who do not want to work on the problem set should still spend time reading the problem statements. They are also encouraged to explore connections between the fundamental principles presented here and empirical data presented in other textbooks. In this sense, this book is complementary to several excellent textbooks on boundary-layer meteorology, including *Boundary Layer Climates* by T. R. Oke, *An Introduction to Boundary Layer Meteorology* by R. B. Stull, *The Atmospheric Boundary Layer* by J. R. Garratt, *Turbulence in the Atmosphere* by J. C. Wyngaard, *Micrometeorology* by T. Foken, and *Atmospheric Boundary Layer: Integrating Air Chemistry and Land Interactions* by J. Vilá-Guerau de Arellano, C. C. van Heerwaarden, B. J. H. van Stratum, and K. van den Dries.

Readers interested in the history of boundary-layer meteorology should consult the books cited above. The book volume *A Voyage through Turbulence*, edited by P. A. Davidson, Y. Kaneda, K. Moffatt, and K. R. Sreenivasan, also provides an excellent historical perspective.

A problem set in each chapter serves to reinforce the concepts presented in the main text of that chapter. Each set consists of about 20 questions of varying levels of difficulty. The most difficult questions, marked by an asterisk, are essentially small research projects constructed from the published literature. Hints on how to solve these difficult questions are usually found in one of the references listed at the end of the chapter. When answering questions, you should pay attention to details, such as physical units and a number of significant digits, and should try to develop a good “number sense”. Often it is these details that will be used to judge whether you have mastered the material. For example, the net radiation of a natural surface falls in the range of -100 to 700 W m^{-2} , but something has gone wrong if your answer is -150 W m^{-2} .

The source files for the graphics included in this book are available on the author’s website. Users may find them helpful for lecture preparation and classroom discussion. An open online course based on this textbook is under development and, once completed, will be released to the general public via the author’s website.

Chapter 2

Fundamental Equations

2.1 Coordinate Systems

Vector quantities, such as the flux, the velocity, and the scalar concentration gradient, are generally expressed in a right-handed Cartesian coordinate frame. In the discussion of momentum, mass, and energy conservation, the frame's origin is at a fixed position, and the directions of its three axes are also fixed. The horizontal x -axis may be pointing to the north, the y -axis pointing to the west, and the z -axis aligned with and in the opposite direction of the gravitational force. The instant velocity vector is $\mathbf{v} = \{u, v, w\}$, and the gradient vector of a scalar quantity a is $\nabla a = \{\partial a / \partial x, \partial a / \partial y, \partial a / \partial z\}$.

A special type of Cartesian coordinate, the *micrometeorological coordinate*, utilizes the observed wind vector in the surface layer to orient its two horizontal axes (Fig. 2.1). This is a right-handed system, with its x -axis aligned with the mean horizontal velocity vector, its y -axis in the crosswind or lateral direction, and its z -axis normal to the surface. On a flat terrain, the z -axis is in the opposite direction of the gravitational force. The mean velocity vector is $\bar{\mathbf{v}} = \{\bar{u}, \bar{v}, \bar{w}\}$, where the overbar denotes time averaging. A typical averaging length is 30 min. If wind direction shifts from one 30-min observation to the next, the coordinate's x - and y -axis will shift accordingly. By definition, the lateral mean velocity component \bar{v} in the surface layer is always zero. A non-zero mean vertical velocity \bar{w} is permissible for individual observations, although the long-term average of \bar{w} should be very close to zero. Above the surface layer, \bar{v} may be non-zero due to wind directional change with height.

Wind measurements are made in an instrument coordinate. For proper data interpretation, coordinate rotation is required to express velocity statistics and flux quantities in the micrometeorological coordinate. By forcing \bar{v} to zero and aligning the $x-y$ plane with the local terrain, we only need to consider the u and w component when computing the surface momentum flux. More importantly, coordinate rotation removes errors due to instrument tilt. The vertical velocity is especially sensitive to

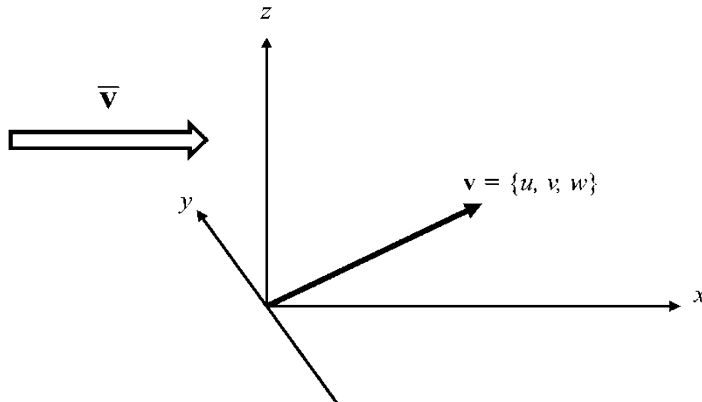


Fig. 2.1 The micrometeorological coordinate

tilt errors. If the anemometer is tilted at angle α , the mean vertical velocity measured by the instrument, \bar{w}_1 , will consist of two components:

$$\begin{aligned}\bar{w}_1 &= \bar{w} \cos(\alpha) + \bar{u} \sin(\alpha) \\ &\simeq \bar{w} + \bar{u} \sin(\alpha)\end{aligned}\quad (2.1)$$

To obtain a sense of how large the tilt error is, consider a tilt angle of $\alpha = 1$ degree into the wind and a horizontal mean velocity of $\bar{u} = 3 \text{ m s}^{-1}$. The second term on the right side of Eq. 2.1 is 0.05 m s^{-1} . In comparison, a typical true mean vertical velocity in the surface layer is on the order of 0.01 m s^{-1} or less. Flux quantities are also sensitive to tilt errors. After removal of the tilt errors, the resulting vertical fluxes are in the correct reference plane, that is, a plane parallel to the local terrain surface. The reader should consult the references listed at the end of this chapter on how to perform coordinate rotation (e.g., Kaimal and Finnigan 1994; Wilczak et al. 2001).

If the interest is flow in the whole atmospheric boundary layer, an alternative coordinate system may be deployed. In this system, the x -axis is aligned with the geostrophic wind vector, which is given as a known external forcing parameter. The lateral mean velocity \bar{v} is zero at the top of the boundary layer but is non-zero in the surface layer.

2.2 Principle of Momentum Conservation

The principle of momentum conservation is a direct consequence of Newton's second law of motion. It states that the time rate of change of the momentum of an air parcel is equal to the sum of all the forces experienced by the parcel. Applied to an air parcel, the conservation equation takes the general form:

$$\frac{d\mathbf{v}}{dt} = \frac{1}{m} \sum \mathbf{F} = \sum \mathbf{f} \quad (2.2)$$

where m is mass, F is force, and \mathbf{f} is force normalized by mass and has the dimensions of acceleration (m s^{-2}). In component form, Eq. 2.2 becomes

$$\frac{\partial u}{\partial t} + u \frac{\partial u}{\partial x} + v \frac{\partial u}{\partial y} + w \frac{\partial u}{\partial z} = -\frac{1}{\rho} \frac{\partial p}{\partial x} + fv + \nu \nabla^2 u, \quad (2.3)$$

$$\frac{\partial v}{\partial t} + u \frac{\partial v}{\partial x} + v \frac{\partial v}{\partial y} + w \frac{\partial v}{\partial z} = -\frac{1}{\rho} \frac{\partial p}{\partial y} - fu + \nu \nabla^2 v, \quad (2.4)$$

$$\frac{\partial w}{\partial t} + u \frac{\partial w}{\partial x} + v \frac{\partial w}{\partial y} + w \frac{\partial w}{\partial z} = -\frac{1}{\rho} \frac{\partial p}{\partial z} - g + \nu \nabla^2 w, \quad (2.5)$$

where ρ is air density, p is pressure, f is the Coriolis parameter, ν is kinematic viscosity, g is gravitational acceleration, and

$$\nabla^2 = \frac{\partial^2}{\partial x^2} + \frac{\partial^2}{\partial y^2} + \frac{\partial^2}{\partial z^2} \quad (2.6)$$

is the Laplace operator. We have used the relationship between the total and partial derivative operations:

$$\frac{d}{dt} = \frac{\partial}{\partial t} + u \frac{\partial}{\partial x} + v \frac{\partial}{\partial y} + w \frac{\partial}{\partial z}. \quad (2.7)$$

Four forces appear in Eqs. 2.3, 2.4, and 2.5, all being normalized by mass and having the dimensions of acceleration. They are the pressure gradient force, the Coriolis force, the gravitational force, and the frictional force.

The *pressure gradient force*,

$$-\frac{1}{\rho} \nabla p = -\frac{1}{\rho} \left\{ \frac{\partial p}{\partial x}, \frac{\partial p}{\partial y}, \frac{\partial p}{\partial z} \right\}, \quad (2.8)$$

is a body force, meaning that it acts on every part of the air parcel regardless of whether the part is at the parcel's boundary or whether it is in the interior. This force is the ultimate reason for why the air moves from one place to another. The horizontal pressure gradient associated with a mid-latitude high-pressure system is about 1 hPa per 100 km, and the corresponding horizontal pressure gradient force per unit mass is on the order of $1 \times 10^{-3} \text{ m s}^{-2}$. The pressure gradient force associated with mesoscale circulations, such as the land-sea breeze, can be several times larger.

Pressure is not a standard prognostic variable in boundary-layer meteorological research. Unlike in dynamic meteorology where p is an unknown quantity to be solved from the equations of motion, in most situations encountered in boundary-layer meteorology the pressure gradient force is taken as a known external parameter. There are, however, at least two exceptions. First, the pressure gradient force near windbreaks, forest edges, and other isolated obstacles is several orders of magnitude larger than that at the synoptic scale. The exact value depends largely on wind speed and morphology and geometric configuration of these obstacles. The set of equations governing the flow disturbed by the obstacles must include the pressure gradient force as part of its predicting variables. Second, in the air layer occupied by a plant canopy, p is greater on the upstream side than on the downstream side of plant elements. This microscale discontinuity in the pressure field manifests itself as a retarding force on the flow and must be considered in the momentum equations (Chap. 5).

The *Coriolis force*, also a body force, arises from the fact that our coordinate frame is moving along with the rotating Earth. Its vector form is $\{fv, -fu, 0\}$. In the atmospheric boundary layer, this force acts to deflect the momentum of the air parcel in the $x - y$ plane. Its vertical component is approximately zero because the Coriolis effect on the vertical motion is negligible in comparison to the gravitational force. The *Coriolis parameter*, f , is dependent on latitude, ϕ , as

$$f = 2\Omega \sin \phi \quad (2.9)$$

where $\Omega (= 7.27 \times 10^{-5} \text{ s}^{-1})$ is the Earth's angular rotation velocity. According to Eq. 2.9, the Coriolis effect vanishes at the equator and increases with increasing latitude. In the northern hemisphere, the mid-latitude f value is approximately $1 \times 10^{-4} \text{ s}^{-1}$. In the southern hemisphere, f is negative. The Coriolis force increases linearly with the horizontal velocity of motion. At a horizontal air velocity of 10 m s^{-1} , the force per unit mass is approximately $1 \times 10^{-3} \text{ m s}^{-2}$ in magnitude, which is comparable to that of the pressure gradient force.

The *gravitational force*, the second term on the right side of the Eq. 2.5, is the third body force exerted on the air parcel. This force only appears in the vertical momentum equation. It is always directed downward as indicated by its negative sign. The gravitational force on a unit mass is equal to the gravitational acceleration $g (= 9.8 \text{ m s}^{-2})$ and is much greater than the horizontal pressure gradient force and the Coriolis force. In the mean atmospheric state, it is balanced by $-(1/\rho)\partial p/\partial z$, the vertical pressure gradient force of equally large magnitude. This state of balance is referred to as the *hydrostatic equilibrium*.

The *viscous force*, $\{\nu \nabla^2 u, \nu \nabla^2 v, \nu \nabla^2 w\}$, is an internal force due to the action of molecular friction. This force is local, existing only at the boundary of the air parcel and acting to reduce the air parcel's momentum. It is much smaller than the pressure gradient force except in the thin interfacial layer very close to the surface (Problem 2.3).

2.3 Conservation of Mass

The concentration of carbon dioxide in the atmosphere can be expressed as *mass density*, defined as mass per unit volume and denoted by ρ_c , or *mass mixing ratio*, defined as the ratio of the mass of carbon dioxide to the mass of dry air in the same air volume and denoted as s_c . They are related to one another, as

$$s_c = \frac{\rho_c}{\rho_d}, \quad (2.10)$$

where ρ_d is the mass density of dry air. The principle of dry air mass conservation is written for ρ_d , and that of carbon dioxide can be written for either ρ_c or s_c . The principles established for carbon dioxide are equally applicable to other trace gases in the atmosphere.

The mass conservation of dry air can be understood with a highly simplified situation shown in Fig. 2.2 (top panel). Here the flow exists only in the x direction. Let us consider, in the Cartesian coordinate, a small rectangular prism whose dimensions are δx , δy , and δz , in the x , y , and z direction, respectively. At a macroscopic scale, the prism is small enough to be considered essentially as a point in space. At a microscopic scale, the fluid parcel enclosed in the prism still contains numerous molecules. The continuum hypothesis states that properties of the fluid parcel, such as temperature, humidity, and CO₂ mixing ratio, vary between positions in a continuous fashion. Inside the prism, dry air is neither produced nor destroyed. Air enters the left side of the prism at velocity u_1 and dry air density $\rho_{d,1}$ and exits the right side at velocity u_2 and density $\rho_{d,2}$. The net *mass flux* is $-\delta y \delta z (u_2 \rho_{d,2} - u_1 \rho_{d,1})$ and is balanced by the time change of the mass in the prism:

$$\delta x \delta y \delta z \frac{\delta \rho_d}{\delta t} = -\delta y \delta z (u_2 \rho_{d,2} - u_1 \rho_{d,1}), \quad (2.11)$$

or

$$\frac{\delta \rho_d}{\delta t} + \frac{\delta u \rho_d}{\delta x} = 0, \quad (2.12)$$

where the notation δ is used for finite difference terms. Shrinking the prism to infinitesimally small dimensions, we obtain the derivative form of Eq. 2.12:

$$\frac{\partial \rho_d}{\partial t} + \frac{\partial u \rho_d}{\partial x} = 0. \quad (2.13)$$

Equation 2.13 can be easily extended to three dimensions, as

$$\frac{\partial \rho_d}{\partial t} + \frac{\partial u \rho_d}{\partial x} + \frac{\partial v \rho_d}{\partial y} + \frac{\partial w \rho_d}{\partial z} = 0. \quad (2.14)$$

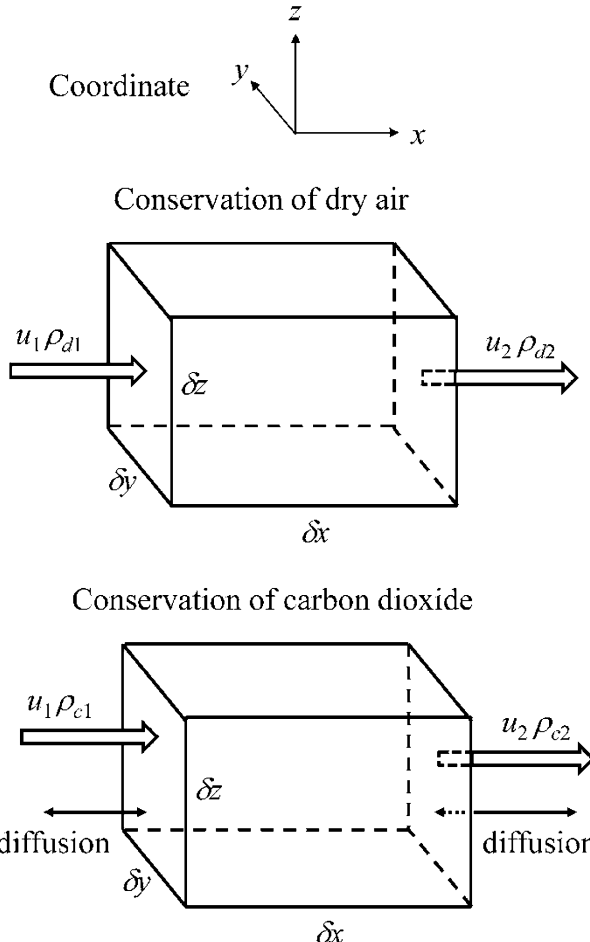


Fig. 2.2 A rectangular prism in a one-dimensional flow illustrating the mass conservation of dry air (top) and carbon dioxide (bottom)

Equation 2.14 is the general form of the *continuity equation*. Making use of Eq. 2.7, we can also rewrite it as

$$\frac{d\rho_d}{dt} + \rho_d \left(\frac{\partial u}{\partial x} + \frac{\partial v}{\partial y} + \frac{\partial w}{\partial z} \right) = 0. \quad (2.15)$$

With two modifications, the conservation equation for the mass density of CO₂, ρ_c , can be derived in a similar fashion. In the simplified situation shown in Fig. 2.2 (bottom panel), carbon dioxide enters or exits the prism both by mass flow $u\rho_c$ and by molecular diffusion $\kappa_c \partial \rho_c / \partial x$, where κ_c is molecular diffusivity of carbon dioxide

in air. Furthermore, carbon dioxide can be produced by sources inside the prism. Taking these two additional factors into account, the complete mass conservation equation for ρ_c is

$$\frac{\partial \rho_c}{\partial t} + \frac{\partial u \rho_c}{\partial x} + \frac{\partial v \rho_c}{\partial y} + \frac{\partial w \rho_c}{\partial z} = S_c + \kappa_c \nabla^2 \rho_c, \quad (2.16)$$

where S_c is a source term.

Equation 2.16 can be rearranged to a form analogous to Eq. 2.15:

$$\frac{d\rho_c}{dt} + \rho_c \left(\frac{\partial u}{\partial x} + \frac{\partial v}{\partial y} + \frac{\partial w}{\partial z} \right) = S_c + \kappa_c \nabla^2 \rho_c. \quad (2.17)$$

Strictly speaking, the source term S_c is not zero because CO_2 can be produced by oxidation of other compounds, such as methane and carbon monoxide, in the atmosphere. The rate of production is, however, negligible in comparison to the diffusion and the transport terms. Non-air elements, such as plant foliage, can be sources or sinks of CO_2 , but they are not allowed to exist in the infinitesimally small prism depicted in Fig. 2.2. Later in Chap. 8, we will incorporate the plant source term into the CO_2 mass conservation by performing a volume-averaging operation.

Atmospheric modelers do not use Eq. 2.16 or 2.17 in their model calculations. The primary reason is that ρ_c is not a conserved quantity, meaning that its time rate of change, $d\rho_c/dt$, in a parcel-following coordinate is not zero in situations where no sources are present, even with the molecular term being negligible. (Only by introducing the additional condition of incompressibility is ρ_c conserved.) Instead, their models are based on the conservation equation for the mass mixing ratio, s_c . It can be shown from Eqs. 2.10, 2.15, and 2.17 that the s_c conservation equation is

$$\frac{ds_c}{dt} = \frac{S_c}{\rho_d} + \kappa_c \nabla^2 s_c, \quad (2.18)$$

(Problem 2.4; Lee and Massman 2011). Later in the book, we will show that eddy fluxes based on the mass mixing ratio are consistent with this modeling principle, but those based on the mass density are not (Chap. 9).

Water vapor is an important gas in the atmosphere. The conservation of its mass density, ρ_v , and mass mixing ratio, s_v , is given by

$$\frac{\partial \rho_v}{\partial t} + \frac{\partial u \rho_v}{\partial x} + \frac{\partial v \rho_v}{\partial y} + \frac{\partial w \rho_v}{\partial z} = S_v + \kappa_v \nabla^2 \rho_v, \quad (2.19)$$

and

$$\frac{ds_v}{dt} = \frac{S_v}{\rho_d} + \kappa_v \nabla^2 s_v, \quad (2.20)$$

where κ_v is molecular diffusivity of water vapor in air and S_v is a vapor source term. If clouds are present in the boundary layer, the source term should be kept in the conservation equation to account for phase changes of water (evaporation of cloud droplets or condensation of water vapor to the liquid form). In a cloud-free boundary layer, the source term S_v can be omitted.

In mesoscale and synoptic scale weather systems, the vertical scale of motion is much smaller than the horizontal scale of motion. The continuity equation can be simplified to

$$\frac{\partial u}{\partial x} + \frac{\partial v}{\partial y} + \frac{\partial w}{\partial z} = 0. \quad (2.21)$$

This is the *incompressibility condition*. In this book, we call Eq. 2.21 the strong form of incompressibility, to distinguish it from the weak form of incompressibility at eddy scales. Under the condition set by Eq. 2.21, ρ_d becomes a conserved quantity, and ρ_c is also conserved in the absence of a source and molecular diffusion in the flow domain. Equation 2.21 should be used with caution. Problems 2.7, 2.8, and 2.12 are three examples that do not satisfy this condition.

2.4 Conservation of Energy

In the previous section, we deployed an imaginary rectangular prism to construct the mass conservation equations. In this Eulerian frame of reference, the prism is rigid, the air moves through the prism, and the observer remains in a fixed position keeping track of the mass balance between the mass flow, the diffusive flux, and the local time rate of change. That the prism is rigid makes this reference frame less ideal for constructing the heat conservation equation. Instead, we resort to a more convenient Lagrangian frame of reference, a reference frame that moves along with and at exactly the same speed of an imaginary air parcel. The time rate of change in this coordinate is formally expressed as the total derivative d/dt .

According to the first principle of thermodynamics, the time rate of change of the internal energy of the air parcel can be caused by energy added by an internal or external source, by the loss of energy to its surroundings through molecular diffusion, and by the work done to the environment through its volume expansion. In their classic text *Transport Phenomena*, Byron Bird, Warren Stewart, and Edwin Lightfoot express the principle of energy conservation as

$$\rho_d c_p \frac{dT}{dt} = \frac{dp}{dt} + \rho_d c_p S_T + \rho_d c_p \kappa_T \nabla^2 T, \quad (2.22)$$

(Bird et al. 2006), where c_p is the specific heat of air at constant pressure, T is temperature, S_T is a heat source term, and κ_T is molecular diffusivity of heat in air. The term on the left side of Eq. 2.22 is the time rate of increase in internal energy

in the parcel-following Lagrangian frame. On the right side of the equation, the first term represents the work done by volume expansion, the second term represents energy source term, and the third term represents net energy exchange with the surroundings via molecular diffusion.

The heat addition can come from an internal source, such as latent heat release from cloud condensation, or from an external source, such as net absorption of radiation energy. Small amounts of heat can also be generated internally by dissipation of turbulent kinetic energy and by chemical reactions. The heat source term is an important component of the energy conservation of a cloudy boundary layer but is generally omitted in cloud-free conditions.

Using relationships for ideal gases and the continuity equation (Eq. 2.15), we obtain from Eq. 2.22 another expression of the energy conservation:

$$\rho_d c_v \frac{dT}{dt} = -p \left(\frac{\partial u}{\partial x} + \frac{\partial v}{\partial y} + \frac{\partial w}{\partial z} \right) + \rho_d c_p S_T + \rho_d c_p \kappa_T \nabla^2 T, \quad (2.23)$$

where c_v is specific heat of air at constant volume. Equation 2.23 is less familiar to us than Eq. 2.22. We will come back to Eq. 2.23 in the discussion of different incompressibility constraints.

Equation 2.22 is awkward to use because it involves two prognostic variables, T and p . To overcome this problem, we introduce a composite variable called *potential temperature*:

$$\theta = T \left(\frac{p}{p_0} \right)^{-R_d/c_p}, \quad (2.24)$$

where p_0 is pressure at the mean sea level and R_d is the ideal gas constant for dry air. Here θ has the same dimension as T (K) and can be interpreted as the temperature the air parcel would have if it were moved adiabatically to the sea level (Fig. 2.3). The adiabatic process is a theoretical construct. It assumes that in the parcel's descent, no heat is lost via molecular diffusion to the surroundings, no molecules escape from the parcel, no heat source exists within the parcel, and changes to its temperature result only from the work done through its volume contraction. Despite these simplifications, θ is a useful variable for describing the thermal property of the atmosphere. Combining Eqs. 2.22 and 2.24, we obtain the conservation equation for θ :

$$\frac{d\theta}{dt} = S_\theta + \kappa_T \nabla^2 \theta, \quad (2.25)$$

where

$$S_\theta = S_T \left(\frac{p}{p_0} \right)^{-R_d/c_p}. \quad (2.26)$$

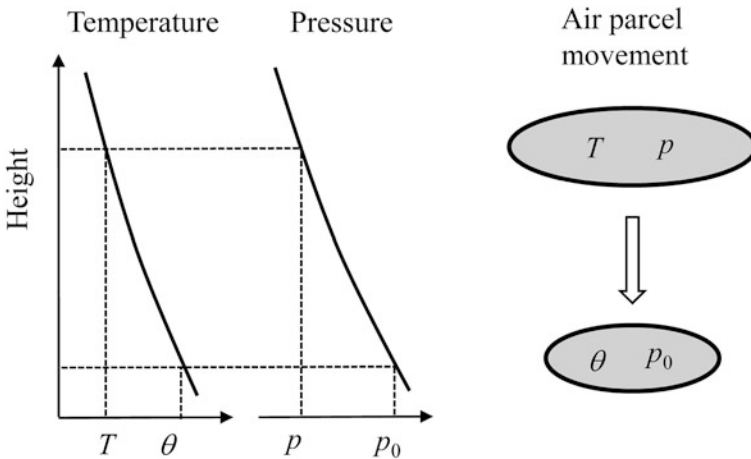


Fig. 2.3 In the adiabatic decent, an air parcel will shrink in response to increasing environmental pressure with decreasing altitude. The compression causes the parcel's temperature to rise

The superiority of working with θ over T is now apparent. Besides the fact that p has disappeared from the conservation equation, θ is a conserved variable in the adiabatic process.

2.5 The Ideal Gas Law

The deal gas law exists in several forms. The most common one relates pressure, a state variable, to two other state variables, density and temperature, as

$$p_d = \rho_d R_d T, \quad (2.27)$$

for dry air,

$$p_v = \rho_v R_v T, \quad (2.28)$$

for water vapor, and

$$p_c = \rho_c R_c T, \quad (2.29)$$

for carbon dioxide, where p_d , p_v , and p_c are partial pressure of dry air, water vapor, and carbon dioxide, respectively. The ideal gas constants are

$$R_d = \frac{R}{M_d}, \quad (2.30)$$

for dry air,

$$R_v = \frac{R}{M_v}, \quad (2.31)$$

for water vapor, and

$$R_c = \frac{R}{M_c}, \quad (2.32)$$

for carbon dioxide, where R ($= 8.314 \text{ J mol}^{-1} \text{ K}^{-1}$) is the universal gas constant and M_d ($= 0.029 \text{ kg mol}^{-1}$), M_v ($= 0.018 \text{ kg mol}^{-1}$), and M_c ($= 0.044 \text{ kg mol}^{-1}$) are molecular mass of dry air, water vapor, and carbon dioxide, respectively.

Combining the first law of thermodynamics and the ideal gas law for dry air (Eq. 2.27), we obtain the relationship

$$c_p - c_v = R_d. \quad (2.33)$$

The mass mixing ratio can be obtained from the partial pressures, as

$$s_c = \frac{M_c p_c}{M_d p_d}, \quad (2.34)$$

for carbon dioxide, and

$$s_v = \frac{M_v p_v}{M_d p_d}, \quad (2.35)$$

for water vapor. Traditionally, s_c is expressed in dimensions of $\mu\text{g g}^{-1}$ or mg kg^{-1} , and s_v in g kg^{-1} .

Similarly, the CO_2 *molar mixing ratio*, defined as the number of carbon dioxide molecules to the number of dry air molecules, can be obtained from

$$\chi_c = \frac{p_c}{p_d}. \quad (2.36)$$

The water vapor molar mixing ratio is given by

$$\chi_v = \frac{p_v}{p_d}. \quad (2.37)$$

The standard dimensions for χ_c and χ_v are $\mu\text{mol mol}^{-1}$ or ppm and mmol mol^{-1} , respectively.

The Dalton's law of partial pressures states

$$p = p_d + p_v + p_c + \dots \simeq p_d + p_v, \quad (2.38)$$

where p is total atmospheric pressure and is approximated by the sum of p_d and p_v . Contributions from carbon dioxide and other trace gases can be omitted without any significant consequences.

Finally, denoting the mass density of moist air as ρ and its ideal gas constant as R_m , we have the ideal gas law for moist air:

$$p = \rho R_m T, \quad (2.39)$$

Equation 2.39 is rarely used because the ideal gas “constant” R_m is no longer a constant but rather depends on humidity. Instead, we use a modified version:

$$p = \rho R_d T_v, \quad (2.40)$$

by introducing a new composite variable called *virtual temperature*

$$T_v = T(1 + 0.61q), \quad (2.41)$$

where q is *specific humidity*, defined as the ratio of the mass of water vapor to the mass of moist air, and is related to the water vapor mixing ratio as

$$q = \frac{s_v}{1 + s_v}. \quad (2.42)$$

2.6 The Surface Energy Balance

In Sect. 2.4, we applied the energy conservation principle to the air moving above the surface, focusing on the internal energy change. Energy conservation must also be satisfied at the surface, in that the flows of energy from and to the surface should be in balance. There are four forms of energy flow at the surface: (i) transfer of energy by electromagnetic waves (*radiation flux*), (ii) heat removed from the surface by evaporation or added to the surface by condensation of water (*latent heat flux*), (iii) transfer of heat by air motion (*sensible heat flux*), and (iv) molecular heat diffusion into or out of the surface (*conduction heat flux*).

Consider first a large, smooth, and bare soil surface. Let K_{\downarrow} be the total solar radiation incident on the surface. The radiation energy is in the shortwave band, with a wavelength range from about $0.3 \mu\text{m}$ to about $3 \mu\text{m}$. A fraction of K_{\downarrow} is reflected away from the surface:

$$K_{\uparrow} = \alpha K_{\downarrow}, \quad (2.43)$$

where α is *albedo*. The rest of the radiation is absorbed by the topmost soil layer. The surface also receives longwave radiation, L_{\downarrow} , from the atmosphere, with wavelength greater than $3 \mu\text{m}$. The fourth stream of radiation energy, the outgoing longwave

radiation from the surface, L_{\uparrow} , consists of a small portion of L_{\downarrow} reflected by the surface and radiation emitted by the surface:

$$L_{\uparrow} = (1 - \epsilon)L_{\downarrow} + \epsilon\sigma T_s^4, \quad (2.44)$$

where ϵ is emissivity, $\sigma (= 5.67 \times 10^{-8} \text{ W m}^{-2} \text{ K}^{-4})$ is the Stefan-Boltzmann constant, and T_s is surface temperature. The surface *net radiation*, $R_{n,0}$, is the balance of these four components:

$$R_{n,0} = K_{\downarrow} - K_{\uparrow} + L_{\downarrow} - L_{\uparrow}. \quad (2.45)$$

Since soils do not allow radiation penetration, we can assume that the soil layer that absorbs the solar radiation is infinitely thin and therefore has no mass or internal energy. So energy conservation requires that the flows of energy be in balance (Fig. 2.4a). Assuming no net horizontal energy flows in or out of the local domain, we can describe the surface energy balance with

$$R_{n,0} = H_0 + \lambda E_0 + G_0, \quad (2.46)$$

where H_0 is the surface sensible heat flux, λE_0 is the surface latent heat flux, and G_0 is the heat flux into the soil due to conduction.

Equation 2.46 follows the standard micrometeorological *sign convention*: $R_{n,0}$ is positive if the surface gains energy in the form of radiation and negative if the

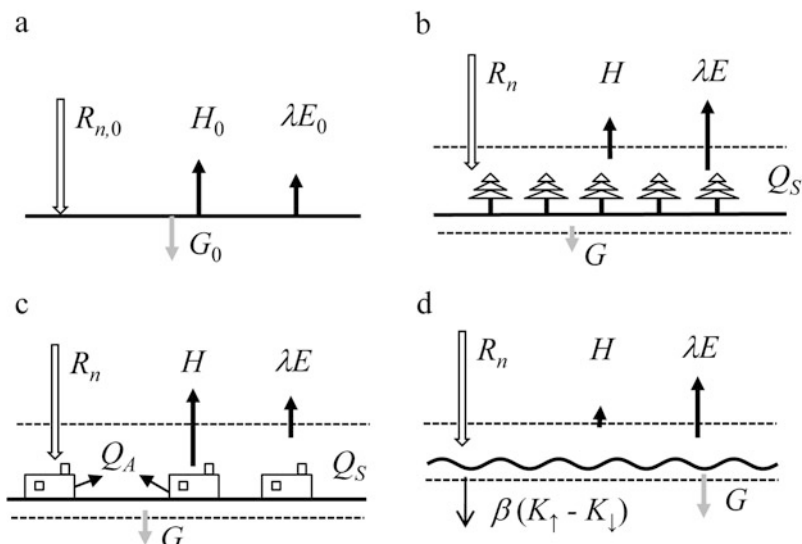


Fig. 2.4 The surface energy balance. (a), an idealized surface; (b), vegetated land; (c), urban land; (d), water surface

surface loses radiation energy; H_0 , λE_0 , and G_0 are positive if the fluxes are directed away from the surface and negative if they are directed toward the surface. Here E_0 is the surface evaporation rate or water vapor flux. The surface latent heat flux is the product of E_0 and the latent heat of vaporization λ ($= 2466 \text{ J g}^{-1}$ at temperature of 15°C).

Equation 2.46 and Fig. 2.4a depict an idealized situation in which all the energy fluxes are computed or hypothetically measured at the surface. This is usually true in a land surface model. In field campaigns, the net radiation and the sensible and the latent heat fluxes are measured at some height above the surface and the soil heat flux at a small depth beneath the surface, as shown in Fig. 2.4b. Some energy may be converted into internal energy and stored in the biomass and in the top soil layer, causing their temperatures to change. The appropriate energy balance equation is

$$R_n = H + \lambda E + G + Q_s, \quad (2.47)$$

where Q_s is a heat storage term. The sign convention for Q_s is that it is positive if the system (soil plus biomass) has gained internal energy and negative otherwise. We have dropped subscript “0” from the energy flux terms to indicate that they are not measured at the surface.

In an urban land, anthropogenic heat release, Q_A , is an additional energy input. The energy balance equation is

$$R_n + Q_A = H + \lambda E + G + Q_s. \quad (2.48)$$

The anthropogenic heat term is always positive.

Shifting attention now from land to water, we note that solar radiation, especially that in the visible waveband (wavelength $0.4\text{--}0.7 \mu\text{m}$), can penetrate deep into the water column. We can no longer assume that shortwave radiation absorption occurs in an infinitely thin surface water layer. Rather, the “surface” energy balance is constructed for a water layer of finite thickness (Fig. 2.4d). The complete energy balance equation is

$$R_n = H + \lambda E + G + Q_s + \beta(K_{\downarrow} - K_{\uparrow}), \quad (2.49)$$

where β is the fraction of net shortwave radiation that transmits through the surface water layer. Nearly all the solar radiation energy in the near-infrared waveband (wavelength from 0.7 to about $3 \mu\text{m}$) is absorbed in the top 0.6 m of the water column, so the surface water layer in land surface models is conveniently set to a thickness of 0.6 m .

In the above discussion, we have omitted minor energy sources and sinks in the natural environment, such as the kinetic energy released by raindrops upon impact on the surface, the chemical energy going into the biomass via photosynthesis, the heat released by microbial and plant respiration, and the heat produced by viscous dissipation of turbulent kinetic energy.

2.7 Problems

2.1* A sonic anemometer is mounted with its orientation toward N and at a downward tilt angle of 1° from the horizontal plane (Fig. 2.5). The instrument expresses the velocity in a right-handed Cartesian coordinate $\{x_1, y_1, z_1\}$. Assume that the true air velocity is 5.00 m s^{-1} and the velocity vector lies perfectly in a horizontal plane. Determine the vertical velocity w_1 in the z_1 direction as a function of wind direction. This would be the vertical velocity measured by the instrument. Note that wind direction is 0° if wind blows from N, 90° if from E, and so on.

2.2 Show that the viscous terms in Eqs. 2.3, 2.4, and 2.5 have the dimensions of acceleration.

2.3 The mean velocity profile in the surface layer under neutral stability is described by the logarithmic function

$$\bar{u} = \frac{u_*}{k} \ln\left(\frac{z}{z_0}\right), \quad (2.50)$$

where $k (=0.4)$ is the von Karman constant, u_* is friction velocity, z is height, and z_0 is momentum roughness. Assume that the mean lateral and vertical velocity components are zero, and $u_* = 0.52 \text{ m s}^{-1}$. Calculate the viscous force for two heights $z = 0.05$ and 10 m . Use a kinematic viscosity value of $\nu = 1.48 \times 10^{-5} \text{ m}^2 \text{ s}^{-1}$ at temperature 15°C for your calculations.

2.4 Derive the conservation equation for the CO_2 mass mixing ratio (Eq. 2.18) from Eqs. 2.15 and 2.17.

2.5 Using the ideal gas law relations and the continuity equation, derive the energy conservation Eq. 2.23 from Eq. 2.22.

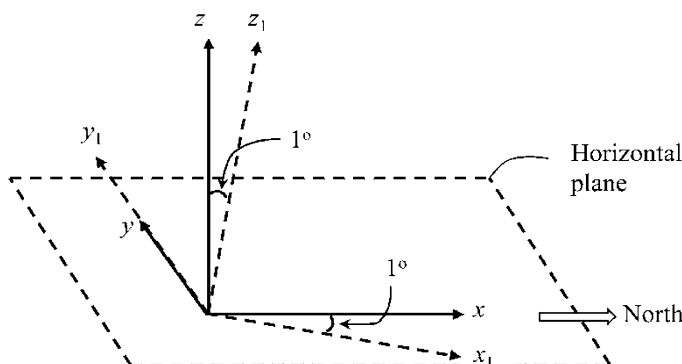


Fig. 2.5 A tilted instrument coordinate $\{x_1, y_1, z_1\}$

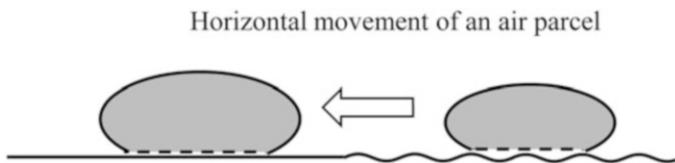


Fig. 2.6 Movement of an air parcel from a cool lake to a hot cement parking lot

2.6 Derive the potential temperature conservation Eq. 2.25 from the energy conservation Eq. 2.22.

2.7 Which of the following quantities of the air parcel are conserved during the dry adiabatic process shown in Fig. 2.3: air pressure, dry air density, air temperature, potential temperature, water vapor density, water vapor partial pressure, water vapor mixing ratio, carbon dioxide density, carbon dioxide partial pressure, and carbon dioxide mixing ratio? Is the incompressibility condition satisfied? (Note that no phase change of water occurs in the dry adiabatic process.)

2.8 An air parcel moves horizontally from a lake surface to a hot paved parking lot (Fig. 2.6). The situation is diabatic because the parcel can now exchange materials and energy with the surface through its bottom boundary which is in contact with the surface. Which of the quantities listed in Problem 2.7 are conserved? Is the incompressibility condition satisfied?

2.9 Show that the diffusion term of the energy conservation equation (third term on the right side of Eq. 2.22) has the same dimensions as the internal energy change term (term on the left) and the volume expansion term (first term on the right). In what dimensions should the source term S_T be?

2.10 The atmospheric pressure is 1000.2 hPa, the water vapor molar mixing ratio is 19.27 mmol mol⁻¹, and the carbon dioxide molar mixing ratio is 400.4 $\mu\text{mol mol}^{-1}$. Determine the partial pressures of dry air, water vapor, and carbon dioxide. What is the mass density of dry air, water vapor, and carbon dioxide if the air temperature is 15.0 °C?

2.11 CO₂ is a well-mixed gas in the lower atmosphere, meaning that its long-term mean mixing ratio does not vary with height. The global mean CO₂ molar mixing ratio was 396.5 $\mu\text{mol mol}^{-1}$ in 2013. Estimate the vertical CO₂ mass density gradient in the atmospheric boundary layer of the standard atmosphere. (Hints: In the standard atmosphere, the pressure and the temperature are 1013.2 hPa and 15.0 °C at the sea level and 898.7 hPa and 8.5 °C at the altitude of 1000 m. Use a typical water vapor mixing ratio of 15 g kg⁻¹ for both heights.)

2.12 An air parcel is adiabatically lifted upward from the sea level. Its initial temperature is 20.0 °C, its water vapor pressure is 6.22 hPa, and its CO₂ mass density is 800.0 mg m⁻³. What will be its temperature and CO₂ mass density when the parcel reaches the pressure height of 700 hPa?

- 2.13** The annual mean carbon dioxide flux of a forest is $-0.37 \text{ mg CO}_2 \text{ m}^{-2} \text{ s}^{-1}$. Express the flux in the dimensions of $\mu\text{mol m}^{-2} \text{ s}^{-1}$, $\text{g C m}^{-2} \text{ y}^{-1}$, $\text{g CO}_2 \text{ m}^{-2} \text{ y}^{-1}$, and $\text{t C ha}^{-1} \text{ y}^{-1}$.
- 2.14** A typical CH_4 flux in a mid-latitude wetland is $200 \text{ nmol m}^{-2} \text{ s}^{-1}$ in the warm season. Express the flux in the dimensions of $\mu\text{g CH}_4 \text{ m}^{-2} \text{ s}^{-1}$ and $\text{mg CH}_4 \text{ m}^{-2} \text{ d}^{-1}$.
- 2.15** The daily mean water vapor flux is $0.074 \text{ g m}^{-2} \text{ s}^{-1}$. How much water, in mm of water depth, is lost via evaporation in 1 day?
- 2.16** One estimate of the solar radiation incident on the Earth's surface is 175 W m^{-2} , the global mean surface albedo is 0.126, and the mean incoming and outgoing longwave radiations are 344 and 396 W m^{-2} , respectively (Zhao et al. 2013). Determine the global mean surface net radiation. The global mean annual precipitation is 1030 mm. If this precipitation water flux is balanced exactly by the surface evaporation rate, what are the global mean surface latent heat flux and sensible heat flux?
- 2.17** Bowen ratio, β , is the ratio of the surface sensible heat flux to the latent heat flux. A Bowen ratio apparatus determines β of a surface by measuring the vertical gradients of air temperature and humidity above the surface. The measured β is combined with simultaneous measurements of the available energy (net radiation $R_{n,0}$, soil heat flux G_0) to calculate the surface latent heat flux λE_0 . On the basis of the energy balance principle, derive an expression that relates λE_0 to β , $R_{n,0}$, and G_0 .
- 2.18** The incoming shortwave and longwave radiations are 750 and 419 W m^{-2} , respectively, at a subtropical lake at noon on a summer day. The lake surface temperature is 25.3°C , and the surface albedo is 0.06. Assuming that the lake surface is a black body, calculate the surface net radiation.
- 2.19** The water vapor pressure is 12.2 hPa , the atmospheric pressure is 984.5 hPa , the air temperature is 17.6°C , and the molar mixing ratio of CO_2 is $409.7 \mu\text{mol mol}^{-1}$. Find the CO_2 mass density in mg m^{-3} .
- 2.20** The air temperature is 15.9°C , the atmospheric pressure is 998.3 hPa , and the water vapor mass density is 23.6 g m^{-3} . Find the vapor mass and molar mixing ratios.
- 2.21** The methane and nitrous oxide molar mixing ratios are 2.89 ppm and 401.2 ppb , respectively. Find their mass mixing ratios.

References

- Bird RB, Stewart WE, Lightfoot EN (2006) Transport phenomena, 2nd edn. Wiley, New York, 905pp
- Kaimal JC, Finnigan JJ (1994) Atmospheric boundary layer flows: their structure and measurement. Oxford University Press, Oxford, 289pp

- Lee X, Massman W (2011) A perspective on thirty years of the Webb, Pearman and Leuning density corrections. *Bound-Layer Meteorol* 139:37–59
- Wilczak JM, Oncley SP, Stage SA (2001) Sonic anemometer tilt correction algorithms. *Bound-Layer Meteorol* 99:127–150
- Zhao L, Lee X, Liu S (2013) Correcting surface solar radiation of two data assimilation systems against FLUXNET observations in North America. *J Geophys Res Atmos* 118:9992–9564

Chapter 3

Governing Equations for Mean Quantities

3.1 Reynolds Decomposition

Motion in the atmospheric boundary layer is generally turbulent. The action of turbulence is evident when we observe the smoke plume released from a smokestack. The plume may whirl around, meander sideways, or loop up and down. These erratic patterns are visual clues of eddies at work. If we measure the flow with a fast-responding anemometer, we will find that the velocity fluctuates with time in a seemingly random manner. Air temperature, humidity, and other scalars also exhibit irregular temporal fluctuations. Details of the flow are impossible to predict. We have no way of determining the exact travel path of a smoke puff or predicting how the velocity changes from one second to the next. Rather our goal is to quantify the mean state of the atmosphere by performing averaging operation on the atmospheric properties.

Consider a continuous time series shown in Fig. 3.1. In a standard *Reynolds decomposition*, the instant value, a , is decomposed into a mean (\bar{a}) and a fluctuating part (a'):

$$a = \bar{a} + a', \quad (3.1)$$

where the mean part is given by

$$\bar{a} = \frac{1}{T} \int_0^T a dt, \quad (3.2)$$

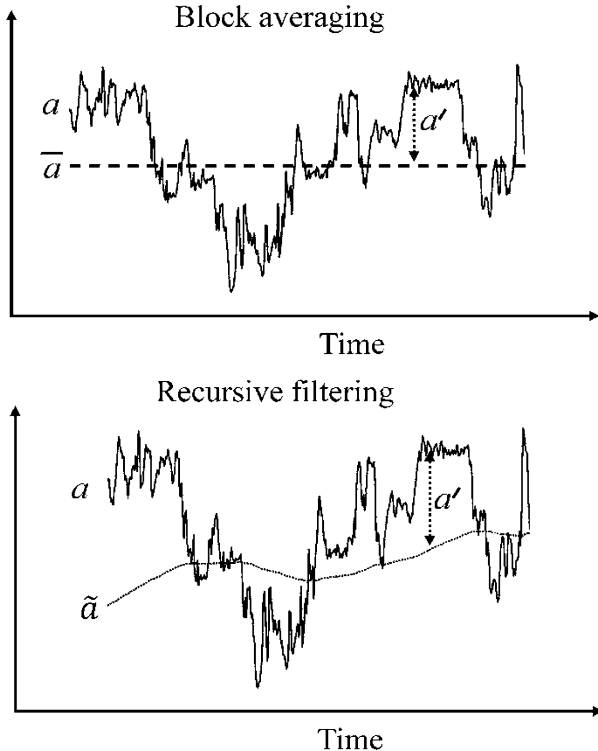


Fig. 3.1 Block averaging (top) and recursive filtering (bottom)

where T is averaging length and overbar denotes time averaging. This averaging operation is called *block averaging*. The Reynolds mean and fluctuating parts observe the following three rules:

$$\bar{\bar{a}} = \bar{a}, \quad (3.3)$$

$$\overline{a'} = 0, \quad (3.4)$$

and

$$\overline{ba'} = 0, \quad (3.5)$$

where \bar{b} is the Reynolds mean of variable b . An alternative expression to Eq. 3.5 is that the Reynolds mean of the product of a constant and the fluctuations of a variable is zero.

If a is a continuous function of time and space, time averaging and partial derivative operations are commutable:

$$\frac{\partial \bar{a}}{\partial t} = \frac{\partial \bar{a}}{\partial t}, \quad \frac{\partial \bar{a}}{\partial x} = \frac{\partial \bar{a}}{\partial x}, \quad \frac{\partial \bar{a}}{\partial y} = \frac{\partial \bar{a}}{\partial y}, \quad \frac{\partial \bar{a}}{\partial z} = \frac{\partial \bar{a}}{\partial z}. \quad (3.6)$$

These equations represent the fourth rule of Reynolds averaging. However, time averaging is not commutable with the total time derivative operation (Problem 3.5).

In Reynolds notation, the variance of a is $\overline{a'^2}$, and the covariance between a and b is $\overline{a'b'}$, where b' is the fluctuating part of b .

In field observations or modeling studies, time series data are obtained at discrete sampling intervals, t_f . This interval is constant in field measurements but can be variable in modeling studies. In the following, we only consider constant t_f . Operationally, the mean in the Reynolds decomposition is computed as

$$\bar{a} = \frac{1}{n} \sum_1^n a_i, \quad (3.7)$$

where n is the number of samples in a given observation interval and is equal to T/t_f and subscript i denotes measurement at time step i . The fluctuating part is given by

$$a'_i = a_i - \bar{a}. \quad (3.8)$$

The Reynolds properties (Eqs. 3.3, 3.4, and 3.5) still hold. The variance and covariance terms are computed as

$$\overline{a'^2} = \frac{1}{n} \sum_1^n a'^2_i, \quad (3.9)$$

$$\overline{a'b'} = \frac{1}{n} \sum_1^n a'_i b'_i. \quad (3.10)$$

A typical averaging length is 30 min, and a typical sampling interval is 0.1 s.

The averaging length and the sampling interval can be optimized through an *ogive analysis* on the covariance between temperature and the vertical velocity, $w'T'$ (Bradford et al. 2001). In the atmospheric boundary layer, eddies responsible for fluctuations seen in the T and w time series come in different sizes. Their contributions to the total covariance may be determined by a Fourier transformation of the signals from the time domain to the frequency domain. In the frequency domain, signals associated with larger eddies are registered at lower frequencies. The averaging length should be long enough so that the captured eddy contributions exceed some preset threshold, e.g., 99% of the total covariance. In practice, we look for an asymptotic behavior of cumulative contribution starting from the high-frequency end (Fig. 3.2a). The reciprocal of the frequency at which the cumulative curve starts to flatten is a good choice for T . Similarly, an optimal sampling interval should be short enough so that small eddies whose frequencies are greater than $1/t_f$ can be ignored. It can be determined by the asymptotic behavior of the cumulative contribution, but this time with the summation starting from the low-frequency end (Fig. 3.2b).

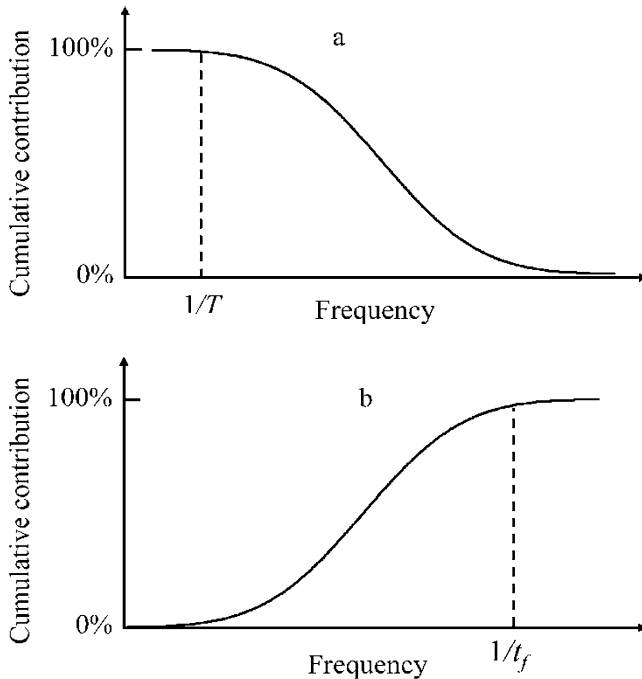


Fig. 3.2 Two ogives

Recursive filtering is another form of time averaging operation. In this case, measurement at previous time steps is used to compute a slow-varying trend at the current time step, and the fluctuating component is taken as the deviation of the total signal from this trend (Fig. 3.1). The most common recursive filter mimics the effect of a simple R-C circuit and operates mathematically as

$$\tilde{a}_i = \left(1 - \frac{t_f}{\tau}\right) \tilde{a}_{i-1} + \frac{t_f}{\tau} a_i, \quad (3.11)$$

and

$$a'_i = a_i - \tilde{a}_i \quad (3.12)$$

where τ is the filter's constant or “averaging length.” The variance and covariance statistics are then calculated with the fluctuating quantities according to Eqs. 3.9 and 3.10. This operation was attractive in the era of primitive computers because computation of Reynolds statistics could be done online without the need to store high-frequency raw data. A drawback is that it does not satisfy the Reynolds rules (Eqs. 3.3, 3.4, and 3.5) because the filtered part \tilde{a}_i is not constant over time but instead consists of a mean component and a slow-varying fluctuating component. The mean governing equations, which form the theoretical basis for interpretation of the flow and the associated diffusion processes, are however derived from these

rules. So statistics resulting from recursive filtering are not consistent with these equations, and their interpretation can be ambiguous.

Time averaging is the only practical choice of averaging operation for measurements made at a single point in space. In a model domain, both time averaging and spatial averaging can be used. A common *spatial averaging* operator involves data in the x - y plane, as

$$\langle a \rangle = \frac{1}{A} \iint_{D_A} a \, dx \, dy, \quad (3.13)$$

for the mean part, and

$$a'' = a - \langle a \rangle \quad (3.14)$$

for the fluctuating part, where A is area of the averaging domain D_A in the x - y plane. The variance and covariance are calculated similarly to Eqs. 3.9 and 3.10. This averaging operation filters out unwanted horizontal variations, producing a smooth vertical profile $\langle a \rangle$ as a function of time. The spatial averaging operation satisfies the same Reynolds rules defined by Eqs. 3.3, 3.4, 3.5, and 3.6 except that the temporal averaging is replaced by spatial averaging and temporal fluctuations by spatial fluctuations.

Several situations call for other averaging operations in order to obtain the desired mean properties of the flow. *Line averaging* is used for turbulence measurements taken on an airplane, with each averaging path coinciding with a horizontal transect of the airplane's flight path. The fluctuating part is now a composite signal of temporal and spatial variations. In large-eddy simulation of the flow, volume averaging over the model's grid spacing is applied to the governing equations to obtain grid mean variables. Fluctuations associated with eddies smaller than the grid size are not resolved; instead their roles in transport processes are captured by subgrid parameterizations. Volume averaging is also used to formulate a canopy drag force on the flow from pressure variations inside a plant canopy (Chap. 5).

3.2 Flow Incompressibility

Having established familiarity with the Reynolds rules, we are now ready to derive governing equations for the mean flow quantities. Let us start with the simple equation of incompressibility (Eq. 2.21) to illustrate how this is done. Decomposing the velocity components into a mean and a fluctuating part, we can rewrite Eq. 2.21 as

$$\frac{\partial(\bar{u} + u')}{\partial x} + \frac{\partial(\bar{v} + v')}{\partial y} + \frac{\partial(\bar{w} + w')}{\partial z} = 0. \quad (3.15)$$

Performing block averaging on this equation, applying the Reynolds rules, and noting the fact that averaging and addition are commutable, we obtain

$$\frac{\partial \bar{u}}{\partial x} + \frac{\partial \bar{v}}{\partial y} + \frac{\partial \bar{w}}{\partial z} = 0. \quad (3.16)$$

This is the incompressibility equation for the mean velocities. Subtracting Eq. 3.16 from Eq. 3.15, we obtain the incompressibility constraint on the fluctuating velocities:

$$\frac{\partial u'}{\partial x} + \frac{\partial v'}{\partial y} + \frac{\partial w'}{\partial z} = 0. \quad (3.17)$$

According to Eq. 3.16, a mean vertical motion must be present to compensate for horizontal flow divergence. Non-zero flow divergence exists if the flow field is not horizontally homogeneous. The relationship between \bar{w} and horizontal flow divergence, $\partial \bar{u}/\partial x + \partial \bar{v}/\partial y$, is

$$\bar{w}(z) = \int_0^z - \left(\frac{\partial \bar{u}}{\partial x} + \frac{\partial \bar{v}}{\partial y} \right) dz' \quad (3.18)$$

where \bar{w} is zero at the surface.

The strong incompressibility condition (Eq. 2.21) allows us to study the dynamics of atmospheric flows. In Chap. 2, we introduced three momentum equations. There are however four unknowns (u, v, w, p) in these equations. With the addition of Eq. 2.21, the number of equations is the same as the number of unknowns. In mathematical terms, the system is now said to be closed. System closure is a necessary condition before a solution can be sought. Similarly, Eq. 3.16 aids our efforts to solve the mean momentum equations.

When dealing with the transport of heat and gases in the atmospheric boundary layer, we should treat the incompressibility constraint with caution, or else erroneous results may arise. If we accept the strong incompressibility constraint, we would not permit any work to be performed by an air parcel on its surroundings. According to Eqs. 2.21 and 2.23, the heat conservation equation would be reduced to

$$\rho_d c_v \frac{dT}{dt} = \rho_d c_p S_T + \rho_d c_p \kappa_T \nabla^2 T. \quad (3.19)$$

Applying the Reynolds averaging operation, we would obtain an eddy flux term, $\rho_d c_v w' T'$. This is an incorrect formulation for the surface sensible heat flux.

In the case of gaseous transport, if we accept Eq. 2.21, we would obtain from Eq. 2.17 the following mass conservation equation:

$$\frac{d\rho_c}{dt} = S_c + \kappa_c \nabla^2 \rho_c \quad (3.20)$$

This equation has the same form as the conservation equation for the mixing ratio s_c (Eq. 2.18). Since S_c is negligible, Eq. 3.20 predicts erroneously that ρ_c is a conserved quantity, much like the potential temperature, during the adiabatic process. Later in Chap. 9, we will show that Eq. 3.20 would lead to the wrong conclusion that the eddy flux term $\overline{w' \rho'_c}$ is equivalent to the true surface-air exchange of carbon dioxide under steady-state and horizontal homogeneity conditions. In other words, density effects on the eddy flux of carbon dioxide would vanish completely under the incompressibility assumption.

In the following derivation of mean governing equations, we will avoid using Eq. 2.21, but will need Eq. 3.17 to obtain Reynolds covariance terms. Equation 3.17 is a *weak form of the incompressibility constraint*. Even though it can be derived from Eq. 2.21, use of Eq. 3.17 does not imply that the instant velocity components satisfy Eq. 2.21. At present, we do not know how to quantify the uncertainty Eq. 3.17 may introduce to observational and modeling studies in boundary-layer meteorology.

3.3 The Mean Equations for Velocity, Mixing Ratio, and Potential Temperature

The derivation of governing equations on the mean velocity components is relatively straightforward. Applying Reynolds decomposition to momentum Eqs. 2.3, 2.4, and 2.5, performing block averaging, and using the Reynolds rules (Eqs. 3.3, 3.4, 3.5, and 3.6), we obtain

$$\begin{aligned} \frac{\partial \bar{u}}{\partial t} + \bar{u} \frac{\partial \bar{u}}{\partial x} + \bar{v} \frac{\partial \bar{u}}{\partial y} + \bar{w} \frac{\partial \bar{u}}{\partial z} = \\ -\frac{1}{\bar{\rho}} \frac{\partial \bar{p}}{\partial x} + f \bar{v} + \nu \nabla^2 \bar{u} + \left(-\frac{\partial \bar{u}'^2}{\partial x} - \frac{\partial \bar{u}' \bar{v}'}{\partial y} - \frac{\partial \bar{u}' \bar{w}'}{\partial z} \right), \end{aligned} \quad (3.21)$$

$$\begin{aligned} \frac{\partial \bar{v}}{\partial t} + \bar{u} \frac{\partial \bar{v}}{\partial x} + \bar{v} \frac{\partial \bar{v}}{\partial y} + \bar{w} \frac{\partial \bar{v}}{\partial z} = \\ -\frac{1}{\bar{\rho}} \frac{\partial \bar{p}}{\partial y} - f \bar{u} + \nu \nabla^2 \bar{v} + \left(-\frac{\partial \bar{u}' \bar{v}'}{\partial x} - \frac{\partial \bar{v}'^2}{\partial y} - \frac{\partial \bar{v}' \bar{w}'}{\partial z} \right), \end{aligned} \quad (3.22)$$

and

$$\begin{aligned} \frac{\partial \bar{w}}{\partial t} + \bar{u} \frac{\partial \bar{w}}{\partial x} + \bar{v} \frac{\partial \bar{w}}{\partial y} + \bar{w} \frac{\partial \bar{w}}{\partial z} = \\ -\frac{1}{\bar{\rho}} \frac{\partial \bar{p}}{\partial z} - g + \nu \nabla^2 \bar{w} + \left(-\frac{\partial \bar{u}' \bar{w}'}{\partial x} - \frac{\partial \bar{v}' \bar{w}'}{\partial y} - \frac{\partial \bar{w}'^2}{\partial z} \right), \end{aligned} \quad (3.23)$$

where we have used the weak incompressibility constraint (Eq. 3.17) to obtain the Reynolds covariance terms. For example, to derive Eq. 3.21 from Eq. 2.3, we have used

$$\begin{aligned} u' \frac{\partial u'}{\partial x} + v' \frac{\partial u'}{\partial y} + w' \frac{\partial u'}{\partial z} &= \frac{\partial u'^2}{\partial x} + \frac{\partial u'v'}{\partial y} + \frac{\partial u'w'}{\partial z} - u' \left(\frac{\partial u'}{\partial x} + \frac{\partial v'}{\partial y} + \frac{\partial w'}{\partial z} \right) \\ &= \frac{\partial u'^2}{\partial x} + \frac{\partial u'v'}{\partial y} + \frac{\partial u'w'}{\partial z}. \end{aligned} \quad (3.24)$$

These mean equations bear strong similarity to the momentum equations for the instant velocities (Eqs. 2.3, 2.4, and 2.5). The terms on the left side of Eqs. 3.21, 3.22, and 3.23 represent mean acceleration, and on the right side of the equations, the pressure gradient force, the Coriolis force, and the molecular friction force are now expressed with mean flow quantities. The extra terms in the parentheses consist of spatial derivatives of Reynolds variances (e.g., $\overline{u'^2}$) and covariances (e.g., $\overline{u'w'}$). Like molecular friction, these terms act as retarding forces on the mean motion. Thus, a consequence of velocity fluctuations is that they slow down the air motion. Resulting from averaging of the nonlinear terms, such as $u(\partial w/\partial z)$, in the original equations, the Reynolds velocity covariances represent *turbulent momentum fluxes* or transport of momentum by turbulent eddies.

The governing equations for the carbon dioxide mean density ($\bar{\rho}_c$) and mixing ratio (\bar{s}_c) and the mean potential temperature ($\bar{\theta}$) can be derived similarly from Eqs. 2.16, 2.18, and 2.25

$$\begin{aligned} \frac{\partial \bar{\rho}_c}{\partial t} + \frac{\partial \bar{u} \bar{\rho}_c}{\partial x} + \frac{\partial \bar{v} \bar{\rho}_c}{\partial y} + \frac{\partial \bar{w} \bar{\rho}_c}{\partial z} = \\ \kappa_c \nabla^2 \bar{\rho}_c - \left(\frac{\partial \overline{u' \rho'_c}}{\partial x} + \frac{\partial \overline{v' \rho'_c}}{\partial y} + \frac{\partial \overline{w' \rho'_c}}{\partial z} \right), \end{aligned} \quad (3.25)$$

$$\begin{aligned} \frac{\partial \bar{s}_c}{\partial t} + \bar{u} \frac{\partial \bar{s}_c}{\partial x} + \bar{v} \frac{\partial \bar{s}_c}{\partial y} + \bar{w} \frac{\partial \bar{s}_c}{\partial z} = \\ \kappa_c \nabla^2 \bar{s}_c - \left(\frac{\partial \overline{u' s'_c}}{\partial x} + \frac{\partial \overline{v' s'_c}}{\partial y} + \frac{\partial \overline{w' s'_c}}{\partial z} \right), \end{aligned} \quad (3.26)$$

and

$$\begin{aligned} \frac{\partial \bar{\theta}}{\partial t} + \bar{u} \frac{\partial \bar{\theta}}{\partial x} + \bar{v} \frac{\partial \bar{\theta}}{\partial y} + \bar{w} \frac{\partial \bar{\theta}}{\partial z} = \\ \kappa_T \nabla^2 \bar{\theta} - \left(\frac{\partial \overline{u' \theta'}}{\partial x} + \frac{\partial \overline{v' \theta'}}{\partial y} + \frac{\partial \overline{w' \theta'}}{\partial z} \right). \end{aligned} \quad (3.27)$$

Once again, the Reynolds averaging operation has produced additional terms. These terms consist of spatial derivatives of velocity-scalar covariances and are given in the parentheses on the right side of the equations. In analogy to molecular diffusion, these covariances represent turbulent transport of carbon dioxide and sensible heat. In other words, the result of velocity and scalar fluctuations is a diffusive transport of energy and materials in the atmosphere. Turbulent transport is one factor contributing to the local time rate of change in the mean scalar quantities (first term on the left side of Eqs. 3.25, 3.26, and 3.27). Other contributors of the temporal change are horizontal (second and third term on the left) and vertical advection (third term on the left) and molecular diffusion (first term on the right).

We have omitted the source terms in the above equations. This omission is acceptable for CO₂ because chemical production of CO₂ in free air is negligible and is a good approximation for heat in a cloud-free and clean boundary layer. If clouds are present or if the boundary layer contains a large amount of aerosols, a source term should be put back in Eq. 3.27 to account for absorption and emission of radiation energy and phase changes of water.

The equation for the mean water vapor mixing ratio, \bar{s}_v , has the same form as Eq. 3.26

$$\begin{aligned} \frac{\partial \bar{s}_v}{\partial t} + \bar{u} \frac{\partial \bar{s}_v}{\partial x} + \bar{v} \frac{\partial \bar{s}_v}{\partial y} + \bar{w} \frac{\partial \bar{s}_v}{\partial z} = \\ \kappa_v \nabla^2 \bar{s}_v - \left(\frac{\partial \bar{u}' s'_v}{\partial x} + \frac{\partial \bar{v}' s'_v}{\partial y} + \frac{\partial \bar{w}' s'_v}{\partial z} \right), \end{aligned} \quad (3.28)$$

(Problem 3.8). In this equation, the Reynolds velocity-vapor mixing ratio covariances represent turbulent diffusion fluxes of water vapor in the atmosphere.

Equations 3.16, 3.21, 3.22, 3.23, 3.26, 3.27, and 3.28 comprise the theoretical framework that underpins quantitative analysis of phenomena in the atmospheric boundary layer. Modelers use these equations to predict flow patterns and diffusion transport in the atmospheric boundary layer. Experimentalists use them as guidance to design field campaigns and for data interpretation.

3.4 Simplified One-Dimensional Equations

Surface boundary conditions strongly affect the vertical distributions of velocity, temperature, and gaseous abundance in the atmospheric boundary layer. The vertical gradients of these quantities are generally much larger than their horizontal gradients. To emphasize the surface influence, we introduce two approximations, (i) that horizontal velocity derivatives are zero:

$$\frac{\partial \bar{u}}{\partial x} = \frac{\partial \bar{v}}{\partial x} = \frac{\partial \bar{u}}{\partial y} = \frac{\partial \bar{v}}{\partial y} = 0, \quad (3.29)$$

and (ii) that horizontal derivatives of the temperature and the gaseous mixing ratios are zero:

$$\frac{\partial \bar{s}_v}{\partial x} = \frac{\partial \bar{s}_v}{\partial y} = 0, \quad \frac{\partial \bar{s}_c}{\partial x} = \frac{\partial \bar{s}_c}{\partial y} = 0, \quad \frac{\partial \bar{\theta}}{\partial x} = \frac{\partial \bar{\theta}}{\partial y} = 0. \quad (3.30)$$

The first approximation states that the flow is horizontally homogeneous, and the second implies that the surface source strengths of heat, water vapor, and carbon dioxide are invariant in the $x - y$ directions. From now on, we will also ignore the molecular terms because they are much smaller in magnitude than their turbulent counterparts. With these approximations, the mean equations are reduced to the one-dimensional form:

$$\frac{\partial \bar{u}}{\partial t} = -\frac{1}{\bar{\rho}} \frac{\partial \bar{p}}{\partial x} + f \bar{v} - \frac{\partial \bar{u}' w'}{\partial z}, \quad (3.31)$$

$$\frac{\partial \bar{v}}{\partial t} = -\frac{1}{\bar{\rho}} \frac{\partial \bar{p}}{\partial y} - f \bar{u} - \frac{\partial \bar{v}' w'}{\partial z}, \quad (3.32)$$

$$\frac{\partial \bar{\theta}}{\partial t} = -\frac{\partial \bar{w}' \theta'}{\partial z}, \quad (3.33)$$

$$\frac{\partial \bar{s}_v}{\partial t} = -\frac{\partial \bar{w}' s'_v}{\partial z}, \quad (3.34)$$

and

$$\frac{\partial \bar{s}_c}{\partial t} = -\frac{\partial \bar{w}' s'_c}{\partial z}. \quad (3.35)$$

The vertical momentum equation is no longer needed because horizontal flow homogeneity implies zero flow divergence and therefore zero mean vertical velocity everywhere in the domain (Eq. 3.18). Except for pressure, quantities that appear in these equations are functions of t and z but are invariant in the $x - y$ plane.

At first glance, the assumption of horizontal flow homogeneity seems contradictory. Air motion owes its existence to the pressure gradient force. The same force, when interacting with the surface friction, will generate horizontal flow divergence. So strictly speaking, the spatial velocity derivatives $\partial \bar{u} / \partial x$ and $\partial \bar{v} / \partial y$ cannot be zero as long as the wind is blowing. Fortunately, in the absence of a local disturbance to the flow, the effect of flow divergence is much weaker than the Coriolis and the pressure gradient force and can be omitted from the momentum equations. In Chap. 2, we said that these two forces are on the order of $1 \times 10^{-3} \text{ m s}^{-2}$. The flow divergence rate frequently used for scale analysis of synoptic weather systems is on the order of $1 \times 10^{-5} \text{ s}^{-1}$. Assuming that all divergence occurs in the x direction so that $\partial \bar{u} / \partial x = 1 \times 10^{-5} \text{ s}^{-1}$ and that a typical \bar{u} is 10 m s^{-1} , the horizontal advection term, $\bar{u}(\partial \bar{u} / \partial x)$, is on the order of $1 \times 10^{-4} \text{ m s}^{-2}$.

We have now established a complete set of equations for the one-dimensional atmospheric boundary layer. The choice of which equations to use will depend on the task at hand. To study flow dynamics in a neutral boundary layer, the two momentum equations (Eqs. 3.31 and 3.32) will suffice. In neutral stability, turbulence is generated by vertical wind shear, and buoyancy does not play a role. If the atmosphere is stratified, or if we are interested in heat and water vapor transport, we will also need Eqs. 3.33 and 3.34 to account for buoyancy generation and destruction of turbulence and to quantify the transport processes. The study of transport of carbon dioxide will require all the five equations, relying on Eqs. 3.31, 3.32, 3.33, and 3.34 for determining flow characteristics and on Eq. 3.35 for determining turbulent transport of carbon dioxide.

The surface influence is felt most strongly in the atmospheric surface layer. Figure 3.3 shows typical mean profiles of wind speed, air temperature, humidity, and carbon dioxide concentration over a plant canopy in the daytime. These profile shapes can be used to infer how the associated Reynolds covariances should behave.

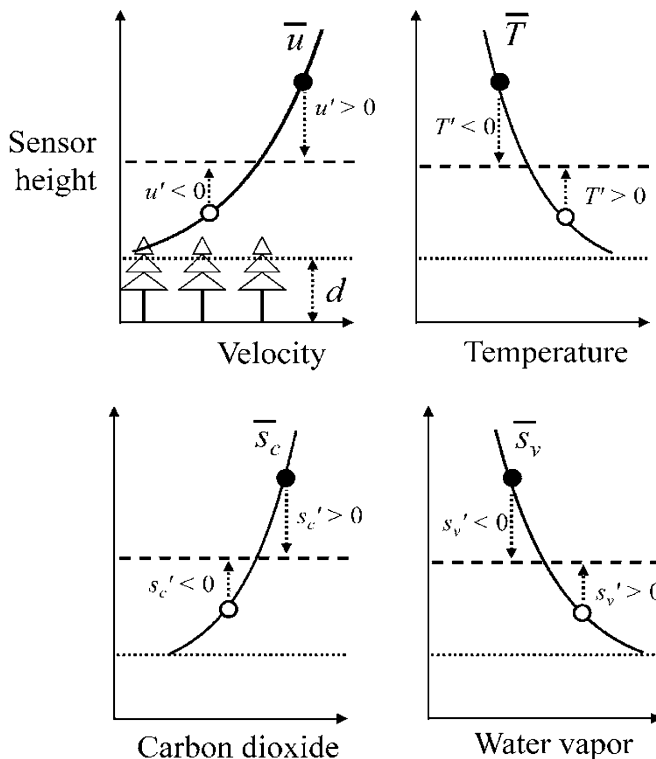


Fig. 3.3 Daytime profiles of mean quantities and Reynolds fluctuations in the atmospheric surface layer over a vegetation canopy: u , horizontal velocity; T , temperature; s_v , water vapor mixing ratio; s_c : CO₂ mixing ratio; d , displacement height. The *open* and *closed* symbols indicate upward and downward moving eddies, respectively, and the *arrows* indicate their directions of movement

Turbulent motion is a mixture of upward and downward moving eddies. An upward moving eddy creates a positive fluctuating vertical velocity ($w' > 0$). It is imprinted with conditions of its point of origin, which is characterized by lower horizontal velocity, and is warmer, more humid, and less abundant in carbon dioxide than the mean state at the observational height. The instrument will likely register $u' < 0$, $T' > 0$, $s'_v > 0$, and $s'_c < 0$. Conversely, there is a tendency that $u' > 0$, $T' < 0$, $s'_v < 0$, and $s'_c > 0$ in association with a downward moving eddy ($w' < 0$). Averaging over a large number of eddies, we expect $\overline{u'w'} < 0$, $\overline{w'T'} > 0$, $\overline{w's'_v} > 0$, and $\overline{w's'_c} < 0$.

We can also predict the behavior of those covariances that do not involve the vertical velocity. In the situation shown in Fig. 3.3, the $u - T$ covariance is negative. More generally, the $u - T$ covariance is in opposite sign as the $w - T$ covariance in the atmospheric surface layer.

3.5 The Closure Problem

A fundamental challenge in the studies of turbulent flow is that the number of unknowns exceeds the number of mean equations. This *closure problem* arises from the fact Reynolds averaging generates variances and covariances from nonlinear terms in the instant equations. In the one-dimensional situation described above, ten variables (\bar{u} , \bar{v} , $\bar{\theta}$, \bar{s}_v , \bar{s}_c , $\overline{u'w'}$, $\overline{v'w'}$, $\overline{w'\theta'}$, $\overline{w's'_v}$, $\overline{w's'_c}$) are unknown, but we only have five equations to constrain them. To circumvent the problem, we will need five more equations. The additional equations, called *turbulence closure parameterizations*, are not derived from fundamental laws of thermodynamics and physics. Rather they are empirical expressions that capture our understanding on how Reynolds covariances should behave in the atmospheric boundary layer.

The most common parameterization scheme relates a Reynolds covariance to the spatial gradient of the relevant mean quantity. Specifically, the five covariances in Eqs. 3.31, 3.32, 3.33, 3.34, and 3.35 are given as

$$\overline{u'w'} = -K_m \frac{\partial \bar{u}}{\partial z}, \quad (3.36)$$

$$\overline{v'w'} = -K_m \frac{\partial \bar{v}}{\partial z}, \quad (3.37)$$

$$\overline{w'\theta'} = -K_h \frac{\partial \bar{\theta}}{\partial z}, \quad (3.38)$$

$$\overline{w's'_v} = -K_v \frac{\partial \bar{s}_v}{\partial z}, \quad (3.39)$$

$$\overline{w's'_c} = -K_c \frac{\partial \bar{s}_c}{\partial z}. \quad (3.40)$$

The free parameters in these equations, K_m , K_h , K_v , and K_c , are termed *eddy diffusivities*, all having the dimensions of $\text{m}^2 \text{s}^{-1}$. Subscripts m , h , v , and c are used to denote eddy diffusivity for momentum, sensible heat, water vapor, and carbon dioxide, respectively. Combining the parameterization Eqs. 3.36, 3.37, 3.38, 3.39, and 3.40 with the governing Eqs. 3.31, 3.32, 3.33, 3.34, and 3.35, we have the same number of equations as the number of unknowns, and it is now possible to seek solutions. The Ekman wind profile in Chap. 6 is a good demonstration for how this is done.

Equations 3.36, 3.37, 3.38, 3.39, and 3.40 state that the strength of turbulent diffusion is proportional to the spatial gradient of the mean state quantity of interest. The negative sign in these equations ensures that the diffusion flux is directed down the gradient from a position of higher to a position of lower momentum, temperature, or gaseous concentration. This *flux-gradient relationship* is consistent with the inference we have made regarding the sign of the Reynolds covariances (Fig. 3.3). If the surface source or sink is turned off, turbulent diffusion will eventually destroy the vertical gradient. In these respects, turbulent and molecular diffusion are similar. In molecular transport, diffusion is accomplished by Brownian motion of molecules, with molecular diffusivity being proportional to the product of molecular mean free path and mean vibration velocity. In turbulent transport, diffusion is achieved by movement of eddies, and eddy diffusivity can be formulated in a similar way, using a velocity scale for the eddies and a length scale for their mean “travel path,” as we will demonstrate shortly.

Turbulent and molecular diffusion are different in two aspects. The first major distinction is that molecular diffusivity is a property of the fluid, and eddy diffusivity is a property of the flow. In an isothermal fluid, molecular diffusivity is constant everywhere, whereas eddy diffusivity is highly variable in space and time depending on local velocity and distance to the surface. Secondly, molecular diffusivity depends on molecular mass. For example, molecular diffusivity of water vapor in the atmosphere is 60% greater than that of carbon dioxide. In contrast, turbulent diffusion is not discriminating. Turbulent eddies are equally efficient in transporting heat, carbon dioxide, water vapor, and any other scalar quantities of interest. We can safely assume

$$K_h = K_v = K_c. \quad (3.41)$$

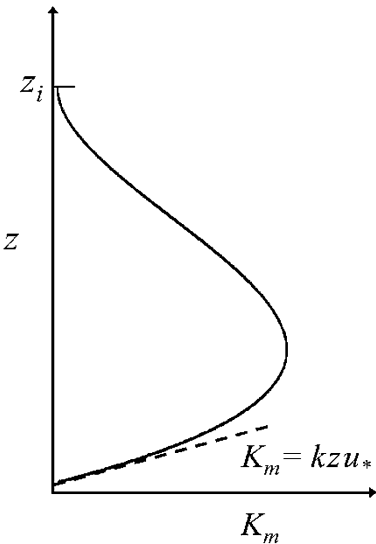
In the following, we will present formulations for K_h only, but it is understood that the same formulations are also applicable to eddy diffusion of other scalars.

Experimental evidence shows that shear-generated eddies transport momentum and scalars with equal efficiency, resulting in

$$K_m = K_h, \quad (3.42)$$

under neutral and stable conditions. Equation 3.42 does not hold in unstable conditions where buoyancy-generated eddies transport scalars much more efficiently than momentum and K_m is smaller than K_h . In other words, the turbulent Prandtl

Fig. 3.4 Eddy diffusivity for momentum in a neutral boundary layer, where u_* is friction velocity and z_i is boundary-layer depth. The solid line represents parameterization Eq. 3.52 and the dashed line is its asymptotic behavior in the surface layer



number and the turbulent Schmidt number, defined as the ratio of the momentum eddy diffusivity to the eddy diffusivity for heat and to the eddy diffusivity for mass, respectively, are equal to unity in neutral and stable conditions and are less than unity in unstable conditions.

Under neutral stability, eddy diffusivity over a smooth surface is parameterized as

$$K_m = K_h = kz u_* \quad (3.43)$$

where the proportionality factor k is the von Karman constant, u_* is *friction velocity*, and z is height above the surface (Fig. 3.4). Extensive wind tunnel studies and micrometeorological measurements have shown that the best value for k is 0.4. Here u_* is an eddy velocity scale and

$$l = kz, \quad (3.44)$$

is an eddy length scale called Prandtl's mixing length. Formally, u_* is defined as

$$u_* = (-\overline{u'w'})^{1/2}, \quad (3.45)$$

in the micrometeorological coordinate (Fig. 2.1) or

$$u_* = [(\overline{u'w'})^2 + (\overline{v'w'})^2]^{1/4}, \quad (3.46)$$

in a general Cartesian coordinate. The u_* definition is based on the velocity covariances measured in the surface layer.

If the surface upwind of the observational point is sufficiently large and uniform, the turbulent fluxes will be nearly constant with height in the surface layer. It follows from Eqs. 3.36, 3.43, and 3.45 that under the constant flux approximation, the solution for \bar{u} is given by

$$\bar{u} = \frac{u_*}{k} \ln \frac{z}{z_o} \quad (3.47)$$

where z_o is *momentum roughness*. Equation 3.47 describes the classic logarithmic wind profile. Other mean quantities are also logarithmic in the surface layer. For example, the mean potential temperature is given by

$$\bar{\theta} - \bar{\theta}_o = \frac{\theta_*}{k} \ln \frac{z}{z_{o,h}}, \quad (3.48)$$

where $z_{o,h}$ is *thermal roughness*, $\bar{\theta}_o$ is potential temperature at height $z_{o,h}$, and θ_* is a potential temperature scale defined as

$$\theta_* = -\frac{\overline{w'\theta'}}{u_*}. \quad (3.49)$$

We note that the logarithmic solutions for \bar{u} and $\bar{\theta}$ are obtained only from the turbulence parameterization scheme and the actual governing equations (Eqs. 3.31 and 3.33) are not used. Above the surface layer where the turbulent fluxes are no longer constant with height, we will need the governing equations to predict the vertical distributions of these mean quantities.

The eddy diffusivity parameterization given by Eq. 3.43 is valid only under a restrict set of conditions: air stability is neutral, the surface is void of rough elements, and z is small (< approximately 50 m). The parameterization can be modified for other situations. In comparison to neutral stability, eddy diffusion is more efficient in unstable conditions and less efficient in stable conditions. The above parameterization is modified to

$$K_m = \frac{kzu_*}{\phi_m}, \quad K_h = \frac{kzu_*}{\phi_h}, \quad (3.50)$$

where ϕ_m and ϕ_h are empirical *stability correction functions*. They are less than one in unstable conditions and greater than one in stable conditions (Chap. 4).

In the middle and upper boundary layer, the eddy length scale is smaller than predicted by the Prandtl's mixing length model. Several modifications to Eq. 3.44 have been proposed to force a good match between calculated and observed wind profiles in the upper boundary layer and in the free atmosphere. A frequently used parameterization for neutral stability is

$$l = kz \left(1 - \frac{z}{z_i}\right)^2, \quad (3.51)$$

where z_i is boundary-layer depth, and the momentum eddy diffusivity is given by

$$K_m = kz \left(1 - \frac{z}{z_i}\right)^2 u_*, \quad (3.52)$$

(Fig. 3.4).

Over a plant canopy, the correct eddy length scale is $k(z - d)$, and

$$K_m = \frac{k(z - d)u_*}{\phi_m}, \quad K_h = \frac{k(z - d)u_*}{\phi_h}, \quad (3.53)$$

where d is the height of a displacement plane. The mean profiles are still logarithmic but are offset upward by the *displacement height*, d (Fig. 3.3).

In statistics, Reynolds variances and covariances, such as $\overline{u'^2}$ and $\overline{u'w'}$, are second-order moments, and mean state quantities, such as \bar{u} , are first-order moments. In the above flux-gradient relationships, the second-order moments are determined by local gradients of the first-order moments. This parameterization scheme is referred to as *local first-order closure*. The scheme has gained widespread acceptance because it is a natural extension of our understanding of molecular diffusion, is computationally simple, and is reasonably accurate in the surface layer. However, if eddies involved in turbulent transport are larger than the scale of the local gradient, the turbulent flux can be partially or totally decoupled from the local gradient. In a convective boundary layer, eddies generated by thermal convection are able to penetrate the whole boundary layer, and mixing is so efficient that the vertical gradient of potential temperature in the middle of the boundary layer may vanish completely. However, there can still exist a substantial upward heat flux, which would not be possible according to Eq. 3.38.

A similar situation exists inside a plant canopy. Coherent eddies generated by strong wind shear near the top of the canopy are large enough to impact the whole canopy layer. The flux-gradient relationships are no longer accurate in the canopy airspace. In the extreme case, the flux may flow against or counter the local gradient. Counter-gradient flux is not permissible by local first-order parameterization unless we adopt a physically meaningless negative eddy diffusivity.

In an alternative *nonlocal first-order parameterization*, the total flux is made up of a local gradient flux contributed by small eddies and a nonlocal transport contributed by large eddies. The x -component momentum flux is given by

$$\overline{u'w'} = -K_m \left(\frac{\partial \bar{u}}{\partial z} - \gamma_m \right), \quad (3.54)$$

where γ_m is a positive correction factor representing large-eddy contribution (Hong and Pan 1996). Similar expressions can be written for fluxes of heat, water vapor, and trace gases.

Second-order closure is another alternative to local first-order closure. Instead of directly parameterizing Reynolds covariances, we now derive from the instant

budget equations for these second-order moments. We will discuss how this is done in Chap. 4. New third-order moments, such as $\overline{u'v'w'}$, will unavoidably emerge from the Reynolds averaging operation. Closure parameterization is performed on the third-order moments. For example, $\overline{u'v'w'}$ is parameterized as

$$\overline{u'v'w'} = -l_1 \bar{e}^{1/2} \left(\frac{\partial \overline{u'v'}}{\partial z} + \frac{\partial \overline{u'w'}}{\partial y} + \frac{\partial \overline{v'w'}}{\partial x} \right), \quad (3.55)$$

(Mellor 1973), where l_1 is an eddy length scale and \bar{e} is turbulent kinetic energy. Generally, closure parameterization at the third order improves the realism of calculated mean state quantities and can accommodate nonlocal transport to some extent.

A drawback of second-order closure is that it contains many more free parameters than first-order closure, some of which are impossible to verify experimentally. For this reason, second-order closure is not suitable for experimental determination of surface eddy fluxes.

3.6 Quantifying Eddy Fluxes

In the previous section, we may have left the impression that Reynolds covariances are a source of frustration because they create a difficult closure problem. In this section, we will show that they actually represent an opportunity for observational studies of surface-air interactions. We will also exploit the surface-layer closure parameterization for formulation of surface boundary conditions on the mean state of the atmospheric boundary layer.

Experimental Strategies

In the micrometeorological literature, Reynolds covariances are synonymous with eddy fluxes. The four most commonly used eddy flux quantities are

$$\text{Eddy flux of momentum : } F_m = -\overline{u'w'} (= u_*^2), \quad (3.56)$$

$$\text{Eddy flux of sensible heat : } F_h = \bar{\rho}_d c_p \overline{w'\theta'}, \quad (3.57)$$

$$\text{Eddy flux of water vapor : } F_v = \bar{\rho}_d (\overline{w's'_v}), \quad (3.58)$$

$$\text{Eddy flux of carbon dioxide : } F_c = \bar{\rho}_d (\overline{w's'_c}). \quad (3.59)$$

The reader is reminded that in these eddy flux equations, all the covariance terms are expressed in the micrometeorological coordinate. The mean dry air density, $\bar{\rho}_d$,

and specific heat at constant pressure, c_p , appear in Eq. 3.57 to ensure that F_h has the energy flux dimensions of W m^{-2} . For a similar reason, we have included $\bar{\rho}_d$ in Eqs. 3.58 and 3.59.

Because eddy covariance instruments measure T instead of θ , we also define eddy flux of sensible heat as

$$F_h = \bar{\rho}_d c_p (\overline{w' T'}). \quad (3.60)$$

Equation 3.57 is the surface flux boundary condition for Eq. 3.33, while Eq. 3.60 is a more correct formulation for the true surface-air exchange of sensible heat. The two formulations differ by the factor $(p/p_0)^{-R_d/c_p}$ (Eq. 2.24). This difference is negligible at low altitudes but can be noticeable at high altitudes. At an altitude of 2 km, F_h from Eq. 3.60 is 7% smaller in magnitude than that from Eq. 3.57.

In steady-state and under advection-free conditions, Eqs. 3.58, 3.59, and 3.60 are equivalent to the total surface source strength of water vapor, carbon dioxide, and sensible heat (Chap. 8). This fact has motivated us to establish micrometeorological methods for quantifying the eddy fluxes. The most direct method of measuring the eddy fluxes, called *eddy covariance*, requires deployment of fast-responding instruments for sampling the velocity components, the gaseous concentrations, and temperature. The Reynolds covariances, $\overline{w' s'_v}$, $\overline{w' T'}$, and $\overline{w' s'_c}$ are first computed from the recorded high-frequency time series of w , s_v , s_c and T . The appropriate fluxes are then converted from the covariances. An extensive discussion on eddy covariance can be found in Chap. 8.

In absence of fast-responding instruments, we can determine the fluxes using the first-order closure assumption and measurement of the mean state quantities at two heights above the surface. The *flux-gradient method* computes the flux using the flux-gradient relationships (Eqs. 3.36, 3.37, 3.38, 3.39, and 3.40). Expressing the vertical gradients in finite difference form, we obtain

$$F_m = K_m \frac{\bar{u}_2 - \bar{u}_1}{z_2 - z_1}, \quad (3.61)$$

$$F_h = -\bar{\rho}_d c_p K_h \frac{\bar{T}_2 - \bar{T}_1}{z_2 - z_1}, \quad (3.62)$$

$$F_v = -\bar{\rho}_d K_v \frac{\bar{s}_{v,2} - \bar{s}_{v,1}}{z_2 - z_1}, \quad (3.63)$$

$$F_c = -\bar{\rho}_d K_c \frac{\bar{s}_{c,2} - \bar{s}_{c,1}}{z_2 - z_1}, \quad (3.64)$$

where subscript 1 and 2 denote measurement at height z_1 and z_2 . The eddy diffusivity parameters are determined from

$$K_m = \frac{k z_g u_*}{\phi_m}, \quad K_h = K_v = K_c = \frac{k z_g u_*}{\phi_h}, \quad (3.65)$$

where z_g is the geometric mean of the two measurement heights

$$z_g = [(z_2 - d)(z_1 - d)]^{1/2}. \quad (3.66)$$

The stability correction functions, ϕ_m and ϕ_h , are also evaluated at height z_g . We use the geometric rather than arithmetic mean height to improve the accuracy of the finite difference approximation.

An observant reader may notice that Eqs. 3.61, 3.62, 3.63, 3.64, and 3.65 involve circular reasoning. Because ϕ_m and ϕ_h are functions of u_* and F_h (Chap. 4), calculation of K_m and K_h requires that F_m and F_h be known before F_m and F_h can be determined. In practice, this dilemma is resolved with an iterative procedure (Problem 4.18, Chap. 4). First, an initial guess value for u_* and one for K_h are obtained from

$$u_* = kz_g \frac{\bar{u}_2 - \bar{u}_1}{z_2 - z_1}, \quad K_h = kz_g u_*, \quad (3.67)$$

by assuming neutral stability ($\phi_m = 1$ and $\phi_h = 1$). Next, a guess value for F_h is calculated with Eq. 3.62. Third, the guess values of u_* and F_h are used to obtain updated ϕ_m , ϕ_h , K_m , and K_h . Fourth, improved estimates of F_m and F_h are calculated with Eqs. 3.61 and 3.62 using the updated K_m and K_h . These steps are repeated until a convergence criterion is met.

In some field campaigns, the flux-gradient method is deployed in combination with the eddy covariance method. The eddy covariance method is used for the determination of F_m and F_h , and the flux-gradient method is used for the determination of the gaseous fluxes. In this configuration, the gaseous eddy diffusivity is computed with the eddy covariance data, and the interactive procedure is no longer required.

The *Bowen ratio method*, a variation of the flux-gradient method, is frequently used to determine the water vapor flux. Bowen ratio, β , is the ratio of the surface sensible flux (F_h) to the surface latent heat flux (λF_v). Dividing Eq. 3.62 by Eq. 3.63 and noting equality of eddy diffusivity for sensible heat and water vapor, we obtain

$$\beta = \gamma \frac{\bar{T}_2 - \bar{T}_1}{\bar{e}_{v,2} - \bar{e}_{v,1}}, \quad (3.68)$$

where $\gamma = \bar{p}_d c_p / (0.621\lambda)$ is the psychrometric constant ($\simeq 0.66 \text{ hPa K}^{-1}$) and $e_{v,2}$ and $e_{v,1}$ are water vapor pressure measured at the two heights. In steady state, $H = F_h$, and $E = F_v$. Combining these relations with energy balance Eqs. 2.47 and 3.68, we obtain

$$F_v = E = \frac{1}{\lambda} \frac{R_n - G - Q_s}{1 + \beta}. \quad (3.69)$$

This method requires measurement of the available energy, in addition to the two-level measurement of air temperature and humidity. Because it completely avoids

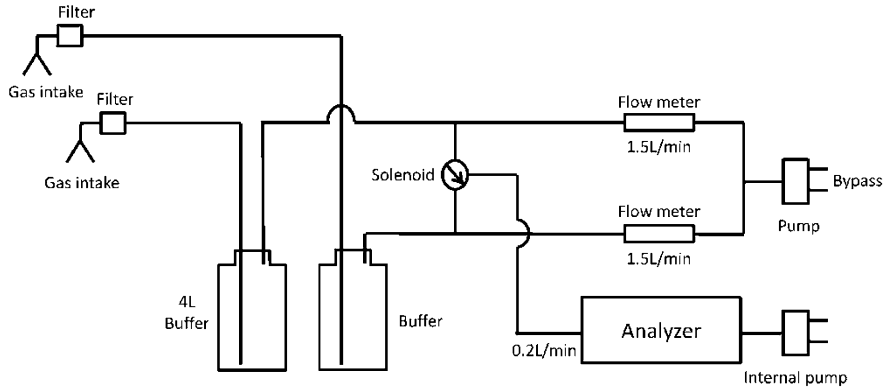


Fig. 3.5 Schematic diagram of a modified Bowen ratio apparatus for carbon dioxide and methane flux measurement. Air is drawn from intakes at two heights above the surface. A closed-path analyzer subsamples the two air streams sequentially for simultaneous detection of water vapor, methane, and carbon dioxide concentrations. The eddy flux of water vapor is measured separately with an eddy covariance system. The buffer volumes are used to smooth out turbulent fluctuations so representative samplings can be obtained. In this particular configuration, the switching interval is 60 s, and the buffer time lasts about three switching intervals

eddy diffusivity calculation, the Bowen ratio method can be used in situations where no accurate eddy diffusivity parameterization exists, such as in the air layer above the floor of a forest, as long as there are reasons to believe that equality of eddy diffusivity holds.

The *modified Bowen ratio method*, another extension of the flux-gradient method, aims to determine the eddy flux of a trace gas (Businger 1986; Meyers et al. 1996). We will use carbon dioxide to demonstrate how it works. Let us suppose that the carbon dioxide analyzer available for the experiment is not fast enough for eddy covariance measurement, but produces accurate measurement of mean carbon dioxide concentration at two heights above the surface (Fig. 3.5, $\bar{s}_{c,2}$ and $\bar{s}_{c,1}$). In parallel to the carbon dioxide measurement, measurement is also made of water vapor concentration at the same heights ($\bar{s}_{v,2}$ and $\bar{s}_{v,1}$) and of the water vapor flux via eddy covariance (F_v). Manipulation of Eqs. 3.63 and 3.64 yields

$$F_c = \frac{\bar{s}_{c,2} - \bar{s}_{c,1}}{\bar{s}_{v,2} - \bar{s}_{v,1}} F_v. \quad (3.70)$$

On the assumption that eddy transport does not discriminate against either water vapor or carbon dioxide, the eddy diffusivity parameter is canceled out. In this respect, the method is no different from the traditional Bowen ratio method except that it is modified for trace gas applications.

Modeling Strategies

We have shown that the flux-gradient relationships, when expressed in finite-difference form, enable us to devise three methods for quantifying experimentally surface eddy fluxes. Our next task is to convert the relationships to integral forms for use in modeling studies.

A key point to remember here is that Reynolds covariances or eddy fluxes are constant with height in the surface layer. Dividing Eq. 3.36 by K_m and integrating with respect to z , we obtain

$$\overline{u'w'} \int_{z_o}^z \frac{1}{K_m} dz' = -\bar{u}, \quad (3.71)$$

This equation can be rearranged to

$$F_m = -\overline{u'w'} = \frac{\bar{u}}{r_{a,m}}, \quad (3.72)$$

where

$$r_{a,m} = \int_{z_o}^z \frac{1}{K_m} dz', \quad (3.73)$$

is the *aerodynamic resistance* to momentum transfer. The integral form of the heat flux relationship is

$$\frac{F_h}{\bar{\rho}_d c_p} = \frac{\bar{\theta}_o - \bar{\theta}}{r_{a,h}}, \quad (3.74)$$

where the aerodynamic resistance to heat transfer, $r_{a,h}$, is given by

$$r_{a,h} = \int_{z_{o,h}}^z \frac{1}{K_h} dz' \quad (3.75)$$

and $\bar{\theta}_o$ is the mean potential temperature at height $z_{o,h}$. The water vapor and carbon dioxide flux relationships can be rearranged into similar forms.

The resistance concept is based on *Ohm's law analogy*. Ohm's law states that electric current, or flow of electrons, is inversely proportional to the electric resistance of a load and is proportional to the voltage differential across the load. This analogy has been put into good use in boundary-layer meteorology. In the case of heat transfer, the heat flux is the equivalent of electric current, and the surface-to-air temperature difference is the equivalent of voltage differential. Figure 3.6 is the schematic diagram of a simple "circuit" with a single "resistor" to describe diffusion through the surface layer. Other situations require use of multiple resistors

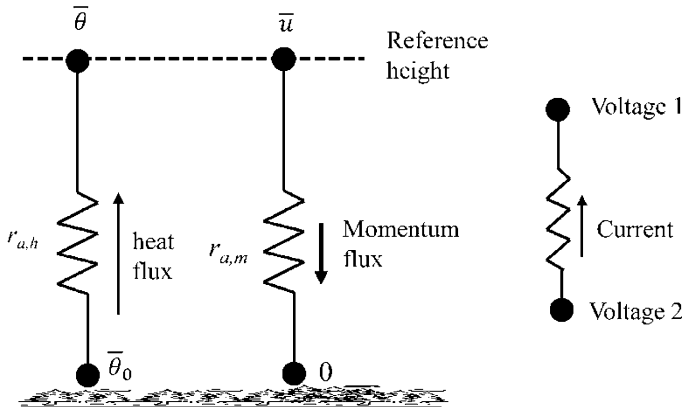


Fig. 3.6 Flow of electric current in a one-resistor circuit and the analogous transfer of momentum and heat in the surface layer

(Chap. 10). The plant transpiration pathway consists of the stomatal opening, the leaf boundary layer, and the atmospheric surface layer, and in Ohm's law analogy, water vapor diffusion encounters three resistances connected in series, the stomatal resistance, the leaf boundary-layer resistance, and the aerodynamic resistance. Some multilayer canopy evapotranspiration and photosynthesis models are represented by a network of resistances with parallel and serial nodes of connection. One important distinction between circuit analysis and turbulent diffusion is that electric resistances are constant, whereas the diffusion resistances are highly variable. Being an inverse property of eddy diffusivity, the aerodynamic resistance is a measure of diffusion inefficiency: it is high if the diffusion layer is thick and decreases with increasing wind speed, surface roughness, or air instability.

The integral relationships are the preferred choice for land surface models. The main function of a land surface model is to compute the surface fluxes from forcing variables prescribed at some height above the surface. In a fully coupled or online mode, the forcing variables, such as \bar{u} and $\bar{\theta}$ in Eqs. 3.72 and 3.74, are provided by an atmospheric model at the first grid height. The computed fluxes then serve as the surface boundary conditions for the atmospheric model.

In the literature on ocean atmospheric boundary layers, the surface fluxes are often described with bulk formulations as

$$F_m = C_D \bar{u}^2, \quad (3.76)$$

$$\frac{F_h}{\bar{\rho}_d c_p} = C_H \bar{u} (\bar{\theta}_o - \bar{\theta}), \quad (3.77)$$

$$\frac{F_v}{\bar{\rho}_d} = C_E \bar{u} (\bar{s}_{v,o} - \bar{s}_v), \quad (3.78)$$

where $\bar{\theta}_o$ is assumed to be the same as the temperature of the water surface and $\bar{s}_{v,o}$ is vapor mixing ratio at the water surface, which is determined from the saturation vapor pressure at temperature $\bar{\theta}_o$. In these equations, C_D , C_H , and C_E are the *transfer coefficients* for momentum, sensible heat, and water vapor, respectively. These dimensionless parameters, also referred to as the drag coefficient, the Stanton number, and the Dalton number, respectively, are related to the diffusion resistances as

$$C_D = \frac{1}{\bar{u}r_{a,m}}, \quad C_H = \frac{1}{\bar{u}r_{a,h}}, \quad C_E = \frac{1}{\bar{u}r_{a,v}}, \quad (3.79)$$

where $r_{a,v}$ is the aerodynamic resistance to water vapor transfer.

3.7 Problems

- 3.1** Prove the first three Reynolds rules (Eqs. 3.3, 3.4, and 3.5).
- 3.2** Calculate the variance of temperature (T) and vertical velocity (w) and the $T-w$ covariance using the time series data in Table 3.1.
- 3.3*** Some people define the fluctuating part of quantity a as

$$a'_i = a_i - \hat{a}_i, \quad (3.80)$$

where subscript i denotes measurement at time step i and \hat{a} is the value from the linear regression of a against time (Fig. 3.7). This procedure is called linear detrending. It can be shown that

$$\hat{a}_i = \bar{a} + b \left(t_i - \frac{1}{n} \sum_1^n t_i \right), \quad (3.81)$$

Table 3.1 Time series of temperature T ($^{\circ}\text{C}$) and vertical velocity w (m s^{-1}). Time t is in s

t	1	2	3	4	5	6	7	8	9	10	11	12
T	20.0	20.2	19.7	19.8	20.1	20.3	20.3	20.2	20.2	19.7	20.0	20.0
w	-0.52	-0.02	-0.09	0.07	-0.01	-0.13	-0.41	-0.60	-0.72	-0.35	-0.26	-0.45
t	13	14	15	16	17	18	19	20	21	22	23	24
T	20.1	22.3	20.1	19.9	20.0	20.0	20.0	20.1	20.6	20.7	20.5	20.8
w	0.32	0.00	-0.10	0.43	-0.42	0.25	0.41	0.74	1.29	1.31	1.60	1.36

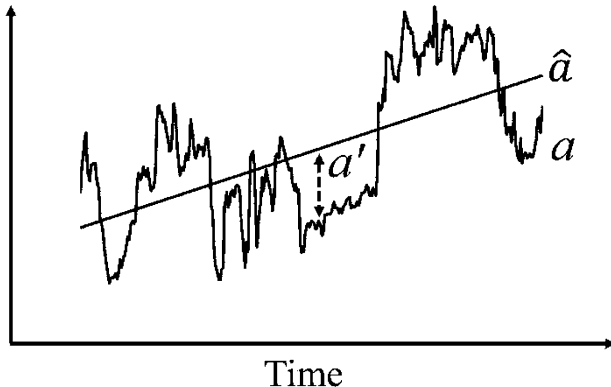


Fig. 3.7 Linear detrending of a time series

where n is the number of observations, t is time, and $b = b_1/b_2$, with b_1 and b_2 given by

$$b_1 = \sum_1^n a_i t_i - \frac{1}{n} \sum_1^n a_i \sum_1^n t_i,$$

and

$$b_2 = \sum_1^n t_i t_i - \frac{1}{n} \sum_1^n t_i \sum_1^n t_i,$$

(Gash and Culf 1996). The detrended fluctuations are then used to compute the variance using Eq. 3.9 and covariance using Eq. 3.10. Show (i) that $\overline{a'_i} = 0$ and that (ii) the detrended variance and covariance are smaller in magnitude than their counterparts computed from the standard block averaging procedure. Verify these conclusions with the data given in Table 3.1.

3.4 The total kinetic energy per unit mass of air is given by

$$E_T = \frac{1}{2}(u^2 + v^2 + w^2).$$

Using the Reynolds averaging rules, show that the mean total kinetic energy, \bar{E}_T , is the sum of the mean flow kinetic energy, \bar{E} , and the turbulent kinetic energy, \bar{e} :

$$\bar{E}_T = \bar{E} + \bar{e},$$

where

$$\bar{E}_T = \frac{1}{2}(\bar{u}^2 + \bar{v}^2 + \bar{w}^2),$$

$$\bar{E} = \frac{1}{2}(\bar{u}'^2 + \bar{v}'^2 + \bar{w}'^2),$$

and

$$\bar{e} = \frac{1}{2}(\bar{u}'^2 + \bar{v}'^2 + \bar{w}'^2).$$

3.5 Show that the time averaging and the total derivative operations are not commutable, that is,

$$\overline{\frac{df}{dt}} \neq \frac{d\bar{f}}{dt}. \quad (3.82)$$

3.6 The horizontal velocity divergence $\partial\bar{u}/\partial x + \partial\bar{v}/\partial y$ is $2 \times 10^{-6} \text{ s}^{-1}$ in a mid-latitude anticyclone. Estimate the associated mean vertical velocity at the height of 20 m above the surface.

3.7 The momentum flux $\bar{u}'\bar{w}'$ is -0.36 and $0 \text{ m}^{-2} \text{ s}^{-2}$ at the surface and at the top of a shear-dominated boundary layer (height = 1000 m), respectively. Find the vertical divergence of the turbulent momentum flux, $\partial\bar{u}'\bar{w}'/\partial z$. Is the flux divergence much larger in magnitude than the molecular term, $\nu\nabla^2\bar{u}'$? (Use your result for Problem 2.3 to answer this question.)

3.8 Using the Reynolds rules and the weak incompressibility constraint (Eq. 3.17), derive from Eq. 2.20 the governing equation for the mean water vapor mixing ratio (Eq. 3.28).

3.9 Derive from Eq. 2.16 the governing equation from the mean mass density $\bar{\rho}_c$ (Eq. 3.25). Do you need the weak incompressibility constraint for this derivation?

3.10 Show that the eddy sensible heat flux, F_h , has the dimensions of W m^{-2} and the eddy water vapor flux, F_v , has the dimensions of $\text{kg m}^{-2}\text{s}^{-1}$.

3.11 In the situation shown in Fig. 3.3, do you expect the $T - s_v$ covariance to be positive or negative? What about the $u - s_c$ covariance?

3.12 Figure 3.8 shows the relationship between friction velocity (u_*) and horizontal velocity (\bar{u}) observed at a measurement height of 8.50 m above the surface of a shallow lake and over a wheat field at a measurement height of 2.55 m above its zero-plane displacement. Determine the surface momentum roughness and surface drag coefficient from the slope of the regression. Which dataset represents the lake experiment?

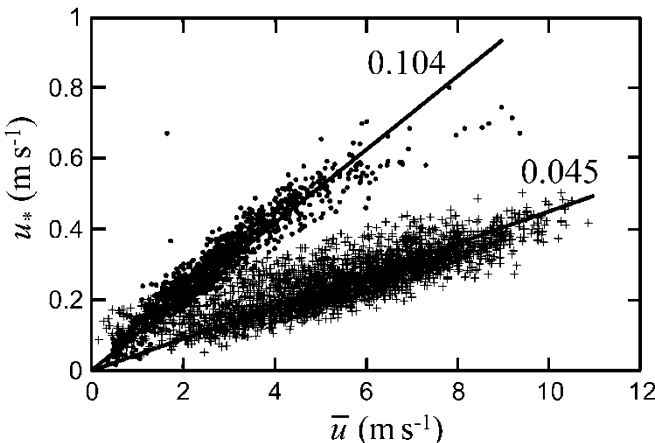


Fig. 3.8 Relationship between friction velocity (u_*) and horizontal velocity \bar{u} over a lake surface and a wheat field. Solid lines represent regression fit to the data and numbers next to the lines indicate slopes of the regression

3.13 In some climate models, a grid cell can have multiple subgrid surface types. Each surface interacts independently with the overlaying atmosphere through forcing variables specified at the first model grid level. This level is usually at the so-called blending height where the atmosphere is well mixed horizontally (i.e., no subgrid variations at this height). Assume that a grid cell consists of a smooth (momentum roughness $z_o = 0.001 \text{ m}$) and a rough surface ($z_o = 0.50 \text{ m}$), air stability is neutral, the blending height is 50 m, and wind speed at the blending height is 5.00 m s^{-1} . Calculate the friction velocity for each of the two surfaces. What is the wind speed at the 2-m height above these surfaces?

3.14 Two temperature sensors are mounted at heights of 2.0 and 4.0 m above the zero plane displacement of a grass surface whose momentum roughness is 0.02 m . The sensors have a precision of $0.05 \text{ }^{\circ}\text{C}$. Wind speed at the upper measurement height is 4.00 m s^{-1} , and surface sensible heat flux is 35 W m^{-2} . Assume that air stability is neutral. What is the temperature difference between the two measurement heights? Are these sensors good enough to resolve the difference? Repeat the calculation for a forest whose momentum roughness is 1.0 m . Can you resolve the temperature difference with the same sensors?

3.15 Air temperature is 22.3 and $21.9 \text{ }^{\circ}\text{C}$, and water vapor pressure is 18.1 and 17.4 hPa at heights of 1.0 and 2.3 m above a soil surface, respectively. What is the Bowen ratio?

3.16 The carbon dioxide flux of a lake system is on the order of $0.01 \text{ mg m}^{-2} \text{ s}^{-1}$. If a broadband carbon dioxide analyzer has a precision of 0.2 ppm , is it good enough for the flux-gradient measurement of the flux? Assume that the carbon dioxide

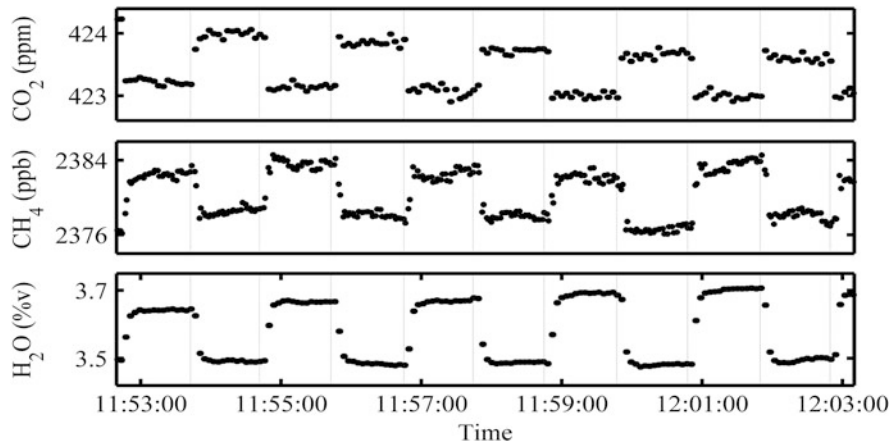


Fig. 3.9 Time series of carbon dioxide, methane, and water vapor molar mixing ratio obtained with a modified Bowen ratio system (Data source: Xiao et al. 2014)

concentration measurement takes place at heights of 1.0 and 3.0 m above the water surface, the friction velocity is 0.15 m s^{-1} , and air stability is neutral.

3.17* Figure 3.9 shows the instant concentrations of three gases over a lake surface measured by a gas analyzer using the configuration shown in Fig. 3.5. The step changes correspond to times when the analyzer switched from one air intake to another. The surface water vapor flux, measured by eddy covariance, is $0.082 \text{ g m}^{-2} \text{ s}^{-1}$ for the period shown in Fig. 3.9. Using the modified Bowen ratio method, determine the surface flux of methane, in units of $\mu\text{g m}^{-2} \text{ s}^{-1}$, and the flux of carbon dioxide, in units of $\text{mg m}^{-2} \text{ s}^{-1}$ with the data shown in Fig. 3.9.

3.18 Show that in neutral stability, the aerodynamic resistance to momentum transfer and to heat transfer is given by

$$r_{a,m} = \frac{1}{k^2 \bar{u}} \left(\ln \frac{z - d}{z_o} \right)^2, \quad (3.83)$$

and

$$r_{a,h} = \frac{1}{k^2 \bar{u}} \ln \frac{z - d}{z_o} \ln \frac{z - d}{z_{o,h}}. \quad (3.84)$$

Assume that wind speed is measured at a reference height of 10.0 m above the zero plane displacement. Use the typical value of 0.14 for the roughness ratio $z_{o,h}/z_o$. Plot these resistances as a function of wind speed for a grass surface (momentum roughness $z_o = 0.10 \text{ m}$) and for a forest ($z_o = 1.00 \text{ m}$). Discuss how wind speed and surface roughness affect the aerodynamic resistances.

3.19 In neutral stability, even though equality of eddy diffusivity holds for heat and for momentum (cf., Eq. 3.43) in the atmospheric surface layer, the aerodynamic resistance to heat transfer, $r_{a,h}$, is larger than that to momentum transfer, $r_{a,m}$. The difference, $r_e = r_{a,h} - r_{a,m}$, termed *excess resistance*, is explained by the fact that in the laminar layer in immediate contact with the surface, momentum transfer is much more efficient than heat transfer: the former is accomplished by a form drag associated with pressure discontinuity, whereas the latter is carried out by molecular diffusion. Show that the excess resistance to heat transfer is given by

$$r_e = \frac{1}{ku_*} \ln \frac{z_o}{z_{o,h}}.$$

Using the information provided in Problem 3.18, compare r_e and $r_{a,h}$ for the grass surface and the forest surface over a wind speed range of 1–5 m s⁻¹.

3.20 A typical value for C_H and C_E of lakes and oceans is 1×10^{-3} . The surface temperature of a lake is 18.0 °C, and air at the height of 10.0 m above the lake has a temperature of 17.0 °C, a relative humidity of 65%, and a wind speed of 4.0 m s⁻¹. The lake is at the mean sea level. Calculate the surface sensible heat flux and the latent heat flux. The saturation vapor pressure is given by

$$e_v^* = 6.1365 \exp \left(\frac{17.502t}{240.97 + t} \right), \quad (3.85)$$

(Licor 2001), where e_v^* is in hPa and t is in °C.

References

- Bradford WB, Davis KJ, Yi C, Bakwin PS, Zhao CL (2001) Long-term carbon dioxide fluxes from a very tall tower in a Northern forest: flux measurement methodology. *J Atmos Oceanic Technol* 18:529–542
- Businger JA (1986) Evaluation of the accuracy with which dry deposition can be measured with current micrometeorological techniques. *J Appl Meteorol* 25:1100–1124
- Gash JHC, Culf AD (1996) Applying a linear detrend to eddy correlation data in realtime. *Bound-Layer Meteorol* 79:301–306
- Hong SY, Pan HL (1996) Nonlocal boundary layer vertical diffusion in a medium-range forecast model. *Mon Weather Rev* 124:2322–2339
- Licor (2001) LI-610 portable dew point generator instruction manual. LI-COR, Inc, Lincoln
- Mellor GL (1973) Analytic prediction of the properties of stratified planetary surface layers. *J Atmos Sci* 30:1061–1069
- Meyers TP, Hall ME, Lindberg SE, Kim K (1996) Use of the modified Bowen-ratio technique to measure fluxes of trace gases. *Atmos Environ* 30:3321–3329
- Xiao W, Liu S, Li H, Xiao Q, Wang W, Hu Z, Hu C, Gao Y, Shen J, Zhao X, Zhang M, Lee X (2014) A flux-gradient system for simultaneous measurement of the CH₄, CO₂ and H₂O fluxes at a lake-air interface. *Environ Sci Technol* 48:14490–14498

Chapter 4

Generation and Maintenance of Atmospheric Turbulence

4.1 Energy Pools and Energy Transfers

In this chapter, we study mechanisms by which turbulent eddies develop and dissipate kinetic energy. The kinetic energy contained in turbulent eddies is a measure of the vigor of atmospheric turbulence. Owing to the action of the viscous force, kinetic energy is constantly and irreversibly transferred into internal energy of the atmosphere. New kinetic energy must be supplied, or else turbulent motion would be replaced by laminar flow, and the atmospheric boundary layer would lose much of its diffusion power. Our approach is based on two principles introduced in Chaps. 2 and 3: Reynolds decomposition and momentum conservation. We will use them to derive budget equations governing the mean flow kinetic energy and the turbulent kinetic energy. Energy transfer mechanisms are then examined in the context of these equations.

Kinetic energy is the energy of motion. The kinetic energy of an air parcel with mass m and moving at velocity \mathbf{V} is $\frac{1}{2}m|\mathbf{V}|^2$. For convenience, we will drop m in our discussion, and our formulations are for kinetic energy per unit mass of air.

Kinetic energy is a scalar and in theory is independent of the coordinate frame chosen for the velocity vector \mathbf{V} . However, practical situations dictate that kinetic energy is transferred in preferred spatial directions, and a properly chosen coordinate system can elucidate much deeper insights into the transfer processes than an arbitrary coordinate. Here we use the pressure gradient force to help us orient the coordinate axes, as shown in Fig. 4.1. In this right-handed Cartesian coordinate, the x -axis is at a right angle to the force and is tangent to the isobars, the y -axis is aligned with the direction of the force, and the z -axis is pointed upward. The total kinetic energy per unit mass is the sum of the components in the three orthogonal directions:

$$E_T = \frac{1}{2} (u^2 + v^2 + w^2). \quad (4.1)$$

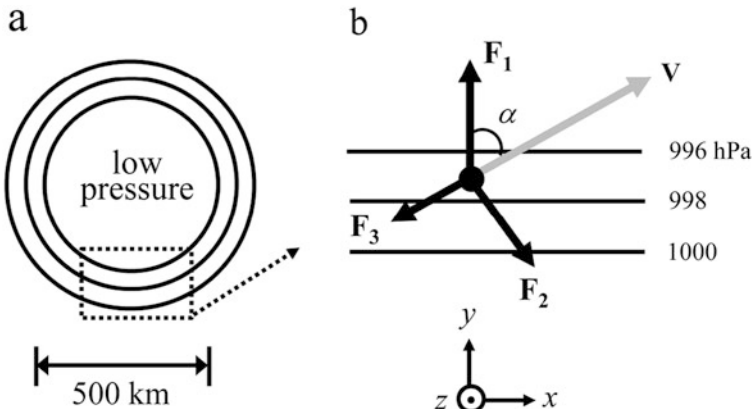


Fig. 4.1 A Cartesian coordinate for the kinetic energy equations: bird's eye view of a low-pressure system in the Northern hemisphere (a) and an enlarged view of the same system (b). Lines are isobars along which pressure is equal. \mathbf{V} is horizontal velocity, \mathbf{F}_1 is pressure gradient force, \mathbf{F}_2 is Coriolis force, and \mathbf{F}_3 is friction force

Using the Reynolds averaging rules, we can separate the total kinetic energy into the *mean flow kinetic energy* (MKE), \bar{E} , and the *turbulent kinetic energy* (TKE), \bar{e} :

$$\bar{E}_T = \bar{E} + \bar{e}. \quad (4.2)$$

where

$$\bar{E}_T = \frac{1}{2}(\bar{u}^2 + \bar{v}^2 + \bar{w}^2), \quad (4.3)$$

$$\bar{E} = \frac{1}{2} (\bar{u}^2 + \bar{v}^2 + \bar{w}^2), \quad (4.4)$$

and

$$\bar{e} = \frac{1}{2} (\bar{u'^2} + \bar{v'^2} + \bar{w'^2}). \quad (4.5)$$

(Problems 3.4 and 4.1). These quantities are in dimensions of $\text{m}^2 \text{s}^{-2}$. To obtain kinetic energy density in the familiar SI energy units of J m^{-3} , we should multiply them by the air density ρ in kg m^{-3} .

Energy in the atmosphere is conveniently divided into four pools: internal energy, available potential energy, MKE, and TKE (Fig. 4.2). Internal energy, or heat energy, is the kinetic energy of molecular motion. Available potential energy refers to the portion of the potential energy in the atmosphere that can be converted to kinetic energy. It is computed against a reference state in which the atmosphere is statically neither stable nor unstable and no horizontal pressure gradient exists.

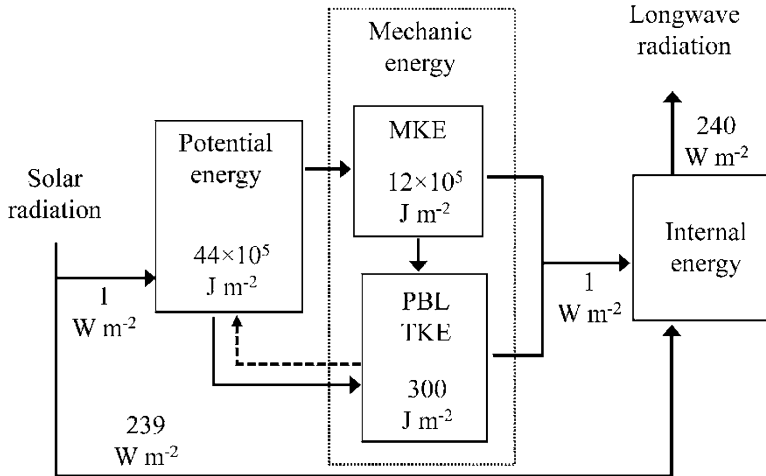


Fig. 4.2 Transfer of energy between four pools. The TKE pool size is based on the study by Mellor and Yamada (1982). Estimates of the other energy pools and of the fluxes are global mean values from Peixoto and Oort (1992)

The available potential energy pool is maintained by uneven solar radiation heating, which generates horizontal pressure gradients and static instability. Globally, the majority of solar radiation flux (239 W m^{-2}) is either directly converted to internal energy by atmospheric absorption or is redistributed to the atmosphere from the surface by latent heat and sensible heat exchanges. Only a small fraction of the solar radiation flux, about 1 W m^{-2} , passes through the intermediary mechanical energy pools before being converted to internal energy. Atmospheric motions, whether large or small, are supported by this small stream of solar radiation flux. The TKE pool is the smallest of these pools. The total TKE in the atmospheric boundary layer is about 300 J m^{-2} . Although no reliable estimates exist, the TKE in the air column above the boundary layer is probably several times smaller than the TKE in the boundary layer. It is this small energy pool that makes the boundary layer uniquely different from the rest of the atmosphere.

In the atmosphere, the mean motion and the turbulent motion occur in two nonoverlapping scale ranges separated by a large scale gap (Fig. 4.3; Wyngaard 2004). This scale gap is the basis for the idea that atmospheric kinetic energy can be divided into the mean and the turbulent pools. Models of the mean motion, or *Reynolds averaging models*, require that the two motions be cleanly isolated from one another. In the model domain, model grid spacings are strategically chosen to coincide with the scale gap. Energy transfer between the two pools and the effect of turbulence on the mean motion are expressed through turbulence closure schemes. The predicted quantities are grid mean values and carry no information on details of the turbulent motion. With today's computing power, it is tempting to use small horizontal grid sizes. However, too small a grid spacing would contaminate the mean

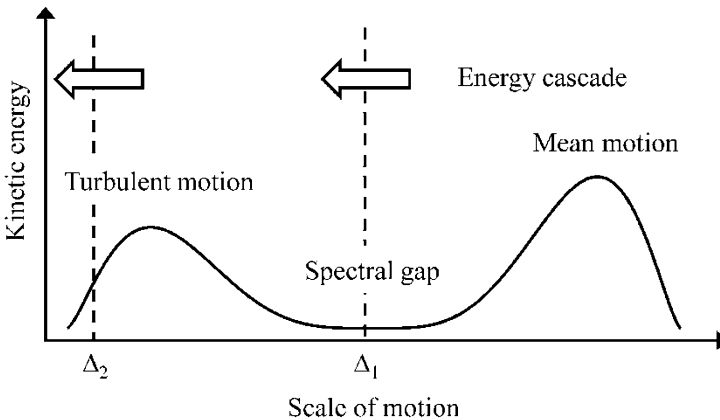


Fig. 4.3 A schematic diagram showing the cascade of kinetic energy. Here Δ_1 is grid spacing of a Reynolds averaging model, and Δ_2 is grid spacing of a large-eddy simulation model

flow with the energy contained in large eddies and thus violate the principle of two-pool compartmentalization. In this regard, Reynolds averaging models are different from large-eddy simulation models. In large-eddy simulation, the grid spacing is much smaller than the scale gap so that large eddies are explicitly resolved.

The relationship between the MKE and the TKE pools represents a simple form of *energy cascade*. Energy cascade is the process in which kinetic energy is transferred from motions of larger scale to motions of smaller scale. The largest eddies obtain their energy from the mean flow. These large eddies will deform and break up, and the energy is then passed onto smaller eddies. The process continues down the scale, in a fashion similar to a waterfall cascading down a hill slope, until the kinetic energy turns into energy of molecular motion or internal energy. In eddy motion, even at the smallest scale, molecules are moving in groups. Molecular motion, on the other hand, is totally erratic, with each molecule moving randomly and independently of its neighboring molecules.

Atmospheric stability is another important concept in connection with mechanic energy transfer. Turbulent eddies can obtain their energy via two pathways, with one from the mean flow and the other from the potential energy pool. This latter pathway is bidirectional, meaning that eddies can also convert kinetic energy to potential energy. As we will demonstrate shortly, atmospheric stability is a measure of the relative strength of these two pathways.

4.2 Budget of the Mean Flow Kinetic Energy

We consider a one-dimensional atmosphere in which Reynolds averages can vary in the vertical direction but are invariant in the horizontal directions. Multiplying both sides of Eq. 3.31 by \bar{u} , we obtain the budget equation for the mean flow kinetic energy in the x direction:

$$\frac{1}{2} \frac{\partial \bar{u}^2}{\partial t} = f \bar{u} \bar{v} + \overline{u'w'} \frac{\partial \bar{u}}{\partial z} - \frac{\partial \overline{u'w'} \bar{u}}{\partial z} + v \bar{u} \nabla^2 \bar{u}. \quad (4.6)$$

In this derivation, we have applied the chain rule of differentiation:

$$\bar{u} \frac{\partial \overline{u'w'}}{\partial z} = \frac{\partial \overline{u'w'} \bar{u}}{\partial z} - \overline{u'w'} \frac{\partial \bar{u}}{\partial z}.$$

The viscous term has been put back in this equation for the sake of completeness. The pressure gradient term has disappeared from this equation because the x -axis is orthogonal to the pressure gradient force (Fig. 4.1).

The budget equation for the mean flow kinetic energy in the y direction can be derived in a similar way, such that

$$\frac{1}{2} \frac{\partial \bar{v}^2}{\partial t} = -\frac{\bar{v}}{\bar{\rho}} \frac{\partial \bar{p}}{\partial y} - f \bar{u} \bar{v} + \overline{v'w'} \frac{\partial \bar{v}}{\partial z} - \frac{\partial \overline{v'w'} \bar{v}}{\partial z} + v \bar{v} \nabla^2 \bar{v}. \quad (4.7)$$

Adding Eqs. 4.6 and 4.7 and noting that there is no mean kinetic energy in the z direction in this one-dimensional flow, we obtain the complete MKE budget equation:

$$\begin{aligned} \frac{\partial \bar{E}}{\partial t} &= -\frac{\bar{v}}{\bar{\rho}} \frac{\partial \bar{p}}{\partial y} + \left(\overline{u'w'} \frac{\partial \bar{u}}{\partial z} + \overline{v'w'} \frac{\partial \bar{v}}{\partial z} \right) \\ &\quad - \left(\frac{\partial \overline{u'w'} \bar{u}}{\partial z} + \frac{\partial \overline{v'w'} \bar{v}}{\partial z} \right) + (v \bar{u} \nabla^2 \bar{u} + v \bar{v} \nabla^2 \bar{v}). \end{aligned} \quad (4.8)$$

The time rate of change of the MKE in the boundary layer is a net balance of four terms. The top portion of Fig. 4.4 provides a summary of various MKE transfer mechanisms. The first term on the right side of Eq. 4.8 is always positive, representing *production of mean kinetic energy* from the work done by the pressure gradient force on the moving air. As you may recall, an uneven pressure field is indicative of the existence of available potential energy. Through the interaction of the pressure gradient force with the flow, the available potential energy is transformed to kinetic energy.

Mathematically, the MKE production term is the inner product of the horizontal velocity vector \mathbf{V} and the pressure gradient force vector \mathbf{F}_1 (Fig. 4.1):

$$\begin{aligned} -\frac{\bar{v}}{\bar{\rho}} \frac{\partial \bar{p}}{\partial y} &= \mathbf{V} \cdot \left(\frac{-\nabla_H \bar{p}}{\bar{\rho}} \right) \\ &= \frac{1}{\bar{\rho}} |\mathbf{V}| |-\nabla_H \bar{p}| \cos \alpha, \end{aligned}$$

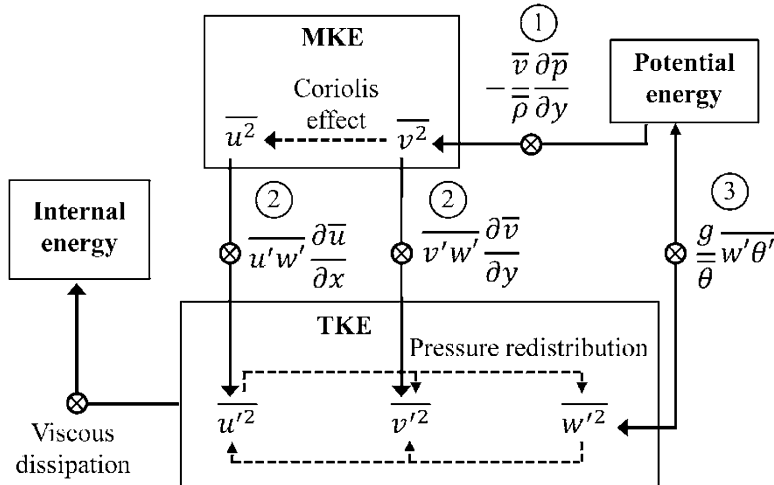


Fig. 4.4 Mechanisms of kinetic energy transfer in the atmospheric boundary layer. Pathway 1: production of mean flow kinetic energy (MKE) by the pressure gradient force. Pathway 2: shear destruction of MKE and production turbulent kinetic energy (TKE). Pathway 3: buoyancy production and destruction of TKE (Modified from Shaw 1987)

where α is the angle between \mathbf{V} and \mathbf{F}_1 and $\nabla_H = \{\partial/\partial x, \partial/\partial y\}$ is the horizontal gradient operator. In order for the mean flow to extract energy from the available potential energy pool, α must be less than 90° . The most efficient production of MKE occurs when $\alpha = 0^\circ$ or when the air is moving in the exact direction of the pressure gradient force. In contrast, there is no MKE production if the flow is geostrophic or orthogonal to the pressure gradient force.

Unlike the pressure gradient force, the Coriolis force does not produce kinetic energy. Its role is reversed in the two component equations. In Eq. 4.7, the Coriolis term, the second term on the right of the equation, is negative, representing removal of energy. This term also appears in Eq. 4.6 (the first term on its right side), but is positive, representing production of energy. The effect is canceled out in the derivation of the complete MKE equation (Eq. 4.8). In other words, the role of the Coriolis force is merely one of *kinetic energy redistribution*: it deflects energy in the y direction to the x direction. In a typical atmospheric boundary layer, this redistribution effect is very strong, so much so that more kinetic energy is found in the x direction than in the y direction, recalling that the y -axis is aligned with the pressure gradient force, or the direction along which MKE is first produced, and the x -axis is tangent to the isobars. We expect

$$\frac{1}{2} \bar{u}^2 > \frac{1}{2} \bar{v}^2.$$

Graphically, this means that angle α in Fig. 4.1 is greater than 45° .

The second term on the right side of Eq. 4.8 represents *shear destruction of mean kinetic energy*. Because the momentum fluxes, $\bar{u}'w'$ and $\bar{v}'w'$, and the velocity gradients, $\partial\bar{u}/\partial z$ and $\partial\bar{v}/\partial z$, are opposite in sign (Eqs. 3.36 and 3.37), this term is negative. In the next section, we will learn that the same term appears in the TKE budget equation but is positive. So the vertical wind shear plays two roles: it maintains a downward momentum flux (Fig. 3.3; Eq. 3.36) and at the same time cascades kinetic energy from the mean motion to the turbulent motion.

The third term on the right side of Eq. 4.8 acts to redistribute the MKE energy. This can be demonstrated by integrating it with respect to z from the surface to the top of the boundary layer (z_i):

$$\int_0^{z_i} \left(\frac{\partial \bar{u}'w' \bar{u}}{\partial z} + \frac{\partial \bar{v}'w' \bar{v}}{\partial z} \right) dz = (\bar{u}'w' \bar{u} + \bar{v}'w' \bar{v})|_{z_i} - (\bar{u}'w' \bar{u} + \bar{v}'w' \bar{v})|_0 \quad (4.9)$$

This integral is zero because the velocities are zero at the ground and the Reynolds covariances vanish at the top of the boundary layer. Therefore, the term represents *transport of mean kinetic energy* between different vertical positions. It does not destroy nor create kinetic energy.

The last term, *viscous dissipation of mean kinetic energy* to internal energy, can be simplified in the one-dimensional flow to

$$\nu \bar{u} \nabla^2 \bar{u} + \nu \bar{v} \nabla^2 \bar{v} = \nu \left(\bar{u} \frac{\partial^2 \bar{u}}{\partial z^2} + \bar{v} \frac{\partial^2 \bar{v}}{\partial z^2} \right). \quad (4.10)$$

It is generally much smaller than the other terms and is also much smaller than viscous dissipation of TKE (Problem 4.2).

Two examples in Fig. 4.5 illustrate the size of the MKE and the TKE pools and the strength of the energy transfer pathways in a shear-driven (left) and a buoyancy-driven boundary layer (right) based on a large-eddy simulation study. The two cases are set up similarly in the study except for the surface sensible heat flux. In the first case, the heat flux is zero, and all turbulence is produced by shear. In the second case, a moderate heat flux of 240 W m^{-2} is prescribed in the model domain, and turbulence is dominated by buoyancy production. The shear destruction of MKE differs by a factor of 4.5 between the two cases. An inference from the MKE budget equation is that the angle α between the velocity vector \mathbf{V} and the pressure gradient force vector \mathbf{F}_1 in Fig. 4.1 is larger in the buoyancy-driven boundary layer than in the shear-driven boundary layer, because only a small MKE production is required to balance the shear destruction of MKE in the buoyancy-driven flow. To put it differently, a larger surface heat flux will bring the flow in the boundary layer closer to being geostrophic.

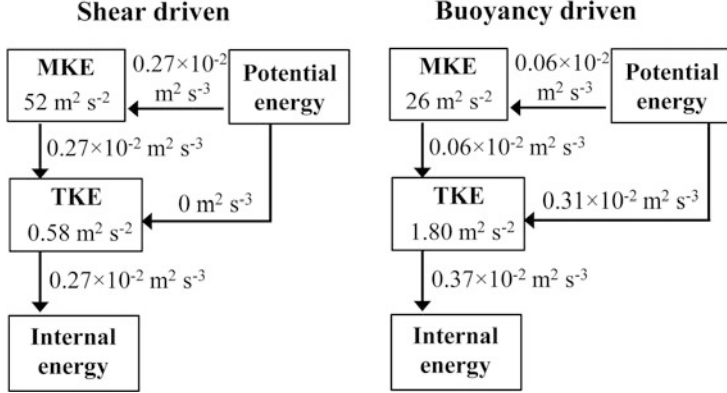


Fig. 4.5 Kinetic energy budget in a shear-driven (*left*) and a buoyancy-driven (*right*) boundary layer. All values are column means for the air layer between the ground surface and the top of the boundary layer. Results are based on Moeng and Sullivan (1994)

4.3 Budget of the Turbulent Kinetic Energy

The derivation of budget equations for the TKE components, $\frac{1}{2}\overline{u'^2}$, $\frac{1}{2}\overline{v'^2}$, and $\frac{1}{2}\overline{w'^2}$, which are second-order moments, is time consuming. Here we outline the essential steps, using $\frac{1}{2}\overline{u'^2}$ as an illustration. The same steps are used in the derivation of budget equations for $\frac{1}{2}\overline{v'^2}$ and $\frac{1}{2}\overline{w'^2}$ and for other second-order moments, such as the Reynolds stress ($\overline{u'w'}$) and the temperature variance ($\overline{\theta'^2}$), from the corresponding instant equations given in Chap. 2. First, we replace every quantity in the instant momentum Eq. 2.3 by the sum of its Reynolds mean and fluctuating part:

$$\frac{\partial(\bar{u} + u')}{\partial t} + (\bar{u} + u') \frac{\partial(\bar{u} + u')}{\partial x} + \dots = -\frac{1}{\bar{\rho} + \rho'} \frac{\partial(\bar{p} + p')}{\partial x} + \dots \quad (4.11)$$

Second, we obtain the governing equation for u' by subtracting the mean momentum Eq. 3.21 from Eq. 4.11:

$$\frac{\partial u'}{\partial t} + \bar{u} \frac{\partial u'}{\partial x} + u' \frac{\partial \bar{u}}{\partial x} + u' \frac{\partial u'}{\partial x} \dots = -\frac{1}{\bar{\rho}} \frac{\partial p'}{\partial x} + \frac{\rho'}{\bar{\rho}^2} \frac{\partial \bar{p}}{\partial x} + \dots \quad (4.12)$$

Third, we obtain the full governing equation for $\frac{1}{2}\overline{u'^2}$ by multiplying Eq. 4.12 with u' and performing Reynolds averaging:

$$\frac{1}{2} \frac{\partial \overline{u'^2}}{\partial t} + \frac{1}{2} \bar{u} \frac{\partial \overline{u'^2}}{\partial x} + \overline{u'^2} \frac{\partial \bar{u}}{\partial x} + \overline{u'^2} \frac{\partial u'}{\partial x} + \dots = -\frac{1}{\bar{\rho}} \frac{\partial u' p'}{\partial x} + \frac{1}{\bar{\rho}} \overline{p' \frac{\partial u'}{\partial x}} + \dots \quad (4.13)$$

where we have omitted the small term

$$\frac{\overline{u' \rho'}}{\overline{\rho^2}} \frac{\partial \bar{p}}{\partial x},$$

and have used the chain rule of differentiation,

$$\frac{1}{\overline{\rho}} \overline{u' \frac{\partial p'}{\partial x}} = \frac{1}{\overline{\rho}} \frac{\partial \overline{u' p'}}{\partial x} - \frac{1}{\overline{\rho}} \overline{p' \frac{\partial u'}{\partial x}}.$$

Fourth, in the one-dimensional boundary layer, all horizontal spatial derivatives of Reynolds means can be dropped from Eq. 4.13. The final result is

$$\frac{1}{2} \frac{\partial \overline{u'^2}}{\partial t} = -\overline{u' w'} \frac{\partial \bar{u}}{\partial z} - \frac{1}{2} \frac{\partial \overline{u'^2 w'}}{\partial z} + \frac{1}{\overline{\rho}} \overline{p' \frac{\partial u'}{\partial x}} + f \overline{u' v'} + \nu \overline{u' \nabla^2 u'}. \quad (4.14)$$

Application of the same steps to momentum Eqs. 2.4 and 2.5 yields budget equations for $\frac{1}{2} \overline{v'^2}$ and $\frac{1}{2} \overline{w'^2}$:

$$\frac{1}{2} \frac{\partial \overline{v'^2}}{\partial t} = -\overline{v' w'} \frac{\partial \bar{v}}{\partial z} - \frac{1}{2} \frac{\partial \overline{v'^2 w'}}{\partial z} + \frac{1}{\overline{\rho}} \overline{p' \frac{\partial v'}{\partial y}} - f \overline{u' v'} + \nu \overline{v' \nabla^2 v'}, \quad (4.15)$$

$$\frac{1}{2} \frac{\partial \overline{w'^2}}{\partial t} = \frac{g}{\theta} \overline{w' \theta'} - \frac{1}{2} \frac{\partial \overline{w'^3}}{\partial z} - \frac{1}{\overline{\rho}} \frac{\partial \overline{w' p'}}{\partial z} + \frac{1}{\overline{\rho}} \overline{p' \frac{\partial w'}{\partial z}} + \nu \overline{w' \nabla^2 w'}. \quad (4.16)$$

The first term on the right side of Eq. 4.16 is a consequence of the hydrostatic relation

$$\frac{1}{\overline{\rho}} \frac{\partial \bar{p}}{\partial z} = -g,$$

and the ideal gas law approximation

$$\frac{\rho'}{\overline{\rho}} = -\frac{\theta'}{\theta}.$$

The complete TKE budget equation is obtained by summing Eqs. 4.14, 4.15, and 4.16:

$$\frac{\partial \bar{e}}{\partial t} = \left(-\overline{u' w'} \frac{\partial \bar{u}}{\partial z} - \overline{v' w'} \frac{\partial \bar{v}}{\partial z} \right) + \frac{g}{\theta} \overline{w' \theta'} - \frac{\partial \overline{ew'}}{\partial z} - \frac{1}{\overline{\rho}} \frac{\partial \overline{w' p'}}{\partial z} - \epsilon, \quad (4.17)$$

where

$$\epsilon = -\nu \overline{u' \nabla^2 u'} - \nu \overline{v' \nabla^2 v'} - \nu \overline{w' \nabla^2 w'}, \quad (4.18)$$

and

$$e = \frac{1}{2} (u'^2 + v'^2 + w'^2). \quad (4.19)$$

The weak incompressibility Eq. 3.17 has been used to eliminate the pressure fluctuation terms, as

$$\overline{p' \frac{\partial u'}{\partial x}} + \overline{p' \frac{\partial v'}{\partial y}} + \overline{p' \frac{\partial w'}{\partial z}} = \overline{p' \left(\frac{\partial u'}{\partial x} + \frac{\partial v'}{\partial y} + \frac{\partial w'}{\partial z} \right)} = 0. \quad (4.20)$$

In the atmospheric surface layer, it is customary to express Reynolds statistics in the micrometeorological coordinate (Chap. 2), and the TKE budget equation can be simplified to

$$\frac{\partial \bar{e}}{\partial t} = -\overline{u'w'} \frac{\partial \bar{u}}{\partial z} + \frac{g}{\theta} \overline{w'\theta'} - \frac{\partial \overline{ew'}}{\partial z} - \frac{1}{\bar{\rho}} \frac{\partial \overline{w'p'}}{\partial z} - \epsilon. \quad (4.21)$$

Because the x -axis is now aligned with the mean surface wind vector, the mean velocity in the y direction (\bar{v}) is numerically zero.

The TKE budget in the atmospheric boundary layer can now be understood by examining Eq. 4.17. The first term on the right side of the equation is always positive, representing *shear production of turbulent kinetic energy*, and is balanced exactly by shear destruction of MKE (Fig. 4.4). The energy generated supports velocity fluctuations in the horizontal directions (Eqs. 4.14 and 4.15). In a shear-dominated flow, shear generation is stronger in the x direction than in the y direction, so kinetic energy in the x direction is greater than kinetic energy in the y direction, that is, $\frac{1}{2}\overline{u'^2} > \frac{1}{2}\overline{v'^2}$.

The second term on the right side of Eq. 4.17 represents *buoyancy production and destruction of turbulent kinetic energy*. This energy transfer pathway is restricted to the vertical direction and does not directly affect kinetic energy in the horizontal directions, since the term appears only in the vertical component equation (Eq. 4.16). In unstable conditions, because the covariance $w'\theta'$ is positive, turbulent eddies gain kinetic energy from the potential energy pool via the buoyancy effect. To understand this connection, we should remember that in unstable conditions, air parcels have a tendency to rise continuously after a slight upward perturbation. Let us imagine a warm air parcel being pushed upward by a positive buoyancy force. Continuity requires that some cooler air must come down to fill its place. As a result, the center of gravity of the air column will be lowered ever so slightly, causing a reduction in the potential energy. The opposite occurs in stable conditions, in which $w'\theta'$ is negative and kinetic energy is converted to potential energy via the buoyancy effect. Over the 24-h cycle, the buoyancy term is generally a net source of TKE on land because the 24-h mean $w'\theta'$ is positive.

The third and fourth terms on the right side of Eq. 4.17 represent *turbulent and pressure transport of turbulent kinetic energy*, respectively. Like the transport term

in the MKE budget Eq. 4.8, they move energy between different levels but do not create or destroy energy in the flow domain.

The last term on the right side of Eq. 4.17 represents *viscous dissipation of turbulent kinetic energy* into internal energy or kinetic energy of molecular motion. An important distinction between eddy motion and molecular motion is that eddy velocities, u' , v' , and w' , are molar properties of macroscopic nature that describe movement of groups of molecules, whereas molecular motion is of microscopic nature and characterized by total randomness. The quantity ϵ given by Eq. 4.18 is always positive. To demonstrate this, let us consider the first term on the right side of the equation. The chain rule of differentiation yields

$$\begin{aligned}
 -\nu \overline{u' \nabla^2 u'} &\equiv -\nu u' \left(\frac{\partial^2 u'}{\partial x^2} + \frac{\partial^2 u'}{\partial y^2} + \frac{\partial^2 u'}{\partial z^2} \right) \\
 &= -\nu \left[\frac{\partial}{\partial x} \left(u' \frac{\partial u'}{\partial x} \right) + \frac{\partial}{\partial y} \left(u' \frac{\partial u'}{\partial y} \right) + \frac{\partial}{\partial z} \left(u' \frac{\partial u'}{\partial z} \right) \right] \\
 &\quad + \nu \left[\left(\frac{\partial u'}{\partial x} \right)^2 + \left(\frac{\partial u'}{\partial y} \right)^2 + \left(\frac{\partial u'}{\partial z} \right)^2 \right] \\
 &\approx \nu \left[\left(\frac{\partial u'}{\partial x} \right)^2 + \left(\frac{\partial u'}{\partial y} \right)^2 + \left(\frac{\partial u'}{\partial z} \right)^2 \right] > 0. \tag{4.22}
 \end{aligned}$$

The same rearrangement can be made to the other two terms on the right side of Eq. 4.18 to show that they are also positive.

According to Eq. 4.22, ϵ can be determined from spatial gradients of the velocity fluctuations. Most of the data on ϵ found in the literature, however, have been derived indirectly as a residual from measurements of other terms in Eq. 4.17.

Examination of the component Eqs. 4.14, 4.15, and 4.16 reveals additional insights. We have already noted that wind shear produces TKE only in the horizontal directions and that buoyancy produces TKE only in the vertical direction. An interesting situation exists under neutral stability, in which $w'\theta'$ is zero, and therefore there is no buoyancy production of TKE. Since the two transport terms in Eq. 4.16 (the second and third terms on the right side) do not produce TKE either, it seems logical to suggest that no kinetic energy can be maintained in the vertical direction or that the vertical velocity variance, w'^2 , should be close to zero. The truth is that vertical velocity fluctuations can be quite vigorous in neutral stability. The kinetic energy in this case is supplied by *pressure redistribution* via the covariance between pressure fluctuations and w gradient fluctuations, the fourth term on the right side of the vertical component Eq. 4.16, which must be positive. Since the net effect of pressure fluctuations is zero as required by the *continuity constraint* (Eq. 4.20), a positive covariance involving the vertical velocity, $p'(\partial w'/\partial z)$, must be balanced by negative covariances involving the horizontal velocities, $p'(\partial u'/\partial x) + p'(\partial v'/\partial y)$, the latter of which appear in the horizontal component Eqs. 4.14 and 4.15. In other

words, pressure fluctuations act to redistribute to the vertical direction the kinetic energy produced by wind shear in the horizontal directions. The mechanism of pressure redistribution is also referred to as return to isotropy. In isotropic turbulence, the strength of velocity fluctuations is equal in all three orthogonal directions.

Pressure redistribution can reverse its direction. In a buoyancy-dominated boundary layer, buoyancy production of TKE is much stronger than shear production (Fig. 4.5). Some large-eddy simulations show that the two horizontal kinetic energy components ($\frac{1}{2}\bar{u'^2}$, $\frac{1}{2}\bar{v'^2}$) are approximately equal to the vertical component ($\frac{1}{2}\bar{w'^2}$) despite the low rate of shear production, suggesting that some of the kinetic energy produced by buoyancy in the vertical direction is redistributed by pressure fluctuations to the horizontal directions (Fig. 4.4).

Similar to the MKE discussion, the Coriolis force appears in the two horizontal component Eqs. 4.14 and 4.15 (the fourth term on the right side), but its effect is canceled out in the total TKE equation. Measurements in a forest landscape indicate that the covariance between the two horizontal velocities, $\bar{u'v'}$, is slightly positive at a mean value of $0.05 \text{ m}^2 \text{ s}^{-2}$. So the term $f\bar{u'v'}$ is on the order of $5 \times 10^{-6} \text{ m}^2 \text{ s}^{-3}$, which is much smaller than the other TKE budget terms (Fig. 4.5) and can be safely ignored.

4.4 Air Stability

Air stability refers to the vertical moving tendency of an air parcel in response to a small disturbance. The parcel's vertical movement can be assumed adiabatic, meaning that no heat is lost from the parcel via molecular diffusion to the surroundings, no molecules escape from the parcel, no heat source exists within the parcel, and its internal pressure is always the same as the environmental pressure. The parcel's temperature will decrease as it moves upward due to its volume expansion. In hydrostatic equilibrium and without condensation or evaporation, the first law of thermodynamics predicts that the vertical rate of change in the parcel's temperature, or the dry adiabatic lapse rate, should be -9.8 K km^{-1} . Now consider a situation where the environmental temperature displays a faster decrease with height than the dry adiabatic lapse rate (Fig. 4.6a). Let us suppose that a small parcel at height z_1 is displaced upward to height z_2 by an external disturbance. After reaching height z_2 , the parcel will be slightly cooler than its original state at z_1 but warmer than the environmental air at z_2 . So the parcel will act as if it were a hot air balloon because it feels an upward buoyancy force and will have the tendency to continue the upward movement. (If the parcel is displaced downward in the thought experiment, it will become denser than the surrounding air and will continue to sink downward.) The situation is statically unstable.

The amplification of a small vertical disturbance represents the mechanism by which buoyancy produces turbulence (Fig. 4.7a). To an observer at height z_2 , the rising air parcel in the thought experiment is essentially a turbulent eddy causing fluctuations in observed time series.

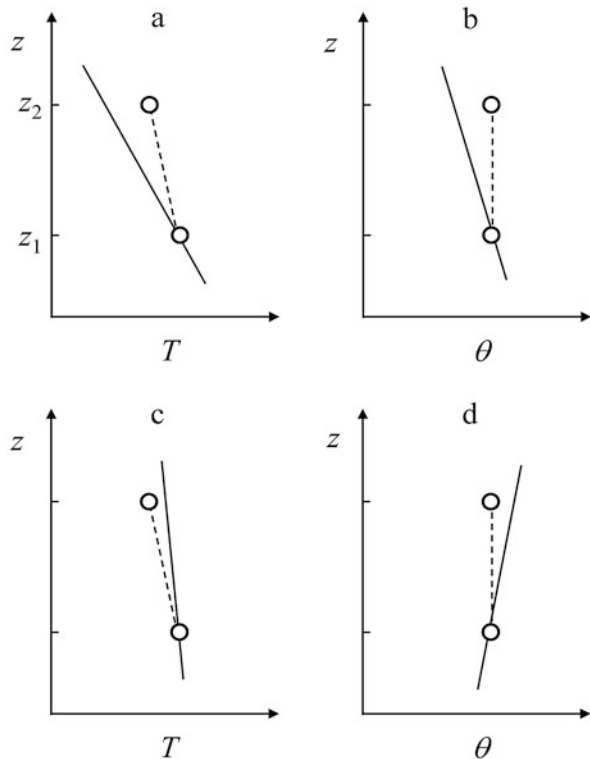
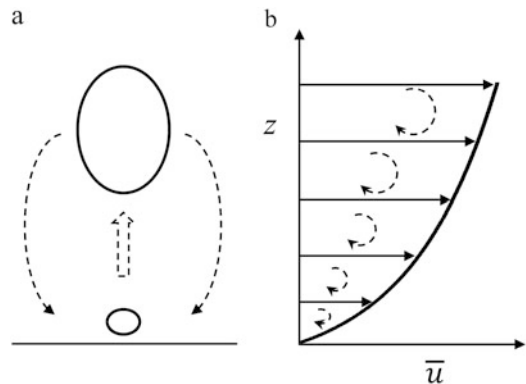


Fig. 4.6 Determining air stability using profiles of air temperature (a and c) and potential temperature (b and d). Solid lines indicate environmental profiles. Dashed lines indicate the temperature that an air parcel originating from height z_1 would have in its vertical movement

Fig. 4.7 Production of turbulence: (a) buoyancy production and (b) shear production



If the environmental temperature decreases more slowly with height than the dry adiabatic lapse rate, the air is statically stable (Fig. 4.6c). An air parcel displaced from z_1 to z_2 will be cooler than the surrounding air. As a consequence, buoyancy will force the parcel downward to its original position. In other words, any small perturbation will be damped out by buoyancy. Suppression of vertical perturbations is a universal characteristic of stable stratification and explains why turbulence is weakened in stable conditions. Inversion layers, in which air temperature increases with height, are particularly stable and are barriers to turbulent transport.

An air layer is called neutral if its environmental temperature changes with height at a rate equal to the dry adiabatic lapse rate. Under neutral conditions, turbulence is generated mechanically by wind shear (Fig. 4.7b). In the presence of wind shear and a viscous force, the flow is dynamically unstable such that a small initial perturbation will become amplified, leading to overturning motion. Shear generation of turbulence also occurs in unstable air and is possible in stable air if the gradient Richardson number, defined in Eq. 4.27 below, is smaller than the critical value of 0.25.

The diagnosis of air stability is often made with potential temperature profiles (Fig. 4.6b, d). Since the potential temperature of an air parcel is constant in the dry adiabatic process, the stability criteria can be stated as

$$\begin{aligned} < 0 && \text{unstable} \\ \frac{\partial \bar{\theta}}{\partial z} = 0 && \text{neutral} \\ > 0 && \text{stable} \end{aligned} \quad (4.23)$$

where $\bar{\theta}$ is the potential temperature of the atmosphere.

So far, our description of air stability has remained qualitative. If $\partial \bar{\theta} / \partial z$ is negative, we know that the air layer is unstable, but we do not know how unstable it is. Under weak wind conditions, a slightly negative potential temperature gradient can allow formation of deep, penetrating eddies, so the air layer can be very unstable. If the wind is strong, energetic eddies are less likely to take shape, even under conditions of a large negative potential temperature gradient. Quantitative stability parameters are needed to capture the combined effect of wind and thermal stratification.

One such parameter, called the *flux Richardson number*, expresses the combined effect by comparing the relative strength of buoyancy production and destruction and shear production of turbulence according to the TKE budget Eq. 4.17:

$$R_f = \frac{\text{buoyancy production}}{\text{shear production}} = \frac{\frac{g}{\bar{\theta}} \overline{w' \theta'}}{\overline{u' w'} \frac{\partial \bar{u}}{\partial z} + \overline{v' w'} \frac{\partial \bar{v}}{\partial z}}. \quad (4.24)$$

For historical reasons, the negative sign in the shear production term is omitted. In the surface layer, Eq. 4.24 can be simplified to

$$R_f = \frac{\frac{g}{\bar{\theta}} \overline{w' \theta'}}{\frac{u' w'}{\partial z} \bar{u}}. \quad (4.25)$$

Since the denominator of Eq. 4.24 is negative, R_f is opposite in sign to the eddy sensible heat flux. The stability criteria can be stated as

< 0	unstable	
$R_f = 0$	neutral	(4.26)
> 0	stable	

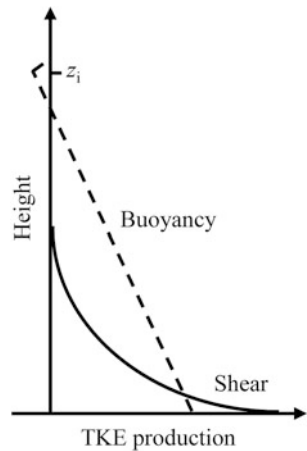
In a type of motion called *forced convection*, shear-generated turbulence dominates the flow, and R_f approaches zero. Both buoyancy and wind shear contribute to turbulence generation if R_f is negative, and buoyancy destroys turbulence if R_f is positive. A R_f value of -1 occurs when buoyancy production of turbulence is at the same level as shear production, indicating strong instability. Numerically, R_f does not have a lower bound. In the limit of *free convection*, at which shear production vanishes, R_f approaches negative infinity. However, R_f is bounded by the theoretical upper limit of 1, beyond which turbulence cannot exist because buoyancy destruction of turbulence would exceed shear production of turbulence. Experimental data suggest that the actual upper limit is about 0.21, on the account that viscous dissipation is a sink of TKE in addition to buoyancy destruction.

The flux Richardson number is strongly dependent on height. In a typical convective boundary layer, the buoyancy production term decreases linearly with height, but the shear production term is highest near the surface, where the wind shear is strongest, and decreases more rapidly with height (Fig. 4.8). We expect R_f to be close to zero near the surface and to approach large negative values in the upper boundary layer.

Some people prefer to determine air stability with vertical gradients of the mean temperature and the wind speed because their measurements are more readily available than measurements of the heat and the momentum fluxes, especially in the upper boundary layer. The *gradient Richardson number*, R_i , serves this purpose, where

$$R_i = \frac{\frac{g}{\bar{\theta}} \frac{\partial \bar{\theta}}{\partial z}}{\left(\frac{\partial \bar{u}}{\partial z} \right)^2 + \left(\frac{\partial \bar{v}}{\partial z} \right)^2}, \quad (4.27)$$

Fig. 4.8 Profiles of shear production and buoyancy production of turbulence in a convective boundary layer



or

$$R_i = \frac{\frac{g}{\bar{\theta}} \frac{\partial \bar{\theta}}{\partial z}}{\left(\frac{\partial \bar{u}}{\partial z} \right)^2}, \quad (4.28)$$

in the surface layer. Using the first-order closure parameterization discussed in Chap. 3 (Eqs. 3.36, 3.37, and 3.38), it is straightforward to show that the gradient Richardson number is related to the flux Richardson number, as

$$R_i = \frac{K_m}{K_h} R_f, \quad (4.29)$$

where K_m and K_h are eddy diffusivity for momentum and for heat, respectively. The stability criteria now become

$$\begin{aligned} < 0 & \quad \text{unstable} \\ R_i = 0 & \quad \text{neutral} \\ > 0 & \quad \text{stable} \end{aligned} \quad (4.30)$$

Consistent with Eq. 4.23, Eq. 4.30 indicates that stability classes are solely determined by the vertical potential temperature gradient. Field observations show that $R_i \simeq R_f$ under neutral and stable conditions. In unstable conditions, the turbulent Prandtl number, K_m/K_h , is less than one owing to the fact that convective eddies are less efficient in transporting momentum than heat, so R_i is smaller in magnitude than R_f .

Even though air stability is a strong function of height, neither R_f nor R_i shows explicitly the height dependence. This deficiency is circumvented by the *Monin-Obukhov stability parameter*, ζ . In contrast to the gradient Richardson number, the ζ formulation avoids gradient quantities but relies instead on flux quantities to determine air stability. This parameter is for use in the atmosphere surface layer where measurement of fluxes is relatively easy. Even if direct measurement of fluxes is not available, we can constrain ζ with an iterative routine and the flux-gradient relationships (Problem 4.18). Essentially ζ is a variation of the flux Richardson number. Differentiating Eq. 3.47 with respect to z and omitting stability effects, we obtain an approximation to $\partial \bar{u} / \partial z$:

$$\frac{\partial \bar{u}}{\partial z} \simeq \frac{u_*}{kz}. \quad (4.31)$$

Eliminating $\partial \bar{u} / \partial z$ from Eq. 4.25 with Eq. 4.31 and noting that $\overline{u'w'} = -u_*^2$, we obtain an approximation to R_f ,

$$R_f \simeq \zeta = \frac{z}{L}, \quad (4.32)$$

where the Obukhov length, L , is given by

$$L = -\frac{u_*^3}{k \left(\frac{g}{\bar{\theta}} \right) \overline{w'\theta'}}.$$

Equation 4.32 indicates that air stability (or instability) increases linearly with height. This is because L is determined with the surface friction velocity and heat flux and therefore is invariant with height. The sign of L determines stability classes: air is unstable if L is negative and stable otherwise. The magnitude of L is a measure of the vertical extent of shear dominance in turbulence production. In unstable conditions, shear production and buoyancy production are approximately equal at height $z = -L$, shear production dominates over buoyancy production below the height $z = -L$, and vice versa above $z = -L$. An infinitely large L indicates neutral stability, under which shear production dominates throughout the boundary layer.

We can also derive the Monin-Obukhov stability parameter, a dimensionless number, from the *Monin-Obukhov similarity theory*. The theory states that turbulence in a horizontally homogeneous surface layer is controlled by four dimensional variables: z , u_* , $\overline{w'\theta'}$, and $g/\bar{\theta}$. Dimensional analysis reveals that ζ is the simplest dimensionless combination of these four basic variables and that many Reynolds quantities after normalization with one or more of these variables are functions of ζ . For example, the normalized velocity gradient is a function of ζ . This function is denoted by ϕ_m , as

$$\phi_m(\zeta) = \frac{kz}{u_*} \frac{\partial \bar{u}}{\partial z}. \quad (4.33)$$

Manipulation of Eq. 4.33 and the flux-gradient Eq. 3.36 yields Eq. 3.50, indicating that ϕ_m is a function that corrects stability effects on the momentum eddy diffusivity. Likewise, the normalized potential temperature gradient,

$$\phi_h(\zeta) = \frac{kz}{\theta_*} \frac{\partial \bar{\theta}}{\partial z}, \quad (4.34)$$

is a stability correction function for the heat eddy diffusivity. Both ϕ_m and ϕ_h are equal to one in neutral stability, are less than one in unstable conditions, and are greater than one in stable conditions. Their forms have been determined experimentally, as

$$\phi_m = (1 - 16\zeta)^{-1/4}, \quad (4.35)$$

and

$$\phi_h = (1 - 16\zeta)^{-1/2}, \quad (4.36)$$

for $-5 < \zeta < 0$, and

$$\phi_m = \phi_h = 1 + 5\zeta \quad (4.37)$$

for $0 \leq \zeta < 1$ (Fig. 4.9). In these functions, the von Karman constant k takes the value of 0.4.

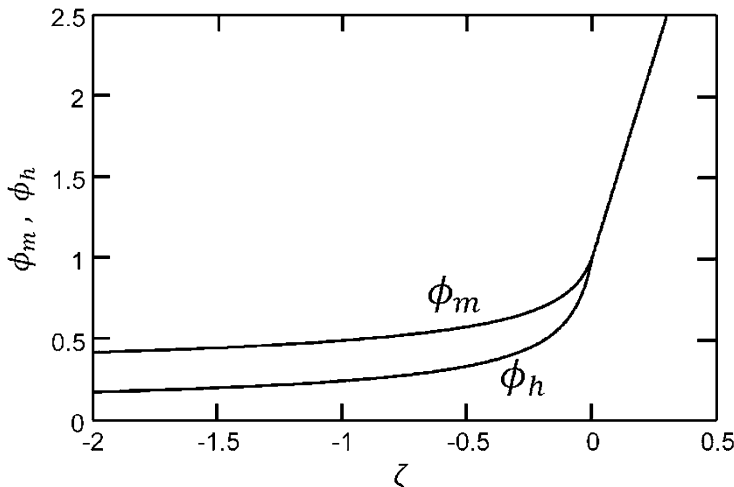


Fig. 4.9 Monin-Obukhov stability functions

Equation 4.32 is valid in the surface layer above a smooth surface. If the surface is occupied by vegetation or buildings, the height is measured in reference to the displacement height, so

$$\zeta = \frac{z - d}{L}. \quad (4.38)$$

4.5 Problems

4.1 Generate a synthetic time series dataset for the three instant velocity components. Calculate the mean total kinetic energy, the mean flow kinetic energy, and the turbulent kinetic energy. Verify that your results satisfy Eq. 4.2.

4.2 The friction velocity is 0.32 m s^{-1} , and stability is neutral. (a) Calculate the shear destruction and viscous dissipation of MKE and (b) the viscous dissipation of TKE, at the height of 10.0 and 0.5 m in the surface layer. Assume that the TKE transport terms are negligible, the atmosphere is at steady state, and the mean velocity profile can be described by the logarithmic model with a momentum roughness of 0.1 m (Eq. 2.50). How much larger is the viscous dissipation of TKE than the viscous dissipation of MKE?

4.3 The normalized TKE dissipation in the surface layer is defined as

$$\phi_\epsilon = \frac{k z \epsilon}{u_*^3}.$$

Obtain an expression for ϕ_ϵ as a function of the Monin-Obukhov stability parameter ζ from the surface layer TKE budget Eq. 4.21, assuming that the transport terms are negligible and the atmosphere is in a steady state. Plot this expression for the stability range $-1.0 < \zeta < 0.2$. Some field observations show that $\phi_\epsilon = 1.24$ in neutral stability. If this is true, is TKE transported into or out of the surface layer?

4.4 The horizontal pressure gradient is 0.02 hPa km^{-1} . The horizontal velocity is 10.0 m s^{-1} . The angle between the horizontal velocity vector and the pressure gradient force vector is 60° . Calculate the MKE production.

4.5 Calculate column total rates of shear and buoyancy production of TKE, in units of W m^{-2} , for the convective boundary layer depicted in Fig. 4.5 (right panel). Assume that the depth of the boundary layer is 1000 m and the air density is 1.20 kg m^{-3} .

4.6 It has been frequently observed that a convective boundary layer collapses quickly in late afternoon after the surface stops producing sensible heat flux. The collapse time can be approximated by the time needed for viscous dissipation to consume all the TKE. Estimate the collapse time using the data shown in Fig. 4.5 for the buoyancy-driven boundary layer. In your calculation, ignore shear and buoyancy

production of TKE after the surface sensible heat flux has vanished and assume that viscous dissipation continues at the initial rate of $0.37 \times 10^{-2} \text{ m}^2 \text{ s}^{-3}$.

4.7* Improve the collapse time calculation in Problem 4.6 by deploying a time-dependent parameterization for the dissipation term, as

$$\epsilon = \frac{\bar{e}^{3/2}}{\Lambda} \quad (4.39)$$

where Λ is a length scale and is related to the eddy mixing length (Eq. 3.52; Fig. 3.4) as

$$\Lambda = Bl$$

with the coefficient $B = 5.0$.

4.8 Let us define a dimensionless TKE as

$$\phi_e = \frac{\bar{e}}{u_*^2}.$$

Obtain an expression for ϕ_e as a function of the Monin-Obukhov stability parameter ζ for the surface layer from the parameterization Eq. 4.39 and the surface TKE budget Eq. 4.21. Assume in your derivation that the air is at steady state and that the transport terms are negligible. Use the expression to estimate \bar{e} for the following conditions: (1) $u_* = 0.28 \text{ m s}^{-1}, \zeta = -0.5$; (2) $u_* = 0.28 \text{ m s}^{-1}, \zeta = 0$; (3) $u_* = 0.15 \text{ m s}^{-1}, \zeta = 0$; (4) $u_* = 0.15 \text{ m s}^{-1}, \zeta = 0.2$. Comment on how friction velocity and air stability affect TKE in the surface layer.

4.9 The vertical TKE flux, $\overline{ew'}$, is 0.825 and $0.044 \text{ m}^3 \text{ s}^{-3}$ at the heights of 300 and 600 m above the ground, respectively, in a shear-driven boundary layer. Calculate the vertical turbulent TKE transport. Does the transport term contribute to a gain or a loss of local TKE in the $300\text{--}600 \text{ m}$ air layer?

4.10 Determine if each of the air layers indicated in Fig. 4.10 is unstable, neutral, or stable.

4.11 Show that the flux Richardson number and the gradient Richardson number are dimensionless and that the Obukhov length has the dimension of length.

4.12 Calculate the Monin-Obukhov stability parameter ζ and the eddy diffusivity for momentum (K_m) and for heat (K_h) using the data shown in Table 4.1.

4.13* Integration of Eqs. 4.33 and 4.34 with respect to z yields

$$\frac{\bar{u}(z)}{u_*} = \frac{1}{k} \left[\ln \frac{z}{z_o} - \Psi_m(\zeta) \right], \quad (4.40)$$

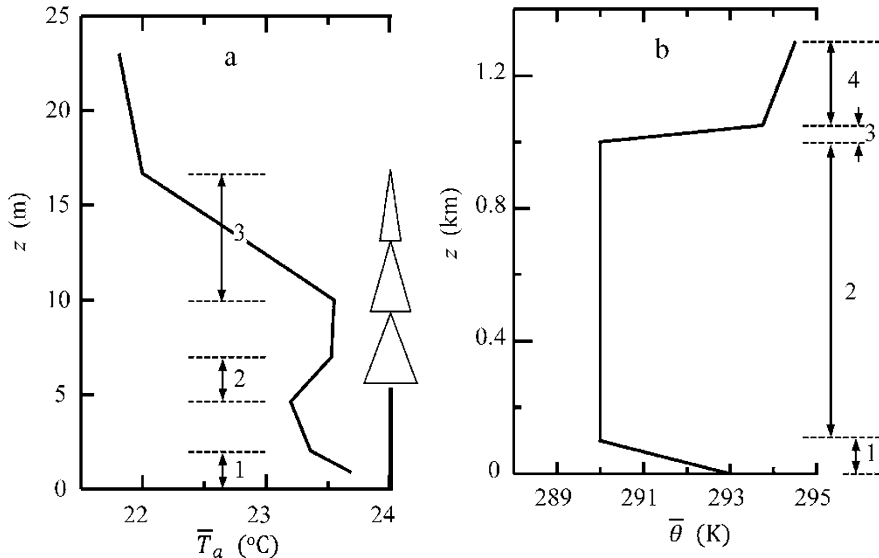


Fig. 4.10 Profile of air temperature in a forest at midday (a) and profile of potential temperature in a daytime convective boundary layer (b)

Table 4.1 Observed friction velocity u_* (m s^{-1}) and sensible heat flux F_h (W m^{-2}) at a measurement height of 3.5 m above the surface of a shallow lake and at 15.2 m above the displacement height of a forest

Time	Lake					Forest				
	u_*	F_h	ζ	K_m	K_h	u_*	F_h	ζ	K_m	K_h
00:10	0.09	0.1				0.14	21.6			
12:40	0.24	33.4				0.32	436.8			

$$\frac{\bar{\theta}(z) - \theta_o}{\theta_*} = \frac{1}{k} \left[\ln \frac{z}{z_{o,h}} - \Psi_h(\xi) \right], \quad (4.41)$$

where

$$\Psi_m = \int_{z_{o,L}/L}^{\xi} [1 - \phi_m(\xi)] \frac{d\xi}{\xi} \simeq \int_0^{\xi} [1 - \phi_m(\xi)] \frac{d\xi}{\xi},$$

and

$$\Psi_h = \int_{z_{o,h}/L}^{\xi} [1 - \phi_h(\xi)] \frac{d\xi}{\xi} \simeq \int_0^{\xi} [1 - \phi_h(\xi)] \frac{d\xi}{\xi}$$

are called integral similarity or stability functions (Paulson 1970). The mean wind and potential temperature profiles now deviate from the logarithmic relations (Eqs. 3.47 and 3.48) due to stability effects. Show that

$$\begin{aligned}\Psi_m &= \Psi_h = -5\zeta, \zeta \geq 0 \\ \Psi_m &= \ln \left[\left(\frac{1+x^2}{2} \right) \left(\frac{1+x}{2} \right)^2 \right] - 2 \arctan x + \frac{\pi}{2}, \zeta < 0 \\ \Psi_h &= 2 \ln \left(\frac{1+x^2}{2} \right), \zeta < 0\end{aligned}\quad (4.42)$$

where $x = (1 - 16\zeta)^{1/4}$.

4.14 Show from Eqs. 3.75, 3.79, 3.83, and 4.40, 4.41, 4.42 that the aerodynamic resistances and the transfer coefficients in stratified air can be expressed as

$$r_{a,m} = \frac{1}{k^2 \bar{u}} \left[\ln \frac{z}{z_o} - \Psi_m(\zeta) \right]^2, \quad (4.43)$$

$$r_{a,h} = \frac{1}{k^2 \bar{u}} \left[\ln \frac{z}{z_o} - \Psi_m(\zeta) \right] \left[\ln \frac{z}{z_{o,h}} - \Psi_h(\zeta) \right], \quad (4.44)$$

$$C_D = k^2 \left[\ln \frac{z}{z_o} - \Psi_m(\zeta) \right]^{-2}, \quad (4.45)$$

$$C_H = k^2 \left[\ln \frac{z}{z_o} - \Psi_m(\zeta) \right]^{-1} \left[\ln \frac{z}{z_{o,h}} - \Psi_h(\zeta) \right]^{-1}. \quad (4.46)$$

Calculate the resistances and the transfer coefficients for a grass (momentum roughness $z_o = 0.02$ m) and a bare soil ($z_o = 0.002$ m) at $\zeta = -0.5, 0$, and 0.2 . Assume in your calculation that wind speed is 3.0 m s^{-1} , the roughness ratio $z_{o,h}/z_o$ is 0.14, and reference height z is 5.0 m. Which surface is more sensitive to stability effects?

4.15 Using the data in Table 4.2, compute the gradient Richardson number for the air layer between the heights of 0 and 100 m and between the heights of 100 and 200 m.

Table 4.2 Horizontal velocities (\bar{u} and \bar{v}) and potential temperature ($\bar{\theta}$) in an atmospheric boundary layer. Observation height is denoted by z

z (m)	\bar{u} (m s^{-1})	\bar{v} (m s^{-1})	$\bar{\theta}$ (K)
0	0	0	287.0
100	6.9	0.8	285.2
200	7.3	1.0	284.6

4.16 Show that the gradient Richardson number in the surface layer is related to the Monin-Obukhov stability parameter as

$$R_i = \zeta \phi_h / \phi_m^2. \quad (4.47)$$

Plot this relationship over the stability range $-2 < \zeta < 2$.

4.17 Plot the turbulent Prandtl number, defined as the ratio of the eddy diffusivity for momentum (K_m) to the eddy diffusivity for heat (K_h), as a function of the Monin-Obukhov stability parameter (ζ) over the stability range $-2 < \zeta < 2$.

4.18* In an observation in a potato farm, air temperature and wind speed are 19.86°C and 1.46 m s^{-1} at the height of 1.57 m and 19.39°C and 1.85 m s^{-1} at the height of 2.91 m above the ground. The displacement height is 0.70 m . (1) Use an iterative method to determine the Monin-Obukhov stability parameter (ζ), the momentum flux (F_m), and the eddy sensible heat flux (F_h) from the flux-gradient Eqs. 3.61 and 3.62. In your calculation, you should use the geometric mean height (Eq. 3.66) for ζ . (2) Calculate the gradient Richardson number and compare it with that predicted by Eq. 4.47.

4.19 The following conditions are reported for an atmospheric surface layer: sensible heat flux $\rho_d C_p \overline{w' \theta'} = 350.2 \text{ W m}^{-2}$, momentum flux $-\overline{u' w'} = 0.12 \text{ m}^{-2} \text{ s}^{-2}$, vertical velocity gradient $\partial \bar{u} / \partial z = 0.03 \text{ s}^{-1}$, and potential temperature $\bar{\theta} = 298.1 \text{ K}$. Find (1) the buoyancy and the shear production of turbulent kinetic energy and (2) the flux Richardson number.

4.20 (1) Find the momentum and the heat eddy diffusivity at the height of 3.5 m above the surface if the friction velocity u_* is 0.25 m s^{-1} and the Monin-Obukhov stability parameter ζ is -0.3 . (2) Repeat the calculation but with a ζ value of 0.3 . How does thermal stratification impact turbulent diffusion?

References

- Mellor GL, Yamada T (1982) Development of a turbulence closure model for geophysical fluid problems. Rev Geophys Space Phys 20:851–875
 Moeng CH, Sullivan PP (1994) A comparison of shear- and buoyancy-driven planetary boundary layer flows. J Atmos Sci 51:999–1022
 Paulson CA (1970) The mathematical representation of wind speed and temperature in the unstable atmospheric surface layer. J Appl Meteorol 9:857–861
 Peixoto JP, Oort AH (1992) Physics of climate. American Institute of Physics, New York, 520pp
 Shaw R (1987) Lecture notes on boundary-layer meteorology. University of California, Davis
 Wyngaard JC (2004) Toward numerical modeling in the “Terra Incognita”. J Atmos Sci 61:1816–1826

Chapter 5

Flow in Plant Canopies

5.1 Canopy Morphology

Vegetation habitats occupy a large portion of the terrestrial land on earth, their total area equaling the area of all smooth surfaces (glaciers, deserts and lakes) combined. Forming a porous medium called the canopy layer, plant elements alter the air flow in several significant ways. They slow down the air motion by absorbing its momentum, increase turbulence intensity by generating small eddies in their wakes, enhance atmospheric humidity by water evaporation, exchange radiation energy and sensible heat with the atmosphere, and serve as sources and sinks of numerous trace gases. In this chapter, we will investigate the dynamic aspects of the canopy flow and leave treatment of the energy and gaseous exchanges to Chap. 8.

We use three parameters, canopy height, h , plant area index, L , and plant area density, a , to describe canopy morphology. Here a refers to the amount of one-sided plant surface area in a unit volume of space, and L is the total plant surface area above a unit ground area. They are related to one another as

$$L = \int_0^h a \, dz. \quad (5.1)$$

In the growing season, L is approximately equal to leaf area index.

Other plant morphological attributes are not considered by our canopy flow theory. In the canopy layer between the ground surface and the height h , the fraction of space occupied by plant elements is small, typically less than 0.05%, and is ignored. Even though leaves in a real canopy are clustered along stems and branches, we assume that our averaging volume is sufficiently large so that the clumping does not influence volume mean flow. We also assume that interactions of plant elements with the mean flow do not depend on their orientation or shape.

5.2 Canopy Volume Averaging

The Reynolds mean equations derived in Chap. 3 are still valid at any point in the air pocket between plant elements. But the problem becomes intractable if we attempt to solve the equations directly. We would need to deal with pressure and velocity variations between neighboring plant elements. We would also face the insurmountable difficulty of specifying boundary conditions at the surface of every single plant element. Even if we were able to overcome these challenges, such microscale details of the flow would be of little value to most practical problems.

A more fruitful strategy is to perform one additional averaging operation, called *canopy volume averaging*, on the Reynolds mean equations (Raupach and Shaw 1982). Let $\bar{\Phi}$ be a Reynolds mean quantity. It can be decomposed into a volume mean part, $[\bar{\Phi}]$, and a deviation from the volume mean, $\bar{\Phi}''$,

$$\bar{\Phi} = [\bar{\Phi}] + \bar{\Phi}'', \quad (5.2)$$

where

$$[\bar{\Phi}] = \iiint_Q \bar{\Phi} dQ. \quad (5.3)$$

The averaging volume, Q , imagined here as a thin rectangular prism (Fig. 5.1), is small enough so that macroscopic features of the flow are preserved and is big enough so that microscale variations associated with individual plant elements are smoothed out (Finnigan 2000). The vertical dimension of the averaging volume is much smaller than its horizontal dimensions to help resolve vertical variations of the flow. In canopies where plants are regularly spaced, such as in row crops, the horizontal dimensions extend several rows of plants. In natural habitats, the averaging volume encompasses a distance that is several times the average plant spacing.

Similar to the Reynolds averaging rules (Eqs. 3.3, 3.4, and 3.5), the canopy volume averaging operation observes the following properties:

$$[[\bar{\Phi}]] = [\bar{\Phi}], \quad (5.4)$$

$$[\bar{\Phi}'''] = 0, \quad (5.5)$$

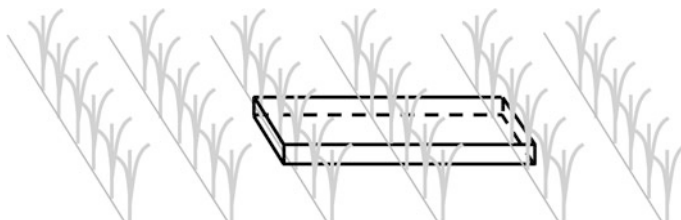


Fig. 5.1 An averaging volume in the canopy air space

and

$$[[\bar{\Psi}] \bar{\Phi}''] = 0, \quad (5.6)$$

where $\bar{\Psi}$ is the Reynolds mean of quantity Ψ . Reynolds mean variables are continuous functions of time, so differentiation with respect to time and volume averaging are commutable:

$$\left[\frac{\partial \bar{\Phi}}{\partial t} \right] = \frac{\partial [\bar{\Phi}]}{\partial t}, \quad (5.7)$$

However, commutation between volume averaging and spatial differentiation

$$\left[\frac{\partial \bar{\Phi}}{\partial x} \right] = \frac{\partial [\bar{\Phi}]}{\partial x}, \quad \left[\frac{\partial \bar{\Phi}}{\partial y} \right] = \frac{\partial [\bar{\Phi}]}{\partial y}, \quad \left[\frac{\partial \bar{\Phi}}{\partial z} \right] = \frac{\partial [\bar{\Phi}]}{\partial z}, \quad (5.8)$$

cannot be automatically assumed because some Reynolds mean quantities are not continuous in the canopy airspace.

A classic example is pressure discontinuity. Let us consider a hypothetical canopy whose plant elements are thin vertical plates arranged at a regular interval in the x direction (Fig. 5.2). The mean pressure, \bar{p} , is low in the wake of the first element and increases with x until the upwind face of the next element. The pattern repeats itself, with discontinuity occurring at each plant element. In the gap between two adjacent elements, $\partial \bar{p}'' / \partial x$ is positive. It follows then:

$$\left[\frac{\partial \bar{p}}{\partial x} \right] = \left[\frac{\partial([\bar{p}] + \bar{p}'')}{\partial x} \right] = \left[\frac{\partial[\bar{p}]}{\partial x} \right] + \left[\frac{\partial \bar{p}''}{\partial x} \right] = \left[\frac{\partial \bar{p}''}{\partial x} \right] > 0.$$

However, Eq. 5.8 gives rise to:

$$\left[\frac{\partial \bar{p}}{\partial x} \right] = \left[\frac{\partial([\bar{p}] + \bar{p}'')}{\partial x} \right] = \frac{\partial[[\bar{p}] + \bar{p}'']}{\partial x} = \frac{\partial[[\bar{p}]]}{\partial x} + \frac{\partial[\bar{p}'']}{\partial x} = 0,$$

which is clearly an erroneous result.

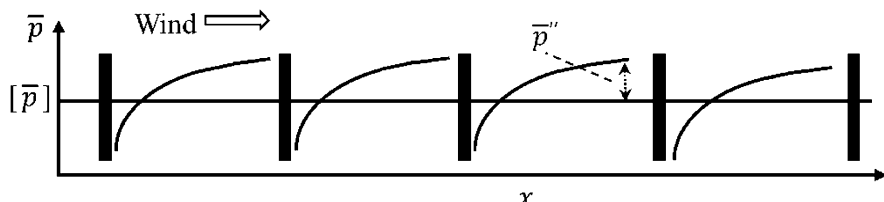


Fig. 5.2 Pressure variation in a hypothetical canopy. Modified after Raupach and Shaw (1982)

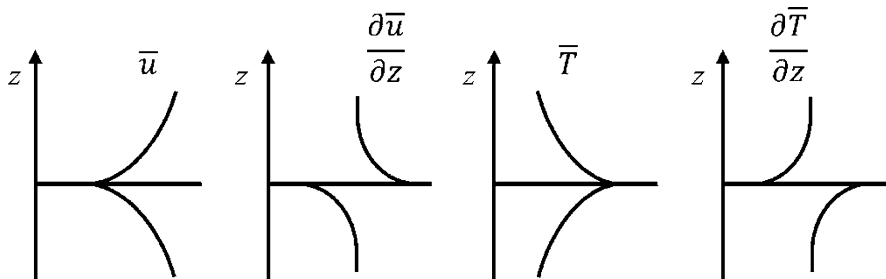


Fig. 5.3 Vertical profiles of Reynolds mean velocity and temperature and their vertical derivatives above and below a horizontal leaf

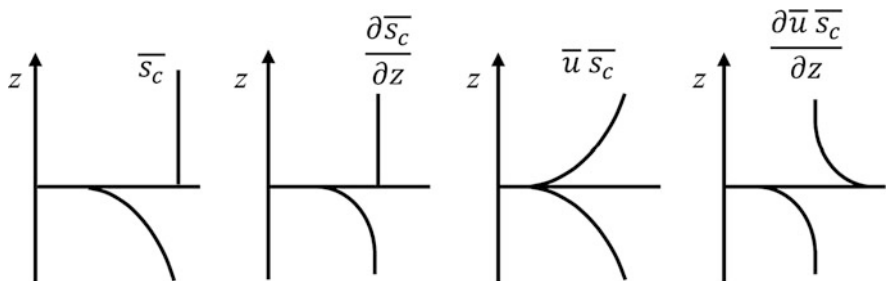


Fig. 5.4 Vertical profiles of Reynolds mean CO₂ mixing ratio, the product of the mixing ratio and the mean velocity, and their vertical derivatives above and below a photosynthesizing hypostomatus leaf

Three more examples of discontinuity, all concerning a horizontal leaf, are illustrated in Figs. 5.3 and 5.4. The mean velocity, \bar{u} , is zero at the surface on both sides of the leaf due to the no-slip condition. But its vertical derivative, $\partial \bar{u} / \partial z$, is discontinuous at the surface. The commutation property (Eq. 5.8) holds for \bar{u} but not for $\partial \bar{u} / \partial z$, that is,

$$\left[\frac{\partial \bar{u}}{\partial z} \right] = \frac{\partial [\bar{u}]}{\partial z}, \quad (5.9)$$

and

$$\left[\frac{\partial^2 \bar{u}}{\partial z^2} \right] \neq \frac{\partial}{\partial z} \left[\frac{\partial \bar{u}}{\partial z} \right]. \quad (5.10)$$

A consequence of Eq. 5.10 is that the Laplace operator and volume averaging do not commute on \bar{u} or \bar{u}'' . Similarly, if we assume that the leaf is a good heat conductor, the property holds for the mean temperature, \bar{T} , but not for its vertical derivative. The third example describes CO₂ distribution at the leaf, which we suppose is a hypostomatus type with stomata present on its lower side and is photosynthesizing.

The product of the CO₂ mass mixing ratio and the velocity, $\bar{s}_c \bar{u}$, observes the commutation property owing to the no-slip condition, but the mean mass mixing ratio itself, its vertical derivative, and the vertical derivative of $\bar{s}_c \bar{u}$ do not.

In the above examples, the criterion for judging whether a variable observes the commutation property is based on continuity because our imaginary plant elements are infinitely thin. For a real canopy consisting of plant elements of finite thickness or volume, a more general criterion can be stated as follows: volume averaging and spatial differentiation are commutable if the variable is constant on the surface of each plant element, and are not commutable otherwise. This result is a consequence of Slattery's averaging theorem on fluid motion in porous media (Whitaker 1969; Li et al. 1990). The theorem is expressed as

$$\left[\frac{\partial \bar{\Phi}}{\partial x} \right] = \frac{\partial [\bar{\Phi}]}{\partial x} - \frac{1}{Q} \sum \iint_{A_i} \bar{\Phi} n_x dA, \quad (5.11)$$

for flow in canopies, where A_i is the surface of plant element i ; the summation is performed to include all the elements in the space bounded by volume Q (Fig. 5.1), and n_x is the x -component of the unit normal vector of the surface pointing outward to the canopy airspace. Similar expressions can be written for the y and the z derivative. The surface integral, the second term on the right of Eq. 5.11, can be interpreted as an emergent property arising from canopy volume averaging and is zero if $\bar{\Phi}$ is constant on A_i according to the divergence theorem in calculus.

In the next section and later in Chap. 8, we will show that non-zero surface integrals are mathematical expressions of canopy effects on the volume mean flow. In momentum conservation, surface integrals of \bar{p}'' and the spatial derivatives of \bar{u}'' are equivalent to canopy momentum sinks. Likewise, surface integrals of the spatial derivatives of \bar{T} and \bar{s}_c represent a canopy heat source and a carbon dioxide source, respectively.

5.3 The Mean Momentum Equations

Following tradition, we express the momentum equations in the micrometeorological coordinate system (Fig. 2.1). Unlike the Cartesian coordinate anchored by the pressure gradient force vector in Chap. 4 (Fig. 4.1), here the x -axis is aligned with the mean wind direction in the surface layer above the canopy.

Applying canopy volume averaging to Eq. 3.16 and noting that the commutation property (Eq. 5.8) holds for Reynolds mean velocities, we obtain the incompressibility equation for the volume mean flow:

$$\frac{\partial[\bar{u}]}{\partial x} + \frac{\partial[\bar{v}]}{\partial y} + \frac{\partial[\bar{w}]}{\partial z} = 0. \quad (5.12)$$

Subtraction of Eq. 5.12 from Eq. 3.16 yields the governing equation on the spatial fluctuations of Reynolds mean velocities:

$$\frac{\partial \bar{u}''}{\partial x} + \frac{\partial \bar{v}''}{\partial y} + \frac{\partial \bar{w}''}{\partial z} = 0. \quad (5.13)$$

Under the canopy volume averaging scheme, the Reynolds mean momentum Eq. 3.21 becomes

$$\begin{aligned} \frac{\partial[\bar{u}]}{\partial t} + [\bar{u}] \frac{\partial[\bar{u}]}{\partial x} + [\bar{v}] \frac{\partial[\bar{u}]}{\partial y} + [\bar{w}] \frac{\partial[\bar{u}]}{\partial z} = \\ -\frac{1}{[\bar{\rho}]} \frac{\partial[\bar{p}]}{\partial x} + \nu \nabla^2[\bar{u}] + \left(-\frac{\partial[\bar{u}'^2]}{\partial x} - \frac{\partial[\bar{u}'\bar{v}']} {\partial y} - \frac{\partial[\bar{u}'\bar{w}']} {\partial z} \right) \\ -\frac{1}{[\bar{\rho}]} \left[\frac{\partial \bar{p}''}{\partial x} \right] + \nu [\nabla^2 \bar{u}''] + \left(-\frac{\partial[\bar{u}''\bar{u}'']}{\partial x} - \frac{\partial[\bar{u}''\bar{v}'']}{\partial y} - \frac{\partial[\bar{u}''\bar{w}'']}{\partial z} \right). \end{aligned} \quad (5.14)$$

In the derivation, we have used the new incompressibility Eq. 5.13 and have ignored the Coriolis force. We also note that the first four canopy volume averaging properties (Eqs. 5.4, 5.5, 5.6, and 5.7) hold without exception, and the fifth property (Eq. 5.8) holds except for the pressure term and the viscous term as explained above. Similar equations can be written for momentum conservation in the y and z direction.

In comparison to the original Reynolds Eq. 3.21, Eq. 5.14 contains three additional terms. The last term on the right side of the equation consists of spatial derivatives of $[\bar{u}''\bar{u}'']$, $[\bar{u}''\bar{v}'']$, and $[\bar{u}''\bar{w}'']$. Called the dispersive fluxes, these spatial covariances arise from correlation of spatial variations of Reynolds mean variables. In some wind tunnel studies, small dispersive fluxes (less than 10% of the Reynolds fluxes) are detected in the air layer near the ground in sparse canopies made of regularly spaced plants. But in natural canopies, they are negligibly small and will be omitted from now on.

Arising from pressure discontinuity, the term $-1/[\bar{\rho}][\partial \bar{p}''/\partial x]$ represents a *form drag* or momentum sink associated with plant elements. For the hypothetical canopy depicted by Fig. 5.2, it can be shown from Eq. 5.11 that

$$-\left[\frac{\partial \bar{p}''}{\partial x} \right] = \frac{1}{Q} \sum \iint_{A_i} \bar{p}'' n_x dA = -\frac{\sum A_i}{Q} (\bar{p}_+'' - \bar{p}_-''), \quad (5.15)$$

where \bar{p}_+'' and \bar{p}_-'' are perturbation pressure at the windward and lee surface of individual plant elements, respectively, and A_i is one-sided area of one plant element. The pressure deficit is proportional to the kinetic energy of the flow:

$$\bar{p}_+'' - \bar{p}_-'' = C_d [\bar{\rho}][\bar{u}]V, \quad (5.16)$$

where C_d is a canopy drag coefficient, and $V = ([\bar{u}]^2 + [\bar{v}]^2 + [\bar{w}]^2)^{1/2}$. Noting that $a = \sum A_i/Q$ by definition, we obtain from Eqs. 5.15 and 5.16:

$$-\frac{1}{[\bar{\rho}]} \left[\frac{\partial \bar{p}''}{\partial x} \right] = -C_d a [\bar{u}] V \quad (5.17)$$

Even though it is derived for a hypothetical canopy, Eq. 5.17 is a standard form drag parameterization for real canopies. A typical C_d value is 0.2.

The term $\nu [\nabla^2 \bar{u}'']$ represents a viscous drag force imposed by plant elements on the flow. It is much weaker than the form drag force and, along with the term $\nu \nabla^2 [\bar{u}]$, is generally omitted. Alternatively, the canopy drag coefficient can be adjusted slightly upward so that Eq. 5.17 includes the viscous contributions.

In the canopy airspace, volume mean quantities vary much more in the vertical direction than in the horizontal directions. To acknowledge this fact, we now assume that the flow is horizontally homogeneous. For convenience of presentation, from now, on we will drop the volume averaging operator [], but keep in mind that all Reynolds mean quantities have undergone canopy volume averaging. The x -component momentum conservation is given by

$$\frac{\partial \bar{u}}{\partial t} = -\frac{1}{\bar{\rho}} \frac{\partial \bar{p}}{\partial x} - \frac{\partial \bar{u}' w'}{\partial z} - C_d a \bar{u} V + \nu (\nabla^2 \bar{u} + [\nabla^2 \bar{u}'']). \quad (5.18)$$

The local time rate of change of momentum per unit mass is balanced by the pressure gradient force (the first term on the right side of the equation), vertical gradient of the momentum flux (second term), the *canopy drag force* (third term), and the total *viscous drag force* (fourth term).

Similarly, the y component momentum conservation is given by

$$\frac{\partial \bar{v}}{\partial t} = -\frac{1}{\bar{\rho}} \frac{\partial \bar{p}}{\partial y} - \frac{\partial \bar{v}' w'}{\partial z} - C_d a \bar{v} V + \nu (\nabla^2 \bar{v} + [\nabla^2 \bar{v}'']). \quad (5.19)$$

5.4 Analytical Wind Profiles in the Canopy

In order to establish analytical solutions, it is necessary to introduce two additional assumptions: (1) the pressure gradient force is negligible; (2) there is no wind direction shear so that the lateral mean velocity (\bar{v}) is zero. Although they are not valid in the open trunk space of a forest (Sect. 6.2, Chap. 6), these assumptions are reasonable for the foliage layer. Under these assumptions and in steady state, Eq. 5.19 is not needed, and Eq. 5.18 is reduced to a balance between the momentum flux divergence and the canopy drag force:

$$-\frac{\partial \bar{u}' w'}{\partial z} = C_d a \bar{u}^2, \quad (5.20)$$

where the viscous force has been omitted. Equation 5.20 indicates that the momentum flux in the canopy is equal to the cumulative canopy drag:

$$-\bar{u}'\bar{w}' = \int_0^z C_d a \bar{u}^2 dz', \quad (5.21)$$

and the friction velocity squared is equal to the total canopy drag:

$$u_*^2 (= -\bar{u}'\bar{w}'|_{z=h}) = \int_0^h C_d a \bar{u}^2 dz'. \quad (5.22)$$

Solution of the canopy wind profile is aided by first-order closure. Manipulation of Eqs. 3.36 and 5.20 yields

$$K_m \frac{\partial^2 \bar{u}}{\partial z^2} + \frac{\partial K_m}{\partial z} \frac{\partial \bar{u}}{\partial z} = C_d a \bar{u}^2. \quad (5.23)$$

Two classic solutions to Eq. 5.23, both assuming constant a , can be found in the literature (Raupach and Thom 1981). The first solution takes the exponential form:

$$\frac{\bar{u}(z)}{\bar{u}(h)} = \exp \left[\alpha_1 \left(\frac{z}{h} - 1 \right) \right], \quad (5.24)$$

where α_1 is a constant. This solution is based on the mixing length parameterization for K_m :

$$K_m = l^2 \frac{\partial \bar{u}}{\partial z}. \quad (5.25)$$

where l is a mixing length. Equation 5.24 approximates reasonably well wind speed in the middle and upper canopy but does not work close to the ground.

Based on the assumption of proportionality,

$$K_m \propto \bar{u}, \quad (5.26)$$

the second solution is given by

$$\frac{\bar{u}(z)}{\bar{u}(h)} = \left[\frac{\sinh(\alpha_2 z/h)}{\sinh \alpha_2} \right]^{1/2}, \quad (5.27)$$

where α_2 is a constant. Equation 5.27 is more attractive than Eq. 5.24 because it satisfies the no-slip condition at the ground surface where the wind speed vanishes (Fig. 5.5).

The very restrictive conditions under which Eqs. 5.24 and 5.27 are derived are rarely satisfied. In practice, these equations should be regarded as empirical descriptions of the canopy wind profile and α_1 and α_2 as empirical coefficients chosen to ensure a good fit to observational data.

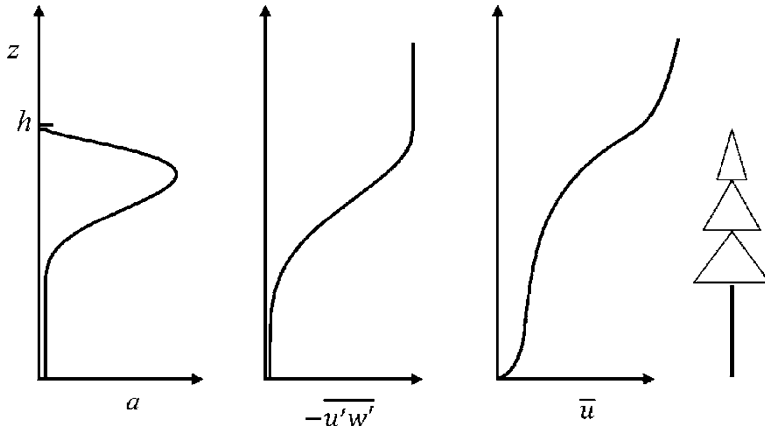


Fig. 5.5 Vertical profile of plant area index (a), momentum flux ($-\bar{u}'\bar{w}'$), and wind speed (\bar{u})

5.5 Budgets of Mean Flow and Turbulent Kinetic Energy

We assume one-dimensional flow and no wind directional shear in the canopy airspace. Under these simplifications, the budget equation for mean flow kinetic energy is obtained simply by multiplying Eq. 5.18 with \bar{u} , as

$$\frac{\partial \bar{E}}{\partial t} = -\frac{\bar{u}}{\bar{\rho}} \frac{\partial \bar{p}}{\partial x} + \bar{u}'\bar{w}' \frac{\partial \bar{u}}{\partial z} - C_d a \bar{u}^3 - \frac{\partial \bar{u}'\bar{w}' \bar{u}}{\partial z} + v \bar{u} (\nabla^2 \bar{u} + [\nabla^2 \bar{u}']). \quad (5.28)$$

We can interpret this equation in a similar way as we did of the MKE Eq. 4.8 for flow in the boundary layer. The first term on the right side of the equation represents production of MKE from the work done by the pressure gradient force; the second and the third term represent removal of MKE by shear and by canopy drag, respectively; the fourth term describes transport; and the fifth term represents viscous dissipation. The transport term is always positive. The total transport is found by integrating the term with respect to z :

$$\int_0^h -\frac{\partial \bar{u}'\bar{w}' \bar{u}}{\partial z} dz = u_*^2 \bar{u}(h). \quad (5.29)$$

The primary source of MKE in the canopy airspace is the MKE transported from above the canopy (Fig. 5.6). To demonstrate this, we note that the MKE budget terms differ by several orders of magnitude. The pressure production is on the order of $1 \times 10^{-3} \text{ m}^2 \text{ s}^{-3}$; the shear, the wake, and the transport term are on the order of $0.1 \text{ m}^2 \text{ s}^{-3}$ (Problem 5.15); and the viscous term is negligible. So in steady state, the

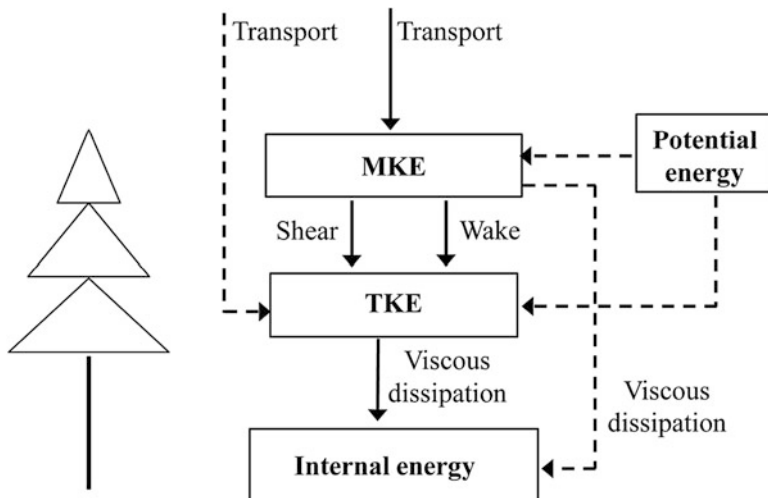


Fig. 5.6 Transfer of kinetic energy in a plant canopy. Solid and dashed lines indicate major and minor pathways, respectively

MKE budget can be written as a balance between the transport term and the MKE loss due to shear and wake destruction:

$$-\frac{\partial \overline{u'w'}\bar{u}}{\partial z} = -\overline{u'w'}\frac{\partial \bar{u}}{\partial z} + C_d a \bar{u}^3. \quad (5.30)$$

Equation 5.30 can also be derived from the simplified momentum conservation Eq. 5.20.

The TKE budget equation is derived from the Reynolds mean TKE equations and canopy volume averaging. In one-dimensional flow, the equation is

$$\frac{\partial \bar{e}}{\partial t} = -\overline{u'w'}\frac{\partial \bar{u}}{\partial z} + C_d a \bar{u}^3 + \frac{g}{\theta} \overline{w'\theta'} - \frac{\partial \overline{ew'}}{\partial z} - \frac{1}{\bar{\rho}} \frac{\partial \overline{w'p'}}{\partial z} - \epsilon. \quad (5.31)$$

This equation has the same form as the surface layer TKE budget Eq. 4.21 except for the second term on its right side. Called *wake production of turbulent kinetic energy*, this term represents the work done against the canopy form drag. Wake production and shear production (the first term on the right) are on the same order of magnitude (Problem 5.14), but differ in the size of eddies they generate: eddies produced by shear have a characteristic horizontal dimension of several times the canopy height, whereas eddies shed by plant elements in their wakes are much more fine-grained, at sizes no greater than the elements themselves. A complete MKE and TKE budget diagram is shown in Fig. 5.6.

If the canopy drag coefficient (C_d) is given, wake production can be calculated from the canopy wind profile (Problem 5.14). But more often than not, C_d is

an unknown empirical coefficient. However, if the momentum flux is measured at multiple levels in the canopy, Eq. 5.20 indicates that wake production can be approximated as

$$C_d \bar{u} \bar{u}^3 = -\bar{u} \frac{\partial \overline{u'w'}}{\partial z}. \quad (5.32)$$

5.6 Shear Instability and Transition to Turbulence

The discussion on the TKE budget is based on the premise that the flow is turbulent to begin with, or else Reynolds decomposition would make little sense. However, neither the TKE budget equations nor the Reynolds momentum equations provide insights on the question about how turbulence is initiated in the first place. To seek the answer, we resort to theory on flow instability. There are two classes of flow instability: convective instability and shear instability. Convective instability is intuitive. It occurs when an air layer is statically unstable (Fig. 4.6). As long as a negative $\partial \bar{\theta} / \partial z$ is maintained, slight perturbations, which always exist in nature due to either small variations in the background state or irregularities of the surface boundary, will grow into detectable eddy motion. Criteria for determining shear instability are, however, less straightforward. How the flow transitions from laminar to turbulent state under the influence of wind shear is the focus of this section.

We wish to identify conditions under which small perturbations may persist and grow into turbulent eddies and characteristics those eddies may possess. The background state is a stratified hydrostatic atmosphere with potential temperature θ_0 , the x -component of the horizontal velocity u_0 , and atmospheric pressure p_0 , all of which are functions of z only. The background vertical velocity w_0 is zero. Small perturbations, denoted by $\tilde{\theta}$, \tilde{u} , \tilde{p} , and \tilde{w} , are superimposed on the background state variables θ_0 , u_0 , p_0 , and w_0 and are expressed in the form of a two-dimensional wave in the $x - z$ plane, or a plane wave, which propagates in the x direction (Fig. 5.7). The flow is inviscid. Under the Boussinesq approximation and the assumption of incompressibility, and with the omission of higher order terms, the general momentum Eqs. 2.3 and 2.5, the continuity Eq. 2.21, and the energy conservation Eq. 2.25 are reduced to a set of linear equations:

$$\frac{\partial \tilde{u}}{\partial t} + u_0 \frac{\partial \tilde{u}}{\partial x} + \tilde{w} \frac{\partial u_0}{\partial z} = -\frac{1}{\rho_0} \frac{\partial \tilde{p}}{\partial x} - C_d \bar{u} \tilde{u} u_0, \quad (5.33)$$

$$\frac{\partial \tilde{w}}{\partial t} + u_0 \frac{\partial \tilde{w}}{\partial x} = -\frac{1}{\rho_0} \frac{\partial \tilde{p}}{\partial z} + g \frac{\tilde{\theta}}{\theta_0} - C_d \bar{w} \tilde{w} u_0, \quad (5.34)$$

$$\frac{\partial \tilde{u}}{\partial x} + \frac{\partial \tilde{w}}{\partial z} = 0, \quad (5.35)$$

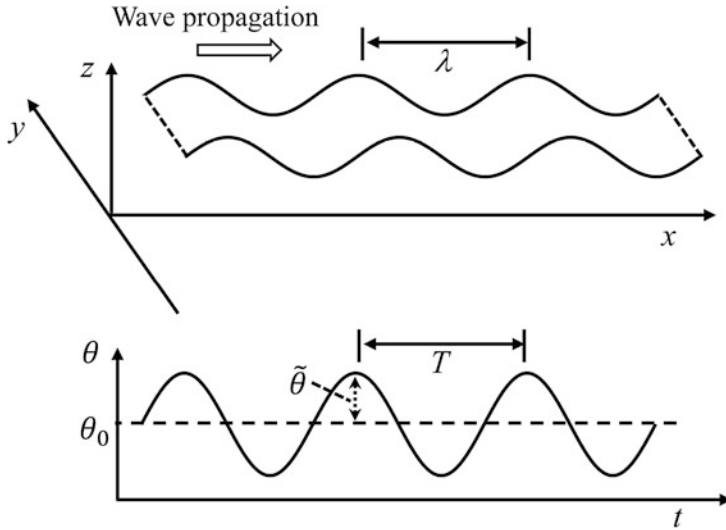


Fig. 5.7 A plane wave with wavelength λ and period T : depiction of the wave in the three-dimensional space (top) and time series observed at a fixed location (bottom)

$$\frac{\partial \tilde{\theta}}{\partial t} + u_0 \frac{\partial \tilde{\theta}}{\partial x} + \tilde{w} \frac{\partial \theta_0}{\partial z} = -C_h a \tilde{\theta} u_0, \quad (5.36)$$

(Lee 1997), where C_h is a canopy heat exchange coefficient. The last terms on the right side of Eqs. 5.33 and 5.34 represent the damping effect of canopy drag on the wave motion, and the term on the right side of 5.36 is a parameterization of damping on the temperature perturbation due to the exchange of heat with plant elements. Because the air layer is assumed statically stable, convective instability can be ruled out, at least in the early stage of wave development. Equations 5.33, 5.34, 5.35, and 5.36 are the foundation for *linear instability analysis*.

To seek a solution using the method of separation of variables, we assume

$$(\tilde{w}, \tilde{\theta}, \tilde{u}, \tilde{p}) = (\hat{w}, \hat{\theta}, \hat{u}, \hat{p})(z) \exp[i(kx - \sigma t)], \quad (5.37)$$

where k is wavenumber, $\sigma (= \sigma_r + i\sigma_i)$ is complex wave angular frequency, and $(\hat{w}, \hat{\theta}, \hat{u}, \hat{p})$ are dependent on z only. The complex functions are used for mathematical convenience, but only their real parts are true solution to the problem. For example, noting that \hat{w} can be written in exponential form as

$$\hat{w} = |\hat{w}(z)| \exp[i\phi_w(z)], \quad (5.38)$$

where $|\hat{w}(z)|$ is the magnitude and $\phi_w(z)$ the phase of \hat{w} , the physically meaningful solution of \tilde{w} is

$$Re\{\tilde{w}\} = |\hat{w}(z)| e^{\sigma_r t} \cos[kx - \sigma_r t + \phi_w(z)]. \quad (5.39)$$

Similar expressions can be written for the solutions of $\tilde{\theta}$, \tilde{u} , and \tilde{p} , all having the same wavenumber and angular frequency but different amplitude and phase. The speed of wave propagation or wave speed (c_r), wave period (T), and wavelength (λ) are related to k and σ_r as:

$$c_r = \frac{\sigma_r}{k}, \quad T = \frac{2\pi}{\sigma_r}, \quad \lambda = \frac{2\pi}{k}. \quad (5.40)$$

The phase of the vertical velocity oscillation, $\phi_w(z)$, is a function of z , and the amplitude, $|\hat{w}(z)| e^{\sigma_i t}$, is a function of z and t .

The wave growth rate, σ_i , is a critical parameter in controlling wave behaviors. The shear instability criteria can be stated as

> 0	unstable
$\sigma_i = 0$	neutral
< 0	stable

(5.41)

If σ_i is positive, the wave is unstable because its amplitude will grow exponentially with time (Fig. 5.8), which will lead to wave breaking and eventually generation of turbulence. In this unstable mode, the background laminar flow may transition to turbulent motion. In contrast, if σ_i is negative, the wave is in stable mode: any initial perturbation will die away with time, and no turbulence can emerge. The status is neutral if $\sigma_i = 0$.

According to Raupach et al. (1996), one unstable wave mode, linked to inflection point instability, can be understood through a plane mixing layer analogy. Mathematically, an inflection point is the height across which the double derivative of wind speed with respect to z changes sign or at which wind shear is at its maximum. A plane mixing layer forms downstream of two air layers separated by a horizontal and frictionless plane, each having its own constant velocity before arriving at the

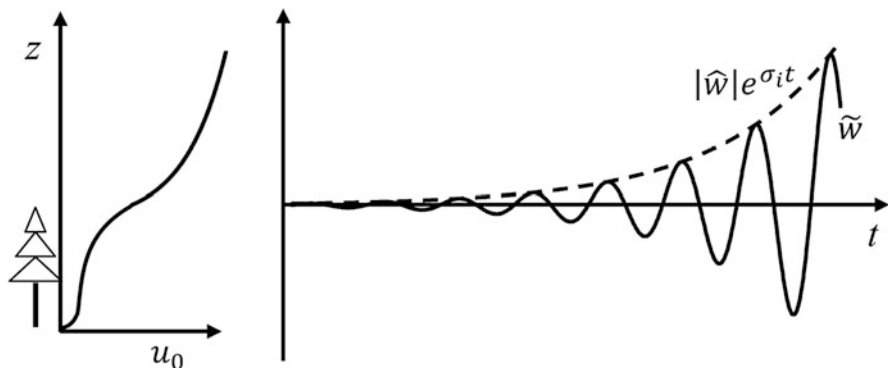


Fig. 5.8 An unstable or growing wave near the inflection point of the canopy wind profile

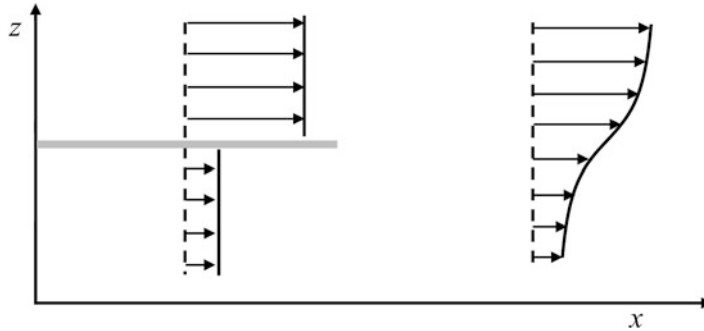


Fig. 5.9 Velocity profile in a plane mixing layer

edge of the plane (Fig. 5.9). Mixing of the two layers generates a velocity profile that bears strong resemblance to the canopy wind profile (Fig. 5.8), the most important feature being an inflection point in the middle of the mixing layer where the shear is at a maximum. According to Rayleigh's theorem on parallel shear flows, having an inflection point in the background velocity profile is a necessary condition for shear instability. Linear instability analysis reveals that the wavelength of the fastest-growing unstable mode is 3 to 5 times the depth of the mixing layer. The mixing layer depth of a canopy flow is proportional to canopy height \$h\$, and the inflection point instability theory explains why coherent eddies found in the canopy flow are scaled with \$h\$.

The plane mixing analogy can be further refined by including the canopy and the static stability effects. Two major tasks of linear instability analysis are (i) to determine the types of the background flow that permit unstable modes and (ii) to characterize the wavelength and wave speed of the permitted wave motion. Substitution of Eq. 5.37 into Eqs. 5.33, 5.34, 5.35, and 5.36 yields a set of equations for \$(\hat{w}, \hat{\theta}, \hat{u}, \hat{p})\$. Elimination of variables from these equations leads to

$$\frac{d^2\hat{w}}{dz^2} + \frac{1}{b_1}(C_d a u_0) \frac{d\hat{w}}{dz} - \left(\frac{N^2 k^2}{b_1 b_2} + \frac{ik}{b_1} \frac{d^2 u_0}{dz^2} + k^2 \right) \hat{w} = 0, \quad (5.42)$$

where \$N\$ is the Brunt-Väisälä frequency defined as

$$N = \left(\frac{g}{\theta_0} \frac{d\theta_0}{dz} \right)^{0.5},$$

and

$$b_1 = ik \left(u - \frac{\sigma}{k} \right) + C_d a u_0, \quad b_2 = ik \left(u - \frac{\sigma}{k} \right) + C_h a u_0.$$

In the absence of a plant canopy, Eq. 5.42 is reduced to the Taylor-Goldstein equation.

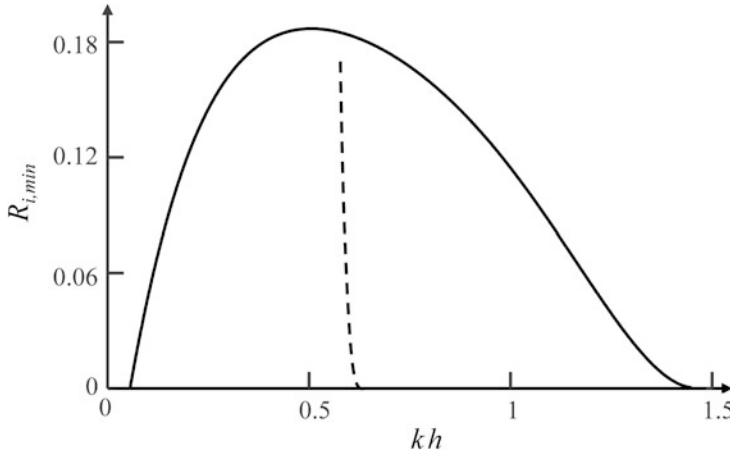


Fig. 5.10 Boundary of unstable mode in the wavenumber-static stability plane (solid line) and relationship between the minimum gradient Richardson number and the wavenumber of the fastest-growing wave (dashed line)

Equation 5.42 allows numerous solutions. We are interested in a parameter bound or eigenmode, usually in the parameter space of the minimum gradient Richardson number ($R_{i,\min}$) versus k , that delineates unstable solutions from stable solutions for a specific background profile of u_0 and of θ_0 (or N). Search for the parameter bound is accomplished with a numerical procedure applied to Eq. 5.42.

An eigenmode example is illustrated in Fig. 5.10. The corresponding background u_0 and N profiles are given in Problems 5.19 and the leaf area density profile in Problem 5.10 ($L = 4$). Miles theorem states that a necessary condition for shear instability is that $R_{i,\min}$ is smaller than 0.25. For flow in this idealized canopy, the critical Richardson number is about 0.20, which is smaller than the theoretical value of 0.25 due to the canopy drag effect on the wave motion. Above the critical value, no unstable solution can be found, but below the critical value, a range of unstable solutions is permissible. For example, at $R_{i,\min} = 0.06$, a wave solution whose wavenumber falls anywhere between $0.15/h$ and $1.20/h$ is unstable, meaning that small perturbations will grow with time.

Among all the unstable waves, only the fastest-growing one is believed to be able to dominate the flow and to become observable. The wavenumber of the fastest-growing wave is approximately $0.6/h$ (Fig. 5.10), and the corresponding wavelength is

$$\lambda \simeq 10 h. \quad (5.43)$$

The linear analysis also predicts that the fastest-growing wave should propagate at the speed given by

$$c_r \simeq 1.6u_0(h). \quad (5.44)$$

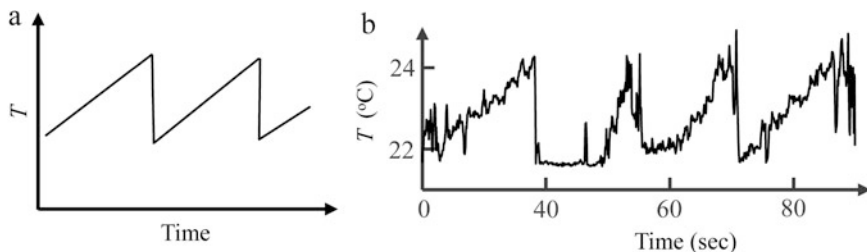


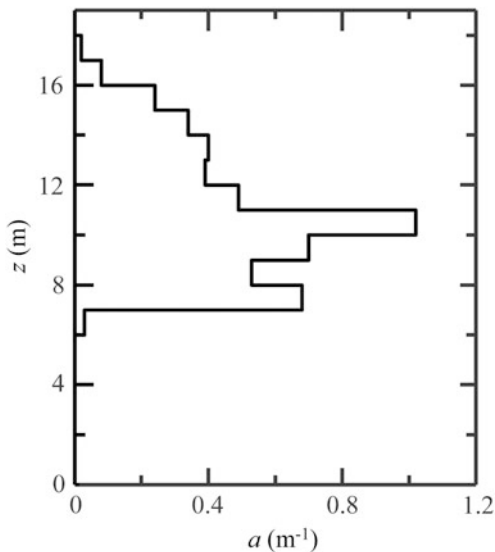
Fig. 5.11 (a) Idealized temperature ramps: a gradual rise with time in air temperature followed by an abrupt drop; (b) temperature ramps observed over a forest

Despite the simplistic representation of the background state and canopy morphology, these predictions are in reasonable agreement with observed wave features. For example, field observations show that the wavelength of canopy waves is proportional to canopy height, although with a lower proportionality coefficient of about 4 than the predicted value of 10. Observations also confirm an implicit assumption of the linear analysis: that the wave propagates in the direction of the mean wind (Lee and Barr 1998).

Shear instability is proposed as the main mechanism for the generation of coherent eddies in the canopy flow in stable as well as in neutral and unstable conditions. These eddies are coherent as opposed to totally random because in the resulting time series, we find orderly, nearly repeatable patterns, such as temperature ramps (Fig. 5.11; Gao et al. 1989). Believed to have grown out of shear instability, they retain the essential features predicted by the linear wave theory: their horizontal length scale and time scale are comparable to the wavelength and the wave period of the fastest-growing wave, and they propagate in the direction of the mean wind and at a speed slightly faster than wind speed at the canopy top. These coherent eddies are highly energetic. They play a prominent role in the transport of momentum, heat, and gases between the canopy and the overlaying atmosphere.

In summary, plant elements play two roles in the shear instability mechanism. The first role is the creation, through the canopy drag force on the background flow, of an inflection point, which triggers instability and the subsequent waves and coherent eddies. The persistent nature of the inflected profile explains why coherent eddies are a common occurrence near the top of the canopy. The second role is related to the damping effect of canopy drag on wave motions. A linear analysis shows that this role is minor, limited to waves whose wavelengths are shorter than that of the fastest-growing wave.

Fig. 5.12 Vertical distribution of plant area density measured in a Douglas-fir forest



5.7 Problems

5.1 Estimate the plant area index from the vertical distribution of plant area density shown in Fig. 5.12.

5.2 Are spatial differentiation and volume averaging commutable for Reynolds covariances, such as $\overline{u'w'}$ and $\overline{w'T'}$, in a plant canopy? Why or why not?

5.3 Explain why spatial differentiation and volume averaging are not commutable for the mean CO₂ mixing ratio, \bar{s}_c , but are commutable for the velocity and the mixing ratio product, $\bar{u}\bar{s}_c$.

5.4 Derive from Eq. 3.16 the continuity equation for the spatial fluctuating velocities (Eq. 5.13).

5.5 Show that under the canopy volume averaging scheme, the total kinetic energy consists of three parts:

$$[\bar{E}_T] = \text{MKE} + \text{DKE} + \text{TKE},$$

where

$$\text{MKE} = \frac{1}{2}([\bar{u}]^2 + [\bar{v}]^2 + [\bar{w}]^2),$$

$$\text{DKE} = \frac{1}{2}([\bar{u''}\bar{u''}] + [\bar{v''}\bar{v''}] + [\bar{w''}\bar{w''}]),$$

Table 5.1 Wind profile observed in a wind tunnel canopy made of uniform rods (Data source: Raupach and Thom 1981)

z/h	1.0	0.93	0.81	0.70	0.55	0.35	0.20	0.15	0.05	0.02
$\bar{u}(z)/\bar{u}(h)$	1.0	0.89	0.70	0.61	0.45	0.23	0.18	0.17	0.15	0.11

and

$$\text{TKE} = \frac{1}{2}([\bar{u}^2] + [\bar{v}^2] + [\bar{w}^2]).$$

The term DKE represents dispersive kinetic energy.

5.6* Verify that under the assumption of Eqs. 5.25 and 5.26, respectively, Eqs. 5.24 and 5.27 are solutions to Eq. 5.23.

5.7 Compare in a profile plot the wind speed predicted by Eqs. 5.24 and 5.27 ($\alpha_1 = 2.0$ and $\alpha_2 = 4.0$) with the wind speed observed in a wind tunnel canopy (Table 5.1).

5.8 The canopy drag coefficient is 0.2, the wind profile is given by Eq. 5.27 ($\alpha_2 = 4.4$), the plant area density is given in Fig. 5.12, and the wind speed at the top of the canopy is 1.82 m s^{-1} . Calculate the canopy drag force at the height of $z/h = 0.5$.

5.9* A corn pollen grain dislodged from the top of the canopy is transported by the mean wind and falls at a settling velocity of 0.31 m s^{-1} . The canopy height is 2.2 m, wind speed at the canopy top is 2.3 m s^{-1} , and wind speed inside the canopy is described by Eq. 5.24 with $\alpha_1 = 3.0$. How far does the pollen grain travel before it settles on the ground? (Assume that it will not be intercepted by plant elements.)

5.10* Some people interpret the displacement height, d , as the effective height of the mean canopy drag force, such that

$$d = \int_0^h z C_d a \bar{u}^2 dz / \int_0^h C_d a \bar{u}^2 dz, \quad (5.45)$$

(Shaw and Pereira 1982). Use a numerical procedure to quantify d as a function of plant area index, L , according to Eq. 5.45. The plant area density is given by

$$ah = \frac{L}{0.125\sqrt{2\pi}} \exp[-(z/h - 0.65)^2/(2 \times 0.125^2)], \quad (5.46)$$

where a has the dimensions of $\text{m}^{-2} \text{ m}^{-3}$, and the wind profile is given by Eq. 5.24, with the wind extinction coefficient related to L ($0.5 < L < 7$) as $\alpha_1 = -0.0296L^2 + 0.6565L + 0.7010$.

5.11 The plant area of a forest is evenly distributed between the ground and the top of the canopy, with the plant area index of 4.0. The mean wind speed at the top of

the canopy is 1.82 m s^{-1} , and the friction velocity is 0.42 m s^{-1} . Assume that wind speed inside the canopy can be described by Eq. 5.24 with $\alpha_1 = 2.4$. What is the canopy drag coefficient?

5.12 Wind load on an individual tree in a forest can be estimated as

$$\text{Wind load} = \rho C_d A \bar{u}_m^2,$$

where ρ is air density, A is total plant area of the tree, and \bar{u}_m is wind speed at the middle point of its canopy. Calculate wind load on a tree with A of 80 m^2 distributed between heights $z = 0.5h$ and $z = 1h$ in a forest stand whose mean wind profile is given by Eq. 5.24 with $\alpha_1 = 2.2$. Use a value of 0.2 for C_d , 1.20 kg m^{-3} for ρ , and 2.6 m s^{-1} for $\bar{u}(h)$ for your calculation.

5.13 Estimate MKE production by the pressure gradient force and MKE destruction by canopy drag given $\partial \bar{p}/\partial x = 0.01 \text{ hPa km}^{-1}$, $\bar{u} = 1.0 \text{ m s}^{-1}$, $a = 0.4 \text{ m}^{-1}$, and $C_d = 0.2$.

5.14 The plant area density is described by Eq. 5.46, the plant area index is 3.0, the canopy drag coefficient is 0.2, the wind profile is given by Eq. 5.27 ($\alpha_2 = 4.0$), and the wind speed at the top of the canopy is 2.5 m s^{-1} . (1) Determine the momentum flux profile using Eq. 5.21 for heights between the ground and the top of the canopy, (2) calculate shear production and wake production of TKE, and (3) present your results in a profile plot.

5.15 Using the information provided in Problem 5.14 and Eq. 5.30, (1) evaluate the transport, the shear destruction, and the wake destruction term in the MKE budget equation; and (2) compare these terms in a profile plot.

5.16 The wavenumber and the angular frequency of a wave event observed in a forest are 0.102 rad m^{-1} and 0.126 rad s^{-1} , respectively. Calculate the wave speed, wavelength, and wave period.

5.17 Derive Eq. 5.39 from Eqs. 5.37 and 5.38.

5.18 Provide an order-of-magnitude estimate for wavelength and period expected of the waves occurring in a 2-m tall corn canopy.

5.19 The background state is specified as

$$N^2(z)/N^2(h) = (1 - \gamma_1) \exp[-\gamma_2(z/h - 1)] + \gamma_1, \quad (5.47)$$

and

$$u_0(z)/u_0(h) = \begin{cases} \exp[\alpha_2(z/h - 1)], & z/h \leq 1 \\ \alpha_1 \tanh[(\alpha_2/\alpha_1)(z/h - 1)] + 1, & z/h > 1 \end{cases} \quad (5.48)$$

where $N^2(h) = 0.002 \text{ s}^{-2}$, $u_0(h) = 2.5 \text{ m s}^{-1}$, $\alpha_1 = 3.0$, $\alpha_2 = 2.85$, $\gamma_1 = 0.2$ and $\gamma_2 = 2.0$, and $h = 18.0 \text{ m}$. Determine the height of the inflection point and produce a profile plot of the gradient Richardson number for the air layer between $z = 0$ and $z = 3h$, where h is canopy height. Is shear instability likely to occur?

5.20 The growth rate of a wave observed in a forest is $0.0012 \text{ rad s}^{-1}$. How long does it take for the wave amplitude to grow twofold, tenfold, and 100-fold?

References

- Finnigan J (2000) Turbulence in plant canopies. *Annu Rev Fluid Mech* 32:519–571
- Gao W, Shaw RH, Paw U KT (1989) Observation of organized structure in turbulent flow within and above a forest canopy. *Bound-Layer Meteorol* 47:349–377
- Lee X (1997) Gravity waves in a forest: a linear analysis. *J Atmos Sci* 54:2574–2585
- Lee X, Barr AG (1998) Climatology of gravity waves in a forest. *Q J R Meteorol Soc* 124:1403–1419
- Li Z, Lin JD, Miller DR (1990) Air flow over and through a forest edge: a steady-state numerical simulation. *Bound-Layer Meteorol* 51:179–197
- Raupach MR, Finnigan JJ, Brunet Y (1996) Coherent eddies and turbulence in vegetation canopies: the mixing layer analogy. *Bound-Layer Meteorol* 78:351–382
- Raupach MR, Shaw RH (1982) Averaging procedures for flow within vegetation canopies. *Bound-Layer Meteorol* 22:79–90
- Raupach MR, Thom AS (1981) Turbulence in and above plant canopies. *Annu Rev Fluid Mech* 13:97–129
- Shaw RH, Pereira AE (1982) Aerodynamic roughness of a plant canopy: a numerical experiment. *Agric Meteorol* 26:51–65
- Whitaker S (1969) Advances in theory of fluid motion in porous media. *Ind Eng Chem* 61:14–28

Chapter 6

Balance of Forces in the Atmospheric Boundary Layer

6.1 Atmospheric Layers

The lower atmosphere is conveniently divided into several layers with varying degrees of turbulent mixing and with different mechanisms of turbulence production. The framework for our depiction of these layers is the set of one-dimensional governing equations given in Chap. 3. Forces that dominate the flow in each layer are different, so we can make strategic approximations in order to obtain simplified relationships between state and process variables. Diagnosis on where one layer ends and where another begins is made with profiles of potential temperature, wind, humidity, or trace gas concentrations and is refined with observed patterns of time variations of these variables on the 24-h cycle. The distinct vertical structure exists because of strong influences the ground surface exerts on the overlaying atmosphere through momentum absorption and exchanges of energy and materials. However, if the land cover is inhomogeneous, the terrain is sloped, or if the flow is disturbed by mesoscale phenomena (e.g., land-lake breezes) and synoptic weather events (e.g., cold front passage), some of the one-dimensional vertical layering may become indiscernible.

Convective Conditions

Figure 6.1 shows the structure of a typical daytime convective boundary layer on land. The topmost layer is called the *free atmosphere*. Here the air is relatively clean and is void of turbulent motion. Its temperature and moisture do not vary through the diurnal cycle as the heat and moisture sources are normally at the surface. Other variables, such as wind speed and carbon dioxide concentration, also lack appreciable diurnal changes. The potential temperature increases linearly with height, at an average rate of approximately 3.3 K km^{-1} which is equivalent

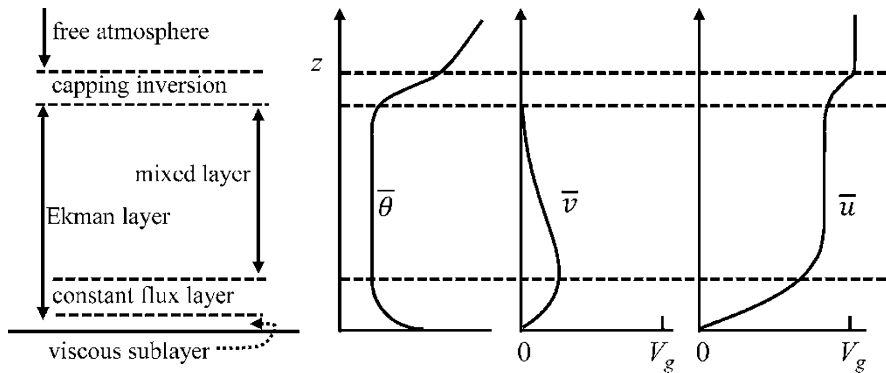


Fig. 6.1 Vertical structure of the atmospheric boundary layer in convective conditions and the corresponding profiles of potential temperature ($\bar{\theta}$) and two horizontal velocity components (\bar{u} and \bar{v}). Layer thickness is not drawn to scale

to an air temperature lapse rate of 6.5 K km^{-1} for the standard troposphere. The air motion follows the geostrophic balance. In the absence of vertical variations of the horizontal pressure gradient, the vertical wind shear is too weak to generate turbulent kinetic energy.

Separating the free atmosphere from the convective boundary layer is a thin interfacial layer called the *capping inversion*. The potential temperature gradient in the capping inversion is much larger than that in the free atmosphere. The large gradient forms in part because energetic convective eddies push air of low potential temperature into the warmer free atmosphere, so when averaged over time, the potential temperature in the interface is lower than one would obtain by extrapolating downward the linear potential temperature profile of the free atmosphere. In some large-eddy simulation studies of midafternoon, fully developed convective boundary layers, the interface is prescribed with an inversion strength of 75 K km^{-1} . A typical height of the capping inversion is about 1 km and a typical thickness is 50 m.

The capping inversion is a barrier to pollution diffusion and is the reason for why the free atmosphere is much cleaner than the boundary layer air, especially in an urban environment. The contrast is most evident on a cloud-free but hazy day, during which time the position of the capping inversion is visually marked by the top of the haze layer. In other words, the inversion layer height controls the vertical extent of pollution dispersion. Bad air quality is often associated with conditions of a capping inversion being close to the ground.

The capping inversion is a leaky barrier in the sense that energy and material transport does occur there, albeit very slowly. The process by which air in the free atmosphere is mixed into the boundary layer is referred to as *entrainment*. One contributor to entrainment is organized eddy structures called thermals. These eddies are essentially large hot air bubbles detached from the ground. Having high buoyancy, they are able to rise energetically to the capping inversion, pushing the

inversion interface upward and causing it to fold. Air of higher potential temperature in the free atmosphere may get pulled under the air in the boundary layer that has lower potential temperature. In the spots where the interface is folded, conditions are statically unstable, leading to formation of small turbulent eddies and mixing of the two air pools (Sullivan et al. 1998). The process repeats itself in an intermittent fashion. As a consequence of entrainment, the height of the inversion layer increases with time.

Below the capping inversion is the *Ekman layer*, named after the Swedish oceanographer V. W. Ekman whose work led to an analytical solution of wind profile in the boundary layer. Air motion in the layer is turbulent owing to shear and buoyancy production of eddies associated with the surface. Because of the nonstoping eddy motion, the surface and the Ekman layer are tightly coupled. The influences of ground surface can rapidly alter, on time scales of minutes, physical properties and chemical compositions of the Ekman layer. Likewise, conditions in the Ekman layer can regulate surface processes. The Ekman layer exists in unstable as well as in neutral and stable conditions. Forced by diurnally changing solar radiation, the surface sensible heat, latent heat, and carbon dioxide fluxes vary through the 24-h cycle. In response, temperature, humidity, and carbon dioxide concentration in the Ekman layer exhibit strong diurnal oscillations.

The upper portion of the Ekman layer is the *mixed layer*. It gets the name because physical and chemical properties are well mixed vertically in this air layer. The best diagnostic indicator of the mixed layer is a uniform potential temperature profile ubiquitous of sounding measurements (Fig. 6.1). Vertical variations in carbon dioxide concentration are also very small, typically less than 1 ppm. The well-mixed situation is found in convective conditions and ceases to exist in a stably stratified Ekman layer.

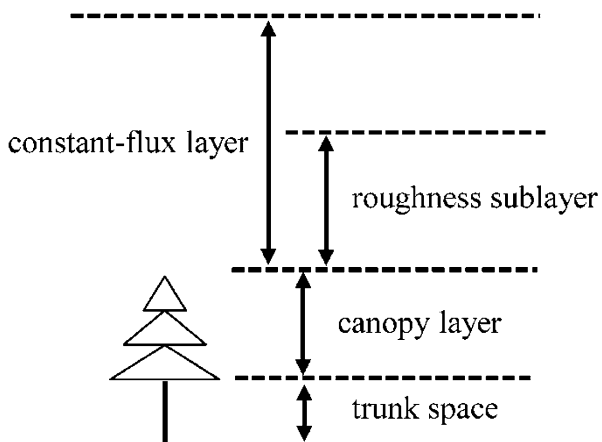
The lower portion of the Ekman layer is the surface layer, also referred to as the *constant-flux layer*. Fluxes of momentum, heat, and gases are approximately constant with height in the surface layer, which spans a depth of tens of meters. Feeling the direct impact of the ground, the surface layer is characterized by diurnal variations in state variables, including temperature, humidity, wind speed, and trace gas concentrations, which are much larger than anywhere else in the atmosphere. The vertical gradient of potential temperature is negative, indicating unstable conditions.

In the thin skin layer in immediate contact of a smooth surface, the motion is dominated by the viscous effect. For this reason, we call it the *viscous sublayer*. According to laboratory studies on channel flow and pipe flow, its thickness is given by

$$\delta_l = 5v/u_* \quad (6.1)$$

Equation 6.1 indicates that δ_l is on the order of 1 mm (Problem 6.3). Within the viscous sublayer, the flow is essentially laminar. Above a height of about $z = 6\delta_l$, the flow becomes fully turbulent and the viscous effect is negligible. In the natural environment, mud flats and ice fields are examples of smooth surfaces where a viscous sublayer can be identified.

Fig. 6.2 Air layers in and above a forest



In a vegetated landscape, viscous effects are confined to thin boundary layers enveloping the individual plant elements, but no viscous sublayer exists at the whole canopy scale. Here the lowest portion of the flow is found in the canopy layer (Fig. 6.2). Immediately above the canopy, there exists a *roughness sublayer* whose thickness is on the order of one canopy height, where turbulence is characterized by coherent eddies generated by inflection point instability (Chap. 5). These eddies transport momentum and scalars more efficiently than eddies found in a smooth-wall surface layer. Because of this fact, the eddy diffusivity parameterization (Eq. 3.53), whose similarity functions are based on observations made in smooth-wall surface layers, has a tendency to underestimate true diffusion efficiency in the roughness sublayer.

Stable Conditions

Figure 6.3 depicts the vertical structure of the boundary layer in early morning hours. The sun is yet to rise. A *surface inversion layer* has developed near the ground as a consequence of longwave radiative cooling of the surface, its depth varying roughly in the range of 100–300 m. Mixing is caused by wind shear and must overcome the negative buoyancy effect. Eddy diffusion is too weak to mix uniformly in the vertical direction either the potential temperature or any other scalar quantity.

The Ekman layer is slightly thicker than the surface inversion layer, but not by much. We know this because the Ekman layer is turbulent. If it were much deeper, turbulent diffusion would have brought heat down to the surface from a greater height and therefore would have extended the inversion layer further upward.

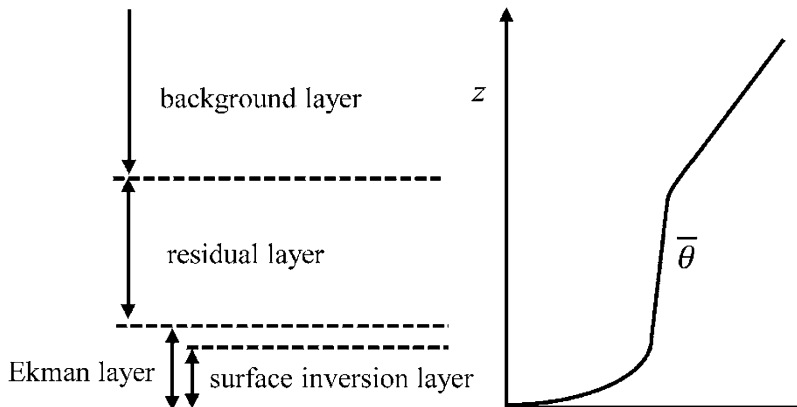


Fig. 6.3 Vertical structure of the atmospheric boundary layer at night and the corresponding potential temperature profile

Above the surface inversion layer is the *residual layer*. Potential temperature in the residual layer often lacks a vertical gradient, leaving the impression that the air is well mixed. But the fact that this layer retains features of a mixed layer of the daylight hours in the previous day indicates just the opposite, that turbulent mixing is nearly absent. At later times, the well-mixed structure left from the previous afternoon may get gradually eroded from the bottom by shear-generated eddies, evolving by the early morning hours into a weak inversion layer with a positive potential temperature gradient falling in the transitional range between those of the surface inversion layer and the tropospheric background. This occurs when the wind shear is moderately strong. In steady state, the flow in the residual layer is geostrophic. In non-steady-state conditions, wind speed can exceed the geostrophic wind speed.

The tropospheric *background layer* is found above the residual layer. Here the flow is geostrophic. The potential temperature gradient is approximately 3.3 K km^{-1} .

Diurnal Evolution

Figures 6.1 and 6.3 are snapshots of the boundary layer representing conditions typical of midafternoon and early morning hours, respectively. A complete pattern of diurnal evolution is shown in Fig. 6.4 for midlatitudes in the summer. Erosion of the surface inversion layer starts shortly after sunrise, and by 9 am local time, a shallow mixed layer has developed. The mixed layer continues to grow with time, to a maximum depth of approximately 1.5 km at around 4 pm. Thereafter buoyancy generation of turbulent kinetic energy begins to slacken. The mixed layer collapses

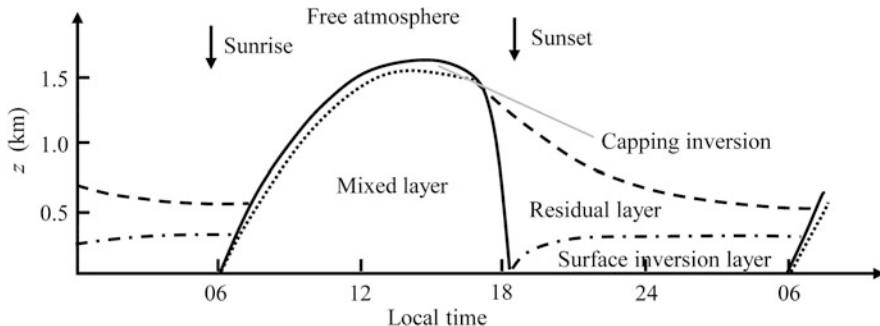


Fig. 6.4 Diurnal evolution of the atmospheric boundary layer

rapidly at around 6 pm, owing to the fact TKE generation cannot overcome TKE viscous dissipation. At this time, the surface longwave radiation flux is still quite high due to a high surface temperature, but the incoming solar radiation is nearly zero, resulting in a negative net radiation and a negative surface sensible heat flux. The reversal in the direction of the surface heat flux marks the onset of surface inversion. The surface inversion layer grows as time progresses into the night, but at a much slower rate than the rate of mixed layer development in the daytime, reaching a depth of about 300 m at midnight. The residual layer, identified from a uniform potential temperature profile, is quite deep at the time of mixed layer collapse and slowly shrinks due to mixing with the tropospheric background air from above and with the surface air from below. The pattern repeats itself the next day.

The temporal pattern shown in Fig. 6.4 is constructed by averaging observations over multiple diurnal cycles to filter out day-to-day weather fluctuations. This smooth composite time evolution is the basis for the concept of an equilibrium atmospheric boundary layer over land (Chap. 11).

Large-scale horizontal advection, not considered in the idealization, can transport heat to the boundary layer from outside of the local domain. In extreme heatwave events, the added heat can sustain through the night a thick residual layer, which then merges with the mixed layer being developed beneath it in the next day. After several days of persistent heat advection, a uniform potential temperature can extend up to 4 km into the atmosphere, creating the impression of a super deep mixed layer (Problem 6.2). A transitional, deep “mixed layer” has also been observed on the Tibetan Plateau. Whether such a thick layer of uniform potential temperature can be called the atmospheric boundary layer is debatable because in the strict fluid mechanic sense, the boundary layer is characterized as a thin layer of fluid at the flow boundary. So far there has been no experimental confirmation that the Ekman layer, and hence the influence of the surface, can extend to a height of 4 km.

6.2 Balance of Forces in Neutral and Convective Conditions

Let us consider a boundary layer in neutral to unstable conditions. The horizontal pressure gradients, $\partial \bar{p} / \partial x$ and $\partial \bar{p} / \partial y$, are prescribed parameters and are assumed to be independent of height and time. The local time rate of change in the mean momentum Eqs. 3.31 and 3.32 is negligible in comparison to other terms in the equations, so the atmosphere is in quasi-steady state.

In the free atmosphere, the Reynolds covariances vanish. The momentum equations are reduced to the *geostrophic relation* or a balance between the pressure gradient force and the Coriolis force:

$$0 = -\frac{1}{\bar{\rho}} \frac{\partial \bar{p}}{\partial x} + f \bar{v}, \quad (6.2)$$

and

$$0 = -\frac{1}{\bar{\rho}} \frac{\partial \bar{p}}{\partial y} - f \bar{u}. \quad (6.3)$$

The two wind components are therefore given by

$$\bar{u} = u_g, \quad \bar{v} = v_g, \quad (6.4)$$

where u_g and v_g , components of the *geostrophic wind* $\mathbf{v}_g = \{u_g, v_g\}$, are given by

$$u_g = -\frac{1}{f} \frac{1}{\bar{\rho}} \frac{\partial \bar{p}}{\partial y}, \quad v_g = \frac{1}{f} \frac{1}{\bar{\rho}} \frac{\partial \bar{p}}{\partial x}. \quad (6.5)$$

In the Ekman layer, the Reynolds terms cannot be omitted. With the help of parameterization Eqs. 3.36 and 3.37, we obtain from Eqs. 3.31 and 3.32:

$$f(\bar{v} - v_g) + \frac{\partial}{\partial z} \left(K_m \frac{\partial \bar{u}}{\partial z} \right) = 0, \quad (6.6)$$

$$-f(\bar{u} - u_g) + \frac{\partial}{\partial z} \left(K_m \frac{\partial \bar{v}}{\partial z} \right) = 0. \quad (6.7)$$

These equations express a three-way balance between the pressure gradient force, the Coriolis force, and the momentum flux divergence. The flux divergence terms represent the frictional force arising from horizontal and vertical velocity cross correlations and ultimately originating from the surface.

If we assume that the momentum eddy diffusivity, K_m , is invariant with height, we obtain the famous *Ekman spiral* solution:

$$\bar{u} = V_g (1 - e^{-\gamma z} \cos \gamma z), \quad \bar{v} = V_g e^{-\gamma z} \sin \gamma z, \quad (6.8)$$

where $\gamma = (f/2K_m)^{1/2}$ and $V_g = (u_g^2 + v_g^2)^{1/2}$. At height:

$$z_i = \pi/\gamma, \quad (6.9)$$

$\bar{v}_g = 0$, and \bar{u}_g is nearly equal to V_g . Height z_i is regarded as the top of the boundary layer. Equation 6.9 shows that z_i increases with increasing K_m , implying a deeper boundary layer in the daytime than at night. The Ekman spiral solution satisfies the no-slip boundary condition at the surface:

$$\bar{u} \rightarrow 0, \quad \bar{v} \rightarrow 0, \quad \text{as } z \rightarrow 0.$$

The wind vector below z_i is veered to the left of the geostrophic wind vector in the northern hemisphere at the angle given by

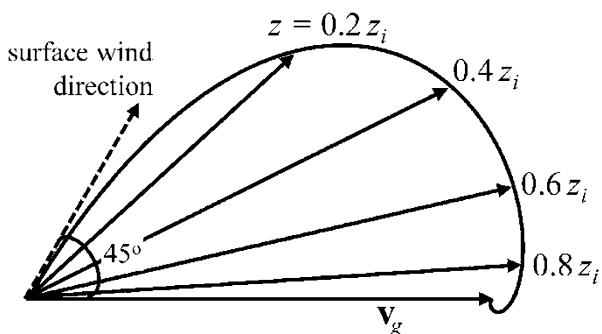
$$\beta = \tan^{-1} \frac{\bar{v}}{\bar{u}}.$$

In the limit $z \rightarrow 0$, $\beta \rightarrow 45^\circ$. This is the predicted angle between surface wind direction and wind direction above the boundary layer. A hodograph of the solution is shown in Fig. 6.5. Arrows in the plot represent wind vectors below height z_i . The tips of the arrows form a spiral-shaped locus line.

The Ekman spiral agrees qualitatively with field observations and numerical modeling results. The prediction that the boundary layer should deepen with increasing K_m has been confirmed experimentally. The Ekman solution approximates reasonably well the neutral wind speed profile above the surface layer.

The prediction about wind directional turning is also in qualitative agreement with observed flow patterns in the lower atmosphere. In a low-pressure system in the northern hemisphere, wind motion in the free atmosphere is tangent to the isobars in a counterclockwise rotation and that near the surface is deflected at an angle toward the center resulting in flow convergence (Fig. 6.6 left panel). In a high-pressure system, the surface wind is deflected outward, and flow divergence takes place in the boundary layer (Fig. 6.6 right panel).

Fig. 6.5 A hodograph showing the Ekman spiral solution for the northern hemisphere



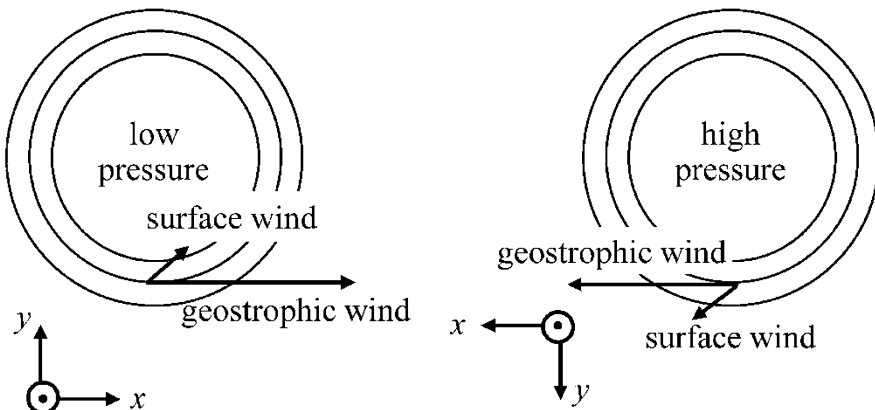


Fig. 6.6 Flow patterns in a low- (*left panel*) and a high-pressure system (*right panel*) in the northern hemisphere

The cross-isobaric transport of momentum and masses is an important mechanism by which the boundary layer influences large-scale atmospheric flows. Flow convergence in the low-pressure system causes rising motion at the top of the boundary layer, a phenomenon called *Ekman pumping*. The rising motion is compensated by sinking motion over a neighboring high-pressure system, thus forming a secondary circulation that interacts with the counterclockwise and clockwise rotations in these systems.

The Ekman solution should be used with caution in the surface layer because it differs from reality in two important details. First, the predicted wind directional shear is too strong. A typical angle of deflection β in the surface layer is about 30° in neutral and stable conditions and is even smaller in unstable conditions. Observational and numerical studies also show that the angle decreases with decreasing surface roughness, approaching zero over the sea and large lakes (Problem 6.9). Second, the predicted wind speed profile in the surface layer is sinusoidal rather than logarithmic (Eq. 3.47), a defect of the constant K_m assumption. The logarithmic solution based on the constant flux assumption is a more accurate description of air motion near the ground.

The standard Ekman solution does not apply to the plant canopy layer where the Coriolis force is negligible due to smallness of the wind speed. The pressure gradient force can also be omitted because it is an order of magnitude smaller than the canopy drag force and the momentum flux divergence. In steady state, the momentum conservation is approximated by a balance between the canopy drag and the momentum flux divergence (Eq. 5.20). The wind speed solution is an exponential function of height (e.g., Eq. 5.24).

The trunk space in some forests is quite open either because of active forest management, such as removal of lower tree branches to promote tree growth, or because low light conditions prevent understory growth. Air in this layer can move

more freely than in the canopy airspace. Here the momentum flux divergence is negligible, and the momentum Eqs. 5.18 and 5.19 are simplified to:

$$0 = -\frac{1}{\bar{\rho}} \frac{\partial \bar{p}}{\partial x} - C_d a \bar{u} V, \quad (6.10)$$

$$0 = -\frac{1}{\bar{\rho}} \frac{\partial \bar{p}}{\partial y} - C_d a \bar{v} V. \quad (6.11)$$

The result is a gradient wind solution whose direction is aligned with the pressure gradient force and whose magnitude is given by:

$$V = \frac{1}{(\bar{\rho} C_d a)^{1/2}} |\nabla_H \bar{p}|^{1/2}, \quad (6.12)$$

(Lee et al. 1994).

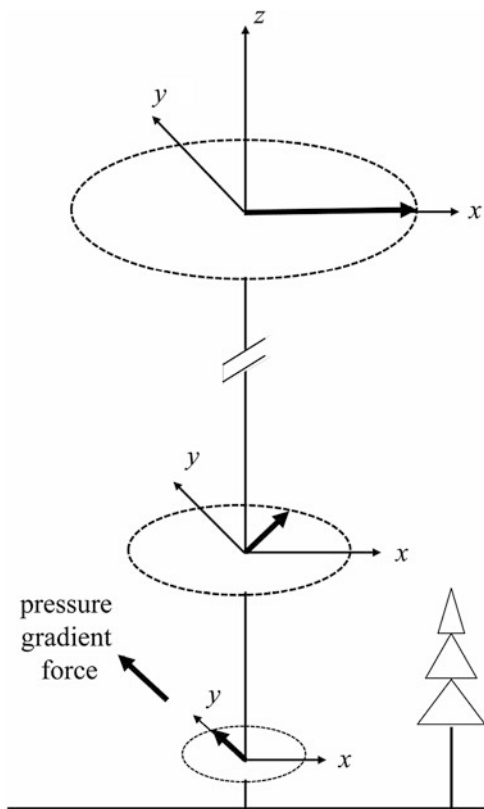
Figure 6.7 shows an extended Ekman spiral for the northern hemisphere. Let us suppose that the pressure gradient force is directed toward north. We expect wind to move from south to north in the trunk space and from west to east in the free atmosphere, with a total directional change of 90°.

The Ekman model predicts that the wind in the boundary layer should always be directed toward lower pressure (Fig. 6.6). Observational studies show that air in the surface layer can in fact move in the opposite direction (Sun et al. 2013). Two situations are known to cause this counter-intuitive phenomenon. The Ekman model is restricted to the conditions of constant pressure gradient and steady state. In a baroclinic atmosphere where the horizontal pressure gradient varies significantly with height and where there exists advection of warm air toward the local domain, solution of the complete momentum equations allows the possibility of wind being directed toward higher pressure. If the boundary layer is not in steady state, inclusion of time-varying terms in the momentum equations can also explain the phenomenon of “wind toward higher pressure” (Sect. 6.3).

6.3 Balance of Forces in Stable Conditions

The balancing of forces changes as air stability switches from being unstable in the day to being stable at night. Let us first consider the upper boundary layer in late afternoon transition. We continue to use the assumption that the pressure gradient force is invariant with height and time. For convenience of discussion, we divide the transition into three stages. In the initial stage, balance is maintained among the Coriolis force, the pressure gradient force, and the momentum flux divergence (Fig. 4.1). The wind profile, a deep Ekman spiral denoted by V_0 in Fig. 6.8, is characterized by weak shear in the upper boundary layer and strong shear near the surface, and the dominant source of TKE in the upper boundary layer is buoyancy

Fig. 6.7 An extended Ekman spiral in the northern hemisphere, showing wind directional shear from the open trunk space of a forest to the top of the boundary layer



generation. The second stage begins shortly before sunset. At this time, buoyancy generation ceases, leading to a decline in turbulence intensity. We still expect a small amount of TKE being transported upward from the lower air layer where strong wind shear continues to produce turbulence, so the decay of turbulence in the upper boundary layer is not as rapid as if viscous dissipation of TKE were to operate on its own. In stage three, as time progresses into early evening, a surface inversion has taken shape. The strong stability associated with surface inversion prevents upward transport of TKE. The upper boundary layer, being essentially cut off from the surface influences, has transformed into the classic residual layer with virtually no turbulent motion. The Coriolis force is now temporarily out of balance with the pressure gradient force. However, the atmosphere has the tendency to reach a new equilibrium state in which balance is restored between the two forces so that the wind speed is equal to the geostrophic speed, V_g , as shown in Fig. 6.8.

In reality, the new equilibrium state is rarely fully established in the residual layer because time change terms in the momentum Eqs. 3.31 and 3.32 can no longer be omitted. In the process of adjustment to the new equilibrium conditions, the wind tends to overshoot beyond the geostrophic wind. This inertial effect, first proposed by Blackadar (1957), leads to a time-dependent *inertial oscillation* solution.

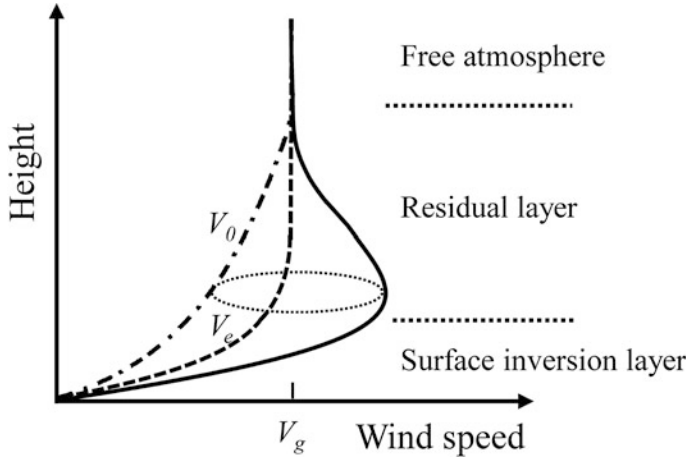


Fig. 6.8 Evolution of wind speed profile in a stable boundary layer: V_0 , initial profile in late afternoon ($V_0 = |v_0|$, $v_0 = \{u_0, v_0\}$); V_e , new equilibrium profile ($V_e = |v_e|$, $v_e = \{u_e, v_e\}$); V_g , magnitude of the geostrophic wind. Modified after van de Weil et al. (2010)

Using Eq. 6.5, we can express the momentum conservation for the residual layer as

$$\frac{\partial}{\partial t}(\bar{u} - u_g) = f(\bar{v} - v_g), \quad (6.13)$$

and

$$\frac{\partial}{\partial t}(\bar{v} - v_g) = -f(\bar{u} - u_g). \quad (6.14)$$

In these equations, the horizontal pressure gradient is assumed constant with time and height, and turbulence is negligible. The initial condition is

$$\bar{u} = u_0, \quad \bar{v} = v_0 \quad \text{at } t = 0.$$

The solution to Eqs. 6.13 and 6.14 is periodic with time, as

$$\bar{u} - u_g = (v_0 - v_g) \sin(ft) + (u_0 - u_g) \cos(ft), \quad (6.15)$$

$$\bar{v} - v_g = (v_0 - v_g) \cos(ft) - (u_0 - u_g) \sin(ft). \quad (6.16)$$

Figure 6.8 is a graphic illustration of the inertial oscillation expressed by the solution. The velocity at a given height is determined by time elapsed from onset of the oscillation and deviation of the initial velocity at this height from the geostrophic wind and is independent of the velocity at other heights. The magnitude of the wind speed oscillates between the lower limit of V_0 and a super-geostrophic upper limit. The strongest wind speed occurs near the top of the surface inversion layer.

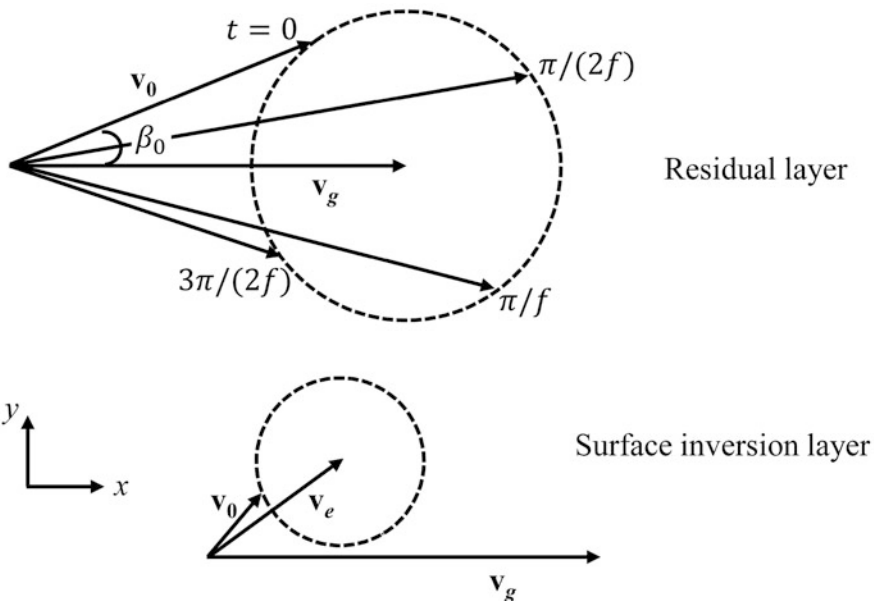


Fig. 6.9 Inertial oscillation solution of the velocity in the residual layer (top) and in the surface inversion layer (bottom) in the northern hemisphere: \mathbf{v}_0 , velocity vector at initial time $t = 0$; \mathbf{v}_e , velocity vector in the new equilibrium state; \mathbf{v}_g , the geostrophic velocity vector

Figure 6.9 (top panel) is another graphic illustration of the inertial oscillation solution at some height in the residual layer. For simplicity, we have adopted a coordinate system whose x -axis is aligned with the geostrophic wind vector and whose y -axis is in the cross-geostrophic direction (Fig. 4.1). The solution is shown in a vector form. The tip of the wind vector falls on a circle in a counterclockwise rotation at successive time steps since $t = 0$. The center of the circle is the tip of the geostrophic wind vector, and the radius is given by

$$V_r = [(V_g - u_0)^2 + v_0^2]^{1/2}. \quad (6.17)$$

In this illustration, the wind becomes super geostrophic at $t \simeq \pi/2f$. The maximum wind speed is $V_g + V_r$, and occurs at the time:

$$t_m = (\pi - \beta_0)/f \quad (6.18)$$

elapsed since the onset of inertial oscillation, where β_0 is the angle between the initial wind vector $\mathbf{v}_0 = \{u_0, v_0\}$ at the height of interest and the geostrophic wind vector $\mathbf{v}_g = \{u_g, v_g\}$.

In the example shown in Fig. 6.9, the y component of the velocity is negative after t becomes greater than about $(3\pi/4f)$. At these times, the wind is directed toward higher pressure. Flow that counters the horizontal pressure gradient can also exist in the surface layer (Problem 6.20).

Let us now turn attention to the surface inversion layer. The above Blackadar's solution is valid only in the residual layer. In the surface inversion layer, the momentum conservation must include the momentum flux divergence. If we omit the time change terms, a new equilibrium state would be achieved by a three-way balance between the pressure gradient force, the Coriolis force, and the flux divergence, as described by Eqs. 6.6 and 6.7. The new equilibrium solution, denoted by \mathbf{v}_e ($= \{u_e, v_e\}$), satisfies the Ekman Eq. 6.8 on the assumption of a constant eddy diffusivity K_m . Because K_m in stable stratification is much smaller than K_m in late afternoon, the equilibrium Ekman spiral is more compressed in the vertical than the initial profile, and $V_e (= |\mathbf{v}_e|)$ is greater than V_0 (Fig. 6.8) in the surface layer.

In order to obtain a true solution for the wind profile, we must include the time change terms in the conservation equations, similar to the situation encountered in the residual layer. The complete momentum equations are

$$\frac{\partial \bar{u}}{\partial t} = f(\bar{v} - v_g) + \frac{\partial}{\partial z} \left(K_m \frac{\partial \bar{u}}{\partial z} \right), \quad (6.19)$$

$$\frac{\partial \bar{v}}{\partial t} = -f(\bar{u} - u_g) + \frac{\partial}{\partial z} \left(K_m \frac{\partial \bar{v}}{\partial z} \right). \quad (6.20)$$

Unfortunately, no analytical solution to Eqs. 6.19 and 6.20 has been found so far. But it is reasonable to extend Blackadar's argument and assume that the wind in the surface inversion layer also oscillates around the new equilibrium state \mathbf{v}_e . Mathematically, this is accomplished by replacing $\{u_g, v_g\}$ with $\{u_e, v_e\}$ in Eqs. 6.13 and 6.14, giving an approximation for the wind solution in the surface inversion layer:

$$\bar{u} - u_e = (v_0 - v_e) \sin(ft) + (u_0 - u_e) \cos(ft), \quad (6.21)$$

$$\bar{v} - v_e = (v_0 - v_e) \cos(ft) - (u_0 - u_e) \sin(ft), \quad (6.22)$$

(van de Weil et al. 2010). Owing to frictional damping effects, the inertial oscillation in the surface inversion layer (Fig. 6.9 bottom panel) is weaker than in the residual layer (Fig. 6.9 top panel). It is useful to point out that Eqs. 6.21 and 6.22 give virtually the same result as Eqs. 6.15 and 6.16 for the frictionless residual layer because \mathbf{v}_e is nearly equal to \mathbf{v}_g above the surface inversion layer.

Inertial oscillations are an important mechanism underlying the formation of *low-level jets* (LLJs), the phenomenon of a local wind maximum at a level typically in the range of 100–500 m above the ground. Although LLJs have been observed in the daytime, they are usually better defined at night. A number of inferences can be made from the inertial oscillation theory:

- The height of nocturnal LLJs is found just above the surface inversion layer. At this height, the inertial oscillation is the strongest. Below this height, the inertial oscillation is damped by frictional effects, and far above this height, the deviation of the initial wind from the geostrophic wind is too weak to cause strong oscillations (Eq. 6.17).

- Nocturnal LLJs are more likely to be observed in early morning than in early evening according to Eq. 6.18. The time of occurrence of the strongest nocturnal LLJ is dependent on latitude. If the inertial oscillation starts at 6 pm local time, the strongest wind is expected at approximately 2:30 am at 55°N and at 6 am at 25°N in the following day.
- In tropical latitudes, the oscillation period is too long to allow the formation of nocturnal LLJs. For example, at 10°N it would take 34 h, a duration longer than the night period, to reach the maximum wind speed. Nocturnal LLJs can still occur, but the mechanisms involved are not related to inertial oscillations. Gravitational acceleration on sloped terrain, for example, is known to cause nocturnal LLJs.
- Clear sky conditions and large surface roughness are two factors that favor the formation of nocturnal LLJs. Surface inversion, a necessary condition for Blackadar's inertial oscillation mechanism, forms more quickly under clear skies than under cloudy skies due to a stronger surface radiative cooling. If the surface is rougher, we expect a greater departure from the geostrophic wind at the onset of the oscillation and therefore a greater wind maximum at a later time (Eq. 6.17).

Figure 6.10 is a conceptual summary of the time progression of events occurring in a typical nocturnal boundary layer (Mahrt 1999). Once a nocturnal LLJ is formed, we expect shear generation of turbulence near the height of the jet where wind shear is maximal and where the air is only weakly stratified. Some of the TKE generated at the jet level is transported downward, intermittently increasing turbulence intensity and weakening thermal stratification near the surface.

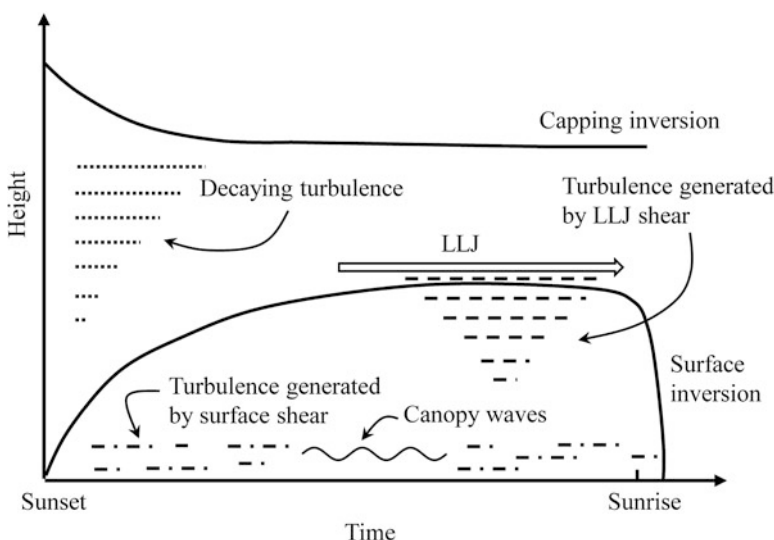


Fig. 6.10 Sequence of events occurring in a nocturnal boundary layer. Modified after Mahrt (1999)

The situation has the appearance of an *upside-down boundary layer* because the main TKE source is elevated instead of being at the surface. Experimental studies show that surface friction velocity is enhanced in the presence of a nocturnal LLJ, creating favorable conditions for eddy covariance measurement of surface-air fluxes of carbon dioxide and other scalar quantities. Conversely, the absence of inertial oscillations in low latitudes is one reason for why surface friction velocity is very weak in tropical eddy covariance sites at night.

6.4 Problems

6.1 Figure 6.11 shows composite profiles of potential temperature observed in Saskatchewan, Canada, in a summer season. Identify (1) the surface inversion layer and the residual layer at 06:15 local time, (2) determine the depth of the boundary layer at 09:15, 13:15, and 17:15, and (3) estimate the vertical potential temperature gradient in the free atmosphere.

6.2 Figure 6.12 shows representative profiles of potential temperature before and during a heatwave event in Voronezh, Russia. Identify the surface inversion layer and the residual layer early in the morning and the “mixed layer” in the afternoon before and during the heatwave event.

Fig. 6.11 Composite profiles of potential temperature in Saskatchewan, Canada, in the summer of 1994. Time marks are local time (Data source: Barr and Betts 1997)

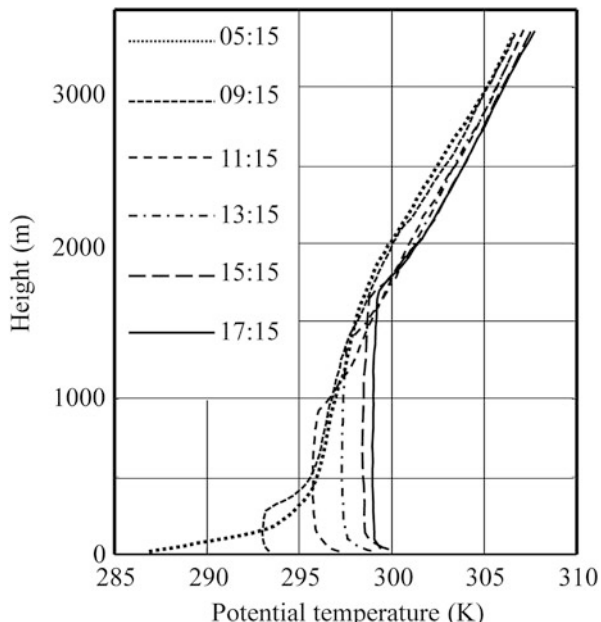
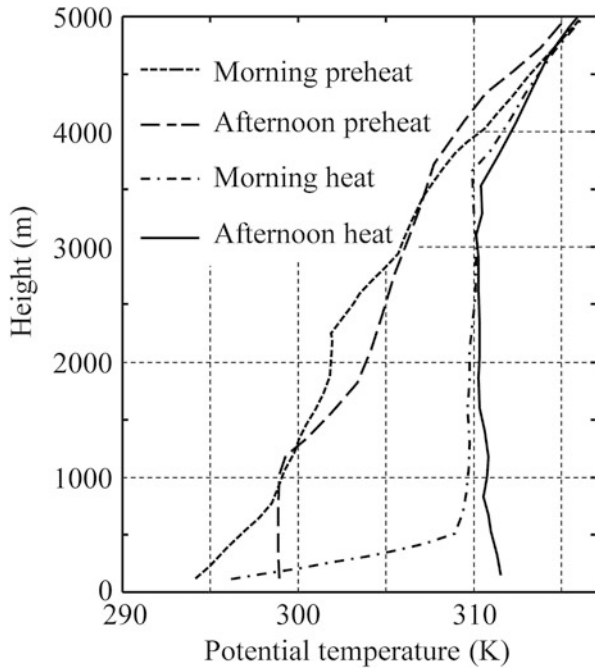


Fig. 6.12 Profiles of potential temperature before and during a mega heatwave event in Voronezh, Russia (Data source: Miralles et al. 2014)



6.3 Estimate the depth of the viscous sublayer using a typical value for surface friction velocity.

6.4 The horizontal pressure gradient is 0.01 hPa km^{-1} . Find the geostrophic wind speed.

6.5 The geostrophic wind speed is 6.0 m s^{-1} . What is the horizontal pressure gradient?

6.6 Calculate the Ekman layer depth using three different values for the momentum eddy diffusivity ($15, 1.0, \text{ and } 0.3 \text{ m}^2 \text{ s}^{-1}$).

6.7 The Ekman layer depth is 1200 m at midday and 300 m at midnight. What are the corresponding momentum eddy diffusivity values according to the Ekman spiral solution?

6.8 Using the eddy diffusivity values found in Problem 6.7, calculate the u and v velocity for the air layer between the ground and the 1500 m height. Present your results in a profile plot. (Hint: use the coordinate shown in Fig. 4.1 and a geostrophic wind speed of 10 m s^{-1} .)

6.9* (1) Obtain a numerical solution to the momentum Eqs. 6.6 and 6.7 using the eddy diffusivity parameterization given by Eq. 3.52, a geostrophic wind speed $V_g = 10.0 \text{ m s}^{-1}$, a surface roughness $z_o = 1.0 \text{ m}$, and a boundary layer depth $z_i = 1100 \text{ m}$ (Blackadar 1962). The surface and the upper boundary conditions are

$$\bar{u} = \bar{v} = 0 \text{ at } z = 0,$$

and

$$\bar{u} = V_g, \quad \bar{v} = 0 \quad \text{at } z = z_i.$$

Air stability is neutral. Surface friction velocity is constrained by the Rossby similarity relation:

$$(u_*/V_g)^2 = k^2 / \{[\ln(\text{Ro } u_*/V_g) - A]^2 + B^2\}, \quad (6.23)$$

where $\text{Ro} [= V_g/(fz_o)]$ is Rossby number, $A \simeq 2$, and $B \simeq 4.5$. Present your result in an Ekman spiral plot similar to Fig. 6.5. (2) Repeat your calculation for $z_o = 0.001$ m, representing a smooth surface, such as a lake or the ocean, but with the other parameters unchanged. How does surface roughness affect the angle between wind direction near the surface and wind direction in the free atmosphere?

6.10 Estimate wind speed in the trunk space of a forest using the pressure gradient value found in Problem 6.5, a canopy drag coefficient of 0.2 and a plant area density of $0.05 \text{ m}^2 \text{ m}^{-3}$. What is the ratio of the wind speed in the trunk space to the geostrophic wind speed?

6.11 In a dispersion experiment in a forest, your instruments are mounted on a tower. Wind measurement above the forest indicates that air is moving from north, so you place a smoke source at some distance due north of the tower, hoping to observe the center of the smoke plume (Fig. 6.13). Will the smoke plume follows a trajectory in the direction of the tower, or is it more likely to veer to the left or right of the tower? Why?

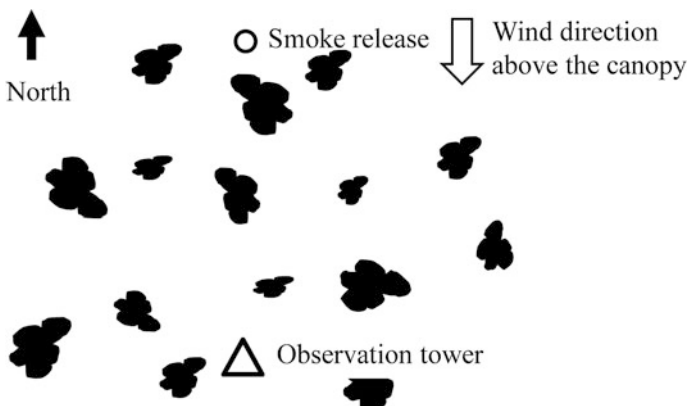


Fig. 6.13 A bird's eye view of a forest site showing tree crowns, a smoke source, and an observational tower. Smoke is released on the ground at some distance away from the observational tower

- 6.12** Derive Eqs. 6.13 and 6.14 from the full momentum Eqs. 3.31 and 3.32. What assumptions are made in your derivation?
- 6.13** Verify that Eqs. 6.15 and 6.16 are a solution to Eqs. 6.13 and 6.14 and satisfy the proper initial condition.
- 6.14** The initial velocity in the residual layer is 4.0 m s^{-1} , and the geostrophic velocity is 9.0 m s^{-1} . The angle between the two velocity vectors is 10.0° . Produce a vector plot of the inertial oscillation similar to the one shown in Fig. 6.9. At about what time does the wind becomes super geostrophic? What is the highest wind speed expected?
- 6.15*** The inertial oscillation starts at time $t = 0$ with a momentum eddy diffusivity of $12.5 \text{ m}^2 \text{ s}^{-1}$, and the eddy diffusivity in the new equilibrium state is $0.5 \text{ m}^2 \text{ s}^{-1}$. The Coriolis parameter $f = 1.14 \times 10^{-4} \text{ s}^{-1}$ (latitude 52°N). Produce a profile of the magnitude of the velocity in the boundary layer for $t = 0 \text{ h}, 2 \text{ h } 11 \text{ min}, 4 \text{ h } 23 \text{ min}, 6 \text{ h } 35 \text{ min}$, and $8 \text{ h } 36 \text{ min}$. At what time(s) do you expect the occurrence of a low-level jet?
- 6.16** Repeat the calculation in Problem 6.15 for a tropical latitude of 8°N . According to your result, is it possible for a low-level jet to establish at this latitude in the evening? Why or why not?
- 6.17** Can we use the Ekman spiral solution to describe wind profiles in a tropical boundary layer near the equator? Why or why not?
- 6.18** The wind is blowing from due south above the atmospheric boundary layer. Provide an estimate of the wind direction at the top of a forest and near the forest floor. (Hint: An open airspace exists between the ground and the forest canopy layer.)
- 6.19** Do you expect a larger wind directional shear in the boundary layer over an urban landscape or over a snow-covered pasture land? Why?
- 6.20*** The geostrophic wind speed V_g is 10.00 m s^{-1} , the initial velocity $\{u_0, v_0\}$ in the surface layer is $\{1.56, 1.34\} \text{ m s}^{-1}$, and the equilibrium velocity $\{u_e, v_e\}$ is $\{5.53, 3.11\} \text{ m s}^{-1}$. Find the velocity at successive time steps after sunset. Present your result in a vector form similar to those shown in Fig. 6.9. Does your result suggest that the surface wind is directed toward higher pressure for some portion of the evening?

References

- Barr AG, Betts AK (1997) Radiosonde boundary layer budgets above a boreal forest. *J Geophys Res* 102:292-5-29212
- Blackadar AK (1957) Boundary layer wind maxima and their significance for the growth of nocturnal inversions. *Bull Am Meteorol Soc* 37:283-290

- Blackadar AK (1962) The vertical distribution of wind and turbulent exchange in a neutral atmosphere. *J Geophys Res* 67:3095–3102
- Lee X, Shaw RH, Black TA (1994) Modelling the effect of barometric pressure gradient on the mean flow within forests. *Agric For Meteorol* 68:201–212
- Mahrt L (1999) Stratified atmospheric boundary layers. *Bound-Layer Meteorol* 90:375–396
- Miralles DG, Teuling AJ, van Heerwaarden CC, Vilá-Guerau de Arellano J (2014) Mega-heatwave temperatures due to combined soil desiccation and atmospheric heat accumulation. *Nat Geosci* 7:345–349
- Sullivan PP, Moeng CH, Stevens B, Lenschow DH, Mayor SD (1998) Structure of the entrainment zone capping the convective atmospheric boundary layer. *J Atmos Sci* 55:3042–3064
- Sun J, Lenscho DH, Mahrt L, Nappo C (2013) The relationships among wind, horizontal pressure gradient, and turbulent momentum transport during CASES-99. *J Atmos Sci* 70:3397–3414
- van de Weil BJH, Moene AF, Steeneveld GJ, Baas P, Bosveld FC, Holtslag AAM (2010) A conceptual view on inertial oscillations and nocturnal low-level jets. *J Atmos Sci* 67:2679–2689

Chapter 7

Tracer Diffusion in the Lower Boundary Layer

7.1 Basic Constraints

This chapter is concerned with the advection and dispersion of materials released in the atmospheric boundary layer. Historical interest in the diffusion problem has been motivated primarily by the need for predicting concentration of air pollutants from smokestacks. Further advances are made by micrometeorologists engaged in surface flux measurement in heterogeneous landscapes. They find it necessary to map out a source footprint impacting their measured flux, using footprint models which are essentially extensions of the traditional diffusion theory concerning pollution sources located at the ground level.

We assume that the release occurs in a trace amount so that dynamics of the flow are unaffected by the source strength and source placement in the boundary layer. Once airborne, the tracer is neither generated nor destroyed by chemical reactions, and the ground is nonabsorbing, so the total mass of the tracer is conserved over time.

The tracer diffusion is subject to four basic constraints (Blackadar 1997; Seinfeld and Pandis 2006). The first one is that of linear superposition. The *principle of linear superposition* states that the total concentration at a given location and time resulting from multiple sources is simply the sum of the concentration resulting from each individual source operating independently of the others. The principle allows us to build diffusion models for more complex source configurations from those for simpler ones. The concentration from a continuous point source can be obtained by time integration of the concentration from an instant point source. A line source can be considered as a large number of point sources arranged next to each other along a linear transect, and its concentration can be derived by spatial integration of the point-source concentration over the transect. An area source problem can be solved by linear superposition of line sources. A canopy source can be viewed as multiple area sources stacked up vertically, and so on.

The second constraint is provided by mass conservation. In one-dimensional flow, the mean tracer mass density, \bar{c} , satisfies the *local mass conservation* equation at all locations except that of the source:

$$\frac{\partial \bar{c}}{\partial t} + \bar{u} \frac{\partial \bar{c}}{\partial x} = -\frac{\partial \bar{u}' c'}{\partial x} - \frac{\partial \bar{v}' c'}{\partial y} - \frac{\partial \bar{w}' c'}{\partial z}, \quad (7.1)$$

where \bar{c} is in dimensions of kg m^{-3} . This equation is obtained by performing Reynolds averaging on the instant mass conservation Eq. 2.16 (with ρ_c replaced by c) and is used in conjunction with the first-order closure assumption:

$$\bar{u}' c' = -K_x \frac{\partial \bar{c}}{\partial x}, \quad \bar{v}' c' = -K_y \frac{\partial \bar{c}}{\partial y}, \quad \bar{w}' c' = -K_z \frac{\partial \bar{c}}{\partial z}, \quad (7.2)$$

where K_x , K_y , and K_z are eddy diffusivity in the along-wind, the crosswind, and the vertical direction, respectively. In the atmospheric boundary layer, K_z can be described with the same parameterizations given in Chap. 3 for scalar quantities.

While Eq. 7.1 is rigorous, Eq. 7.2 has the same drawbacks as any first-order closure parameterization (Chap. 3), including the difficulty in describing the diffusion process in the region very close to the source (Sect. 7.2).

The matter at hand is a forward problem, which starts with a source of known strength and aims to quantify the resulting concentration. In a departure from the standard practice of using the mixing ratio in model equations, tracer diffusion equations are traditionally expressed with the mass density. One advantage of using the mixing ratio over the mass density is that artificial diffusion arising from spatial variations in air density is avoided. Artificial diffusion is undesirable if we wish to solve an inverse problem, for example, to infer source strength from measurements of atmospheric concentration using the flux-gradient or the eddy covariance method. However, in the forward problem, errors due to artificial diffusion are not severe in comparison with other sources of error, such as those associated with dispersion parameters.

The third constraint, termed here as *global mass conservation*, is the mass conservation principle applied to the whole flow domain. Because the tracer is inert, its total mass must be conserved over time. If the total emitted mass from an instant source is Q (in kg), the concentration at any subsequent time satisfies

$$\int_{-\infty}^{\infty} \int_{-\infty}^{\infty} \int_{-\infty}^{\infty} \bar{c} \, dx \, dy \, dz = Q. \quad (7.3)$$

This constraint appears in different forms for a continuous point source (Eqs. 7.25 and 7.27) and a line source (Eq. 7.30). Equation 7.3 and the like are a useful consistency check on statistical models and empirical parameterizations: if your solution violates global mass conservation, you would know that something has gone wrong.

Equation 7.3 does not hold if the tracer is reactive or can be removed by the ground surface or other obstacles in the flow field.

The last constraint states that the probabilities of particle position in the three orthogonal directions (x , y , and z) are independent of each other. *Statistical independence* is an assumed property of turbulent diffusion in the *Lagrangian framework*, in which we follow fluid particles through space and time and imagine that each particle carries with it a small and equal amount of the tracer material. This is in contrast to the Eulerian framework in which tracer advection and dispersion are described in reference to a fixed coordinate system, such as the Cartesian coordinates used by Eqs. 7.1 and 7.2. It is not possible to calculate a particle's trajectory of movement in a deterministic manner, so we resort to statistical description of its behaviors. Let p_z be the probability distribution so that the probability that the particle's position falls between z and $z + dz$ is given by $p_z dz$. By definition, p_z satisfies

$$\int_{-\infty}^{+\infty} p_z dz = 1. \quad (7.4)$$

The probability distributions in the x and y directions, p_x and p_y , are defined similarly. The statistical independence assumption states that the probability of a particle's position in one direction is independent of its positions in the other two directions. Mathematically, this is expressed as

$$p = p_x p_y p_z. \quad (7.5)$$

Here $p dx dy dz$ is the probability that the particle will fall in the space bounded by x to $x + dx$, y to $y + dy$, and z to $z + dz$. Again by definition and in agreement with global mass conservation, we have

$$\int_{-\infty}^{\infty} \int_{-\infty}^{\infty} \int_{-\infty}^{\infty} p dx dy dz = 1. \quad (7.6)$$

Equation 7.5 is a necessary simplification in order for us to derive analytical expressions for flux footprint and for tracer concentration in multiple dimensions. It strictly does not hold in shear-driven flow in the surface layer because the vertical and horizontal velocities of fluid particles are correlated. An upward moving particle whose vertical velocity is positive is likely associated with a negative fluctuating horizontal velocity, and vice versa (Fig. 3.3). In practice, this shortcoming is not too serious as stochastic models that do not invoke the simplification yield similar results.

7.2 Point-Source Diffusion in Homogeneous Turbulence

Instant Point Source

We start with an instant point source located at $x = y = z = 0$ that releases a tracer in the amount of Q (in kg) at time $t = 0$ (i.e., a “puff”). Our goal is to determine the tracer mass density, \bar{c} , as a function of space and time. In the Lagrangian framework, diffusion of the tracer is accomplished by a large ensemble of fluid particles moving along their own independent trajectories (Fig. 7.1). The position of a particle at time t is given by

$$X(t) = \int_0^t u_L dt', \quad Y(t) = \int_0^t v_L dt', \quad Z(t) = \int_0^t w_L dt', \quad (7.7)$$

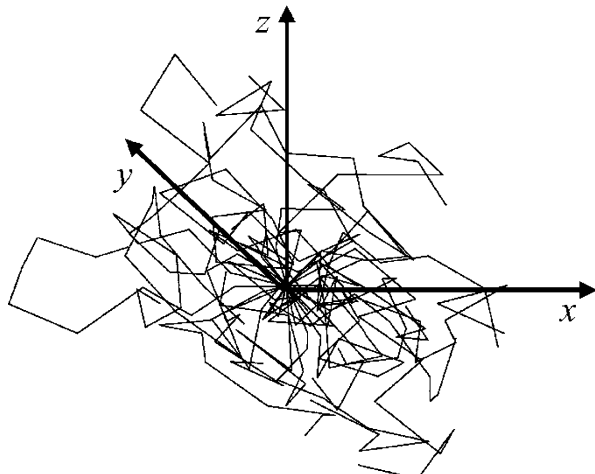
where $\{u_L, v_L, w_L\}$ are the three velocity components of the particle. Because the flow field is turbulent, the velocities and the particle position coordinates are random variables.

Although we cannot determine precisely the trajectory of an individual particle, we can use statistical means to study the collective behavior of the particle plume. The center position of the plume is given by $\{\bar{X}, \bar{Y}, \bar{Z}\}$, and the plume size is measured by the standard deviations of particle position:

$$\sigma_x(t) = (\bar{X}^2)^{1/2}, \quad \sigma_y(t) = (\bar{Y}^2)^{1/2}, \quad \sigma_z(t) = (\bar{Z}^2)^{1/2}. \quad (7.8)$$

Here the overbar denotes averaging over the ensemble of the particles. The standard deviations of the position variables, σ_x , σ_y , and σ_z , termed *dispersion parameters*, become larger with time.

Fig. 7.1 Trajectories of tracer particles dispersing simultaneously from a point source at the origin. Each particle carries an equal amount of tracer material and moves along a random and independent path



The probability distribution function, $p(x, y, z, t)$, describes the likelihood that a particle is in location $\{x, y, z\}$ at time t . When a large ensemble of particles are considered, p is equivalent to particle number density (in m^{-3}). Recalling that each particle carries an equal amount of the tracer, the mean tracer concentration is given by

$$\bar{c}(x, y, z, t) = Qp(x, y, z, t). \quad (7.9)$$

So the task of determining \bar{c} is shifted to finding the probability distribution function p .

The turbulence field is assumed to be homogeneous and unbounded. In *homogeneous turbulence*, Reynolds mean statistics of the flow field, such as the mean velocity and the velocity variance, are invariant in space. It is generally believed that the distributions of particle velocities are Gaussian in homogeneous turbulence. The vertical position of the particle Z is also Gaussian according to the central limit theorem, because Z at time t can be regarded as the sum of w_L values at infinite number of time steps before t (Eq. 7.7), each w_L value being a Gaussian variable and independent of the velocity values at preceding steps. The probability distribution for Z is therefore given by

$$p_z = \frac{1}{\sqrt{2\pi}\sigma_z} \exp\left(-\frac{z^2}{2\sigma_z^2}\right), \quad (7.10)$$

(Fig. 7.2). The probability distributions for the particle's horizontal positions X and Y have an identical form to Eq. 7.10. Using the statistical independence constraint (Eq. 7.5), we obtain the three-dimensional probability function in absence of a mean flow velocity:

$$p(x, y, z, t) = \frac{1}{(2\pi)^{3/2}\sigma_x\sigma_y\sigma_z} \exp\left(-\frac{x^2}{2\sigma_x^2} - \frac{y^2}{2\sigma_y^2} - \frac{z^2}{2\sigma_z^2}\right), \quad (7.11)$$

where the time dependence on the right-hand side of the equation is in σ_x , σ_y , and σ_z .

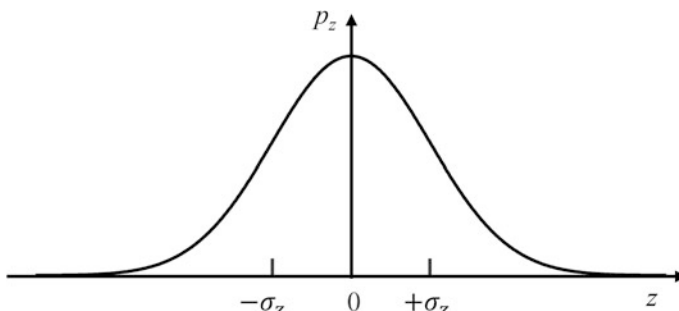


Fig. 7.2 Gaussian distribution function for particle vertical position

It follows from Eqs. 7.9 and 7.11 that the expression for the mean concentration is

$$\bar{c}(x, y, z, t) = \frac{Q}{(2\pi)^{3/2}\sigma_x\sigma_y\sigma_z} \exp\left(-\frac{x^2}{2\sigma_x^2} - \frac{y^2}{2\sigma_y^2} - \frac{z^2}{2\sigma_z^2}\right). \quad (7.12)$$

Note that the center of the plume in this case remains fixed at the origin.

If there is a mean velocity \bar{u} , the center of the plume will be transported at the speed of the moving fluid, and Eq. 7.12 is modified to

$$\bar{c}(x, y, z, t) = \frac{Q}{(2\pi)^{3/2}\sigma_x\sigma_y\sigma_z} \exp\left(-\frac{(x - \bar{u}t)^2}{2\sigma_x^2} - \frac{y^2}{2\sigma_y^2} - \frac{z^2}{2\sigma_z^2}\right). \quad (7.13)$$

Let us now check Eqs. 7.12 and 7.13 against the constraints introduced in the previous section. We have already used the statistical independence constraint in their derivation. Linear superposition requires that if the amount of tracer release is doubled, the concentration should also be doubled everywhere in space, a requirement that both equations satisfy. These equations also satisfy the global mass conservation Eq. 7.3 (Problem 7.1). With regard to local conservation, it can be shown that, by relating the dispersion parameters to the eddy diffusivities as

$$\sigma_x^2 = 2K_x t, \quad \sigma_y^2 = 2K_y t, \quad \sigma_z^2 = 2K_z t, \quad (7.14)$$

Equations 7.12 and 7.13 are solutions to Eqs. 7.1 and 7.2.

Before we can evaluate Eqs. 7.12 and 7.13, we must determine the dispersion parameters. For this purpose, we employ the theory of G. I. Taylor on diffusion in stationary turbulence to establish a relationship of σ_z to turbulent velocity of the fluid. The result can be easily extended to σ_x and σ_y .

In *stationary turbulence*, origin in time does not matter to statistical properties of the fluid particles. To put it differently, the correlation of particle velocity w_L at time t and that at $t + t'$ depends only on time difference t' and not on t or $t + t'$. The Lagrangian autocorrelation can be written as

$$R_L(t') = \frac{\overline{w_L(t)w_L(t+t')}}{\overline{w_L^2}}. \quad (7.15)$$

Its value is unity for $t' = 0$ and zero for $t' \rightarrow \infty$. The function adopted here that satisfies these requirements is

$$R_L(t') = \exp(-t'/T_L), \quad (7.16)$$

where T_L is the Lagrangian integral time scale. It follows from Eq. 7.7, its derivative counterpart $w_L = dZ/dt$, and Eqs. 7.8 and 7.15 that

$$\begin{aligned}
\overline{w_L^2} \int_0^t R_L(t') dt' &= \overline{w_L(t) \int_0^t w_L(t+t') dt'} \\
&= \overline{w_L(t) Z(t)} \\
&= \frac{dZ(t)}{dt} Z(t) \\
&= \frac{1}{2} \frac{d}{dt} \sigma_z^2(t).
\end{aligned} \tag{7.17}$$

Combining Eqs. 7.16 and 7.17 yields an ordinary differential equation for σ_z^2 :

$$\overline{w_L^2} [1 - \exp(-t/T_L)] T_L = \frac{1}{2} \frac{d}{dt} \sigma_z^2(t). \tag{7.18}$$

The solution to Eq. 7.18 is

$$\sigma_z^2(t) = 2\overline{w_L^2} T_L^2 [t/T_L - 1 + \exp(-t/T_L)]. \tag{7.19}$$

In practice, the Lagrangian velocity variance is approximated by the Eulerian velocity variance,

$$\overline{w_L^2} = \sigma_w^2,$$

where $\sigma_w^2 = \overline{w'^2}$. But the Lagrangian time scale must be determined empirically.

Figure 7.3 depicts the time evolution of vertical diffusion of a tracer released by an instant point source. Two distinct regions exist. In the region close to the source called the *near field*, the plume size grows linearly with time because according to Eq. 7.19,

$$\sigma_z(t) \simeq \sigma_w t \quad \text{for small } t. \tag{7.20}$$

In the *far field* or large t , the plume size is proportional to the square root of time:

$$\sigma_z(t) \simeq \sigma_w (2T_L t)^{1/2} \quad \text{for large } t. \tag{7.21}$$

A paradoxical situation arises from these asymptotic limits. Earlier, we said that the flow we are dealing with is spatially homogeneous. This requires that eddy diffusivity K_z is invariant with location. In the far field, comparison of Eqs. 7.14 and 7.21 yields

$$K_z = \sigma_w^2 T_L, \tag{7.22}$$

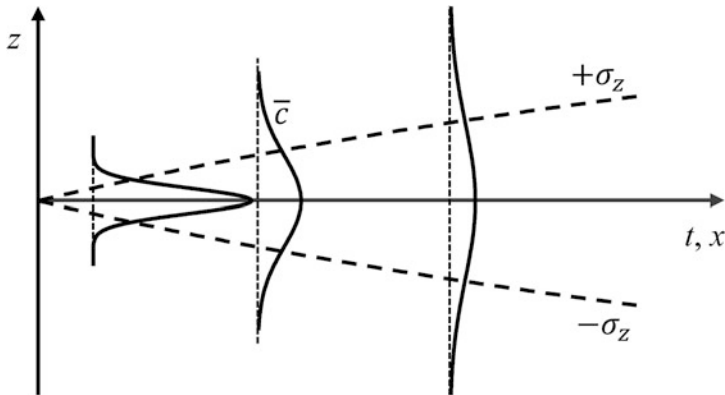


Fig. 7.3 Vertical diffusion of a tracer released by an instant point source into air that moves at a constant speed

so K_z is indeed a constant. In the near field, however, K_z varies with time or advection distance:

$$K_z = \frac{1}{2} \sigma_w^2 t = \frac{1}{2} \frac{\sigma_w^2 x}{\bar{u}}. \quad (7.23)$$

The contradiction reveals that tracer dispersion in the near field is not completely random and cannot be described accurately by the simple Fick's law type of closure parameterization (Eq. 7.2). The near-field influence is sometimes called effects of persistence.

Continuous Point Source

Another important source category is the continuous point source. Let us suppose that a source at the origin emits a tracer at a constant rate Q (in kg s^{-1}). After long enough time, the tracer concentration \bar{c} will be in steady state. According to the linear superposition principle, \bar{c} can be obtained by time integration of the instant source solution

$$\begin{aligned} \bar{c}(x, y, z) &= \int_0^\infty \frac{Q}{(2\pi)^{3/2} \sigma_x \sigma_y \sigma_z} \exp\left(-\frac{(x - \bar{u}t')^2}{2\sigma_x^2} - \frac{y^2}{2\sigma_y^2} - \frac{z^2}{2\sigma_z^2}\right) dt' \\ &\approx \frac{Q}{2\pi \bar{u} \sigma_y \sigma_z} \exp\left(-\frac{y^2}{2\sigma_y^2} - \frac{z^2}{2\sigma_z^2}\right). \end{aligned} \quad (7.24)$$

Equation 7.24 is the standard *Gaussian plume model*. In performing the time integration, we have assumed that spread of the plume caused by diffusion in the

along-wind direction is negligible in comparison to transport by the mean wind. The dependence on x is implicit because the dispersion parameters are expressed as functions of downwind distance from the source. (In Eq. 7.19, t is replaced by x/\bar{u} .)

To conserve mass, the total mean transport across the $y-z$ plane at any downwind location must be equal to Q :

$$\int_{-\infty}^{\infty} \int_{-\infty}^{\infty} \bar{u} \bar{c} dy dz = Q. \quad (7.25)$$

This global mass conservation requirement is met by Eq. 7.24.

7.3 Gaussian Plume Model for Elevated Sources in the Boundary Layer

Smokestacks are the most common continuous point sources in the atmospheric boundary layer. We use the Gaussian plume model to relate the smoke concentration from a stack with wind speed and dispersion conditions in the boundary layer. Let the z -axis be height above the ground, the x -axis be distance downwind from the source, and the y -axis be distance in the crosswind direction from the centerline of the smoke plume. The source is elevated above the ground, at the stack height of z_1 . The source coordinates are $\{0, 0, z_1\}$. The smoke plume bears some resemblance to a cone suspended in midair (Fig. 7.4). Its vertical cross section has an elliptical-shaped outline, whose vertical and crosswind radius are approximately $2\sigma_z$ and $2\sigma_y$, respectively.

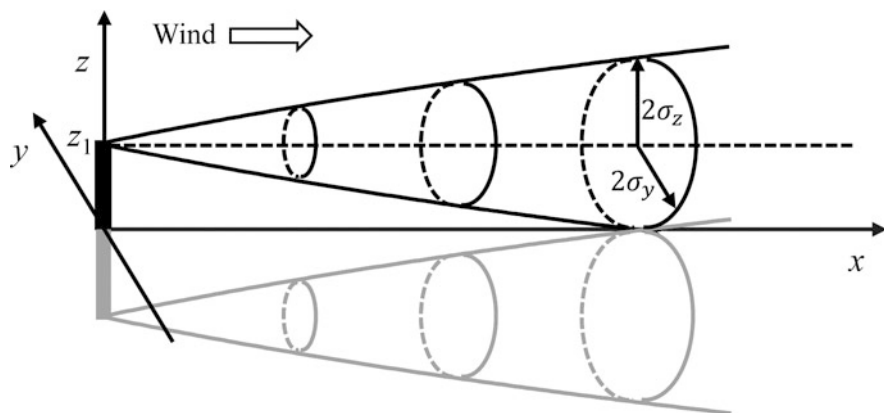


Fig. 7.4 Smoke plume from a smokestack in the atmospheric boundary layer. Ground reflection is achieved by adding a mirror source below the surface

Two modifications are made to the model to improve its realism for air quality modeling. First, we must consider the presence of the ground surface. Unlike the unbounded flow discussed in the previous section, the flow is now confined above the ground which is a physical barrier to smoke diffusion. We assume that the ground does not absorb smoke pollutants. It simply redirects the smoke back to the atmosphere when impinged upon by the smoke plume. This “zero-flux” boundary condition is met by adding a fictitious mirror source with identical strength below the ground surface (Fig. 7.4). The actual smoke concentration is the sum of contributions from the real and the mirror source:

$$\bar{c}(x, y, z; z_1) = \frac{Q}{2\pi\bar{u}\sigma_y\sigma_z} \exp\left(-\frac{y^2}{2\sigma_y^2}\right) \left\{ \exp\left[-\frac{(z - z_1)^2}{2\sigma_z^2}\right] + \exp\left[-\frac{(z + z_1)^2}{2\sigma_z^2}\right] \right\}, \quad (7.26)$$

where Q is the rate of smoke emission in kg s^{-1} and \bar{u} is mean wind speed in the boundary layer.

The mass is conserved in the space bounded by $z > 0$, so global mass conservation is expressed as

$$\int_{-\infty}^{+\infty} \int_0^{+\infty} \bar{u} \bar{c} dz dy = Q. \quad (7.27)$$

Equation 7.26 satisfies this constraint.

If the boundary layer is shallow, or if the smokestack is tall, some smoke particles will be redirected downward by the capping inversion. The reflective effect can be modeled with addition of another mirror source above the inversion layer.

Often for ecosystem and human health considerations, we are concerned with pollution concentration at the ground level. The expression for the ground-level concentration is obtained from Eq. 7.26 by setting z to zero,

$$\bar{c}(x, y, 0; z_1) = \frac{Q}{\pi\bar{u}\sigma_y\sigma_z} \exp\left(-\frac{y^2}{2\sigma_y^2}\right) \exp\left(-\frac{z_1^2}{2\sigma_z^2}\right). \quad (7.28)$$

The second modification made to the Gaussian plume model accounts for influences of wind shear and air stability, two other features that are absent in homogeneous flow. This modification changes the way the dispersion parameters σ_y and σ_z are calculated. Equation 7.14 suggests the following parameterization,

$$\sigma_y^2 = 2K_y x / \bar{u}, \quad \sigma_z^2 = 2K_z x / \bar{u}, \quad (7.29)$$

The behaviors of the vertical diffusivity K_z in relation to wind shear and air stability are known reasonably well (Chap. 3). But the lateral diffusivity K_y is uncertain. A more popular approach relates σ_y and σ_z to x using the Pasquill-Gifford

formulae whose empirical coefficients have been determined for six stability classes from outdoor tracer dispersion experiments (Problem 7.5). Generally σ_y and σ_z increase at faster rates with distance than the square root relationship predicted for homogeneous turbulence (Eq. 7.29), and are greater in more unstable air.

A number of aspects of the modified Gaussian plume model agree with our intuition about how a smoke plume should behave. The highest ground-level concentration is expected below the center of the plume ($y = 0$) at some distance downwind of the stack, in agreement with Eq. 7.28. According to the equation, increasing the stack height should drastically improve air quality at the ground. The smoke concentration increases everywhere in proportion to the rate of smoke emission and in inverse proportion to wind speed. The effect of wind speed can be understood this way: if wind speed is doubled, the same amount of pollutant will get transported over twice the distance, and we expect twice as much dilution volume for the smoke plume and hence half of the pollutant concentration.

The impact of air stability on air quality cannot be deduced from simple intuitive reasoning. As air changes from being stable to being unstable, σ_y and σ_z will become larger at the same downwind distance. The fractional part of Eq. 7.28 becomes smaller but the exponential parts become larger. The overall influence can only be quantified by performing actual calculation with the Pasquill-Gifford formulae and Eq. 7.28. The results are shown in Fig. 7.5. In unstable conditions, the maximum ground-level concentration is much higher, and bad air quality is confined to a region closer to the stack than in neutral and stable conditions.

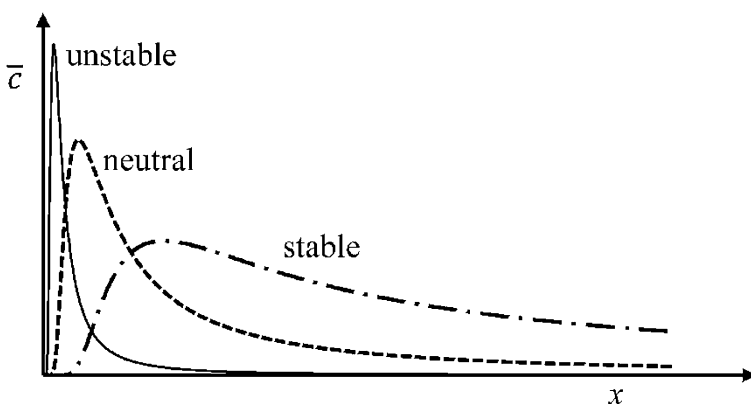


Fig. 7.5 Ground-level concentration below the centerline of a smoke plume in three stability conditions

7.4 Diffusion from Ground-Level Sources

Ground-Level Line Source

Real-world examples of the ground-level line source include highways and streets. As we will learn later in this chapter, this source class also holds a special place in footprint theory because line source solution is an essential building block for flux footprint models.

We consider a line source perpendicular to the mean wind and located at $x = 0$ (Fig. 7.6). The source is infinitely long, so the problem is reduced to finding a solution in two dimensions (x, z) . The global mass conservation constraint now becomes

$$\int_0^\infty \bar{u} \bar{c}(x, z) dz = Q, \quad (7.30)$$

where Q is tracer emission rate per unit length in $\text{kg m}^{-1} \text{s}^{-1}$. In steady state and with omission of longitudinal diffusion, the local mass conservation constraint Eq. 7.1 is simplified to

$$\bar{u} \frac{\partial \bar{c}}{\partial x} = \frac{\partial}{\partial z} \left(K_z \frac{\partial \bar{c}}{\partial z} \right). \quad (7.31)$$

If we assume that the flow field is homogeneous in space, we can obtain a line source solution from the Gaussian plume model for point sources. We divide the line source into equal segments of length dy , turning each into a point source with emission rate of $Q dy$. The concentration resulting from each segment is given by Eq. 7.26 with the source height z_1 set to zero. According to the linear superposition principle, the line source solution is equal to the sum of contributions from all the

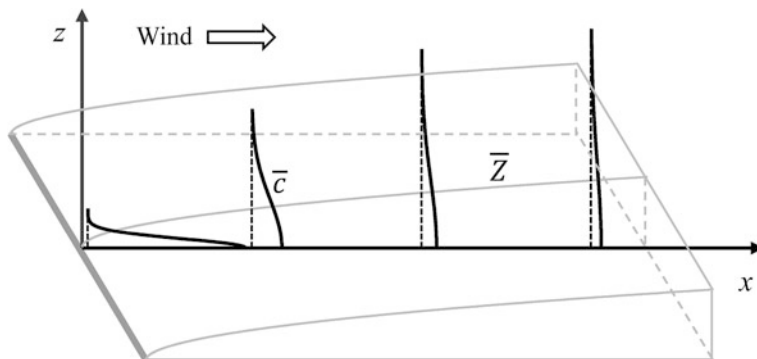


Fig. 7.6 Tracer concentration profiles downwind of a ground-level line source. The upper face of the wedge shape marks the mean plume height

segments and is obtained by integrating Eq. 7.26 with respect to y from negative infinity to positive infinity. The result is represented by

$$\bar{c}(x, z) = \frac{Q}{(\pi K_z \bar{u} x)^{1/2}} \exp\left(-\frac{\bar{u} z^2}{4K_z x}\right). \quad (7.32)$$

In the derivation, the vertical dispersion parameter has been eliminated by using Eq. 7.29.

Equation 7.32 satisfies both the global and the local mass conservation constraints (Problem 7.7). As expected, the tracer is infinitely dense at the source and becomes diluted quickly as we move away, either upward or downwind, from the source. The vertical gradient of its concentration is zero at the ground, ensuring zero tracer flux to the surface. These attributes are boundary conditions for Eq. 7.31 and can be expressed as

$$\bar{c} \rightarrow 0 \quad \text{as } x, z \rightarrow \infty, \quad (7.33)$$

$$\bar{c} \rightarrow \infty \quad \text{at } x = z = 0, \quad (7.34)$$

$$K_z \frac{\partial \bar{c}}{\partial z} = 0 \quad \text{at } z = 0, x > 0. \quad (7.35)$$

In homogeneous turbulence, both the wind speed \bar{u} and the eddy diffusivity K_z are invariant with height. Obviously, the assumption of constant \bar{u} and K_z is too simplistic for flow in the surface layer where these quantities are known to be very sensitive to height. Let us now improve the situation by incorporating the height dependence into our prediction of tracer diffusion.

So far, we have been relying on Lagrangian reasoning to obtain solutions to diffusion problems (in homogeneous turbulence). We wish to change tactic, by solving the local conservation Eq. 7.31 in the Eulerian reference frame for situations where turbulence is not homogeneous. Unfortunately, Eq. 7.31 is not amenable to analytical solution if we use the “correct” form of surface-layer \bar{u} (Eq. 4.40) and K_z profile (Eq. 3.50). But if we approximate them with profiles of the power law form,

$$K_z(z) = K_1 \left(\frac{z}{z_1}\right)^n, \quad \bar{u}(z) = \bar{u}_1 \left(\frac{z}{z_1}\right)^m, \quad (7.36)$$

we obtain an analytical solution as

$$\bar{c}(x, z) = \frac{Qr}{z_1 \bar{u}_1 \Gamma(s)} \left(\frac{z_1^2 \bar{u}_1}{r^2 K_1 x}\right)^s \exp\left(-\frac{z_1^{2-r} \bar{u}_1 z^r}{r^2 K_1 x}\right), \quad (7.37)$$

where K_1 and \bar{u}_1 are eddy diffusivity and wind speed at reference height z_1 , Γ is the gamma function, and

$$r = m - n + 2 > 0, \quad s = (m + 1)/r, \quad (7.38)$$

are two shape factors (Pasquill and Smith 1983). Equation 7.37 satisfies the boundary conditions (Eqs. 7.33, 7.34 and 7.35) and global conservation (Eq. 7.30).

The homogeneous solution is a special case of Eq. 7.37. In homogeneous turbulence, $n = m = 0$, $r = 2$, $s = 1/2$, and $\Gamma(1/2) = \sqrt{\pi}$, and Eq. 7.37 is simplified to Eq. 7.32.

Another special case found in the literature is the application of a constant wind speed and a linear function for K_z (i.e., $K_z = ku_*z$). The corresponding shape factors are: $m = 0$, $n = 1$, $r = 1$, $s = 1$, and $\Gamma(1) = 1$. Under these circumstances, Eq. 7.37 becomes

$$\bar{c}(x, z) = \frac{Q}{ku_*x} \exp\left(\frac{-\bar{u}z}{ku_*x}\right), \quad (7.39)$$

In Eq. 7.37, the effects of stability and surface roughness on tracer diffusion are implicit through the exponents n and m . The exponent n is exactly unity in neutral stability and deviates slightly from unity in stratified conditions. The exponent m is more variable, changing from 0.1 to 0.7, with smaller values for smoother surfaces and more unstable conditions.

In the following, we adopt the approach of A. P. van Ulden (van Ulden 1978) to incorporate the effects of stability and surface roughness. Equation 7.37 can be rewritten as

$$\bar{c}(x, z) = \frac{AQ}{\bar{Z}u_p} \exp\left[-\left(\frac{Bz}{\bar{Z}}\right)^r\right], \quad (7.40)$$

where $A = r\Gamma(2/r)/[\Gamma(1/r)]^2$, $B = \Gamma(2/r)/\Gamma(1/r)$, \bar{Z} is the mean plume height given by

$$\bar{Z} = \int_0^\infty \bar{c}z dz / \int_0^\infty \bar{c} dz, \quad (7.41)$$

and u_p is the mean plume velocity given by

$$u_p = \int_0^\infty \bar{c}\bar{u} dz / \int_0^\infty \bar{c} dz. \quad (7.42)$$

An appropriate r value for neutral conditions is 1.5, giving $A = 0.73$ and $B = 0.66$. For unstable conditions, we recommend $r = 1$ ($A = 1$, $B = 1$) and for stable conditions, $r = 2$ ($A = 0.63$, $B = 0.56$).

We need working expressions for \bar{Z} and u_p in order to evaluate Eq. 7.40. After lengthy manipulation involving Eqs. 7.31, 7.41, and the surface-layer profile relations, we obtain a differential equation for the mean plume height \bar{Z} :

$$\frac{d\bar{Z}}{dx} = \frac{k^2}{[\ln(p\bar{Z}/z_o) - \Psi_h(p\bar{Z}/L)]\phi_h(p\bar{Z}/L)} \quad (7.43)$$

where Ψ_h and ϕ_h are the Monin-Obukhov stability functions for heat (Eqs. 4.36 and 4.42). The coefficient p is dependent on r , but the dependence is weak. A p value of 1.55 is adequate for most situations. In neutral conditions, the solution to Eq. 7.43 is given by

$$x = \frac{\bar{Z}}{k^2} [\ln(p\bar{Z}/z_o) - 1] - \frac{z_o}{k^2} [\ln(p) - 1]. \quad (7.44)$$

This function is implicit and must be inverted either numerically or graphically to find \bar{Z} for a given x . A complete analytical solution to Eq. 7.43 for all stability conditions can be found in the paper by Horst and Weil (1994).

Finally, van Ulden derived the following approximate expressions for the mean plume velocity:

$$u_p = \begin{cases} \frac{u_*}{k} [\ln(0.6\bar{Z}/z_o) + 4.7\bar{Z}/L] & \text{if } \zeta > 0 \\ \frac{u_*}{k} \ln(0.6\bar{Z}/z_o) & \text{if } \zeta = 0 \\ \frac{u_*}{k} [\ln(0.6\bar{Z}/z_o) - \Psi_h(0.6\bar{Z}/L)] & \text{if } \zeta < 0 \end{cases} \quad (7.45)$$

According to Eq. 7.43, the derivative $d\bar{Z}/dx$ is always positive, indicating that the center of the plume will shift progressively upward with increasing travel distance from the source. The plume rises faster in unstable conditions ($\Psi_h > 0, \phi_h < 1$) and more slowly in stable conditions ($\Psi_h < 0, \phi_h > 1$). The Eulerian interpretation of the plume rise phenomenon is that gradient diffusion redistributes the tracer from lower levels where its concentration is higher to higher levels where the concentration is lower, causing the mass center of the plume to rise with travel distance x . In the Lagrangian framework, \bar{Z} represents the mean height of the ensemble of tracer particles released from the source. That \bar{Z} increases with x implies that the mean particle velocity \bar{w}_L must be greater than zero, even though the Eulerian mean vertical velocity \bar{w} is perfectly zero in one-dimensional flows. The positive particle velocity, sometimes called drift velocity, is a consequence of the fact that the vertical pressure gradient force and the gravitational force are slightly out of balance in the surface layer (Legg and Raupach 1982). The small net vertical force acts on the tracer particles, causing them to accelerate upward.

Ground-Level Point Source

We now extend the line source result to tracer diffusion of a ground-level point source. Let the source be located at the origin. Utilizing the statistical independence constraint and assuming that diffusion in the crosswind direction is Gaussian, we

can write the expression for the tracer concentration as

$$\bar{c}(x, y, z) = \{\text{line source solution}\} \times \frac{1}{\sqrt{2\pi}\sigma_y} \exp\left(-\frac{y^2}{2\sigma_y^2}\right), \quad (7.46)$$

where source strength in the line source solution is in the units of kg s^{-1} to maintain dimensional consistency.

7.5 Diffusion in Plant Canopies

For lack of better alternatives, we adopt the Gaussian plume model to describe tracer diffusion from an elevated line source in a real plant canopy. Let z_1 be the source height ($z_1 < h$, where h is canopy height). The source is located at $x = 0$. The expression for the tracer concentration is

$$\bar{c}(x, z; z_1) = \frac{Q}{\sqrt{2\pi}\sigma_z \bar{u}(z_1)} \left\{ \exp\left[-\frac{(z-z_1)^2}{2\sigma_z^2}\right] + \exp\left[-\frac{(z+z_1)^2}{2\sigma_z^2}\right] \right\}, \quad (7.47)$$

where Q is source strength in $\text{kg m}^{-1} \text{s}^{-1}$. The ground reflection is handled in the same way as in Sect. 7.3, by adding contribution from a mirror source below the ground. The mean plume velocity is approximated by wind speed at the source height.

The vertical dispersion parameter is given by the Taylor equation, as

$$\sigma_z^2(x; z_1) = 2\sigma_w^2(z_1) T_L^2 \left[\frac{x}{\bar{u}(z_1)T_L} - 1 + \exp\left(-\frac{x}{\bar{u}(z_1)T_L}\right) \right]. \quad (7.48)$$

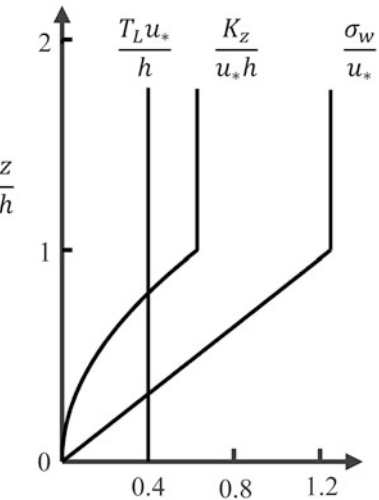
The Lagrangian time scale T_L is approximately constant with height in the canopy airspace and in the roughness sublayer above the canopy (Fig. 7.7), owing to the fact that turbulent diffusion in canopy flow is accomplished primarily by large coherent eddies. Generated by inflection-point instability (Chap. 5), these eddies are large and energetic enough to sweep through the whole canopy layer. For this reason, a single integral time scale can be used for all levels. A common parameterization for T_L is

$$T_L = \beta_1 h / u_* \quad 0 < z < \sim 2h \quad (7.49)$$

(Raupach 1989), where u_* is friction velocity. The profile of the vertical velocity standard deviation σ_w is approximated by

$$\sigma_w(z) = \begin{cases} \beta_2 u_* z / h & z \leq h \\ \beta_2 u_* & z > h \end{cases} \quad (7.50)$$

Fig. 7.7 Diffusion parameters in a plant canopy in neutral stability



The two empirical coefficients β_1 and β_2 are dependent on stability. Observational studies show that $\beta_1 \simeq 0.4$ and $\beta_2 \simeq 1.25$ in neutral conditions.

Despite the highly heterogeneous nature of canopy turbulence, predictions made with Eq. 7.47 agree reasonably well with experimental results (Lee 2004). The success can be attributed to three factors. First, in the near field (with particle travel time less than T_L), the tracer particles are strongly influenced by conditions of the flow at the source, to the extent that they behave as if they were in locally homogeneous turbulence with a velocity scale $\sigma_w(z_1)$ and a time scale T_L (Raupach 1989). Second, the fact that Eq. 7.47 satisfies the global conservation constraint (Eq. 7.30) ensures that, even though its minor details may be imprecise, its prediction of broad patterns is adequate. Third, here T_L is essentially a tuning parameter optimized for dispersion conditions in the canopy.

In the case of a ground-level line source, Eq. 7.37 is preferred over the Gaussian model for calculating the tracer concentration. But the equation requires that the wind speed profile in the canopy be presented as a power law function

$$\bar{u}(z) = \bar{u}_h \left(\frac{z}{h} \right)^m, \quad (7.51)$$

instead of the more accurate exponential function shown in Chap. 5, where \bar{u}_h is wind speed at the top of the canopy. Similarly, the eddy diffusivity profile must also take the power law form. Noting the far-field relationship, $K_z = \sigma_w^2 T_L$, we have from Eqs. 7.49 and 7.50:

$$K_z(z) = K_{z,h} \left(\frac{z}{h} \right)^2, \quad (7.52)$$

where $K_{z,h}$ is eddy diffusivity at the top of the canopy.

We recommend $m = 2$ for moderately dense canopies. Accordingly, Eq. 7.37 becomes

$$\bar{c}(x, z) = \frac{Qh^2\bar{u}_h^{1/2}}{2\sqrt{\pi}(xK_{z,h})^{3/2}} \exp\left(-\frac{z^2\bar{u}_h}{4xK_{z,h}}\right) \quad (7.53)$$

For sparse canopies, Eq. 7.37 with $m = 1$ may give more accurate results.

7.6 Footprint Theory

Footprint Concept

The footprint describes the relative contribution to the measured vertical flux from surface sources in an area upwind of a flux sensor (Schuepp et al. 1990; Horst and Weil 1994; Schmid 2002). The measured turbulent flux is a weighted sum of the surface source strength at various positions in the footprint. The concept of footprint is analogous to the field of view of a camera. Only objects in the field of view can be sensed by the camera. Similarly, only sources within the footprint can be detected by the flux sensor. But there are important differences. Once its position and its internal optical parameters are set, the camera's field of view does not change. In contrast, the flux footprint is not static, instead varying greatly with wind direction (Fig. 7.8) and air stability, and to a lesser extent with surface roughness. Additionally, objects of the same size and reflectivity contribute more or less equally to the intensity of

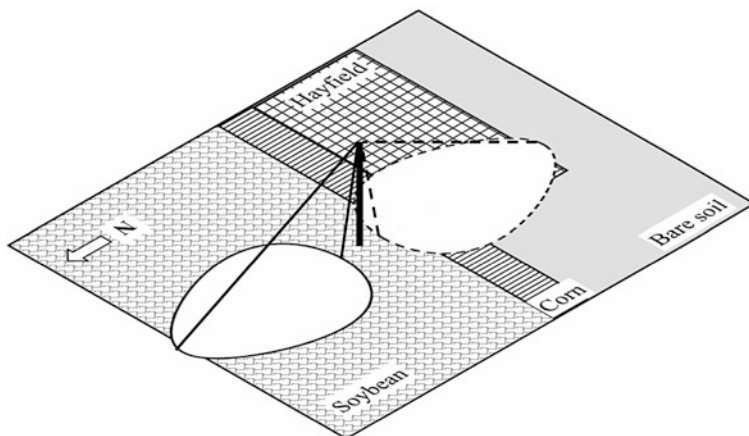


Fig. 7.8 Footprint of a flux sensor located in a soybean field in the vicinity of other land cover types: *solid line* shape, footprint for wind blowing from north; *dashed line* shape, footprint for wind blowing from south

light received by the camera. But the same cannot be said of the flux footprint. A source element makes a disproportionately large contribution to the measured flux if it is located near the center than if it is near the edge of the footprint.

The relative contribution of the surface source to the turbulent flux is defined by a footprint function. Let $\{x_m, y_m, z_m\}$ be the location of the flux sensor and $\{x, y\}$ be the relative distances to the sensor in the horizontal plane. The footprint concept is expressed mathematically as

$$F(x_m, y_m, z_m) = \int_0^{+\infty} \int_{-\infty}^{+\infty} Q(x_m - x, y_m - y) f_2(x, y; x_m, y_m, z_m) dy dx \quad (7.54)$$

where F is the vertical flux of a scalar quantity of interest (in $\text{kg m}^{-2} \text{s}^{-1}$), Q is the surface area source strength of the scalar (in $\text{kg m}^{-2} \text{s}^{-1}$), and f_2 is the footprint function (in m^{-2}). The subscript 2 is used here to indicate that the footprint involves two dimensions (in the x and y directions). Equation 7.54 expresses, on the basis of the linear superposition principle, the measured flux as the integral of weighted contributions of all upwind surface sources. The weighting factor, or the footprint function f_2 , depends on sensor position and horizontal separation distances between the source and the sensor. By definition, f_2 cannot be negative. Footprint theory seeks to determine the footprint function.

We assume that the turbulence is horizontally homogeneous. The surface source strength can vary spatially, but the variation does not influence the dynamics of the flow. Under this assumption, the footprint function is independent of horizontal placement of the flux sensor (Fig. 7.9), that is, $f_2(x, y; x_m, y_m, z_m) = f_2(x, y; z_m)$. Equation 7.54 is changed to

$$F(x_m, y_m, z_m) = \int_0^{+\infty} \int_{-\infty}^{+\infty} Q(x_m - x, y_m - y) f_2(x, y; z_m) dy dx. \quad (7.55)$$

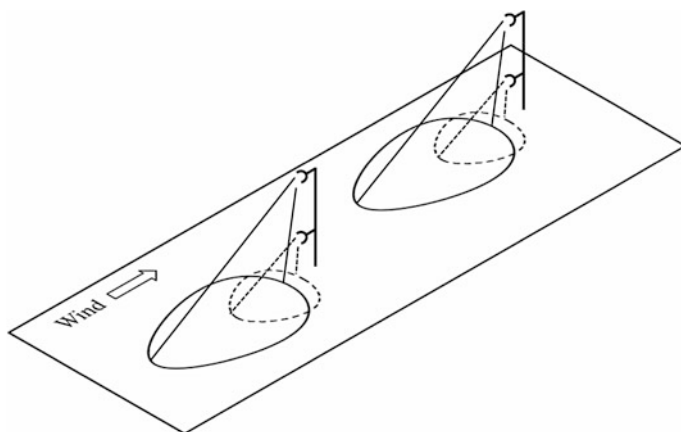


Fig. 7.9 In horizontally homogeneous turbulence, the flux footprint function is independent of horizontal sensor placement but is sensitive to sensor height

The sensor height z_m is still an independent variable for the function f_2 because the flow is vertically inhomogeneous. In other words, if the sensor is relocated horizontally, the flux footprint will not change, but if it is moved to a different level, the flux footprint will change (Fig. 7.9; Problem 7.14).

We need the footprint function to help interpret the flux observed in a landscape where the surface source is variable with horizontal position. In the example illustrated in Fig. 7.8, let us suppose that our goal is to investigate the surface-air exchange of a soybean ecosystem. The observed flux is acceptable when the wind blows from the north since a majority of the flux originates from the soybean field. If the wind shifts 180°, blowing from the south, the footprint will extend far beyond the soybean field, and the observed flux no longer represents the true surface-air exchange of the soybean ecosystem. It is commonplace in post-field data analysis to establish a footprint climatology of the site (Schmid 2002). Observations that do not satisfy a preset footprint threshold are omitted from the analysis.

Method for Finding the Footprint Function

One feature embodied in Eq. 7.55 is that the footprint function is totally independent of how the surface source is configured. We now make full use of this feature, by setting up strategic thought experiments, to determine the flux footprint. Consider first a hypothetical situation in which the surface source strength is constant everywhere in the flow domain. In steady state, the turbulent flux F is identical to Q . It follows from Eq. 7.55 that the footprint function satisfies

$$\int_0^{+\infty} \int_{-\infty}^{+\infty} f_2(x, y; z_m) dy dx = 1. \quad (7.56)$$

Equation 7.56 is a property that we strive to obey when constructing the footprint function.

In the second hypothetical situation, Q is a function of downwind distance x but is independent of crosswind distance y . Equation 7.55 becomes

$$\begin{aligned} F(x_m, z_m) &= \int_0^{+\infty} \int_{-\infty}^{+\infty} Q(x_m - x) f_2(x, y; z_m) dy dx \\ &= \int_0^{+\infty} Q(x_m - x) \left[\int_{-\infty}^{+\infty} f_2(x, y; z_m) dy \right] dx \\ &= \int_0^{+\infty} Q(x_m - x) f_1(x; z_m) dx, \end{aligned} \quad (7.57)$$

where we have introduced the one-dimensional footprint function f_1 (in m^{-1}),

$$f_1(x; z_m) = \int_{-\infty}^{+\infty} f_2(x, y; z_m) dy. \quad (7.58)$$

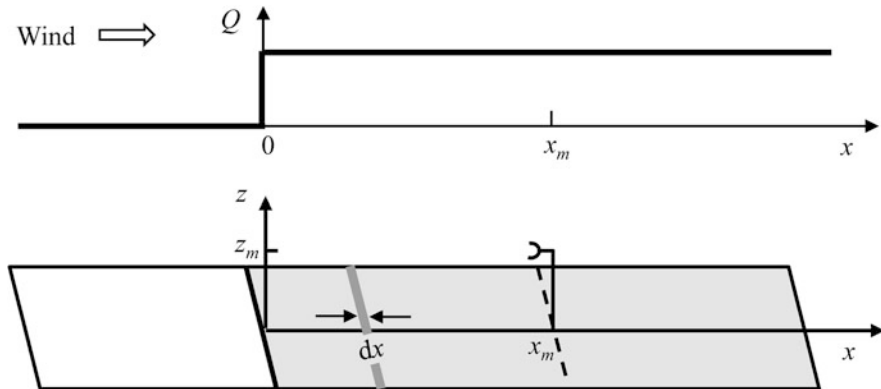


Fig. 7.10 A step change in the surface source strength

It satisfies the integral constraint

$$\int_0^{+\infty} f_1(x; z_m) dx = 1. \quad (7.59)$$

If f_1 is known, we can use the statistical independence constraint to reconstruct the two-dimensional footprint f_2 .

The third hypothetical situation allows us to relate the one-dimensional footprint function f_1 to the solution we have established for a ground-level line source. A step change occurs at $x = 0$ in the surface source strength (Fig. 7.10):

$$Q = \begin{cases} 0 & x < 0 \\ \text{constant } x \geq 0 \end{cases} \quad (7.60)$$

According to Eq. 7.57, the turbulent flux measured at distance x_m downwind from the step change is given by

$$F(x_m, z_m) = \int_0^{x_m} Q f_1(x; z_m) dx. \quad (7.61)$$

We can also determine the flux with the flux-gradient relationship. Let \bar{c}_1 be the concentration resulting from a line source of unit strength, that is, the solution to Eqs. 7.31, 7.33, 7.34, and 7.35 with a source strength of 1. We divide the area source between $x = 0$ and $x = x_m$ into many strips of width dx , turning each into a line source of source strength Qdx . The concentration resulting from each strip is $Q\bar{c}_1 dx$. Linear superposition yields the total concentration at x_m as

$$\bar{c} = \int_0^{x_m} Q \bar{c}_1 dx, \quad (7.62)$$

noting that in this expression, c_1 has dimensions of s m^{-2} . The turbulent flux is given by the flux-gradient relationship as

$$F(x_m, z_m) = -K_z \frac{\partial \bar{c}}{\partial z} \Big|_{x_m, z_m}. \quad (7.63)$$

Substituting Eq. 7.62 into 7.63, we obtain

$$F(x_m, z_m) = \int_0^{x_m} Q \left\{ -K_z \frac{\partial \bar{c}_1}{\partial z} \Big|_{z_m} \right\} dx. \quad (7.64)$$

Comparison of Eq. 7.64 with 7.61 yields a relationship for the one-dimensional footprint function:

$$f_1(x; z_m) = -K_z \frac{\partial \bar{c}_1}{\partial z} \Big|_{z_m}. \quad (7.65)$$

Therefore, we conclude that in horizontally homogeneous turbulence, the one-dimensional footprint function is equal to the product of the vertical eddy diffusivity and the vertical concentration gradient of a unit line source located at $x = 0$. According to this footprint rule, to complete the task of finding the footprint function, we should first determine the line source solution.

Footprint Models

Armed with Eq. 7.65, the rule for the footprint function, we are ready to establish footprint models. The most simple model is the case of a constant wind speed, a linear eddy diffusivity profile, and neutral stability. According to Eq. 7.39, the unit line source solution is given by

$$\bar{c}_1 = \frac{1}{ku_*x} \exp \left(-\frac{u_p z}{ku_*x} \right), \quad (7.66)$$

where we have substituted \bar{u} with the mean plume velocity u_p . It follows from Eq. 7.65 that the one-dimensional footprint function is

$$f_1(x; z_m) = \frac{u_p K_z}{(ku_*x)^2} \exp \left(-\frac{u_p z_m}{ku_*x} \right). \quad (7.67)$$

(Schuepp et al. 1990).

Evaluation of this expression requires that we specify K_z and u_p . Because air stability is assumed to be neutral, we have

$$K_z = ku_*z_m. \quad (7.68)$$

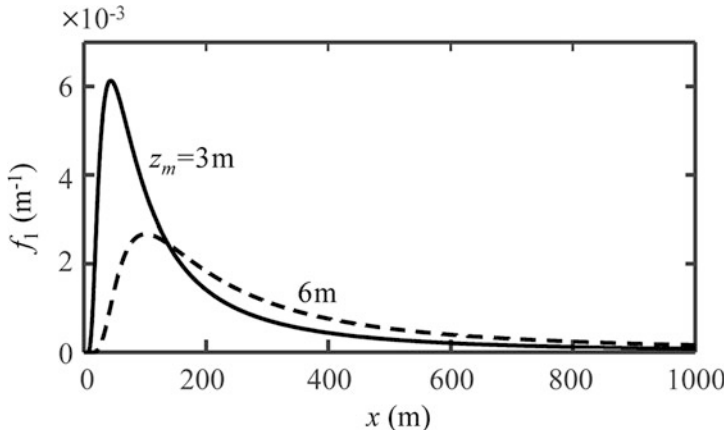


Fig. 7.11 One-dimensional footprint function according to Eq. 7.71 for two measurement heights. The surface roughness is 0.01 m

The mean plume velocity is approximated by the mean wind speed below the sensor height z_m :

$$u_p = \int_{z_0}^{z_m} \bar{u} dz / \int_{z_0}^{z_m} dz \simeq u_* z_u / (k z_m), \quad (7.69)$$

where z_u is a new height scale defined as

$$z_u = z_m [\ln(z_m/z_o) - 1 + z_o/z_m]. \quad (7.70)$$

Combining these equations with Eq. 7.67, we arrive at a working expression for the footprint function (Fig. 7.11):

$$f_I(x; z_m) = \frac{z_u}{k^2 x^2} \exp\left(-\frac{z_u}{k^2 x}\right). \quad (7.71)$$

Several features captured by Eq. 7.71 deserve our attention. The footprint function satisfies Eq. 7.59. It is independent of friction velocity u_* , indicating that, even though wind direction controls the orientation of the flux footprint (Fig. 7.8), wind speed does not influence the relative contribution of the surface source to the observed flux. The insensitivity to wind speed is a universal character of the flux footprint in the surface layer regardless of model choice. The maximum contribution occurs at

$$x_{\max} = z_u / (2k^2). \quad (7.72)$$

This is the distance from the flux sensor at which the surface source has the highest impact on the observed flux. As the measurement height increases, the maximum contribution will shift further away from the sensor.

The one-dimensional footprint function can be extended to two dimensions using the statistical independence constraint:

$$f_2(x, y; z_m) = \frac{z_u}{k^2 x^2} \exp\left(-\frac{z_u}{k^2 x}\right) \times \frac{1}{\sqrt{2\pi}\sigma_y} \exp\left(-\frac{y^2}{2\sigma_y^2}\right). \quad (7.73)$$

Once again we have assumed that diffusion in the lateral direction is Gaussian. The lateral dispersion parameter σ_y can be related to the standard deviation of the lateral velocity σ_v and the plume travel time x/u_p as $\sigma_y = \sigma_v x / u_p$.

Equation 7.71, valid only for neutral stability, can be modified for stratified conditions to

$$f_1(x; z_m) = \frac{Dz_u^b |L|^{1-b}}{k^2 x^2} \exp\left(-\frac{Dz_u^b |L|^{1-b}}{k^2 x}\right), \quad (7.74)$$

on the basis of dimensional analysis, where D and b are two empirical parameters and L is the Obukhov length (Hsieh et al. 2000). Equation 7.74 retains the form of Eq. 7.71 and is dimensionally consistent. Regression fitting of Eq. 7.74 against stochastic modeling results yields $D = 0.28$ and $b = 0.59$ for unstable conditions, $D = 1.0$ and $b = 1$ for neutral conditions, and $D = 2.44$ and $b = 1.33$ for stable conditions. In neutral stability ($|L| \rightarrow \infty$), Eq. 7.74 is reduced to Eq. 7.71.

Another commonly used footprint model is based on the line source solution given by Eq. 7.40, a solution that has been validated in field dispersion experiments. Application of the footprint rule (Eq. 7.65) to the solution yields the following footprint function:

$$f_1(x; z_m) = \frac{k u_*}{\phi_h(z_m/L)} \frac{Ar}{\bar{Z} u_p} \left(\frac{B z_m}{\bar{Z}}\right)^r \exp\left[-\left(\frac{B z_m}{\bar{Z}}\right)^r\right], \quad (7.75)$$

(Horst 1999). The plume velocity given by Eq. 7.45 and the solution of \bar{Z} from Eq. 7.43 are used in the evaluation of this function.

An attractive feature of Eq. 7.75 is that it has incorporated the stability effects. Implementation of the equation requires that the mean plume height \bar{Z} be solved with a numerical procedure, so it is not as convenient as Eqs. 7.71 and 7.74. Another drawback is that the power law profiles are used to obtain the line source solution, but the Monin-Obukhov profiles are used to formulate the expressions for the mean plume velocity and the mean plume height. These two sets of profiles are not entirely compatible. For this reason, the cumulative flux footprint does not always converge to unity as required by Eq. 7.59 (Problem 7.19).

Equations 7.74 and 7.75 can be extended to the lateral dimension as in Eq. 7.73.

The above footprint theory is developed for measurements made in the surface layer. If the flux sensor is positioned in a plant canopy or in the mixed layer, more complex approaches involving stochastic particle dispersion theory may be required.

7.7 Problems

7.1 Verify that the point-source solutions (Eqs. 7.12 and 7.13) satisfy global mass conservation (Eq. 7.3).

7.2 An instantaneous point source at the origin releases 0.4 kg of tracer in a homogeneous flow field. A few seconds later, the tracer plume has spread in three dimensions, with the dispersion parameters $\sigma_x = 5$ m, $\sigma_y = 5$ m, and $\sigma_z = 3$ m. The mean flow velocity is zero. Plot the tracer concentration distribution as a function of z for $x = y = 0$ m and for $x = 10$ m and $y = 0$ m.

7.3 The Lagrangian time scale (T_L) is 100 s and the vertical velocity standard deviation (σ_w) is 0.40 m s^{-1} . The flow field is homogeneous. Determine the vertical dispersion parameter (σ_z) at $t = 1, 10, 50, 100, 200, 500$, and 1000 s. Graph your result as a function of time.

7.4 A point source releases a puff of 1 g of SF₆ in a homogeneous flow field. The fluid velocity is 2.5 m s^{-1} . Using the dispersion parameter values obtained in Problem 7.3, calculate the SF₆ concentration at a downwind distance of 250 m at the time steps indicated. Now repeat the calculation for zero wind speed. How does wind speed affect the tracer dispersion? (Assume that the turbulence is isotropic so that $\sigma_x = \sigma_y = \sigma_z$.)

7.5 The dispersion parameters (σ_y and σ_z) for the atmospheric boundary layer can be described by the Pasquill-Gifford empirical formulae:

$$\sigma_y(x) = \exp[A_y + B_y \ln x + C_y(\ln x)^2], \quad (7.76)$$

$$\sigma_z(x) = \exp[A_z + B_z \ln x + C_z(\ln x)^2], \quad (7.77)$$

where x is distance (in m) downwind from the smokestack. The empirical coefficients in these expressions have been determined experimentally for six stability classes (Table 7.1). Find the dispersion parameter values at downwind distances of 200 and 2000 m for each of the stability classes. Does your result suggest that the smoke plume resembles a perfect cone shape?

7.6 A power plant emits SO₂ at the rate of 0.25 kg s^{-1} from a 50-m tall smokestack. The mean wind speed in the atmospheric boundary layer is 4.0 m s^{-1} . Determine the ground-level concentration of SO₂ below the center of the plume at distances of 50, 100, 200, 500, and 5000 m from the stack for an early morning hour (moderately stable, stability class F; Table 7.1) and a noon hour (extremely unstable;

Table 7.1 Coefficients of the Pasquill-Gifford empirical formulae (Seinfeld and Pandis 2006)

	A	B	C	D	E	F
A_y	-1.104	-1.634	-2.054	-2.555	-2.754	-3.143
B_y	0.9878	1.0350	1.0231	1.0423	1.0106	1.0148
C_y	-0.0076	-0.0096	-0.0076	-0.0087	-0.0064	-0.0070
A_z	4.679	-1.999	-2.341	-3.186	-3.783	-4.490
B_z	-1.7172	0.8752	0.9477	1.1737	1.3010	1.4024
C_z	0.2770	0.0136	-0.0020	-0.0316	-0.0450	-0.0540

Stability class: *A* extremely unstable, *B* moderately unstable, *C* slightly unstable, *D* neutral, *E* slightly stable, *F* moderately stable

stability class A) and compare your estimates with the United States air quality standard. (The 1-h US national ambient air quality standard for SO₂ is 0.2 mg m⁻³.) Responding to complaints from local residents about poor air quality in the area, the engineers plan to raise the stack height to 100 m. Will the increase in the stack height solve the existing air quality problems? Will it create new problems?

7.7 Show that the line source solution (Eq. 7.32) satisfies both global and local mass conservation.

7.8* Show that the mean plume height of a ground-level line source (a) is proportional to the square root of downwind distance in homogeneous turbulence and (b) is proportional to downwind distance in a turbulent flow in which the mean velocity is constant with height but the eddy diffusivity increases linearly with height. Explain why the plume rises faster in the second flow configuration.

7.9 Determine the mean plume height of a ground-level source in the atmospheric surface layer for three surface roughness values: $z_o = 0.001, 0.05$, and 1 m. The air stability is neutral. Graph your result as a function of downwind distance (from 1 to 100 m). How does surface roughness affect the plume rise?

7.10 A ground-level line source emits a tracer at a rate of 0.20 g m⁻¹ s⁻¹ in the atmospheric surface layer. The friction velocity is 0.30 m s⁻¹, the surface roughness is 0.1 m, and air stability is neutral. Determine the mean plume height and the mean plume velocity at a distance of 50 m downwind of the source. Produce a profile plot of the tracer concentration at this location.

7.11 A tracer is released at the mid-canopy height in a plant canopy. The surface friction velocity is 0.30 m s⁻¹, the canopy height is 20.0 m, and air stability is neutral. Estimate (a) the Lagrangian time scale for flow in the canopy and (b) the eddy diffusivity at the source height. Roughly how far does the near field extend downwind of the source?

7.12 In a tracer dispersion experiment in a wind tunnel canopy, a line source at a height of 51 mm releases a tracer at a rate of 1.0 mg m⁻¹ s⁻¹. The canopy height (h) is 60 mm. The friction velocity is 1.03 m s⁻¹, and the wind speed at the source height is 2.8 m s⁻¹. Predict the tracer concentration profile at downwind distances of $x/h = 0.38, 1.32, 2.78, 5.72$, and 11.6 from the source.

7.13* Derive an expression for the mean plume height of a tracer released from a ground-level line source inside a plant canopy. The wind speed and the eddy diffusivity are 2.3 m s^{-1} and $0.24 \text{ m}^2 \text{ s}^{-1}$ at the top of the canopy, and the canopy height is 2.0 m. At what distance downwind of the source does the center of the plume (\bar{Z}) rise to the canopy top?

7.14 Evaluate the one-dimensional footprint function Eq. 7.71 for measurement heights of 3.0 and 9.0 m, with surface roughness of 0.065 m. Present your result in a graphic plot. How does measurement height affect the flux footprint? Repeat the calculation with $z_o = 0.3$ m. How does surface roughness affect the flux footprint?

7.15 Equation 7.32 is the solution for a ground-level line source in homogeneous turbulence. Derive the footprint function using this equation and propose a method for calculating the mean eddy diffusivity and the mean plume velocity in the surface layer. Compare your footprint model with the model described by Eq. 7.71 for surface roughness of 0.04 m, a measurement height of 4.0 m and neutral stability.

7.16 Show that the footprint model consisting of Eqs. 7.43, 7.45, and 7.75 is independent of the surface friction velocity.

7.17 Verify that Eqs. 7.71 and 7.74 satisfy the integral constraint Eq. 7.59.

7.18 Evaluate the one-dimensional footprint function Eq. 7.74 for three stability classes (neutral stability, $L = 100$ m, and $L_s = 50$ m) for a measurement height of 4.0 m and surface roughness of 0.04 m. Present your result in a graphic plot. How does air stability affect the flux footprint?

7.19* Using a numerical procedure, check the footprint function Eq. 7.75 against the integral constraint Eq. 7.59 for a measurement height of 4 m, surface roughness of 0.04 m and neutral stability. Explain why the integral of Eq. 7.75 with respect to distance

$$\int_0^x f_1(x', z_m) dx'$$

does not seem to converge to unity as x increases.

7.20* You want to measure the evapotranspiration flux of a hayfield with an eddy covariance system. The hay field has a fetch, or distance between the instrument tower and the upwind edge of the field, of 160 m. You plan to install the instrument at a height of 2.5 m above the surface. Your footprint threshold is 90%, meaning that at least 90% of the measured evapotranspiration flux should come from the hayfield. Using the footprint function Eq. 7.71, show that your experimental plan does not satisfy the requirement. To what height should you lower the instrument to ensure that the requirement is met?

References

- Blackadar AK (1997) Turbulence and diffusion in the atmosphere. Springer, Berlin, 185pp
- Horst TW (1999) The footprint for estimation of atmospheric-surface exchange fluxes by profile techniques. *Bound-Layer Meteorol* 90:171–188
- Horst TW, Weil JC (1994) How far is far enough? The fetch requirements for micrometeorological measurement of surface fluxes. *J Atmos Ocean Technol* 11:1018–1025
- Hsieh CI, Katul G, Chi T (2000) An approximate analytical model for footprint estimation of scalar fluxes in thermally stratified atmospheric flows. *Adv Water Resour* 23:765–772
- Lee X (2004) A model for scalar advection inside canopies and application to footprint investigation. *Agric For Meteorol* 127:131–141
- Legg J, Raupach MR (1982) Markov-chain simulation of particle dispersion in inhomogeneous flows: the mean drift velocity induced by a gradient in Eulerian velocity variance. *Bound-Layer Meteorol* 24:3–13
- Pasquill F, Smith FB (1983) Atmospheric diffusion, 3rd edn. Wiley, New York, 437pp
- Raupach MR (1989) A practical Lagrangian method for relating scalar concentrations to source distributions in vegetation canopies. *Q J R Meteorol Soc* 115:609–632
- Schmid HP (2002) Footprint modeling for vegetation atmosphere exchange studies: a review and perspective. *Agric For Meteorol* 113:159–183
- Schuepp PH, Leclerc MY, MacPherson JI, Desjardins RL (1990) Footprint prediction of scalar fluxes from analytical solutions of the diffusion equation. *Bound-Layer Meteorol* 50:355–373
- Seinfeld JH, Pandis SN (2006) Atmospheric chemistry and physics: from air pollution to climate change, 2nd edn. Wiley, New York, 1023pp
- van Ulden AP (1978) Simple estimates for vertical diffusion from sources near the ground. *Atmos Environ* 12:2125–2129

Chapter 8

Principle of Eddy Covariance

8.1 Introduction

This chapter examines the relationship between eddy covariance calculations and the concept of net ecosystem exchange. Eddy covariance is a class of micrometeorological method that measures the fluxes of energy, water, and trace gases between the earth's surface and the atmosphere. The data obtained by eddy covariance are used widely by earth science communities. Examples of eddy covariance application include investigation of ecosystem functions, quantification of local carbon and water cycles, measurement of pollution deposition, and parameterization of land-atmosphere interactions for climate models. An essential component of the method is measurement of the vertical air velocity and the scalar of interest at a high time frequency (i.e., 10 Hz). The Reynolds covariance between the two is then calculated from the high-frequency time series to obtain the flux of the scalar.

In a broad mathematical sense, eddy covariance is an inverse problem, which aims to infer from atmospheric measurement the surface source or sink strength of the scalar quantity. By “surface” we mean an ecosystem, which can be a bare land, a water body, or a plant community consisting of both a soil source and elevated plant canopy sources. In exchanging heat and materials with the atmosphere, the ecosystem leaves imprints on the surface layer air by altering temporal and spatial variations of its physical properties and chemical compositions. Eddy covariance exploits the information hidden in these rapidly varying temporal signals. However, the covariance term itself is not equivalent to the rate of net ecosystem exchange and is meaningful only if interpreted in the context of a proper theoretical framework.

Underpinning the principle of eddy covariance is mass and energy conservation (Balocchi et al. 1988; Paw et al. 2000). We will discuss eddy covariance measurement of carbon dioxide by outlining all the key steps involved in the manipulation of its conservation equation. We will then extend the outcomes to water vapor and sensible heat, but without the same level of details presented for carbon dioxide.

8.2 The Canopy Source Term

We start with the Reynolds mean conservation equation for the CO₂ mass mixing ratio s_c (Eq. 3.26). Written for free air, the equation describes the diffusion and transport of CO₂ but does not contain an ecosystem source term. In order to establish the relationship between the Reynolds covariance and the net ecosystem CO₂ exchange, our first priority is to formulate the source term as part of the mass conservation equation.

In Chap. 5, we showed that the operation of canopy volume averaging on the Reynolds mean momentum equations yields a canopy momentum sink term in the form of a drag force on the canopy flow. We now apply the same strategy to the mass conservation Eq. 3.26 (Finnigan 1985). By performing canopy volume averaging and omitting dispersive covariances, we obtain from Eq. 3.26

$$\begin{aligned} \frac{\partial[\bar{s}_c]}{\partial t} + [\bar{u}] \frac{\partial[\bar{s}_c]}{\partial x} + [\bar{v}] \frac{\partial[\bar{s}_c]}{\partial y} + [\bar{w}] \frac{\partial[\bar{s}_c]}{\partial z} \\ = \kappa_c [\nabla^2 \bar{s}_c] - \left(\frac{\partial[u' s'_c]}{\partial x} + \frac{\partial[v' s'_c]}{\partial y} + \frac{\partial[w' s'_c]}{\partial z} \right). \end{aligned} \quad (8.1)$$

The expanded form of the first term on the right of this equation is

$$\kappa_c [\nabla^2 \bar{s}_c] = \kappa_c \left\{ \left[\frac{\partial^2 \bar{s}_c}{\partial x^2} \right] + \left[\frac{\partial^2 \bar{s}_c}{\partial y^2} \right] + \left[\frac{\partial^2 \bar{s}_c}{\partial z^2} \right] \right\}. \quad (8.2)$$

Because the mean CO₂ mixing ratio and its spatial derivatives are generally discontinuous across plant elements (Fig. 5.4), volume averaging and spatial differentiation are not commutable.

The canopy CO₂ source is embodied in Eq. 8.2. To show this, let us first examine the vertical derivative $[\partial^2 \bar{s}_c / \partial z^2]$, which can be expanded to three parts according to Slattery's averaging theorem (Eq. 5.11):

$$\begin{aligned} \left[\frac{\partial^2 \bar{s}_c}{\partial z^2} \right] &= \frac{\partial}{\partial z} \left[\frac{\partial \bar{s}_c}{\partial z} \right] - \frac{1}{Q} \sum \iint_{A_i} \frac{\partial \bar{s}_c}{\partial z} n_z dA \\ &= \frac{\partial^2 \bar{s}_c}{\partial z^2} - \frac{\partial}{\partial z} \left\{ \frac{1}{Q} \sum \iint_{A_i} \bar{s}_c n_z dA \right\} - \frac{1}{Q} \sum \iint_{A_i} \frac{\partial \bar{s}_c}{\partial z} n_z dA, \end{aligned} \quad (8.3)$$

where Q is averaging volume, A_i is the surface of plant element i enclosed in the volume (Fig. 5.1), and n_z is the z component of the unit normal vector of the surface. In Eq. 8.3, Slattery's theorem has been used twice, the first time on $\partial \bar{s}_c / \partial z$ and the second time on \bar{s}_c .

In Eq. 8.3, term 1 on the right side, after being multiplied by the CO₂ molecular diffusivity κ_c , represents vertical divergence of the molecular flux of carbon dioxide and is negligible in comparison to its turbulent counterpart.

To demonstrate the physical meaning of term 2 on the right side of Eq. 8.3, we consider a hypothetical canopy made up of horizontal leaves having an identical mixing ratio at the upper ($\bar{s}_{c,+}$) and at the lower side ($\bar{s}_{c,-}$). In this circumstance, the surface integral is equal to the product of the surface mixing ratio and the surface area of the leaf, and term 2 can be expressed as

$$\text{Term 2} = -\frac{\partial}{\partial z} \left\{ \frac{\sum A_i}{Q} (\bar{s}_{c,+} - \bar{s}_{c,-}) \right\} = -\frac{\partial}{\partial z} \{a(\bar{s}_{c,+} - \bar{s}_{c,-})\}, \quad (8.4)$$

where the plant area density $a = \sum A_i/Q$ by definition. So term 2 describes the vertical gradient of the mixing ratio difference between the two sides of the leaf. More generally, the mixing ratio difference should be replaced by the volume mean value ($[\bar{s}_{c,+}] - [\bar{s}_{c,-}]$) for a real canopy. The difference vanishes for amphistomatous leaves having equal amounts of stomatal openings on both sides but is generally non-zero for hypostomatous leaves whose stomatal openings exist only on the lower side (Fig. 5.4).

Following a similar argument, term 3 on the right of Eq. 8.3 can be written as

$$\text{Term 3} = -2a \left[\frac{\partial \bar{s}_c}{\partial z} n_z \right]. \quad (8.5)$$

This term is much larger than term 2 because the mixing ratio gradient at the leaf surface $\partial \bar{s}_c / \partial z$ is much larger than the vertical gradient of ($[\bar{s}_{c,+}] - [\bar{s}_{c,-}]$) in the canopy airspace, regardless of the leaf stomatal distribution. For this reason, term 2 can be safely omitted. Equation 8.3 is therefore reduced to

$$\left[\frac{\partial^2 \bar{s}_c}{\partial z^2} \right] = -2a \left[\frac{\partial \bar{s}_c}{\partial z} n_z \right]. \quad (8.6)$$

The multiplier 2 in Eq. 8.5 accounts for the fact that a is a one-sided leaf area density, but leaf-air exchange occurs on both sides of the leaf. This is true for sensible heat exchange and is also true for CO₂ and water vapor exchanges with amphistomatous leaves. For CO₂ and water vapor exchanges with hypostomatous leaves, the multiplier should be changed to unity.

The above considerations can be extended to the x and y derivatives in Eq. 8.2. The final result is given as

$$\begin{aligned} \kappa_c [\nabla^2 \bar{s}_c] &= -2\kappa_c a \left\{ \left[\frac{\partial \bar{s}_c}{\partial x} n_x \right] + \left[\frac{\partial \bar{s}_c}{\partial y} n_y \right] + \left[\frac{\partial \bar{s}_c}{\partial z} n_z \right] \right\} \\ &= -2\kappa_c a \left[\frac{\partial \bar{s}_c}{\partial n} \right], \end{aligned} \quad (8.7)$$

where n_x and n_y are the x and y component of the unit normal vector of the leaf surface. Equation 8.7 states that the volume mean Laplacian of \bar{s}_c is proportional to the volume mean inner product of the \bar{s}_c gradient vector at the leaf surface and the unit normal vector of the surface. The inner product is equivalent to the \bar{s}_c gradient in the direction of the normal vector, expressed as $\partial \bar{s}_c / \partial n$.

Therefore, the *canopy CO₂ source term* is given by

$$\bar{S}_{c,p} = -2\bar{\rho}_d \kappa_c a \left[\frac{\partial \bar{s}_c}{\partial n} \right]. \quad (8.8)$$

This source term has the dimensions of $\text{kg m}^{-3}\text{s}^{-1}$ (Problem 8.1). The first subscript c denotes CO₂ as usual, and the additional subscript p reminds us that the source is associated with plant elements and unrelated to the free-air source discussed in Chap. 2.

Canopy volume averaging should be applied to the water vapor conservation equation and the energy conservation equation. Arising from the averaging operation are the *canopy water vapor source term*,

$$\bar{S}_{v,p} = -2\bar{\rho}_d \kappa_v a \left[\frac{\partial \bar{s}_v}{\partial n} \right], \quad (8.9)$$

and the *canopy sensible heat source term*

$$\bar{S}_{T,p} = -2\kappa_T a \left[\frac{\partial \bar{T}}{\partial n} \right]. \quad (8.10)$$

The vapor source term has the dimensions of $\text{kg m}^{-3}\text{s}^{-1}$, and the heat source term has the dimensions of K s^{-1} .

The canopy source terms can be understood with the example of a green leaf exposed to sunlight, as shown in Fig. 8.1. The situation depicted in this figure may be regarded as the composite of multiple leaves enclosed in an averaging volume. The leaf is enveloped by a thin boundary layer, in which diffusion is molecular. Because of photosynthesis, the CO₂ mixing ratio is lower at the surface than outside the boundary layer, resulting in a positive CO₂ mixing ratio gradient $\partial \bar{s}_c / \partial n$ in the leaf boundary layer. The corresponding source term $\bar{S}_{c,p}$ is negative according to Eq. 8.8, indicating removal of CO₂ from the atmosphere. If the removal rate increases, the gradient will become larger. In contrast, the vapor mixing ratio gradient $\partial \bar{s}_v / \partial n$ and the temperature gradient $\partial \bar{T} / \partial n$ are negative in the leaf boundary layer. The vapor source term $\bar{S}_{v,p}$ and the heat source term $\bar{S}_{T,p}$ are positive according to Eqs. 8.9 and 8.10, indicating release of water vapor and heat by the leaf to the atmosphere.

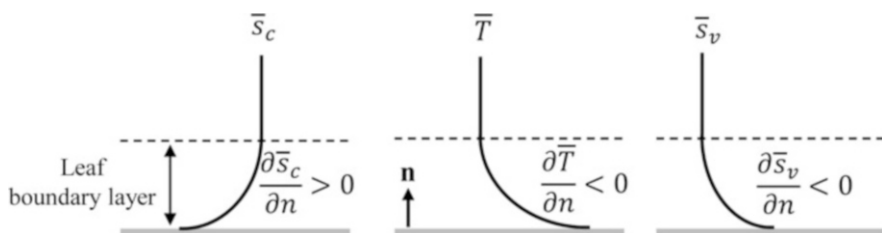


Fig. 8.1 Distribution of the CO₂ mixing ratio (\bar{s}_c), air temperature (T), and the water vapor mixing ratio (\bar{s}_v) across the boundary layer of a photosynthesizing and evaporating leaf. The unit normal vector of the leaf surface is denoted by \mathbf{n} . The vertical scale is exaggerated

For convenience of presentation, from now on we will drop the volume averaging operator [], but we should remember that all Reynolds quantities in the canopy have undergone volume averaging operation. The conservation Eq. 8.1 is rewritten as

$$\frac{\partial \bar{s}_c}{\partial t} + \bar{u} \frac{\partial \bar{s}_c}{\partial x} + \bar{v} \frac{\partial \bar{s}_c}{\partial y} + \bar{w} \frac{\partial \bar{s}_c}{\partial z} = \frac{\bar{S}_{c,p}}{\bar{\rho}_d} - \left(\frac{\partial \bar{u}' s'_c}{\partial x} + \frac{\partial \bar{v}' s'_c}{\partial y} + \frac{\partial \bar{w}' s'_c}{\partial z} \right). \quad (8.11)$$

Equations 8.8, 8.9, 8.10, and 8.11 suggest two approaches to quantifying surface- or ecosystem-air exchanges. In the first approach, parameterizations of the concentration and the temperature gradients at the leaf surface are developed from leaf biochemical and energy balance constraints. These gradient quantities are combined with information on canopy morphology and solar radiation transfer to predict the source strength. The basis for this approach is Eqs. 8.8, 8.9, and 8.10. The second approach determines the total ecosystem source strength as a residual from the other terms in Eq. 8.11, using atmospheric measurements of concentration and velocities in and above the ecosystem. In this chapter, we focus exclusively on the second approach, leaving parameterization of the source terms to Chap. 10.

8.3 The Concept of Net Ecosystem Exchange

The concept of net ecosystem exchange emphasizes whole-ecosystem behaviors instead of detailed knowledge of the source strength at different heights or of individual plant elements in the ecosystem. After all, it is the net ecosystem exchange, not the exchange with individual foliage layers, that constitutes the lower boundary condition for atmospheric models. Integrated over seasonal and annual time scales, the net exchange is an important quantity of ecosystem water and carbon budgets.

The net ecosystem exchange of CO₂ with the atmosphere is defined as the vertical integral of the CO₂ source term,

$$\text{NEE} \equiv \int_0^h \bar{S}_{c,p} dz', \quad (8.12)$$

where h is canopy height. It is understood that the contribution of the ground-level source is included in the integral. The definition follows the usual micrometeorological sign convention: a positive NEE indicates that the ecosystem is a net source of atmospheric CO₂ and a negative NEE indicates a net sink.

Similarly, the net ecosystem exchange of water vapor or the whole-ecosystem evapotranspiration rate and the net ecosystem exchange of sensible heat are given as

$$E \equiv \int_0^h \bar{S}_{v,p} dz', \quad (8.13)$$

and

$$H \equiv \int_0^h \bar{\rho}_d c_p \bar{S}_{T,p} dz'. \quad (8.14)$$

Also referred to as the surface source strength elsewhere in the book (i.e., the Q term in Eq. 7.54), these integrals can vary with horizontal position despite the canopy volume averaging operation, especially in patchy landscapes.

8.4 The Chamber Method

The canopy chamber offers the simplest demonstration on how mass conservation is used to quantify the NEE. Consider first a rectangular-shaped closed chamber made of airtight materials (Fig. 8.2a). No air can exit or enter the chamber, and no diffusion exchange of CO₂ is possible between the interior air and the ambient air. The CO₂ released by the ecosystem cannot go anywhere else except to accumulate in the space enclosed by the chamber. The mass conservation Eq. 8.11 is reduced to a simple balance between the time rate of concentration change and the source term:

$$\frac{\partial \bar{s}_c}{\partial t} = \frac{\bar{S}_{c,p}}{\bar{\rho}_d}. \quad (8.15)$$

Integration of this equation with respect to z through the chamber column yields

$$\text{NEE} = \bar{\rho}_d d \frac{\partial \bar{s}_{c,c}}{\partial t}, \quad (8.16)$$

where $\bar{s}_{c,c}$ is the chamber column mean CO₂ mixing ratio and d is chamber height ($d > h$). In actual field deployments, the air inside the chamber is usually well mixed

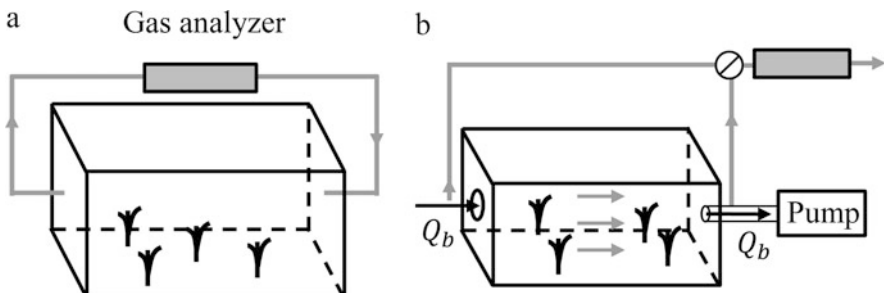


Fig. 8.2 A closed (a) and a dynamic canopy chamber (b) for measuring the net ecosystem exchange

with ventilation fans, and the mixing ratio is measured with a gas analyzer connected to the chamber in a closed loop through which a small stream of air is circulated. Measuring time change of the concentration is sufficient for the determination of the NEE.

A dynamic chamber (Fig. 8.2b) allows air to enter and exit the chamber space at a volume base flow rate of Q_b (in $\text{m}^3 \text{s}^{-1}$). Once again, no diffusion exchange is possible through the chamber walls. In steady state, the mass conservation equation is reduced to a balance between the horizontal advection term and the source term:

$$\bar{u} \frac{\partial \bar{s}_c}{\partial x} = \frac{\bar{S}_{c,p}}{\rho_d}, \quad (8.17)$$

where \bar{u} is the mean flow velocity in the chamber generated by the base flow and $\partial \bar{s}_c / \partial x$ is horizontal gradient in the CO₂ mixing ratio in the chamber. Our chamber is rectangular in shape. Let A_c and A_b be the chamber cross-sectional area and the basal area, respectively, and l and d be its length and height, respectively. Vertical integration of Eq. 8.17 yields

$$\text{NEE} = \bar{\rho}_d \bar{u} d \frac{\partial \bar{s}_{c,c}}{\partial x}. \quad (8.18)$$

Noting that

$$A_c L = A_b d, \quad \bar{u} = \frac{Q_b}{A_c}, \quad \frac{\partial \bar{s}_{c,c}}{\partial x} \simeq \frac{\bar{s}_{c,o} - \bar{s}_{c,i}}{L}$$

we obtain from Eq. 8.18

$$\text{NEE} = \bar{\rho}_d \frac{Q_b}{A_b} (\bar{s}_{c,o} - \bar{s}_{c,i}), \quad (8.19)$$

where $\bar{s}_{c,o}$ and $\bar{s}_{c,i}$ denote the CO₂ mixing ratio at the chamber outlet and inlet, respectively. Measurement of $\bar{s}_{c,o}$ and $\bar{s}_{c,i}$ is accomplished with a gas analyzer interfaced with a three-way valve which connects the analyzer alternately to the inlet or the outlet air. Equation 8.19 states that in steady state, the amount of CO₂ released by the ecosystem over the chamber basal area A_b is equal to the difference between the amount of CO₂ coming out of the chamber outlet and the amount entering the chamber through its inlet.

The chamber method is more versatile than micrometeorological methods. Flux chambers are portable, allowing easy installation and spatial replications. They do not require extensive, uniform, and leveled experimental fields. Specifications required of the sensor are considerably less stringent. Changes in the CO₂ mixing ratio, either in time (Fig. 8.2a) or between the chamber inlet and outlet (Fig. 8.2b), are usually large, so they can be resolved with an analyzer of low measurement precision. But the same analyzer may have difficulty resolving the vertical concentration gradient in the surface layer for use in the flux-gradient method

(Problem 8.7). The analyzer does not need to have a fast time response, which is a prerequisite for eddy covariance applications. For these reasons, fluxes in plot-scale and manipulative experiments are often measured with chambers.

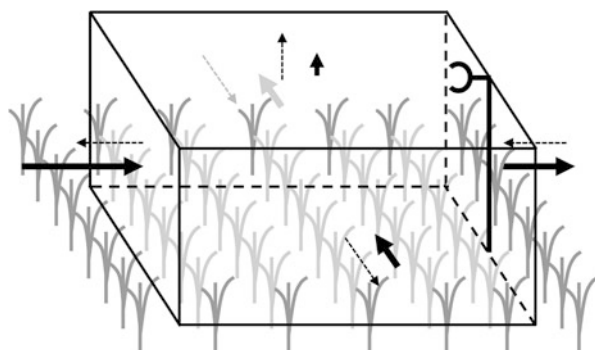
The chamber method has a number of shortcomings. It is labor-intensive, cannot measure the sensible heat exchange, and is impractical for tall ecosystems. The microclimate in the chamber is different from the ambient one, calling into question whether the measured NEE represents the exchange of the ecosystem in unperturbed conditions. Because the chamber has a small footprint, measurement at a single location does not necessarily capture the mean state of the whole ecosystem.

8.5 The Eddy Covariance Control Volume

We use a *control volume* to illustrate the principle of the eddy covariance method (Fig. 8.3). The control volume can be considered as a giant chamber. But unlike a real chamber, its walls, which are imagined, permit the air to flow through without any hindrance. The top face of the volume is at the height of the eddy covariance sensor and is parallel to the local terrain surface. The NEE is calculated as the sum of CO₂ buildup inside the volume and the net CO₂ input into the volume through its top and side faces. Because the volume is large enough to fully encompass the flux footprint, eddy covariance is a true ecosystem-scale methodology.

The eddy covariance control volume should not be confused with the other two air volume concepts discussed in the previous chapters (Fig. 8.4). In Chap. 2, a small rectangular prism was used to help establish the mass conservation equations at a point (Fig. 2.2). At a microscale, the fluid parcel enclosed by the prism contains a large number of molecules because its dimensions are much greater than the molecular free path. At a macroscale, the fluid parcel is much smaller than the smallest turbulent eddies and represents essentially a single point in the flow domain. By comparison, a canopy averaging volume (Fig. 5.1) is larger, enclosing numerous fluid parcels and a sufficient number of plant elements so that stable and continuous canopy flow properties, such as the plant area density, the canopy drag force, and the canopy CO₂ source strength, are produced. However, this averaging volume is still much smaller than the eddy covariance control volume.

Fig. 8.3 Control volume over the flux footprint of an eddy covariance system. Solid arrows indicate mass transport associated with the mean flow velocities and dashed arrows indicate eddy diffusion fluxes



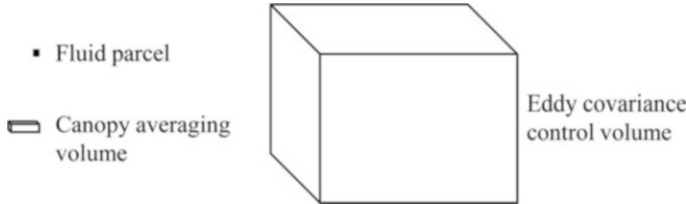


Fig. 8.4 Comparison of three conceptual air volumes at three different scales

Integrating Eq. 8.11 with respect to height and keeping the NEE term on one side and moving all the atmospheric terms to the other side of the conservation equation, we obtain

$$\text{NEE} = \underbrace{\int_0^z \bar{\rho}_d \frac{\partial \bar{s}_c}{\partial t} dz'}_{\text{I}} + \underbrace{\bar{\rho}_d \bar{w}' \bar{s}'_c}_{\text{II}} + \underbrace{\int_0^z \bar{\rho}_d \bar{u} \frac{\partial \bar{s}_c}{\partial x} dz'}_{\text{III}} + \underbrace{\int_0^z \bar{\rho}_d \bar{w} \frac{\partial \bar{s}_c}{\partial z} dz'}_{\text{IV}} + \underbrace{\int_0^z \bar{\rho}_d \frac{\partial \bar{u}' \bar{s}'_c}{\partial x} dz'}_{\text{V}}, \quad (8.20)$$

(Paw et al. 2000; Leuning 2007; Lee and Massman 2011), where the eddy covariance measurement height z is greater than the canopy height h . For simplicity but without loss of generality, this equation is expressed in the micrometeorological coordinate, so all the terms involving the lateral velocity are omitted. Terms on the right side of the equation are storage (Term I), eddy flux (Term II), horizontal advection (Term III), vertical advection (Term IV), and horizontal flux divergence (Term V).

The *storage term* expresses the rate of CO₂ accumulation or depletion in the control volume. It would be equal to the NEE if no CO₂ were allowed to enter or leave the control volume by advection and by turbulent diffusion, similar to the situation of a closed chamber. In actual field observations, the storage term is a minor component of the CO₂ budget except at transitional times of the day when the time rate of concentration change is large, such as at sunrise and at sunset. The diurnal mean value is usually negligible.

The eddy covariance term represents the *eddy flux* of CO₂ through the top face of the control volume. The schematic in Fig. 8.5 explains why the covariance between the vertical velocity and the CO₂ concentration is equivalent to a vertical flux. In this example, the CO₂ density ρ_c is 800 mg m⁻³, and the vertical velocity is 0.5 m s⁻¹. At time $t = 0$ s, an air parcel, which is a cube with sides of 1 m, lay immediately beneath the top plane of the control volume. A second later, the parcel has risen by 0.5 m. In the short interval of 1 s, half of the CO₂ in the cube, or 400 mg, has moved across a portion of the plane whose area is 1 m². Since the flux is defined as the mass

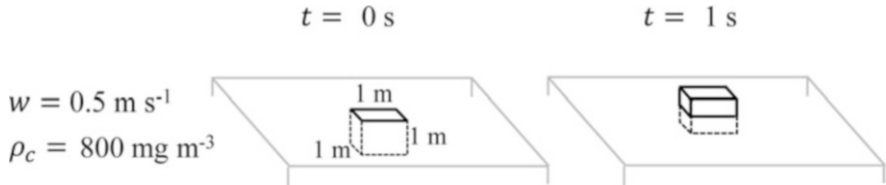


Fig. 8.5 Instant CO₂ flux through the top plane of an eddy covariance control volume caused by upward motion of an air parcel. The parcel's CO₂ density is 800 mg m⁻³ and its vertical velocity is 0.5 m s⁻¹

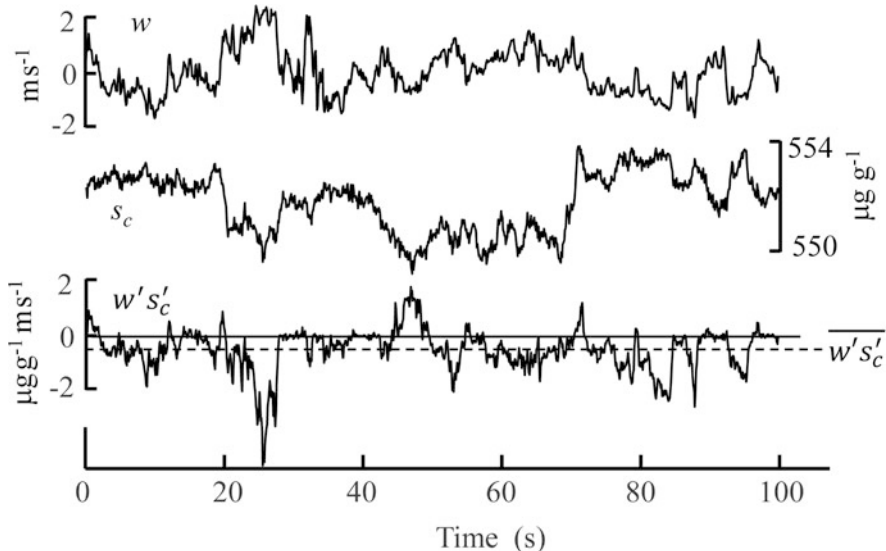


Fig. 8.6 High-frequency time series of the vertical velocity w and the CO₂ mixing ratio s_c and the product of the velocity and the mixing ratio fluctuations $w' s'_c$. The *dashed line* denotes the $w - s_c$ covariance for the time period indicated

per unit area per unit time, the instant flux resulting from the parcel movement is 400 mg m⁻² s⁻¹. More generally, the instant flux is expressed as $w\rho_c$. The average flux is then $\overline{w\rho_c}$, which can be expressed as the sum of the $w - \rho_c$ covariance and an advection flux,

$$\overline{w\rho_c} = \overline{w'\rho'_c} + \overline{w}\overline{\rho_c}, \quad (8.21)$$

according to the Reynolds averaging rules. Provided that the mean vertical velocity \overline{w} is zero, the average flux is equal to the covariance.

In the above illustration (Fig. 8.5), the flux is determined with the CO₂ mass density. We will show later in Chap. 9 that fluctuations in the dry air density cause an artificial CO₂ flux that is unrelated to the net ecosystem exchange. The artifact is avoided if the flux is calculated with the mass mixing ratio s_c , as in Term II of Eq. 8.20. A sample w and s_c time series and their covariance are given in Fig. 8.6.

The *horizontal advection* term describes the advection flux of CO₂ into and out of the control volume via its sides. The advection flux, or the amount of CO₂ carried by the mean wind through a unit cross-sectional area per unit time, is given by $\bar{\rho}_d \bar{u} \bar{s}_c$. If the flow is hypothetically in steady state and the flux at the top face is zero, the mean NEE in the along-wind direction would have to be balanced by the net advection flux,

$$\begin{aligned} \frac{1}{L} \int_0^L (\text{NEE}) dx' &= \frac{1}{L} \int_0^L \int_0^z \bar{\rho}_d \bar{u} \frac{\partial \bar{s}_c}{\partial x} dz' dx' \\ &= \frac{1}{L} \left\{ \int_0^z \bar{\rho}_d \bar{u} \bar{s}_c dz' \Big|_{x=L} - \int_0^z \bar{\rho}_d \bar{u} \bar{s}_c dz' \Big|_{x=0} \right\}, \end{aligned} \quad (8.22)$$

where L is the along-wind dimension of the control volume. Equation 8.22 resembles the mass conservation Eq. 8.19 for a dynamic chamber and can be interpreted similarly. It states that if all other terms were negligible, the net ecosystem exchange would be proportional to the difference in the total advection flux through the downwind face, which is akin to the chamber outlet, and that through the upwind face, which is akin to the chamber inlet, of the control volume. In actual field observations, the difference is very small in magnitude, often falling below instrument detection limits (Problem 8.19).

The vertical advection flux is given by $\bar{\rho}_d \bar{w} \bar{s}_c$. The flux is always zero at the ground surface but can be non-zero at the top of the control volume. *Vertical advection* exists if the mean flow is not horizontally homogeneous. Mass conservation of air requires that any horizontal flow divergence should be balanced by a non-zero mean vertical velocity.

Horizontal flux divergence expresses the CO₂ input into the control volume by turbulent diffusion through its sides. The mean divergence rate is found by integrating the term with respect to x

$$\frac{1}{L} \int_0^L \int_0^z \bar{\rho}_d \frac{\partial \bar{u}' \bar{s}'_c}{\partial x} dz' dx' = \frac{1}{L} \left\{ \int_0^z \bar{\rho}_d \bar{u}' \bar{s}'_c dz' \Big|_{x=L} - \int_0^z \bar{\rho}_d \bar{u}' \bar{s}'_c dz' \Big|_{x=0} \right\}, \quad (8.23)$$

The first and second terms in the curly brackets represent the total horizontal eddy flux at the downwind side and that at the upwind side of the control volume, respectively.

The above formalistic analysis of Eq. 8.20 seems to encourage simultaneous measurement of the advection flux and the turbulent flux on all the five sides of the control volume. Such an experimental strategy, which has been attempted by some research groups (Aubinet et al. 2010), is however prohibitively expensive. Nor does it necessarily yield accurate NEE estimation because no perfectly matched sensors are available for measuring the net advection between opposite sides of the control volume. These logistical limitations force us to deploy just one tower at one location. With sensors mounted on the tower, we are able to measure the vertical eddy flux at the top of the control volume and the storage term. The horizontal

advection and the horizontal flux divergence term cannot be determined, but by placing the tower in an extensive, uniform, and leveled field, they are assumed, along with the vertical advection term, to be negligible. To put the assumption differently, advection and horizontal diffusion are not the pathways that supply the CO₂ taken up by the ecosystem in the control volume. Instead, the uptake is supported by the CO₂ stored in the volume and the CO₂ that diffuses downward through the top face of the volume. Conversely, the CO₂ released by the ecosystem either remains in the volume or escapes by turbulent diffusion to the air layer above the volume.

8.6 Eddy Covariance in Advection-Free Conditions

In the absence of horizontal and vertical advection and horizontal flux divergence, Eq. 8.20 is simplified to

$$\text{NEE} = \int_0^z \bar{\rho}_d \frac{\partial \bar{s}_c}{\partial t} dz' + \bar{\rho}_d \overline{w' s'_c}. \quad (8.24)$$

Equation 8.24 is the basis for the single-tower eddy covariance measurement strategy.

Similarly, the operational expressions that relate eddy covariance measurements to the net ecosystem water vapor and sensible heat exchange are

$$E = \int_0^z \bar{\rho}_d \frac{\partial \bar{s}_v}{\partial t} dz' + \bar{\rho}_d \overline{w' s'_v}, \quad (8.25)$$

and

$$H = \int_0^z \bar{\rho}_d c_p \frac{\partial \bar{T}}{\partial t} dz' + \bar{\rho}_d c_p \overline{w' T'}, \quad (8.26)$$

In the derivation of Eq. 8.26, we have omitted a few additional terms in connection with the pressure force in the energy conservation Eq. 2.22. Applying Reynolds averaging first and canopy volume averaging next on Eq. 2.22 and ignoring heat advection and horizontal heat flux divergence, we obtain the one-dimensional volume mean energy conservation equation:

$$\bar{\rho}_d c_p \left(\frac{\partial \bar{T}}{\partial t} + \frac{\partial \overline{w' T'}}{\partial z} \right) = \frac{\partial \bar{p}}{\partial t} + \bar{\rho}_d C_d a \bar{u}^3 + \frac{\partial \overline{w' p'}}{\partial z} + \bar{\rho}_d c_p \bar{S}_{T,p}. \quad (8.27)$$

The second term on the right side of the equation, which is a consequence of volume averaging of the horizontal pressure gradient $\partial \bar{p}'' / \partial x$, represents the heat generated by air parcel compression. As you may recall, the pressure gradient $\partial \bar{p}'' / \partial x$ is generally positive in the canopy air pockets (Fig. 5.2). As an air parcel

moves between two adjacent plant elements, the rise in pressure will cause it to become slightly compressed and its temperature to increase. Integration of Eq. 8.27 with respect to z yields

$$H = \underbrace{\int_0^z \bar{\rho}_d c_p \frac{\partial \bar{T}}{\partial t} dz'}_{\text{I}} + \underbrace{\bar{\rho}_d c_p \bar{w}' \bar{T}'}_{\text{II}} - \underbrace{\int_0^z \frac{\partial \bar{p}}{\partial t} dz'}_{\text{III}} - \underbrace{\int_0^z \bar{\rho}_d C_d \bar{a} \bar{u}^3 dz'}_{\text{IV}} - \underbrace{\bar{w}' \bar{p}'}_{\text{V}} . \quad (8.28)$$

In this equation, Term I and Term II are the familiar storage and eddy flux terms. Term III is on the order of 0.05 W m^{-2} and can be omitted. The pressure flux $\bar{w}' \bar{p}'$ (Term V) varies in the range of 0 to -8 W m^{-2} , with an annual mean value of -0.6 W m^{-2} according to a field experiment in a temperate forest (Zhang et al. 2011). The compression heat term (Term IV) is on the same order of magnitude as but is in opposite sign to Term V (Problem 8.12). This order-of-magnitude analysis shows that Eq. 8.26 is a very good approximation for Eq. 8.28.

The net ecosystem exchanges of sensible heat and water vapor must satisfy the surface energy balance Eq. 2.47. In advection-free conditions, the equation can be expressed as

$$R_n - G - \left\{ Q_s + \int_0^z \bar{\rho}_d c_p \frac{\partial \bar{T}}{\partial t} dz' + \lambda \int_0^z \bar{\rho}_d \frac{\partial \bar{s}_v}{\partial t} dz' \right\} = \bar{\rho}_d c_p \bar{w}' \bar{T}' + \lambda \bar{\rho}_d \bar{w}' \bar{s}'_v . \quad (8.29)$$

This form of the surface energy balance equation is attractive to experimentalists because all the terms can be measured directly and independently. The group in the curly brackets is the total ecosystem heat storage, including sensible heat storage in the biomass, the top soil and the air column below the eddy covariance sensor, and latent heat storage in the air column. Equation 8.29 is often used as a check on eddy covariance data quality. A large energy imbalance, or that the sum of the measured sensible heat flux and latent heat flux on the right side of the equation is biased too low in comparison to the available energy expressed on the left side of the equation, suggests instrument performance issues or that the site does not meet the criteria – extensive, uniform, leveled – required for eddy covariance application.

8.7 Vertical Advection

Eddy covariance measurements can be adversely affected by horizontal inhomogeneity in the flow field and in the concentration field. The first type of inhomogeneity causes vertical advection, whereas the second type causes horizontal advection. Flow inhomogeneity cannot be totally avoided because no ideal sites (horizontally uniform and perfectly flat) exist. Even if a site is large enough by micrometeorological standards, it may still be influenced by flow patterns driven by land surface heterogeneity at scales larger than the scale of the flux footprint.

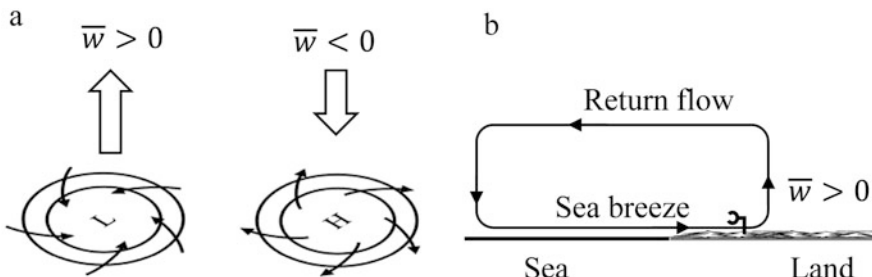
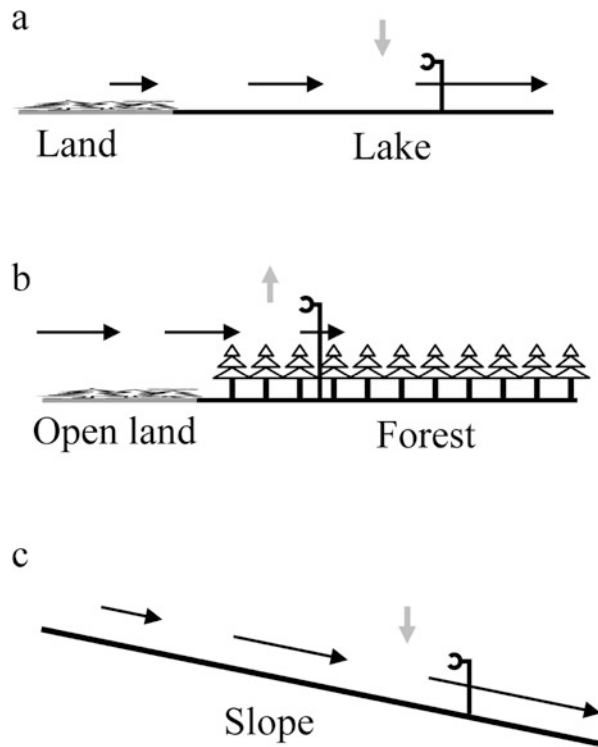


Fig. 8.7 Non-zero mean vertical velocity associated with circulation patterns much larger than the scale of the eddy covariance control volume: (a) bird's-eye view of flow in a synoptic scale low- (L) and high (H)-pressure weather system; (b) cross-sectional view of a mesoscale sea breeze circulation

Fig. 8.8 Nonzero mean vertical velocity associated with local-scale disturbances: (a) flow transition from a land to a lake surface; (b) flow transition at a forest edge; (c) drainage flow on sloped terrain



Figures 8.7, 8.8, and 8.9 depict a few scenarios of flow inhomogeneity over a range of scales. Table 8.1 provides order-of-magnitude estimates of the mean vertical velocity associated with these flow patterns. Mesoscale thermal circulations, such as the sea/lake breeze, and synoptic weather systems (high pressure and low pressure) occur at scales much greater than the scale of the eddy covariance footprint

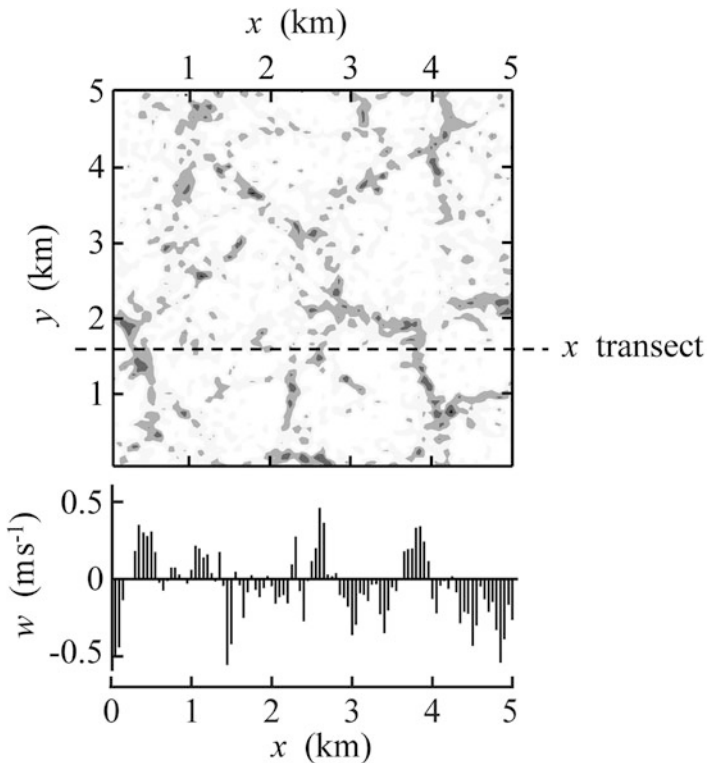


Fig. 8.9 Instant vertical velocity in stationary convection cells simulated by a large-eddy simulation model: a horizontal section of the vertical velocity field at the height of 40 m above the ground (top); vertical velocity along a transect in the x direction shown in the top panel (bottom). Shaded regions indicate ascending motion ($w > 0$)

Table 8.1
Order-of-magnitude estimate
of the mean vertical velocity
in the atmospheric surface
layer

Flow type	Mean vertical velocity (m s^{-1})
Synoptic subsidence	-1×10^{-4}
Sea/lake breeze	1×10^{-3}
Drainage flow	-1×10^{-2}
Forest edge inflow	1×10^{-2}
Stationary convection cell	$\pm 5 \times 10^{-2}$

and the control volume. Transitional flow near a land-lake boundary or at a forest edge and drainage flow on sloped terrain are similar in scale to the control volume.

In convection cells in the daytime atmospheric boundary layer, ascending motion is confined to walls surrounding columns of descending motion, at a horizontal scale of 1–2 km (Fig. 8.9). Under low wind conditions, these *turbulent organized structures* tend to be stationary. The vertical velocity at the measurement tower, even after

time averaging, does not vanish. Several large-eddy simulation studies conclude that under these conditions, an eddy covariance instrument will underestimate the true NEE, leading to an imbalance of the surface energy (e.g., Kanda et al. 2004).

One method to correct the influence of vertical advection is to simply add the vertical advection flux $\bar{\rho}_d \bar{w} \bar{s}_c$ to the right side of Eq. 8.24, on the ground that the advection flux is part of the total vertical flux. The problem with this method is that the advection flux is too large: it is not negligible (approximately $1.5 \mu\text{mol CO}_2 \text{ m}^{-2} \text{ s}^{-1}$) even at an extremely small \bar{w} of $1 \times 10^{-4} \text{ m s}^{-1}$ expected of synoptic weather systems (Table 8.1). The “corrected” NEE would be in serious error.

The appropriate approach to handling vertical advection requires manipulation of the advection term (Term IV, Eq. 8.20). With the help of a linear approximation for the mean vertical velocity,

$$\bar{w}(z') = \frac{z'}{z} \bar{w}(z), \quad (8.30)$$

this term becomes

$$\int_0^z \bar{\rho}_d \bar{w} \frac{\partial \bar{s}_c}{\partial z} dz' = \bar{\rho}_d \bar{w} (\bar{s}_c - \langle \bar{s}_c \rangle), \quad (8.31)$$

where $\langle \bar{s}_c \rangle$ is the column mean mixing ratio below the eddy covariance measurement height,

$$\langle \bar{s}_c \rangle = \frac{1}{z} \int_0^z \bar{s}_c dz'. \quad (8.32)$$

The NEE equation accounting for vertical advection is written as

$$\text{NEE} = \int_0^z \bar{\rho}_d \frac{\partial \bar{s}_c}{\partial t} dz' + \bar{\rho}_d \bar{w}' \bar{s}_c' + \bar{\rho}_d \bar{w} (\bar{s}_c - \langle \bar{s}_c \rangle), \quad (8.33)$$

(Lee 1998). In other words, the NEE calculated from the standard eddy covariance (Eq. 8.24) has a bias error represented by $\bar{\rho}_d \bar{w} (\bar{s}_c - \langle \bar{s}_c \rangle)$.

Figure 8.10 illustrates why the vertical advection flux $\bar{\rho}_d \bar{w} \bar{s}_c$ is an overestimate of the contribution of flow inhomogeneity to the CO_2 mass balance of the control volume. Let us suppose that \bar{w} is negative and that the CO_2 concentration decreases with increasing height. To satisfy the continuity requirement, the negative \bar{w} must be balanced by a horizontal flow divergence. The air entering the volume from above carries less CO_2 than the air moving out from the sides by divergence, causing a net depletion of CO_2 . But the net depletion is much smaller in magnitude than the vertical advection flux itself because the former is proportional to the difference between the CO_2 mixing ratio at the eddy covariance height and the column mean value below the height.

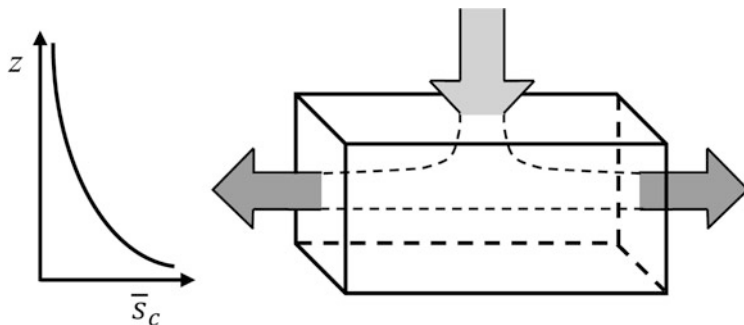


Fig. 8.10 Compensation of downward motion by horizontal flow divergence

Correction for vertical advection is rarely done to hourly eddy covariance data because of the lack of accurate enough measurement of \bar{w} . Nevertheless, several robust inferences can be made from Eq. 8.33. First, the vertical advection of CO₂ is more severe at night than during the day because the vertical CO₂ gradient $\bar{s}_c - \langle \bar{s}_c \rangle$ is greater in magnitude under stable conditions than under unstable conditions. The diurnal asymmetry is a source of systematic bias error in the NEE averaged over the daily cycle or longer periods.

Second, we should avoid placing the measurement tower near flow obstacles and abrupt changes in surface roughness. The forest edge is a case in point. In the forest edge inflow (Fig. 8.8b), a persistently positive \bar{w} is expected due to flow convergence arising from deceleration of the air motion, leading to large advection effects on both daytime and nighttime measurements. It has been reported that the eddy CO₂ flux measured in the forest edge inflow at night is biased too high, sometimes to the extent that it is biologically unreasonable, in comparison to the true ecosystem respiration rate.

Third, drainage flow at night is especially problematic for eddy covariance applications. Under conditions of low wind and clear skies, drainage flow can develop even at a site with a local terrain slope as small as one part per thousand. By the continuity requirement, the divergence along the slope due to gravitational acceleration must be compensated by a downward air motion (Fig. 8.8c). The conditions that are conducive to the formation of drainage flow also promote large accumulation of CO₂ near the ground. When these occur, the eddy covariance measurement (Eq. 8.24) will severely underestimate the true NEE. (Keep in mind that the nighttime NEE describes ecosystem respiration and is positive according to the micrometeorological sign convention.)

Extending the results to sensible heat and water vapor exchanges, we have

$$E = \int_0^z \bar{\rho}_d \frac{\partial \bar{s}_v}{\partial t} dz' + \bar{\rho}_d \bar{w}' \bar{s}'_v + \bar{\rho}_d \bar{w} (\bar{s}_v - \langle \bar{s}_v \rangle), \quad (8.34)$$

and

$$H = \int_0^z \bar{\rho}_d c_p \frac{\partial \bar{T}}{\partial t} dz' + \bar{\rho}_d c_p \bar{w}' \bar{T}' + \bar{\rho}_d c_p \bar{w} (\bar{T} - \langle \bar{T} \rangle). \quad (8.35)$$

These equations are a useful tool for energy balance diagnosis (Problem 8.14).

Equation 8.30 implies that horizontal flow divergence is invariant with height in the surface layer (Eq. 3.18). It is accurate for large flow patterns (Fig. 8.7) but is only approximate for disturbed flows having a scale on the order of the size of the eddy flux footprint (e.g., Fig. 8.8). According to some observational studies, a local disturbance to the flow field can introduce a horizontal concentration gradient so that horizontal advection effects must also be included in the budget equation (Aubinet et al. 2010).

8.8 Horizontal Advection

Horizontal advection represents the contributions of horizontal transport by the mean flow and horizontal diffusion to the mass balance of the eddy covariance control volume. In order for this to occur, there must exist a horizontal concentration gradient, which generally arises from horizontal variations in the source strength. Irrigated farms surrounded by dry land, shoreline areas of a lake, and transitional zones between a wheat field and a rice paddy are examples where horizontal variations in the exchanges of heat, water vapor, and carbon dioxide may be important.

Direct measurement of horizontal advection is much more difficult than the measurement of vertical advection because the former requires deployment of wind sensors and gas analyzers at multiple horizontal locations. If the wind direction is known ahead of the time and is very steady, a pair of towers, positioned at the upwind and the downwind sides of the volume, may suffice. The net advection flux is determined by paired measurements of the horizontal wind speed and the mean concentration (Eq. 8.22). The towers should be separated by a long enough distance to allow a measurable concentration difference to develop between them, but not too long so that gas sampling tubes are not overly extended. Even with a large separation distance, however, the required instrument precision may be unattainable (Problem 8.19). In actual field campaigns, an array of towers arranged in a gridded pattern, instead of just two towers, are needed to account for wind directional shift with time and wind directional shear in plant canopies (Fig. 6.7).

Footprint theory can be used to investigate horizontal advection. To illustrate that horizontal advection and the flux footprint are two interrelated concepts, let us revisit the situation of a step change in surface source strength depicted in Fig. 7.10. The flow is horizontally homogeneous (i.e., no vertical advection) and is in steady state. Mass balance requires that the net ecosystem exchange be equal to the sum of the vertical eddy flux (Term II, Eq. 8.20) and horizontal advection (Term III, with Term V ignored). At a distance far away from the step change ($x \rightarrow \infty$), the advection effect vanishes, the flux footprint is totally confined to the source region being measured, and the measured vertical eddy flux is equal to the surface source strength or the net ecosystem exchange. But measurement locations in the vicinity of the step change are subject to the influence of horizontal advection, the extent of which is determined by the fraction of the footprint that extends beyond the target

region. The fractional contribution of horizontal advection to the local mass balance in this case is given by

$$a_H = 1 - \int_0^x f_1(x'; z) dx'. \quad (8.36)$$

If we adopt the one-dimensional footprint function given by Eq. 7.71 for neutral stability, Eq. 8.36 becomes

$$a_H = 1 - \exp\left(-\frac{z_u}{k_x^2}\right) \quad (8.37)$$

Equation 8.37 states that as *fetch*, or the distance between the instrument tower and the upwind edge of the field, increases, horizontal advection diminishes exponentially.

In the situation shown in Fig. 7.10, the source strength upwind of the target region is zero. The eddy flux bias error is known precisely: the ratio of the observed flux to the true NEE is equal to $1 - a_H$. In actual field experiments, the bias error can be higher or lower than $1 - a_H$ depending on the severity of source heterogeneity.

The discussion of horizontal advection is further aided by two related concepts. The *effective fetch* is the distance at which the fractional contribution a_H is no greater than a preset threshold (Gash 1986). A typical threshold value is 0.1. Flux measurement should ideally be carried out at this distance or further downwind of source discontinuity.

The *internal boundary layer* refers to the air layer in transitional adjustment to a new surface (Fig. 8.11). Several methods exist in the literature for determining the depth of the internal boundary layer as a function of fetch. For the purpose of eddy covariance applications, we recommend that the top of the internal boundary layer should correspond to the height at which a_H is at the threshold value of 0.1. The horizontal advection effect is reduced if the measurement takes place in the internal boundary layer. In Fig. 8.11, sensor A provides more accurate measurement of the surface-air exchange than sensor B because sensor B is located above the internal boundary layer and is subject to a greater influence of horizontal advection.

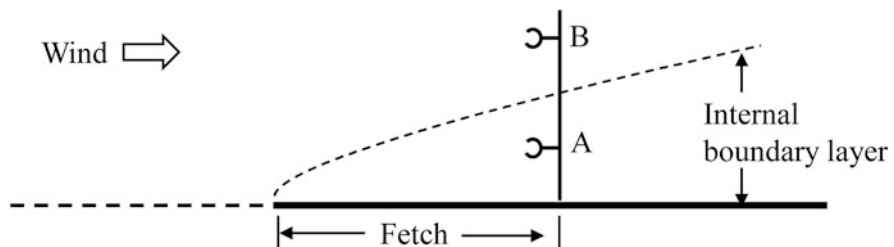


Fig. 8.11 Growth of the internal boundary layer over a new surface

Advection effects can arise from horizontal changes in the horizontal eddy flux (Eq. 8.23). The horizontal eddy flux is generally not zero, even in homogeneous flow, because of a mechanism that involves the vertical momentum transport. Consider the surface layer above a photosynthesizing canopy (Fig. 3.3). A downward moving eddy ($w' < 0$) brings air from aloft where the horizontal velocity is faster ($u' > 0$), contributing to a downward momentum transport. The same eddy is also more enriched in CO₂ ($s'_c > 0$) than the mean air at the measurement height. The net result is an indirect, and in this case positive, correlation between u and s_c through their covarying with w . Dimensional analysis yields

$$\overline{u's'_c} = \alpha_H \frac{\overline{u'w'} \overline{w's'_c}}{\overline{w'^2}}, \quad (8.38)$$

where the coefficient α_H is approximately 2.4 according to data obtained at a forest site. Because $\overline{u'w'}$ is negative in the surface layer, the horizontal eddy flux is opposite in sign to the vertical flux. If the vertical CO₂ flux is directed upward, the horizontal CO₂ flux will be directed against the mean wind direction (Fig. 8.3) and vice versa. The two fluxes are comparable in magnitude except in the free-convection limit at which $\overline{u's'_c}$ vanishes because there is no vertical momentum transport. In neutral stability, the ratio $\overline{u'w'}/\overline{w'^2}$ is about 0.65, and Eq. 8.38 indicates that the horizontal flux is 50% greater in magnitude than the vertical flux. Although the horizontal eddy flux itself can be quite large, its horizontal divergence is negligible in homogeneous to weakly heterogeneous flow.

8.9 Practical Considerations

A typical eddy covariance system consists of a three-dimensional anemometer, a temperature sensor, and a gas analyzer. An ideal system measures the velocities and the gas mixing ratio simultaneously and at the same point in space, has a fast enough time response for capturing contributions of all eddy motions and is mounted in perfect alignment relative to local terrain surface. Deviations from these ideal operating conditions constitute sources of measurement error that should be rectified either in pre-field hardware preparation phase or in post-field data analysis (Baldocchi et al. 1988; Aubinet et al. 2012).

- High-frequency loss: Neither the anemometer nor the gas analyzer is a single-point sensor. Instead, they measure small volumes of air. They cannot detect motion of eddies smaller than their measuring volumes. Characterized by high frequencies in the frequency domain, these eddies play a small but non-negligible role in the overall turbulent transport. Frequency loss also results from sensor separation whereby the gas analyzer is positioned at a short distance away from the anemometer to reduce its interference on the velocity measurement. With respect to closed-path eddy covariance, the concentration measurement takes

place in an enclosed optical cell to which the ambient air is drawn via a small tube. Some high-frequency fluctuations are lost by the time the air arrives at the cell.

- Time delay: In closed-path eddy covariance, the concentration measurement is delayed in reference to the velocity measurement due to the time the air sample spends in the sampling tube. Lack of time synchronization can also result from differences in response time between the anemometer and the gas analyzer and from sensor separation.
- Instrument tilt: It is difficult to level the anemometer perfectly in the field. Tilt errors also occur if the anemometer is leveled but the experimental site is not flat. The vertical velocity measured by a misaligned instrument no longer represents the true vertical motion in the atmosphere. Post-field coordinate rotation must be performed to remove the tilt error. After coordinate rotation, the $x-y$ plane should be parallel to the local terrain surface, and the y -axis should be perpendicular to the Reynolds mean wind vector (Fig. 2.1).
- Low-frequency contributions: Reynolds averaging is a high-pass filtering operation. Its cutoff frequency is roughly equal to the inverse of the averaging length T , meaning that contributions by large eddies whose frequency is smaller than $1/T$ are missed by the averaging process. A typical averaging length of 30–60 min is adequate for stable to moderately unstable conditions but may be too short in very unstable conditions when the eddy transport is dominated by large convection cells.
- Density effects: No gas analyzer can measure the mass mixing ratio directly. What is detected by the analyzer is the intensity of light absorption which is proportional to the mass density in its optical path. Eddy covariance based on the mass density measurement must be corrected for density effects because fluctuations in the gas mass density can result from fluctuations in the dry air mass density, the latter of which are unrelated to the ecosystem-atmosphere gaseous exchange. Correction for the density effects is the subject of the next chapter.

8.10 Problems

8.1 Show that the canopy CO₂ source term $\bar{S}_{c,p}$ has the dimensions of kg m⁻³s⁻¹.

8.2 Calculate the net ecosystem sensible heat exchange using Eqs. 8.10 and 8.14 under these conditions: the leaf temperature is 23.0 °C, the leaf boundary layer thickness is 2 mm, the air temperature outside the leaf boundary layer is 21.0 °C, the mean leaf area density is 0.20 m² m⁻³, the canopy height is 20.0 m, and the soil sensible heat source is negligible.

8.3 Consider a canopy water vapor source strength $\bar{S}_{v,p}$ profile given by

$$\bar{S}_{v,p} = \frac{0.1}{\sqrt{2\pi} \cdot 3} \exp\left[-\frac{(z - 15)^2}{2 \cdot 3^2}\right], \quad (8.39)$$

where $\bar{S}_{v,p}$ is in $\text{g m}^{-3} \text{s}^{-1}$ and z is height above the ground in m. What is the net ecosystem water vapor exchange? What is the corresponding latent heat flux?

8.4 A closed chamber of height 24 cm is used to measure the CO_2 flux of a forest soil. The CO_2 molar mixing ratio in the chamber is 402.1 ppm right after the chamber is placed on the soil and increases to 433.6 ppm 60 s later. The air temperature is 11.5 °C. What is the CO_2 flux?

8.5 An opaque Teflon box of dimensions 30 cm by 60 cm by 30 cm (width by length by height) is used to measure mercury emission of a forest soil. The bottom face of the box is removed. The box is placed on the soil surface. Air is drawn into the box through holes cut into the front at a base flow rate of 11.5 L min^{-1} . The ambient gaseous mercury concentration is 1.80 ng m^{-3} at STP (standard temperature and pressure), and the concentration of the chamber outlet air is 2.53 ng m^{-3} at STP. Determine the gaseous mercury flux. Express your result in $\text{ng m}^{-2} \text{ h}^{-1}$.

8.6 You want to determine the optimal flow rate for a dynamic flux chamber for measurement of the net ecosystem methane exchange of a rice paddy ecosystem. Your chamber has a basal area of 0.1 m^2 , and your analyzer has a precision of 2 ppb. The expected net exchange rate is $2 \mu\text{g CH}_4 \text{ m}^{-2} \text{ s}^{-1}$ according to the published literature. At a base flow rate of 50 L min^{-1} , can your analyzer resolve the concentration difference between the chamber outlet and the inlet. How should the flow rate be adjusted to reduce measurement error?

8.7 The nitrous oxide emission rate of a typical fertilized corn soil in the United States Midwest is $0.3 \text{ nmol m}^{-2} \text{ s}^{-1}$. You want to measure the emission with a dynamic chamber that has a basal area of 0.25 m^2 and a base flow rate of 10 L min^{-1} . How large is the expected concentration difference (in ppb) between the chamber outlet and the inlet? If you attempt to measure the emission with the flux-gradient method, how large do you expect the vertical concentration difference to be between the heights of 2.5 and 3.5 m above the ground? Assume that the canopy height is 2.0 m and the surface friction velocity is 0.25 m s^{-1} . Which of the two methods requires much better instrument precision?

8.8 The column mean CO_2 molar mixing ratio between the ground and the eddy covariance sensor height of 30 m is 380.1 ppm at 18:00 and 395.2 ppm at 24:00 on September 1 and 398.4 ppm at 06:00, 385.0 ppm at 12:00 and 380.2 ppm at 18:00 on September 2. Calculate the CO_2 storage term for periods between 18:00 and 24:00 on September 1 and between 18:00 on September 1 and 18:00 on September 2. Express your results in $\mu\text{mol m}^{-2} \text{ s}^{-1}$.

8.9 The mean air temperature and the water vapor mixing ratio in the air column below an eddy covariance system are 20.1°C and $17.2 \text{ mmol mol}^{-1}$ at 08:00 and increase to 20.6°C and $17.4 \text{ mmol mol}^{-1}$ at 09:00. Calculate the sensible and latent heat storage term in W m^{-2} for this time period. The eddy covariance measurement height is 2.4 m.

8.10 The eddy covariance terms are $\overline{w's'_c} = -0.732 \text{ ppm m s}^{-1}$, $\overline{w's'_v} = 0.203 \text{ mmol mol}^{-1} \text{ m s}^{-1}$, and $\overline{w'T'} = 0.176 \text{ K m s}^{-1}$. Assume that all other terms in the eddy covariance equations are negligible. What are the net ecosystem exchanges of CO₂ (in $\mu\text{mol m}^{-2} \text{ s}^{-1}$), water vapor (in $\text{mmol m}^{-2} \text{ s}^{-1}$), and sensible heat (in W m⁻²)?

8.11 Show that the pressure flux $\overline{w'p'}$ has the dimensions of W m⁻².

8.12 The plant area density is described by Eq. 5.46, the plant area index is 3.0, the canopy drag coefficient is 0.2, the wind profile is given by Eq. 5.27 ($\alpha_2 = 4.0$), and the wind speed at the top of the canopy is 1.5 m s⁻¹. Estimate the rate of heat generation by pressure compression in the canopy (Term IV, Eq. 8.28).

8.13 The landscape consists of two ecosystem types. Both are emitters of a tracer material to the atmosphere. The source strength of type I is N_1 and that of type II is N_2 . According to footprint theory, the vertical flux of the tracer should lie somewhere between N_1 and N_2 . However, the flux in the real world can fall outside the range bounded by N_1 and N_2 . Why?

8.14 Energy imbalance is defined as

$$I = R_n - G - \left\{ Q_s + \int_0^z \bar{\rho}_d c_p \frac{\partial \bar{T}}{\partial t} dz' + \lambda \int_0^z \bar{\rho}_d \frac{\partial \bar{s}_v}{\partial t} dz' \right\} - \left\{ \bar{\rho}_d c_p \overline{w'T'} + \lambda \bar{\rho}_d \overline{w's'_v} \right\}. \quad (8.40)$$

Assume that the imbalance is caused by vertical advection. Determine if I is likely positive or negative for each of the flow types listed in Table 8.1.

8.15 In the presence of drainage flow, is the ecosystem respiration determined with the standard eddy covariance Eq. 8.24 biased high or low? Provide an order-of-magnitude estimate of the bias error.

8.16 Assume that the mean vertical velocity at the eddy covariance measurement height is 0.01 m s⁻¹ in the daytime and -0.01 m s^{-1} at night. Using the data given in Fig. 8.12, estimate the contribution of vertical advection to the CO₂ budget of the eddy covariance control volume for 12:00 and 00:00. Is the daily mean NEE obtained from Eq. 8.24 biased high or low?

8.17 Repeat the calculations in Problem 8.16 but for sensible heat. How does the advection effect bias the daily mean ecosystem sensible heat exchange?

8.18 (a) Write an equation similar to Eq. 8.22 for horizontal heat advection. (b) Using the air temperature profile data given in Table 8.2, calculate the contribution of horizontal advection to the local heat budget at position B shown in Fig. 8.13. Assume that the wind profile is logarithmic with height, the friction velocity is 0.30 m s⁻¹, the surface momentum roughness is 0.05 m, and the eddy covariance measurement height is 2.0 m.

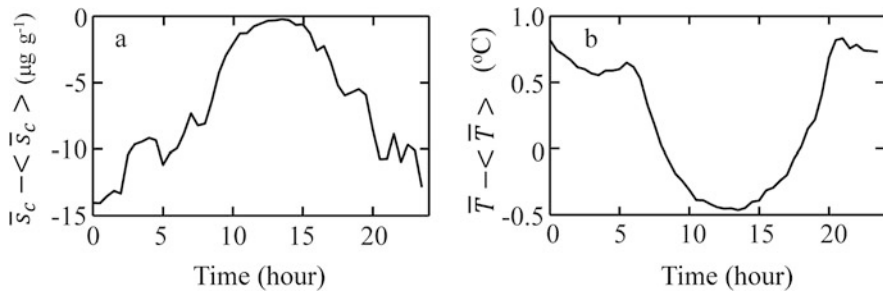


Fig. 8.12 Diurnal variations in the difference (a) between the CO₂ mixing ratio at the eddy covariance height (\bar{s}_e) and the column mean CO₂ mixing ratio below the height ($<\bar{s}_c>$) and (b) between the air temperature at the measurement height (\bar{T}) and the column mean temperature ($<\bar{T}>$) in a temperate forest during a growing season

Table 8.2 Air temperature (T , °C) observed at position A and B shown in Fig. 8.13. The separation distance between A and B is 100 m

z (m)	0.1	0.5	1.0	1.5	2.0
A	20.31	20.18	20.16	20.09	20.07
B	21.53	20.90	20.63	20.47	20.36

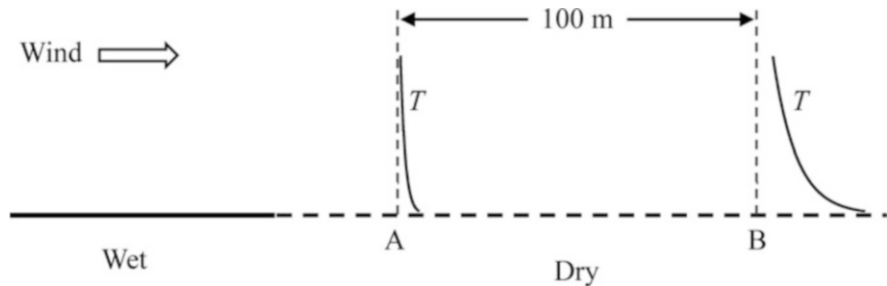


Fig. 8.13 Temperature profile at two locations in a dry field

8.19 The contribution of horizontal advection to the CO₂ budget of the eddy flux control volume (Fig. 8.3) is $4.5 \mu\text{mol m}^{-2} \text{s}^{-1}$. Using Eq. 8.22, estimate the corresponding concentration difference between the upwind and downwind face of the control volume. The horizontal dimension L is 100 m, the eddy covariance height is 20 m, and the mean wind speed below the height is 2 m s^{-1} . Can you measure the concentration difference with a broadband analyzer whose precision is typically no better than 0.2 ppm?

8.20 Find the effective fetch for the following conditions: neutral air stability, measurement height = 2.0 m, and surface roughness = 0.0225 m.

8.21 It is known that ecosystem respiration rarely exceeds $0.4 \text{ mg CO}_2 \text{ m}^{-2} \text{ s}^{-1}$. However, the eddy CO₂ flux measured over a tall forest at night can be as high as $1.0 \text{ mg m}^{-2} \text{ s}^{-1}$. (The measurement tower is located near the boundary that separates the forest from a large hayfield.) Explain reason(s) for this anomaly.

8.22* Using a threshold of 0.1 for the fractional contribution of horizontal advection a_H and Eqs. 7.74 and 8.36, derive an expression for the depth of the internal boundary layer as a function of downwind distance from a step change in surface source strength (Fig. 8.11). Graph your result for a range of surface roughness and stability values and discuss how surface roughness and air stability affect the development of the internal boundary layer.

References

- Aubinet M, Feigenwinter C, Heinesch B, Bernhofer C, Canepa E, Lindroth A, Montagnani L, Rebmann C, Sedlak P, van Gorsel E (2010) Direct advection measurements do not help to solve the nighttime CO₂ closure problem: evidence from three different forests. Agric For Meteorol 150:655–664
- Aubinet M, Vesala T, Papale D (2012) Eddy covariance: a practical guide to measurement and data analysis. Springer, Dordrecht, 438pp
- Baldocchi DD, Hicks BB, Meyers TP (1988) Measuring biosphere-atmosphere exchanges of biologically related gases with micrometeorological methods. Ecology 69:1331–1340
- Finnigan JJ (1985) Turbulent transport in flexible plant canopies. In: Hutchison BA, Hicks BB (eds) The forest-atmosphere interactions. D Reidel Publishing Company, Dordrecht/Lancaster, pp 443–480
- Gash JHC (1986) A note on estimating the effect of a limited fetch on micrometeorological evaporation measurements. Bound-Layer Meteorol 35:409–413
- Kanda M, Inagaki A, Letzel MO, Raasch S, Watanabe T (2004) LES study of the energy imbalance problem with eddy covariance fluxes. Bound-Layer Meteorol 110:381–404
- Lee X (1998) On micrometeorological observations of surface-air exchange over tall vegetation. Agric For Meteorol 91:39–49
- Lee X, Massman W (2011) A perspective on thirty years of the Webb, Pearman and Leuning density corrections. Bound-Layer Meteorol 139:37–59
- Leuning R (2007) The correct form of the Webb Pearman and Leuning equation for eddy fluxes of trace gases in steady and non-steady state, horizontally homogeneous flows. Bound-Layer Meteorol 123:263–267
- Paw UKT, Baldocchi DD, Meyers TP, Wilson KB (2000) Correction of eddy-covariance measurements incorporating both advective effects and density fluxes. Bound-Layer Meteorol 97:487–511
- Zhang J, Lee X, Song G, Han S (2011) Pressure correction to the long-term measurement of carbon dioxide flux. Agric For Meteorol 151:70–77

Chapter 9

Density Effects on Flux Measurements

9.1 Density Effects

Dry air is the media in which the turbulent diffusion of heat, water vapor, and trace gases takes place. Trace gases, such as carbon dioxide and gaseous pollutants, are passive scalars whose diffusion and transport do not alter the dynamic properties of the diffusion media. The same cannot be said of sensible heat and water vapor, which are active scalars. The sensible heat originated from the surface causes the boundary layer to become more unstable, which in turn makes the diffusion more efficient. Conversely, evaporative cooling of the surface and latent heat released by cloud condensation aloft push the boundary layer to a more stable state. These dynamic interactions are handled by the Reynolds mean conservation equations.

The density of dry air is altered by the diffusion of active scalars. Density changes can also arise from external agents, such as sensor self-heating and atmospheric pressure variations. In order to measure the gaseous diffusion properly, we must consider that the media of diffusion itself is changing. The interferences caused by dry air density variations on our ability to measure gaseous fluxes are called *density effects*.

The dry air mass density ρ_d can vary in a number of ways. In the standard atmosphere, ρ_d decreases exponentially with height, from 1.22 kg m^{-3} at the mean sea level to 1.05 kg m^{-3} at 1.5 km, due to the exponential decrease in atmospheric pressure, giving an average vertical density gradient of -0.11 g m^{-4} . The atmospheric boundary layer at any given time can deviate from the structure of the standard atmosphere. At times of a large positive surface heat flux, the ρ_d vertical gradient is positive in the surface layer. When a strong surface layer inversion develops at night, the gradient reverses its sign, and its magnitude can exceed that of the standard atmosphere. At the time scales of eddy motion, ρ_d can fluctuate

rapidly in response to temperature and humidity fluctuations. Most of the density fluctuations are damped in an enclosed environment, such as in a flux chamber and in the optical cell of a closed-path gas analyzer, but the enclosure itself may modify the density through the heating it generates.

A fundamental principle for understanding the density effects is the ideal gas law. So far, we have treated micrometeorological variables one at a time, by utilizing their conservation equations written in isolation from one another. In reality, temperature, pressure, and water vapor and carbon dioxide concentrations are interdependent. For example, spatial and temporal variations in air temperature cause variations in the carbon dioxide mass density, which, if not handled properly, will lead to an artificial carbon dioxide flux. Temperature and carbon dioxide observe their respective conservation equations, and their interdependence is constrained by the ideal gas law.

Another fundamental premise is that no source or sink of dry air exists in the atmospheric boundary layer. In the context of turbulent diffusion in the atmosphere, dry air is a gas mixture including permanent species (oxygen, nitrogen, and argon) but excluding water vapor and other variable trace species (carbon dioxide, ozone, and so on). There is no flux of dry air at the soil surface, and no dry air is generated or destroyed in the air layer above the soil. The amounts of oxygen produced by canopy photosynthesis and removed by respiration and the amount of nitrogen produced by denitrification in the soil are too small to have any measurable consequences on the conservation of dry air. Spatial and temporal variations in the dry air mass density are therefore attributed solely to variations in other state variables. On the other hand, variations in the CO₂ or water vapor mass density can be caused both by the presence of a source or sink in the environment and by changes in the dry air density. An essential task of gas flux measurement is to isolate the portion of the observed signal that is linked to the source of the gas from the unwanted signal brought by dry air density variations.

9.2 Density Corrections to Eddy Covariance Fluxes

Let us consider the density effects on the eddy covariance CO₂ flux in the surface layer over an extensive and uniform surface. The atmosphere is in a steady state. In this particular case, $\bar{\rho}_d \bar{w'} \bar{s'_c}$, the product of the dry air density and the covariance between the vertical velocity and the CO₂ mixing ratio represents the true ecosystem-atmosphere exchange. However, no instruments can measure the mass mixing ratio directly. What is detected by a gas analyzer is the intensity of light absorption which is proportional to the mass density ρ_c of the gas in the analyzer's optical path. The mass density is determined with this proportionality relationship and the analyzer's optical parameters, and the CO₂ flux is calculated as the covariance between the vertical velocity w and ρ_c . Our purpose is to show that correction for the density effects must be made to the covariance $\bar{w'} \bar{\rho'_c}$ to obtain the true surface-air flux.

According to the classic density correction theory of K. K. Webb, G. I. Pearman and R. Leuning (hereafter WPL; Webb et al. 1980), the true CO₂ flux is given as $\overline{w\rho_c}$. Reynolds decomposition yields

$$\overline{w\rho_c} = \overline{w}\overline{\rho_c} + \overline{w'\rho'_c}. \quad (9.1)$$

A similar equation is written for the dry air flux:

$$\overline{w\rho_d} = \overline{w}\overline{\rho_d} + \overline{w'\rho'_d} = 0. \quad (9.2)$$

Equation 9.2 is WPL's way of expressing the constraint of zero dry air flux at the surface. In order for the dry air flux to be zero, there must exist a mean vertical velocity \overline{w} :

$$\overline{w} = -\frac{1}{\overline{\rho}_d} \overline{w'\rho'_d}. \quad (9.3)$$

Combining Eqs. 9.3 and 9.1 yields the true CO₂ flux:

$$\overline{w\rho_c} = \overline{w'\rho'_c} - \frac{\overline{\rho}_c}{\overline{\rho}_d} \overline{w'\rho'_d}. \quad (9.4)$$

The second term on the right of Eq. 9.4 represents correction for the density effects. The covariance $\overline{w'\rho'_c}$ itself can deviate significantly from the true flux $\overline{w\rho_c}$.

The problem is further illustrated with a field experiment in a desert landscape totally void of biological activity. Chemical reactions in arid soils can potentially serve as a sink of atmospheric carbon dioxide, but the sink strength is an order of magnitude smaller than the detection limit of eddy covariance instruments. So the experiment constitutes essentially a zero-flux test. However, the covariance $\overline{w'\rho'_c}$ itself is generally not equal to zero. The process responsible for the fluctuations in ρ_c is fluctuations in the density of the diffusion media, which are highly correlated with fluctuations in the vertical velocity. The result is an artificial CO₂ flux represented by $(\overline{\rho}_c/\overline{\rho}_d)\overline{w'\rho'_d}$, which must be subtracted from the observed covariance $\overline{w'\rho'_c}$ to obtain the expected zero CO₂ flux.

The WPL mean vertical velocity (Eq. 9.3) is a consequence of the density fluctuations, explained by the fact that upward and downward moving eddies travel at different vertical velocities. In unstable conditions, upward moving eddies are less dense than downward moving eddies and must travel at faster speeds in order to maintain a zero dry air flux, thus giving rise to a positive mean vertical velocity. (The covariance $\overline{w'\rho'_d}$ is negative in unstable conditions, as shown below.) This mean velocity is typically less than 1 mm s⁻¹ in magnitude. It cannot be obtained or eliminated by coordinate rotation nor can it be determined from horizontal flow divergence according to the continuity principle (Eq. 3.18). In this regard, it loses the interpretation of a mean flow velocity appropriate to atmospheric flows. Some people call it a “drift velocity.”

To avoid potential confusion associated with the WPL velocity, we now present a new perspective on the density effects that do not need to invoke the concept of this velocity (Massman and Lee 2002). Recall that in steady-state and advection-free conditions,

$$\text{NEE} = \bar{\rho}_d \overline{w' s'_c}, \quad (9.5)$$

(Eq. 8.24). Our task is to convert the $w-s_c$ covariance to the $w-\rho_c$ covariance, the latter of which is measured by eddy covariance instruments. Deployment of the mixing ratio definition and Reynolds decomposition yields

$$s_c = \bar{s}_c + s'_c = \frac{\bar{\rho}_c + \rho'_c}{\bar{\rho}_d + \rho'_d} \quad (9.6)$$

This equation can be rearranged to give s'_c :

$$\begin{aligned} s'_c &= s_c - \bar{s}_c \\ &= \frac{\bar{\rho}_c + \rho'_c}{\bar{\rho}_d + \rho'_d} - \frac{\bar{\rho}_c}{\bar{\rho}_d}, \end{aligned} \quad (9.7)$$

where the Reynolds mean CO₂ mixing ratio is approximated as $\bar{s}_c = \bar{\rho}_c / \bar{\rho}_d$ (Problem 9.1). The denominator of the first term in Eq. 9.7 can be expressed as a Taylor expansion series:

$$\begin{aligned} \frac{1}{\bar{\rho}_d + \rho'_d} &= \frac{1}{\bar{\rho}_d} \frac{1}{1 + \rho'_d / \bar{\rho}_d} \\ &= \frac{1}{\bar{\rho}_d} \left[1 - \frac{\rho'_d}{\bar{\rho}_d} + \left(\frac{\rho'_d}{\bar{\rho}_d} \right)^2 - \dots \right]. \end{aligned} \quad (9.8)$$

Substituting Eq. 9.8 into Eq. 9.7 and keeping only the first-order terms, we obtain

$$s'_c = \frac{1}{\bar{\rho}_d} \left(\rho'_c - \frac{\bar{\rho}_c}{\bar{\rho}_d} \rho'_d \right). \quad (9.9)$$

Combining Eqs. 9.5 and 9.9 yields

$$\text{NEE} = \overline{w' \rho'_c} - \frac{\bar{\rho}_c}{\bar{\rho}_d} \overline{w' \rho'_d}. \quad (9.10)$$

This equation is identical to the original WPL Eq. 9.4.

That Eq. 9.10 is exactly the same as Eq. 9.4 is not a surprise. Both formulations are consequences of the conservation of dry air or, more specifically, of the premise that the source strength of dry air is zero. This premise is embodied in Eq. 9.2 and in the continuity equation. Equation 9.10 can be traced back to the conservation

equation for the CO₂ mixing ratio, which is derived from the conservation equations for dry air and for CO₂. The dry air conservation is expressed by the continuity Eq. 2.14, which makes the implicit assumption that no dry air is generated or removed in the atmospheric boundary layer.

The term $(\bar{\rho}_c/\bar{\rho}_d)w'\rho'_d$ represents density corrections to the eddy covariance CO₂ flux. Because fluctuations in ρ_d cannot be measured directly with eddy covariance instruments, we need an expression for relating ρ'_d to quantities that we can measure.

The formulation for the dry air density fluctuations is based on the ideal gas law. Substituting the ideal gas law relations for dry air and for water vapor (Eqs. 2.27 and 2.28) in the Dalton's law of partial pressures (Eq. 2.38) and replacing their ideal gas constants with the universal gas constant (Eqs. 2.30 and 2.31), we obtain

$$\frac{\rho_d}{M_d} + \frac{\rho_v}{M_v} = \frac{p}{RT}. \quad (9.11)$$

We can rearrange Eq. 9.11 and deploy Reynolds decomposition, yielding

$$\rho_d = \frac{M_d p}{RT} - \mu \rho_v \quad (9.12)$$

$$= \frac{M_d(\bar{p} + p')}{R(\bar{T} + T')} - \mu(\bar{\rho}_v + \rho'_v), \quad (9.13)$$

where $\mu = M_d/M_v$. Applying Reynolds averaging on Eq. 9.13 and omitting higher-order terms (Problem 9.1), we have

$$\bar{\rho}_d = \frac{M_d \bar{p}}{R \bar{T}} - \mu \bar{\rho}_v. \quad (9.14)$$

Reynolds decomposition also gives

$$\rho'_d = \rho_d - \bar{\rho}_d. \quad (9.15)$$

Combining Eqs. 9.13, 9.14, and 9.15 and omitting again higher-order terms, we arrive at an expression for the dry air density fluctuations:

$$\rho'_d = \bar{\rho}_d(1 + \mu \bar{s}_v) \left(\frac{p'}{\bar{p}} - \frac{T'}{\bar{T}} \right) - \mu \rho'_v \quad (9.16)$$

where the mean water vapor mixing ratio is approximated as $\bar{s}_v = \bar{\rho}_v/\bar{\rho}_d$. Equation 9.16 indicates that fluctuations in air temperature, pressure and water vapor density all contribute to the dry air density fluctuations. Of the three factors, temperature fluctuations play the dominant role. Because ρ'_d and T' are opposite in sign, the covariance $w'\rho'_d$ is generally negative in unstable conditions and positive in stable conditions.

Replacing ρ'_d in Eq. 9.10 with Eq. 9.16, we obtain

$$\text{NEE} = \overline{w' \rho'_c} - \bar{\rho}_c (1 + \mu \bar{s}_v) \left(\frac{\overline{w' p'}}{\bar{p}} \right) + \bar{\rho}_c (1 + \mu \bar{s}_v) \left(\frac{\overline{w' T'}}{\bar{T}} \right) + \mu \bar{s}_c (\overline{w' \rho'_v}) \quad (9.17)$$

$$\approx \overline{w' \rho'_c} + \bar{\rho}_c (1 + \mu \bar{s}_v) \left(\frac{\overline{w' T'}}{\bar{T}} \right) + \mu \bar{s}_c (\overline{w' \rho'_v}). \quad (9.18)$$

The second, third, and fourth terms on the right side of Eq. 9.17 are pressure correction, temperature correction, and water vapor correction, respectively. Temperature fluctuations are the largest source of correction. Pressure correction is usually negligible. These corrections can be done in post-field data analysis using the measured Reynolds mean water vapor and CO₂ mixing ratios, temperature, and the vertical velocity covariances $\overline{w' T'}$ and $\overline{w' \rho'_v}$.

Similarly, in the case of water vapor exchange, the density-corrected flux is given by

$$\begin{aligned} E &= \overline{w' \rho'_v} - \frac{\bar{\rho}_v}{\bar{\rho}_d} \overline{w' \rho'_d} \\ &= (1 + \mu \bar{s}_v) \left[\overline{w' \rho'_v} + \bar{\rho}_v \left(\frac{\overline{w' T'}}{\bar{T}} \right) \right], \end{aligned} \quad (9.19)$$

where we have omitted the pressure correction term.

There are two types of eddy covariance system: open path and closed path (Fig. 9.1). Equations 9.18 and 9.19 describe the density effects on measurements made with an open-path eddy covariance system. Having its optical path open to the moving air, the gas analyzer measures the mass density of the target gas in situ.

In the case of a closed-path eddy covariance system, air is drawn from an inlet near the anemometer through a tube to a closed optical cell where the detection takes place. Density corrections must consider the fact that the dry air density is now

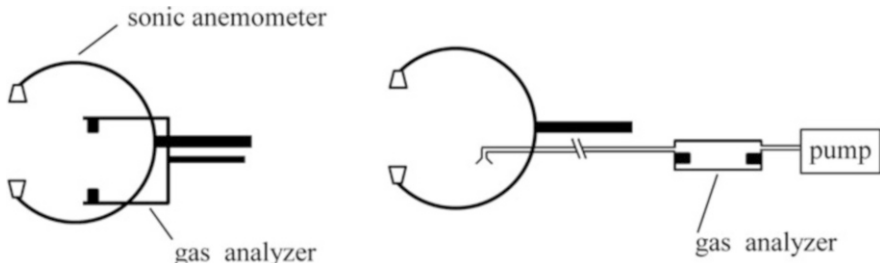


Fig. 9.1 An open-path (left) and closed-path (right) eddy covariance system

being modified by the measurement system itself. Because heat exchange between the air sample and the sampling tube is very efficient, by the time the air arrived at the optical cell of the analyzer, all the temperature fluctuations have vanished. Fluctuations in the gaseous densities are still preserved, especially if the travel time is short (i.e., less than a few seconds) and the flow in the tube is turbulent. It is no longer necessary to correct for the density effect associated with temperature. The only effect that remains to be corrected is associated with water vapor fluctuations. A major advantage of closed-path over open-path eddy covariance is that its density effects are substantially weaker.

The density effects are eliminated altogether if the air sample is dried with a water vapor filter before it arrives at the closed-path gas analyzer. There are no more dry air density fluctuations in the analyzer's optical cell, and the measured trace gas density fluctuations are the true signal attributed to the surface source. This hardware solution improves the measurement in low flux environments, such as over the open ocean, although it comes at the cost of losing the ability to measure the water vapor flux (Miller et al. 2010).

The above numerical density correction procedure assumes that all the variables needed for the corrections are measured perfectly. Errors in these variables can propagate through the correction procedure to the extent that they may completely mask a weak flux signal (Problems 9.7, 9.8 and 9.17). The risk of error propagation is substantially reduced by deploying a closed-path analyzer and by drying the air sample prior to detection to remove the temperature- and humidity-induced density effect, respectively.

9.3 Density Effects on Flux-Gradient Relation

The flux-gradient relation is a first-order turbulence closure scheme developed as an analog of Fick's law of molecular diffusion. Fick's law states that the molecular flux of a gas in a fluid is proportional to its concentration gradient. Standard texts on this topic lack clear guidance on whether the concentration should be the mass mixing ratio or the mass density. In the simple case where the fluid is isothermal, the pressure is the same everywhere, and the gas of interest is the only species undergoing diffusion, the flux can be expressed as the product of a constant (i.e., molecular diffusivity) and the gradient of the mass density. If diffusion of heat or another gas coexists along with that of the target gas, or if a pressure gradient occurs in the direction of diffusion, the simple proportionality relation is no longer precise.

In the micrometeorological literature, the flux-gradient relation is sometimes expressed on the basis of the mass density, as

$$F_c = -K_c \frac{\partial \bar{\rho}_c}{\partial z}, \quad (9.20)$$

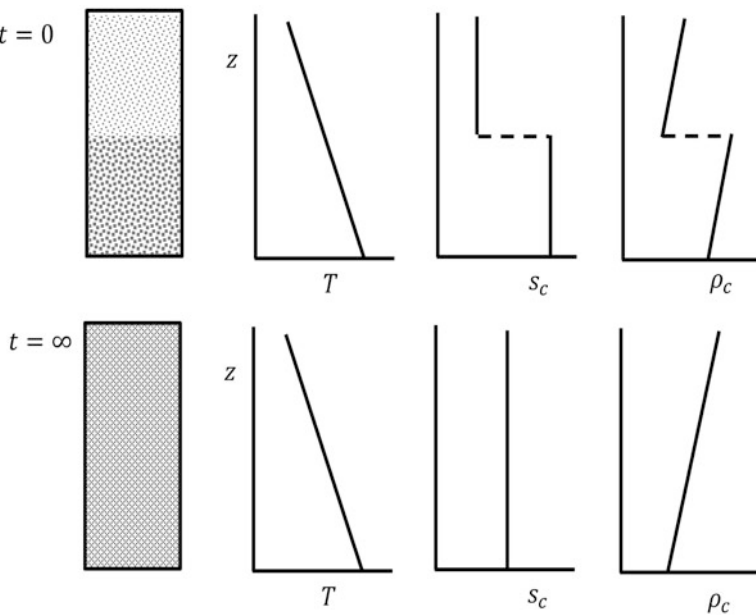


Fig. 9.2 Diffusion of CO_2 in an enclosure: *top*, conditions at time $t = 0$; *bottom*, conditions at a new steady state long after the barrier that separates the upper and the lower compartment was removed

in the case of CO_2 diffusion. Equation 9.20 is dimensionally correct and seems intuitive because it is a natural extension of Fick's law to turbulent flows. However, it suffers from an artifact of artificial diffusion if the density of dry air, the media of diffusion, is variable in space.

A thought experiment, depicted in Fig. 9.2, illustrates this artifact. Initially the enclosure is divided by a solid barrier into two compartments, with the lower compartment containing a higher CO_2 concentration. Convective eddy mixing is maintained by heating supplied at the bottom. Because of the heating, we expect a negative temperature gradient and a positive dry air density gradient in the vertical direction and a heat flux directed from the bottom to the top. Then, the barrier is removed to allow CO_2 exchange between the two compartments. Heat diffusion continues unperturbed. A new steady state will establish after long enough time whereby the CO_2 mixing ratio is uniform in the vertical direction, but its mass density is not. If we accept Eq. 9.20, we would come to the conclusion that a downward CO_2 flux exists in the new steady state even though the enclosure does not contain a CO_2 source or sink. This diffusion flux is purely an artifact of the dry air density variation in the enclosure.

The new steady state shown in Fig. 9.2 resembles conditions of the zero-flux experiment discussed in the previous section. Let us use a numerical example to gain appreciation of the artificial flux (Fig. 9.3). The atmospheric pressure is

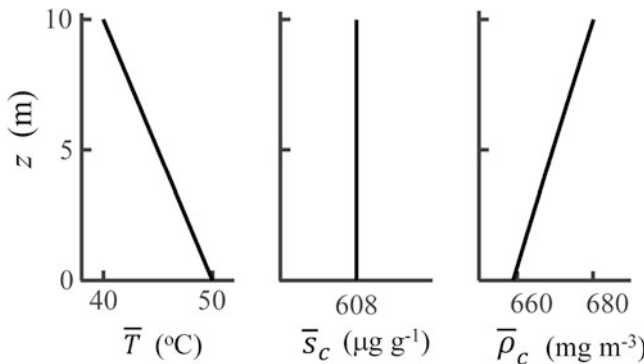


Fig. 9.3 Artificial CO₂ diffusion in the surface layer over a desert landscape completely free of CO₂ source and sink. There is no water vapor in the air, and atmospheric pressure is 1000 hPa

1000 hPa, the air is completely dry, and the CO₂ mass mixing ratio is 608 $\mu\text{g g}^{-1}$ (or a molar mixing ratio of about 400 ppm). A strong temperature gradient is developed from solar radiation heating of the surface. The ideal gas law requires that the CO₂ mass density $\bar{\rho}_c$ should increase with height in order to maintain a constant mixing ratio. For the conditions shown in Fig. 9.3, $\partial\bar{\rho}_c/\partial z = 2.1 \text{ mg m}^{-4}$. At a typical eddy diffusivity value of $0.3 \text{ m}^2 \text{ s}^{-1}$, Eq. 9.20 predicts a large apparent flux of $-0.6 \text{ mg m}^{-2} \text{ s}^{-1}$, a signal comparable to the typical photosynthetic CO₂ uptake rate of an evergreen forest at midday hours. The result is an obvious contradiction to the fact that the desert soil is void of CO₂ sink.

By now you probably have realized that the proper flux-gradient relationship should be based on the mass mixing ratio, not on the mass density, as

$$F_c = -K_c \bar{\rho}_d \frac{\partial \bar{s}_c}{\partial z}. \quad (9.21)$$

Since the covariance of the mixing ratio with the vertical velocity represents the true surface flux, it is logical that the flux be parameterized using the mean mixing ratio gradient. This relation predicts that the vertical flux should be zero in the enclosure after it has reached the new steady state (Fig. 9.2) and in the zero-flux experiment (Fig. 9.3).

The density effects become obvious if we expand Eq. 9.21 using $\bar{s}_c = \bar{\rho}_c / \bar{\rho}_d$:

$$F_c = -K_c \left(\frac{\partial \bar{\rho}_c}{\partial z} - \frac{\bar{\rho}_c}{\bar{\rho}_d} \frac{\partial \bar{\rho}_d}{\partial z} \right). \quad (9.22)$$

This equation differs from Eq. 9.20 in that it contains an additional term describing the vertical dry air density gradient. The gradient $\partial \bar{\rho}_d / \partial z$ is found by differentiating Eq. 9.14 with respect to z . Replacing the result in Eq. 9.22 and omitting the vertical pressure gradient, we obtain

$$F_c = -K_c \left[\frac{\partial \bar{\rho}_c}{\partial z} + (1 + \mu \bar{s}_v) \frac{\bar{\rho}_c}{\bar{T}} \frac{\partial \bar{T}}{\partial z} + \mu \bar{s}_c \frac{\partial \bar{\rho}_v}{\partial z} \right]. \quad (9.23)$$

This is the density correction equation for the CO₂ flux-gradient relationship, akin to the correction Eq. 9.18 for the eddy covariance CO₂ flux. It shows that both temperature and humidity gradients give rise to the density effects. To put it differently, thermal diffusion and water vapor diffusion, as driven by the vertical temperature and water vapor gradients, are sources of the artificial CO₂ flux, which must be corrected in order to obtain the true flux signal.

In the case of water vapor, the correct flux-gradient relation is given as

$$\begin{aligned} F_v &= -K_v \bar{\rho}_d \frac{\partial \bar{s}_v}{\partial z} \\ &= -K_v (1 + \mu \bar{s}_v) \left(\frac{\partial \bar{\rho}_v}{\partial z} + \frac{\bar{\rho}_v}{\bar{T}} \frac{\partial \bar{T}}{\partial z} \right). \end{aligned} \quad (9.24)$$

Equations 9.23 and 9.24 are valid if all the gradient quantities are measured in situ. Although $\partial \bar{T}/\partial z$ must be measured with sensors exposed to ambient air, the gaseous gradients are generally measured with a closed-path analyzer. A typical measurement strategy is to draw air continuously from two intakes above the surface and use the analyzer to measure the two airstreams in an alternate sequence (Fig. 3.5). Because the airstreams are brought to a common temperature, the effect of the temperature gradient vanishes. Furthermore, the density effect associated with water vapor disappears if the air sample is dried before it arrives at the analyzer, and the flux obtained with Eq. 9.20 does not require density corrections. Pre-drying of air samples is a standard practice for trace gas measurement in atmospheric chemistry.

9.4 Density Corrections to Chamber Fluxes

The density effects on chamber fluxes can be examined with the same principles applied to the micrometeorological methods. The measurement equation for a closed chamber is

$$F_c = \rho_d \frac{V}{A} \frac{\partial s_c}{\partial t}, \quad (9.25)$$

where V is chamber volume, A is chamber basal area, and ρ_d and s_c are the density of dry air and the CO₂ mixing ratio in the chamber volume, respectively. This equation is the general form of Eq. 8.16 developed for a rectangular-shaped chamber (Fig. 8.2a). An alternative expression is written in the form of the CO₂ mass density ρ_c , as

$$F_c = \frac{V}{A} \frac{\partial \rho_c}{\partial t}. \quad (9.26)$$

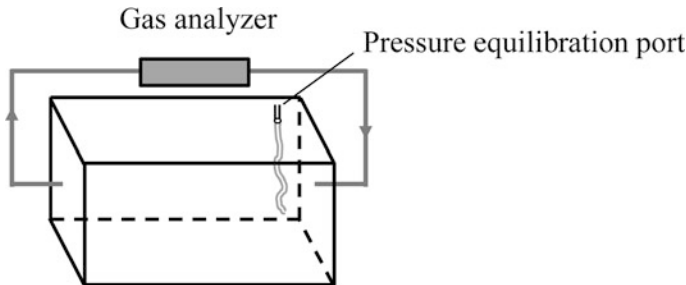


Fig. 9.4 A closed flux chamber equipped with a pressure equilibration port

If the chamber is fully sealed, both Eqs. 9.25 and 9.26 are accurate. This can be shown with a zero-flux or chamber blank test, by placing the chamber on a surface that evaporates water but does not emit or absorb CO₂. Like any other natural systems, this surface does not produce or consume dry air. Water vapor added to the chamber via evaporation increases the vapor pressure and the total pressure, but the partial pressures of dry air and CO₂ remain unchanged. The total amounts of dry air and CO₂, and hence ρ_d , ρ_c and s_c , are constant with time. (The chamber volume is fixed.) Likewise, temperature increase in the chamber has no effect on these quantities because it is compensated by a proportional rise in pressure. Both equations yield a zero flux as desired.

Soil CO₂ emission is very sensitive to pressure perturbation. To reduce the perturbation, some chambers are equipped with a small opening to equalize the pressure inside and outside the chamber (Fig. 9.4; Licor 2003). When evaporation or temperature rise occurs in the chamber, some air will escape through the opening, and overpressure is avoided. Because the amount of CO₂ escaped is proportional to the CO₂ mass mixing ratio, the air leakage does not degrade the accuracy of Eq. 9.25. But Eq. 9.26 requires density corrections. The full density correction equation can be derived from Eq. 9.25, in a similar way to the derivation of Eq. 9.23, yielding

$$F_c = \frac{V}{A} \left[\frac{\partial \rho_c}{\partial t} + (1 + \mu s_v) \frac{\rho_c}{T} \frac{\partial T}{\partial t} + \mu s_c \frac{\partial \rho_v}{\partial t} \right]. \quad (9.27)$$

In the case of a dynamic chamber (Fig. 8.2b), the correct measurement equation is

$$F_c = \rho_d \frac{Q_b}{A_b} (s_{c,o} - s_{c,i}), \quad (9.28)$$

where Q_b is base flow rate (in m³ s⁻¹), A_b is chamber basal area, and $s_{c,o}$ and $s_{c,i}$ are the CO₂ mixing ratio at the chamber outlet and the inlet, respectively. If the flux is computed from the CO₂ mass density measurement, as in

$$F_c = \frac{Q_b}{A_b} (\rho_{c,o} - \rho_{c,i}), \quad (9.29)$$

where $\rho_{c,o}$ and $\rho_{c,i}$ denote the mass density at the chamber outlet and inlet, respectively, density corrections are necessary to account for the differences in air temperature and water vapor density between the chamber interior and the ambient environment.

There is some ambiguity regarding how the base flow Q_b should be measured. One chamber configuration uses a mass flow controller to regulate the flow at a preset rate. A common type of mass flow controller accomplishes the task by measuring the heat transfer of a heated tube through which the chamber air is flown. Because the flow controller is calibrated with dry air, the measurement will be in error if correction is not made to account for the presence of water vapor in the chamber air (Lee 2000). It is known that moisture addition increases the air heat capacity and therefore the efficiency of heat transfer of the heated tube. A small correction for the moisture effect on Q_b is still needed even if the flux is computed from the mass mixing ratio measurement.

9.5 Problems

9.1 Using the Taylor expansion and the Reynolds rules, show that (1) the Reynolds mean CO₂ mixing ratio can be approximated by $\bar{s}_c = \bar{\rho}_c / \bar{\rho}_d$ and (2) the mean dry air density can be approximated by Eq. 9.14.

9.2 Find the dry air density for an air temperature of 15.3 °C, an air pressure of 952.3 hPa, and a water vapor density of 12.9 g m⁻³.

9.3 The standard density correction procedure for eddy covariance is based on Reynolds mean statistics. The correction can also be made by first converting the instant mass density to the mass mixing ratio and then calculating the vertical velocity – mixing ratio covariance to obtain the true flux. Use both methods to compute the CO₂ flux with the short time series data shown in Table 9.1. Do the two methods produce nearly identical results? Why?

Table 9.1 Instant air temperature (T , °C), water vapor density (ρ_v , g m⁻³), CO₂ density (ρ_c , mg m⁻³), and vertical velocity (w , m s⁻¹) measured with an open-path eddy covariance system at several time steps (t , s). The atmospheric pressure is 951.1 hPa

t	1	2	3	4	5	6	7	8	9	10
T	20.47	20.47	20.44	20.56	20.52	20.50	20.87	21.01	20.72	20.79
ρ_v	7.367	7.401	7.403	7.359	7.313	7.343	7.375	7.369	7.425	7.424
$\rho_c - 600$	91.57	91.34	91.17	90.13	91.24	91.65	90.02	89.92	90.14	89.61
w	-0.010	0.730	0.375	0.612	0.998	1.919	1.945	1.991	2.155	1.106
t	11	12	13	14	15	16	17	18	19	20
T	20.68	20.57	20.43	20.10	20.08	20.09	20.10	20.10	20.13	20.39
ρ_v	7.346	7.370	7.195	7.138	7.109	7.086	7.077	7.144	7.244	7.285
$\rho_c - 600$	88.85	90.44	91.48	93.19	94.19	94.13	94.26	94.09	93.81	92.24
w	1.179	0.436	0.223	-0.217	-0.369	-0.494	-0.807	-0.890	-1.188	-0.988

9.4 Without correction for the density effects, is the evaporation rate measured with open-path eddy covariance in unstable conditions biased high or low? What about the measurement made with closed-path eddy covariance?

9.5 An open-path eddy covariance system in the middle of a large parking lot made of concrete yields a $\overline{w' \rho'_v}$ value of $-0.016 \text{ g m}^{-2} \text{ s}^{-1}$ at midday (Ham and Heilman 2003). Does the measurement indicate that condensation is occurring on the concrete surface?

9.6 Calculate the true CO₂ and water vapor flux using these half-hourly mean Reynolds statistics obtained with an open-path eddy covariance system: $\overline{w' \rho'_c} = -1.22 \text{ mg m}^{-2} \text{ s}^{-1}$, $\overline{w' T'} = 0.320 \text{ K m s}^{-1}$, $\overline{w' \rho'_v} = 0.109 \text{ g m}^{-2} \text{ s}^{-1}$, $\overline{\rho}_c = 719.3 \text{ mg m}^{-3}$, $\overline{\rho}_v = 7.94 \text{ g m}^{-3}$, $\overline{T} = 19.2^\circ\text{C}$, and $\overline{p} = 997.2 \text{ hPa}$.

9.7 The annual mean sensible and latent heat flux are 100.3 and 14.9 W m⁻², respectively, in a semiarid plantation forest. Determine the density correction to the annual mean CO₂ flux measured with an open-path eddy covariance system. Use the data given in Problem 9.6 for the mean water vapor density, CO₂ density, air temperature, and air pressure. Now assume that the mean CO₂ density $\overline{\rho}_c$ has been underestimated by 10%. How large is the CO₂ flux bias error caused by propagation of the $\overline{\rho}_c$ measurement error through the density correction procedure? (For your reference, the annual NEE of the forest is $-2.3 \text{ t C ha}^{-1} \text{ y}^{-1}$.)

9.8 The eddy covariance sensible heat flux has a typical random error of 10 W m⁻² in daylight hours. How large is the CO₂ flux uncertainty caused by the density correction procedure if the measurement is made with an open-path eddy covariance system? The CO₂ flux signal of an unpolluted lake is on the order of $1 \mu\text{mol m}^{-2} \text{ s}^{-1}$. Can the eddy covariance system resolve the CO₂ flux signal at hourly intervals?

9.9 Using the information provided in Problem 9.6, estimate the amount of density correction needed for the N₂O flux measured with an open-path eddy covariance system. How large is the correction in comparison with a typical cropland N₂O flux of $0.3 \text{ nmol m}^{-2} \text{ s}^{-1}$? How large is the N₂O flux uncertainty associated with a random error of 10 W m⁻² in the sensible heat flux?

9.10 Derive density correction equations for closed-path eddy covariance. Use the equations to calculate the true CO₂ and water vapor flux using these half-hourly mean Reynolds statistics: $\overline{w' \rho'_c} = -0.45 \text{ mg m}^{-2} \text{ s}^{-1}$, $\overline{w' \rho'_v} = 0.169 \text{ g m}^{-2} \text{ s}^{-1}$, $\overline{w' T'} = 0.205 \text{ K m s}^{-1}$, $\overline{\rho}_c = 708.3 \text{ mg m}^{-3}$, $\overline{\rho}_v = 20.16 \text{ g m}^{-3}$, $\overline{T} = 17.7^\circ\text{C}$, and $\overline{p} = 950.8 \text{ hPa}$.

9.11 In a shipborne experimental campaign in the North Atlantic, the sea-air CO₂ flux was measured with two eddy covariance systems. One was a standard closed-path system, and the other was a closed-path system fitted with a Nafion dryer upstream of its gas analyzer. The latent flux measured with the two systems was 48 and 1.2 W m^{-2} , respectively. During the campaign, the air temperature was 12.9°C , the air pressure was 998.9 hPa, the water vapor pressure was 8.96 hPa, and the CO₂ molar mixing ratio was 380.2 ppm. Compute the density corrections to the CO₂ flux associated with the water vapor density effect. Are the density corrections larger or smaller in magnitude than the true ocean surface CO₂ flux of $-3.1 \text{ mol m}^{-2} \text{ y}^{-1}$?

9.12 Using the information provided in Fig. 9.3 and the flux-gradient relation, determine the true CO₂ flux. The eddy diffusivity is 0.3 m² s⁻¹.

9.13 Some people say that there are no density effects on the water vapor flux if it is measured with a close-path eddy covariance system. Are they correct?

9.14* In a field experiment deploying the flux-gradient method, air is drawn continuously from intakes at two heights above the surface, and measurements of the CO₂ and water vapor densities are made in an alternate sequence by a CO₂/H₂O dual gas analyzer at a common temperature T_c and a common pressure p_c . Simultaneous measurement is also made of air temperature at the same heights. Derive an expression for the determination of the true CO₂ flux from these measurements. (Assume that the eddy diffusivity is known.)

9.15* In a chamber blank test, you place a chamber with a pressure equilibration port (Fig. 9.4) on a surface that evaporates water but does not emit or absorb CO₂. Show that the CO₂ mixing ratio in the chamber does not change with time even though the addition of water vapor will force some air to leak out of the chamber.

9.16 A closed chamber is equipped with a pressure equilibration port so that the pressure inside the chamber is maintained at the same level as the ambient pressure, which can be considered as a constant over the measurement interval. Derive from Eqs. 9.12 and 9.25 the density correction Eq. 9.27 for the chamber CO₂ flux.

9.17 The density correction method assumes that all the variables used for the correction are measured perfectly. In practice, measurement errors are unavoidable and can propagate through the density correction procedure to degrade the quality of trace gas flux data. Assuming that the mean CO₂ density and the mixing ratio are biased low by 5%, estimate the bias error in the annual cumulative CO₂ flux measured with open-path eddy covariance. (The annual mean sensible and latent heat fluxes are 50 and 70 W m⁻², respectively.)

9.18 Open-path eddy covariance systems often register physiologically unreasonable CO₂ uptake signals during the off-season in extreme cold environments (Fig. 9.5). A hypothesized cause of this artificial flux is that the CO₂ analyzer itself generates heat, but the density correction procedure uses temperature fluctuations measured outside the analyzer's optical path and as such fails to fully correct the density effects. How large would an additional heat flux due to sensor self-heating be required to correct the midday CO₂ shown in Fig. 9.5 to zero?

9.19 The sensible and latent heat fluxes are 240.1 and 108.7 W m⁻², respectively; the air temperature is 23.4 °C; the atmospheric pressure is 997.4 hPa; the water vapor and carbon dioxide mixing ratios are 21.2 g kg⁻¹ and 610.7 mg kg⁻¹, respectively; and the covariance $\overline{w' \rho'_c}$ measured with an open-path eddy covariance system is -2.09 mg m⁻² s⁻¹. Find the true net ecosystem CO₂ exchange.

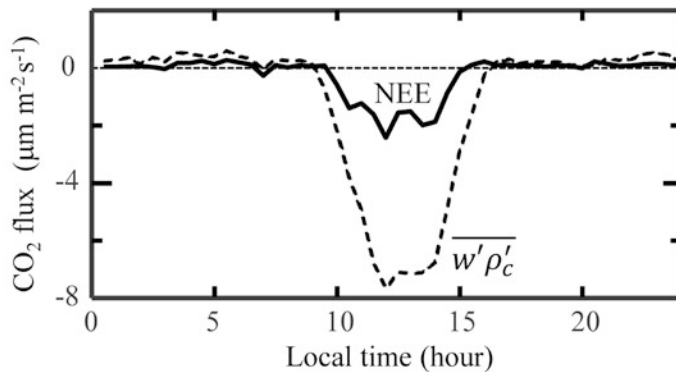


Fig. 9.5 Diurnal composite of the CO₂ flux observed with open-path eddy covariance over a desert ecosystem in Northwest China in a winter dormant season: *dashed line*, covariance between the vertical velocity and the CO₂ density; *solid line*, density-corrected CO₂ flux (Eq. 9.18) (Data source: Wang et al. 2016)

References

- Ham JM, Heilman JL (2003) Experimental test of density and energy balance corrections on carbon dioxide flux as measured using open-path eddy covariance. Agron J 95:1393–1403
- Lee X (2000) Water vapor density effect on measurements of trace gas mixing ratio and flux with a massflow controller. J Geophys Res 105:17807–17810
- Licor (2003) 6400–09 soil CO₂ flux chamber instruction manual. LI-COR Inc, Lincoln
- Massman WJ, Lee X (2002) Eddy covariance flux corrections and uncertainties in long-term studies of carbon and energy exchanges. Agric For Meteorol 113:121–144
- Miller SD, Marandino C, Saltzman ES (2010) Ship-based measurement of air-sea CO₂ exchange by eddy covariance. J Geophys Res 115:D02304
- Wang W, Xu JP, Gao Y, Bogoev I, Cui J, Deng L, Hu C, Liu C, Liu S, Shen J, Sun X, Xiao W, Yuan G, Lee X (2016) Performance evaluation of an integrated open-path eddy covariance system in a cold desert environment. J Atmos Ocean Technol 33:2385–2399
- Webb EK, Pearman GI, Leuning R (1980) Correction of flux measurements for density effects due to heat and water vapor transfer. Q J R Meteorol Soc 106:85–100

Chapter 10

Energy Balance, Evaporation, and Surface Temperature

10.1 Resistance Analogy for Leaf-Scale Fluxes

In this chapter, we aim to develop mathematical models of evaporation and surface temperature. For simplicity of presentation, in this modeling chapter we will omit the overbar on atmospheric variables, but it is understood that these variables are time-averaged quantities. A foundation for these models is the principle of surface energy balance, which states that the flows of energy in various forms must be in exact balance at a surface. At a leaf surface, the principle is expressed as

$$R_{n,l} = H_l + \lambda E_l, \quad (10.1)$$

where $R_{n,l}$ is the net radiation flux, H_l is the sensible heat flux, and E_l is the water vapor flux, all given on the basis of a unit leaf area, and subscript l is used to denote leaf-scale quantities. Because the leaf mass is very small, the internal energy change associated with leaf temperature variations is negligible.

We showed in Chap. 8 that by performing canopy volume averaging, we obtained a canopy sensible heat source term that is proportional to the product of leaf area density and a volume mean temperature gradient across the leaf boundary layer. The proportionality coefficient is $2\kappa_T$, where the factor 2 recognizes that sensible heat exchange occurs on both sides of the leaf but leaf area is measured on one side only (Eq. 8.10). Since we are concerned here with an average leaf of unit surface area, this source term is equivalent to $H_l/\rho_d c_p$. Let l be the leaf boundary layer thickness for heat, T_l be the leaf surface temperature, and T_a be the air temperature outside the boundary layer (Fig. 10.1). The temperature gradient is given by $(T_a - T_l)/l$, and Eq. 8.10 can be written as

$$H_l = \rho_d c_p \frac{T_l - T_a}{r_b}, \quad (10.2)$$

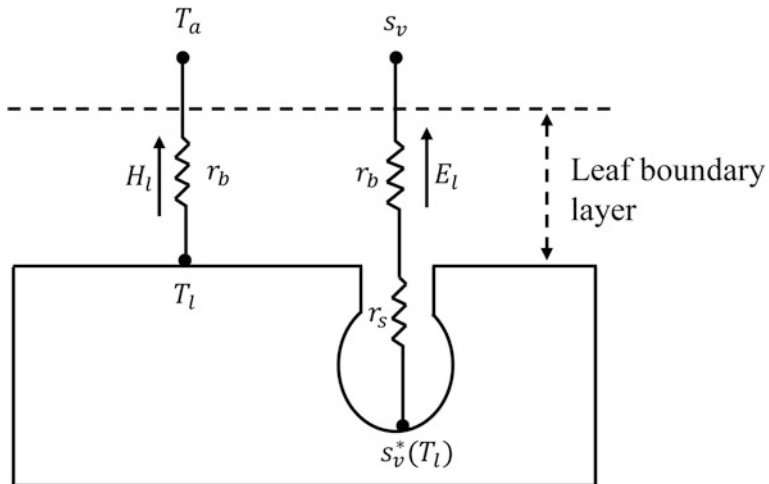


Fig. 10.1 Resistance analogy for sensible heat and water vapor fluxes across the leaf boundary layer. The vertical scale is exaggerated

where

$$r_b = \frac{l}{2\kappa_T} \quad (10.3)$$

is called the *leaf boundary layer resistance* and has the dimensions of sm^{-1} (Fig. 10.1).

Equation 10.2 is the expression of Ohm's law or resistance analogy for heat transfer at the leaf scale. Ohm's law states that electric current is equal to the voltage differential across a load divided by the electric resistance of the load. In our application, the heat flux is equivalent to the electric current, the leaf-to-air temperature difference is equivalent to the voltage differential, and r_b is the analog of the electric resistance that describes the difficulty of heat diffusion in the leaf boundary layer.

A similar expression can be written for water vapor transfer. Because the boundary layer resistance differs by less than 7% between heat and water vapor, the same resistance parameterization will be used for both. The leaf is amphistomatous, having stomata on both sides. (For hypostomatous leaves whose stomata are present only on the lower side, the resistance to water vapor transfer is twice as large.) Generally, the vapor mixing ratio at the leaf surface is not a known quantity, but the vapor mixing ratio in the stomatal cavity is at the saturation value in reference to the leaf temperature. So the interior of the stomatal cavity instead of the leaf surface is used as the starting node of the vapor diffusion pathway. The resistance analogy for water vapor is expressed as

$$E_l = \rho_d \frac{s_v^* - s_v}{r_s + r_b}, \quad (10.4)$$

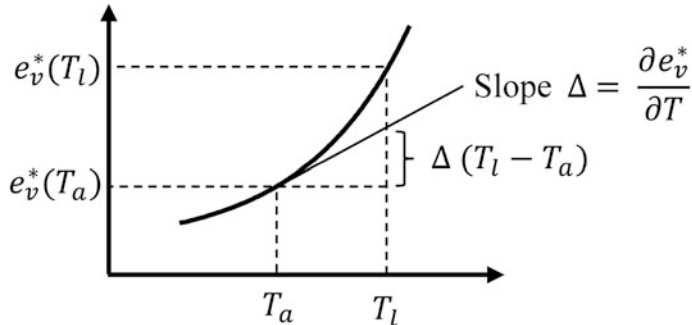


Fig. 10.2 Linear approximation to the saturation vapor pressure function

where r_s , termed the *stomatal resistance*, is an additional resistance the vapor molecules encounter when moving through the stomatal opening and s_v is the vapor mixing ratio outside the leaf boundary layer. Here, the two resistances are connected in series because the vapor molecules must diffuse sequentially through the two pathways (the stomatal opening and the leaf boundary layer). Other situations require connecting diffusion resistances in parallel, such as in some multilayer models of canopy evapotranspiration (Sect. 10.5).

The saturation vapor mixing ratio s_v^* is given by

$$s_v^* = 0.621 e_v^*(T_l)/p_d, \quad (10.5)$$

where $e_v^*(T_l)$ is the saturation vapor pressure at leaf temperature T_l . The factor 0.621 is the ratio of molecular mass of water to that of dry air. Using the Taylor expansion but keeping only the first-order term, we can express $e_v^*(T_l)$ as a linear function of T_l (Fig. 10.2):

$$e_v^*(T_l) \simeq e_v^*(T_a) + \Delta(T_l - T_a), \quad (10.6)$$

where $\Delta = \partial e_v^*/\partial T$, the slope of the saturation vapor pressure at T_a , is a function of temperature, increasing from 1.10 hPa K^{-1} at 15°C to 1.90 hPa K^{-1} at 25°C . Linearizing the saturation vapor pressure function allows us to obtain an analytical solution of the problem.

The relationship between s_v and the vapor pressure e_v is given by

$$s_v = 0.621 e_v / p_d. \quad (10.7)$$

A unique solution exists for the three unknowns (H_l , E_l , and T_l) from the three basic equations (Eqs. 10.1, 10.2, and 10.4). Full implementation of the solution requires parameterizations for the two resistance terms and measurement of the forcing variables ($R_{n,l}$, T_a , e_v , and so on). The boundary layer resistance is commonly parameterized as

$$r_b = \frac{1}{C_l} \sqrt{\frac{d_l}{u_l}} \quad (10.8)$$

where d_l is leaf dimension in m, u_l is wind speed in m s^{-1} , and the leaf heat exchange coefficient C_l is approximately $0.01 \text{ m s}^{-1/2}$ (Oleson et al. 2004). For a larger leaf and at a lower wind speed, the leaf boundary layer is thicker, and Eq. 10.8 indicates that heat transfer is more difficult.

Two parameterizations are commonly used for the stomatal resistance. The Jarvis-Stewart parameterization is a multiplicative method aiming to capture the combined effect of four key environmental controls on stomatal behaviors. Let $r_{s,m}$ be the minimum stomatal resistance observed when the stomata are fully open under conditions of full sunlight, ample soil water, optimal temperature, and zero vapor pressure deficit. The actual stomatal resistance is given as

$$\frac{1}{r_s} = \frac{1}{r_{s,m}} f_1(K_\downarrow) f_2(M) f_3(T_l) f_4(D), \quad (10.9)$$

where K_\downarrow is solar radiation incident on the leaf surface, M is soil moisture status, T_l is leaf temperature, D is *vapor pressure deficit* defined as

$$D = e_v^*(T_a) - e_v,$$

and functions f_1 to f_4 are adjustment factors smaller than unity to account for deviation from the optimal conditions.

The second stomatal resistance parameterization, attributed to Ball et al. (1987) and Collatz et al. (1991), takes the form,

$$\frac{1}{r_s} = m \frac{A_n}{c_s} h_s + b, \quad (10.10)$$

where A_n is net photosynthesis, m and b are empirical coefficients, and c_s and h_s are the CO_2 mixing ratio and relative humidity at the leaf surface, respectively. Equation 10.10 contains fewer site-specific parameters than the more empirical Eq. 10.9 but requires that leaf photosynthesis be modeled concurrently.

Equation 10.4 describes the evaporation of a dry leaf whose source of water vapor is the interior of the stomata. For a wet leaf covered by dew or rainwater, the source of water vapor is the water film on the leaf surface, and the evaporation rate should be calculated by setting the stomatal resistance to zero.

Equations 10.1, 10.2, and 10.4 can be used to derive an expression for the *wet bulb temperature* T_w . This temperature is measured by a thermometer wrapped in wet cloth in a well-ventilated enclosure. The wet cloth behaves just like the water film on a wet leaf. The net radiation energy of the thermometer is negligible, and the evaporation of the wet cloth is supported by sensible heat originated from the air outside the “leaf” boundary layer (Fig. 10.3). The surface energy balance is written as

$$\rho_d c_p \frac{T_w - T_a}{r_b} + \lambda \rho_d \frac{s_v^* - s_v}{r_b} = 0. \quad (10.11)$$

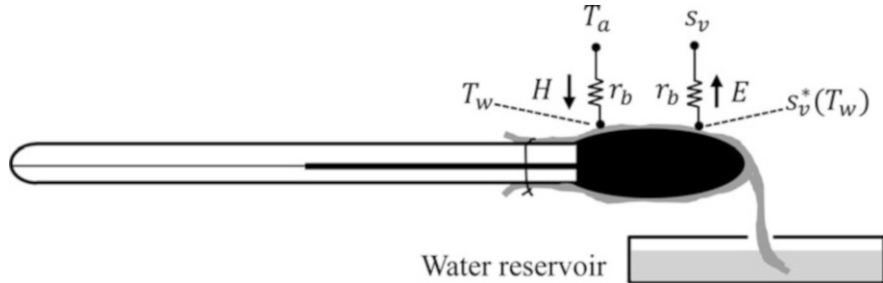


Fig. 10.3 Energy balance of a wet bulb thermometer

Making use of Eq. 10.6, we obtain the solution

$$T_w = T_a - \frac{D}{\Delta + \gamma}, \quad (10.12)$$

where $\gamma = p_d c_p / (0.621\lambda)$ is the *psychrometric constant* ($= 0.66 \text{ hPa K}^{-1}$ at sea level). This solution is independent of r_b . The wet bulb depression $T_a - T_w$ is a measure of air humidity: it is zero at saturation ($D = 0$) and increases with decreasing humidity. The wet bulb temperature is a useful heat stress index (Problem 10.4).

10.2 Canopy Energy Balance and the Big-Leaf Model

The resistance analogy can be easily extended to describing canopy evaporation and sensible heat flux. Ignoring heat storage in the canopy layer, the surface energy balance equation 2.47 becomes

$$R_n - G = H + \lambda E. \quad (10.13)$$

The canopy sensible heat flux is conceptualized to originate from a “big leaf” located at approximately the height of zero-plane displacement. The diffusion pathway is the air layer between this hypothetical leaf and the reference height at which atmospheric forcing variables are measured (Fig. 10.4). Unlike the leaf boundary layer in which diffusion is molecular, this air layer is fully turbulent whose diffusion resistance is the aerodynamic resistance r_a given by Eq. 4.44. (Hereafter we will omit the second subscript h .) The canopy sensible heat flux is expressed as

$$H = \rho_d c_p \frac{T_s - T_a}{r_a} \quad (10.14)$$

where T_s is canopy or surface temperature and T_a is air temperature at the reference height.

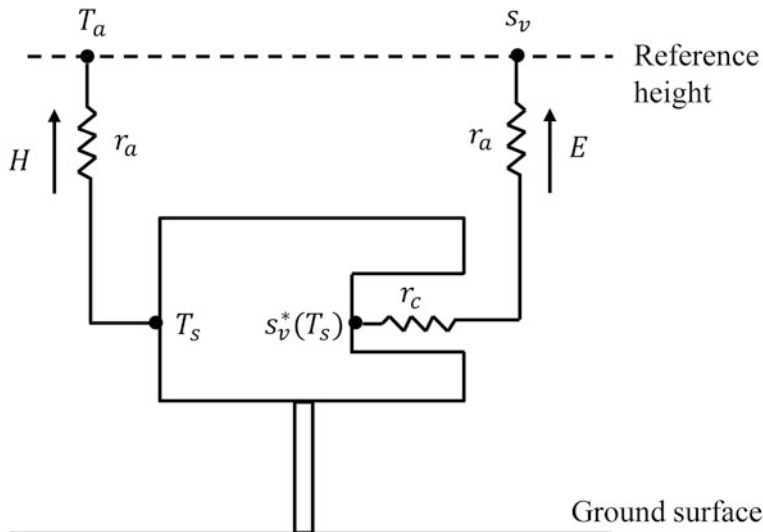


Fig. 10.4 The Penman-Monteith big-leaf model of canopy sensible heat flux and canopy evaporation

To obtain the canopy-scale evaporation rate, we replace the numerous leaf stomata in the canopy by a bulk stoma as the effective source of water vapor. The air inside this “stomatal cavity” is at saturation in reference to the surface temperature. We introduce the *canopy resistance* r_c to represent the diffusion pathway between this imagined stoma and the ambient air. The surface evaporation rate or water vapor flux is given by

$$E = \rho_d \frac{s_v^* - s_v}{r_a + r_c}. \quad (10.15)$$

Deploying the linear approximation

$$e_v^*(T_s) \simeq e_v^*(T_a) + \Delta(T_s - T_a) \quad (10.16)$$

and eliminating T_s and H in favor of E from Eqs. 10.13, 10.14, and 10.15, we obtain the solution for E

$$E = \frac{1}{\lambda} \frac{\Delta(R_n - G) + \rho_d c_p D / r_a}{\Delta + \gamma(r_a + r_c) / r_a} \quad (10.17)$$

This equation is the classic *Penman-Monteith big-leaf model* of evaporation.

Equation 10.17 expresses both physical and physiological controls on surface evaporation. The physical control, also referred to as atmospheric demand, is determined by the energy available for evaporation ($R_n - G$) and the vapor pressure

deficit (D). The physiological control is exerted by the canopy resistance r_c . In wet climates where the canopy resistance is small, surface evaporation is energy-limited, whereas in dry climates, the limiting factor is low soil moisture availability or large r_c .

Because the aerodynamic resistance r_a is generally smaller than the canopy resistance r_c , surface evaporation is not too sensitive to wind speed or turbulence intensity. This is especially true for rough surfaces such as tall forests.

The aerodynamic resistance r_a has a clear physical meaning (it describes the diffusion property of the atmospheric surface layer) and a simple mathematical interpretation (it is the vertical integral of the inverse of the eddy diffusivity) (Eq. 3.75). In comparison, the canopy resistance r_c is much harder to quantify and interpret. If all the leaves in the canopy have the same stomatal resistance, r_c can be considered an effective resistance of a network of L resistors connected in parallel, each having a resistance value r_s , so that

$$r_c = r_s/L, \quad (10.18)$$

where L is leaf area index. The stomatal resistance r_s can be measured directly or estimated with physiological models such as Eq. 10.10.

Equation 10.18 tends to underestimate the canopy resistance of a real canopy because contribution to surface evaporation is not equal among the leaves (Kelliher et al. 1995). Leaves in the upper part of the canopy, being exposed to sunlight, have higher evaporation rate and lower stomatal resistance than those in the lower canopy under low light conditions. An improved estimate of r_c is obtained by averaging the leaf stomatal resistance with a weighting factor in inverse proportion to the solar radiation intensity at different heights in the canopy.

Equation 10.17 can be used to determine *potential evaporation*, or the rate of evaporation that would occur if soil water supply were unlimited. Being a measure of atmospheric demand for evaporation, potential evaporation is a pure atmospheric quantity and is independent of physiological processes. Actual evaporation cannot exceed this theoretical limit. For lakes, wetlands, and ecosystems of short stature (short crops and grasses) and with ample soil moisture, evaporation occurs at the potential rate. Because r_c/r_a under these conditions is either zero or much smaller than unity, the expression for potential evaporation becomes

$$\lambda E = \frac{\Delta}{\Delta + \gamma} (R_n - G) + \frac{\rho_d c_p D}{(\Delta + \gamma) r_a} \quad (10.19)$$

According to empirical data, the second term on the right side of Eq. 10.19 is highly correlated with the first term. The ratio of the second term to the first term is roughly 0.26. Combining this empirical result with Eq. 10.19, we obtain the *Priestley-Taylor equation* for potential evaporation:

$$\lambda E = \alpha \frac{\Delta}{\Delta + \gamma} (R_n - G), \quad (10.20)$$

where $\alpha \simeq 1.26$. Equation 10.20 removes the dependence on the vapor pressure deficit and the aerodynamic resistance. Only available energy and air temperature observations are required to estimate potential evaporation. The equation with the original coefficient value of 1.26 is applicable to lakes and short vegetation. For tall forests, the coefficient α is lower than 1.26 because r_a is very small and the ratio r_c/r_a is no longer negligible even under conditions of high soil water content.

To aid management of cropland irrigation, the World Food and Agriculture Organization proposes a standardized method for computing potential evaporation with the Penman-Monteith equation. The reference surface is a well-watered short grass of height 0.12 m. The canopy resistance takes a standard value of 70 s m^{-1} . The aerodynamic resistance is given by the surface layer relationship in neutral stability:

$$r_a = \frac{1}{k^2 u} \ln \frac{z - d}{z_o} \ln \frac{z - d}{z_{o,h}}. \quad (10.21)$$

where the displacement height $d = 0.08 \text{ m}$, the momentum roughness $z_o = 0.015 \text{ m}$, and the thermal roughness $z_{o,h} = 0.0015 \text{ m}$. The evaporation rate computed with this method is called *reference evaporation*.

10.3 One-Source Model in Remote Sensing Applications

Equations 10.14 and 10.15 form the fundamental basis for modeling surface-air energy and water vapor exchanges, but their application was hindered historically by the lack of surface temperature (T_s) measurement. This difficulty has been overcome by the Penman-Monteith equation: by linearizing the saturation vapor pressure function and by combining these equations with the energy balance equation, we have eliminated T_s as an input variable. However, T_s is now routinely measured by environmental satellites at the landscape scale and by thermal sensors at the field scale. The availability of T_s data has motivated the development of a one-source model as an alternative to the Penman-Monteith model (Kustas and Anderson 2009).

The one-source model is based on the top-down or bird's eye perspective of a thermal sensor mounted above the surface. Different heat sources in the sensor's field of view, including sunlit foliage, shaded foliage, and exposed soil, all contribute to the outgoing longwave radiation L_\uparrow the sensor receives. If the actual surface emissivity is known and the downward longwave radiation is also measured, T_s can be solved from Eq. 2.44. Otherwise, T_s is approximated by the inverted Stefan-Boltzmann law as

$$T_s = (L_\uparrow / \sigma)^{1/4}. \quad (10.22)$$

Since most natural objects emit longwave radiation at nearly the same rate as a blackbody, Eq. 10.22 is reasonably accurate. The one-source model treats the surface as if it were made of a single source having an effective temperature T_s .

Now that T_s is a known quantity, determination of the surface heat fluxes would seem straightforward: the surface sensible heat flux could be calculated with Eq. 10.14 and the latent heat flux as a residual of the surface energy balance (Eq. 10.13). Parameterization of the canopy resistance is no longer required. However, it is found that H calculated with the original resistance formula (Eq. 10.14) is biased too high. To correct this high bias, we must introduce an additional resistance r_m , called the *radiometric resistance*, and rewrite the resistance formula as

$$H = \rho_d c_p \frac{T_s - T_a}{r_a + r_m}. \quad (10.23)$$

The latent heat flux is then computed as

$$\lambda E = R_n - G - H. \quad (10.24)$$

In this modified resistance analogy (Fig. 10.5), we make a distinction between the aerodynamic surface temperature T_o and the radiometric surface temperature T_s . The former is an aerodynamic variable, found by extrapolating the air temperature profile to the height of the thermal roughness $z_{o,h}$ (Eq. 4.41), whereas the latter is a radiative property of the surface involved in the surface radiation and energy balance (e.g., Eq. 10.37 below). These two temperatures do not differ much for a dense canopy. For a bare soil or a spare canopy, T_s can be a few degrees higher than T_o in unstable conditions. The aerodynamic resistance r_a represents the diffusion resistance to heat between $z_{o,h}$ and the reference height. The diffusion resistance between the surface and $z_{o,h}$ is given by the radiometric resistance r_m .

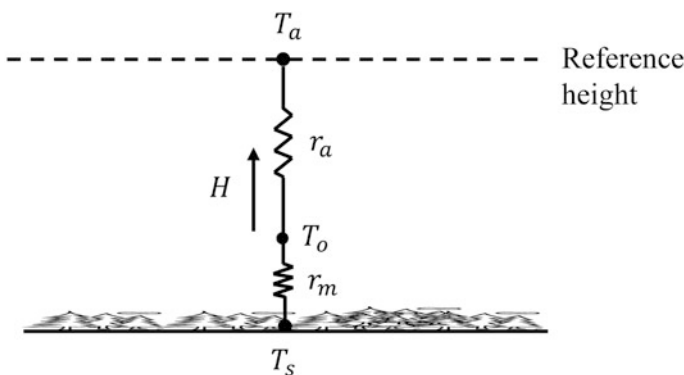


Fig. 10.5 One-source model of sensible heat flux for remote sensing applications. The vertical dimension is not drawn to scale

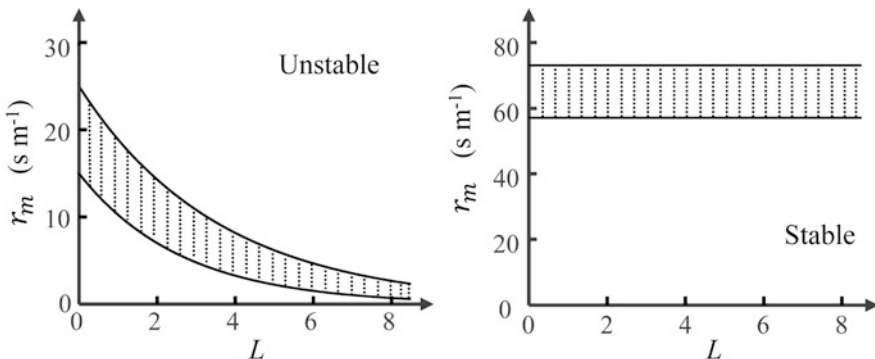


Fig. 10.6 Relationship between the radiometric resistance r_m and leaf area index L in unstable (left) and stable (right) conditions. The two solid lines indicate the uncertainty range of r_m (Data source: Zhao et al. 2016)

Figure 10.6 depicts the general behaviors of the radiometric resistance r_m as a function of leaf area index (LAI) L . In unstable conditions, r_m increases exponentially with decreasing L . As L decreases, the role of soil becomes increasingly important in the surface-air heat exchange. It appears that the laminar layer of the ground-level soil source imposes a stronger barrier to heat diffusion than the leaf boundary layer of the elevated foliage sources. In stable conditions, r_m appears insensitive to L .

The LAI dependence shown in Fig. 10.6 can be regarded as a crude parameterization of r_m . Additional insights on how r_m should behave for different ecosystem types and in various environmental conditions may be obtained by comparing the one-source model with the surface temperature and the whole-ecosystem sensible heat flux predicted by a two-source model (Sect. 10.4).

The Penman-Monteith equation makes the implicit assumption that T_o and T_s are identical. But because the equation has already been constrained by the surface energy balance, errors associated with this assumption are not serious.

10.4 Two-Source Model of Evaporation

Surface evapotranspiration represents the combined contribution of water vapor evaporated from the soil and that transpired from the plants. These component fluxes (soil evaporation and plant transpiration) cannot be isolated with either the big-leaf model or the one-source model. But there are practical reasons for why they should be quantified separately. The transpiration flux draws a continuous flow of water through the plant xylem, which serves as a mechanism of nutrient relocation from the root system in the soil to other parts of the plant. It also cools the foliage so as to avoid high temperature damage in hot weather. Water use efficiency, the ratio of

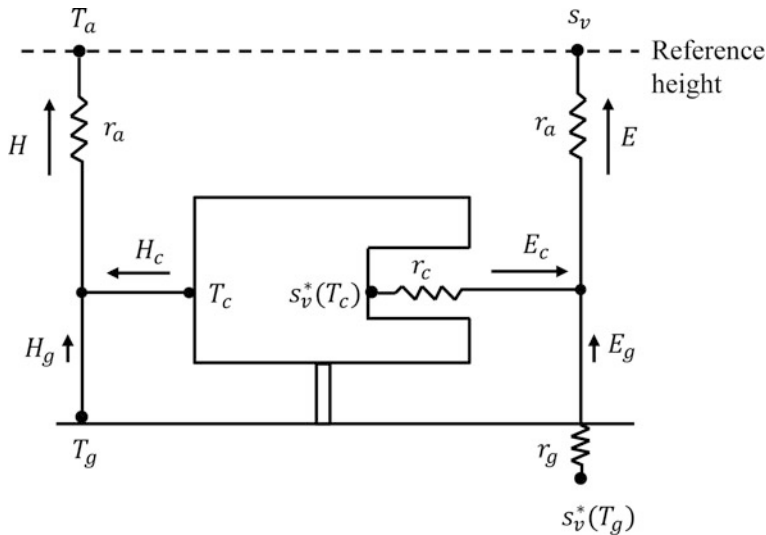


Fig. 10.7 Resistance network of a two-source model of sensible heat and water vapor fluxes (Modified after Shuttleworth and Wallace 1985)

the amount of carbon dioxide assimilated by photosynthesis to the amount of water lost via transpiration, is a relatively stable parameter among C3 and C4 crops. If the transpiration flux is known, cropland productivity can be estimated from the water use efficiency parameter. Soil evaporation, on the other hand, does not participate directly in these biological functions and to a farmer is a stream of wasted water. One goal of farmland water resource management is to minimize soil evaporation.

The two-source model aims to predict soil evaporation E_g and canopy transpiration E_c using parameters that specify biological and soil moisture controls on these fluxes and standard micrometeorological variables measured above the canopy (Shuttleworth and Wallace 1985). Figure 10.7 is a schematic diagram of the model structure. The model is a compromise between simplicity and realism. Specifically, we make three simplifications. First, the canopy airspace has no resistance to the water vapor originated from the ground surface, meaning that soil evaporation occurs in parallel to plant transpiration. This is a fair approximation for a sparse canopy where turbulent mixing in the canopy air is vigorous (Norman et al. 1995). For a closed canopy, this approximation leads to overestimation of E_g , especially if the soil is wet.

Second, soil evaporation is conceptualized to occur at an evaporation front where the vapor mixing ratio is at saturation in reference to the ground temperature T_g . The evaporation front is the ground surface for a soil saturated with water and is at some depth below the surface for a dry soil. In the case of a dry soil, the vapor molecules must move through the pore space in the top soil layer before escaping into the open canopy airspace. The diffusion resistance of this pathway is specified by a bulk ground resistance r_g . Soil moisture control on E_g is realized through parameterization of r_g as a function of soil moisture.

Third, the plants are assumed to be uniformly dispersed in the horizontal directions so that radiation transmission in the canopy can be described by a simple one-dimensional Beer's law model. Features of horizontal inhomogeneity, such as those found in row crops and savanna ecosystems, are filtered out by averaging flux and state variables over a sufficiently large area. The surface is characterized by a single albedo value and a single net radiation flux. The predicted soil evaporation flux is the mean contribution of the soil shaded by the plants and that exposed to sunlight in gaps between the plants. The net radiation of the canopy layer $R_{n,c}$ and that of the ground surface $R_{n,g}$ are given by

$$R_{n,c} = R_n [1 - \exp(-aL)], \quad (10.25)$$

and

$$R_{n,g} = R_n \exp(-aL), \quad (10.26)$$

where R_n is net radiation above the canopy, a is an empirical light extinction coefficient, and L is leaf area index. A widely used value for a is 0.7.

Applying the Penman-Monteith method of derivation separately to the canopy and the soil component, we obtain

$$E_c = \frac{1}{\lambda} \frac{\Delta R_{n,c} + \rho_d c_p D/r_a}{\Delta + \gamma(r_a + r_c)/r_a}, \quad (10.27)$$

and

$$E_g = \frac{1}{\lambda} \frac{\Delta(R_{n,g} - G) + \rho_d c_p D/r_a}{\Delta + \gamma(r_a + r_g)/r_a}. \quad (10.28)$$

The total surface evaporation flux is given by

$$E = E_c + E_g. \quad (10.29)$$

In the limit $L \rightarrow 0$, $R_{n,c}$ vanishes, r_c is infinitely large, and E is contributed solely by soil evaporation. In the other limit ($L \rightarrow$ large values), even though the energy available for soil evaporation ($R_{n,g} - G$) vanishes, E_g does not go to zero as expected because of the vapor pressure deficit term. This problem is a consequence of omitting the resistance to water vapor diffusion in the canopy airspace and can be solved by inclusion of this resistance in a modified version of the two-source model (Fig. 10.9a).

The two-source model can be evaluated against observational data on the component fluxes. Evaluation can also be performed against the surface temperature measured with a thermal sensor. A downward-facing thermal sensor mounted above the canopy senses the longwave radiation emitted by both the canopy and the ground surface. Let f_c be the fraction of its field of view occupied by the canopy.

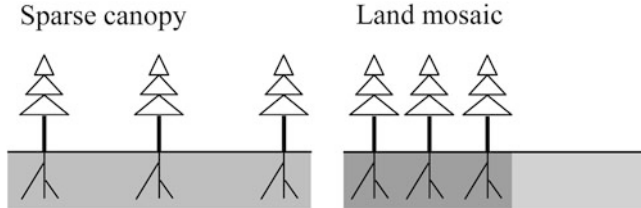


Fig. 10.8 Sparse canopy (left) and land mosaic (right) (Modified after Schultz et al. 2016)

The effective surface temperature measured by this thermal sensor is a weighted mean of the canopy temperature T_c and the ground surface temperature T_g , as

$$T_s = [f_c T_c^4 + (1 - f_c) T_g^4]^{1/4}. \quad (10.30)$$

The two-source model should not be confused with a tile or mosaic scheme used in some climate models. Figure 10.8 illustrates their differences. In this example, both configurations have the same number of plants, but the plants are arranged differently. In the case of a sparse canopy, the plants are dispersed uniformly, creating a savanna-type landscape. These plants and the exposed soil draw water for evaporation from the same soil water pool and share identical atmospheric forcing conditions. The total evaporation flux is the sum of soil evaporation and plant transpiration (Eq. 10.29), whereby weighting of the contributions of the two component fluxes is achieved indirectly by partitioning of the net radiation flux (Eqs. 10.25 and 10.26).

In the land mosaic case shown in Fig. 10.8, the model grid cell consists of two subgrid tiles, with the plants clumped in one tile and the open soil occupying the other, each having its own independent soil water pool. Even though they receive the same amounts of incoming shortwave and longwave radiation (Fig. 10.12), these tiles have different net radiation fluxes because their albedo values and surface temperatures are different. The grid-cell water vapor flux is an area-weighted mean of the two subgrid fluxes:

$$E = a_1 E_1 + a_2 E_2, \quad (10.31)$$

where E_1 and E_2 are water vapor fluxes and a_1 and a_2 are area fractions of the two tiles.

10.5 Improved Representations of Surface-Air Exchange

An obvious way of improving the two-source model is to incorporate the canopy turbulence (Chap. 5) in the model parameterization. The improved version, shown in Fig. 10.9a, includes a bulk foliage resistance, which is an extension of the leaf boundary layer resistance at the canopy scale, to the transpiration vapor

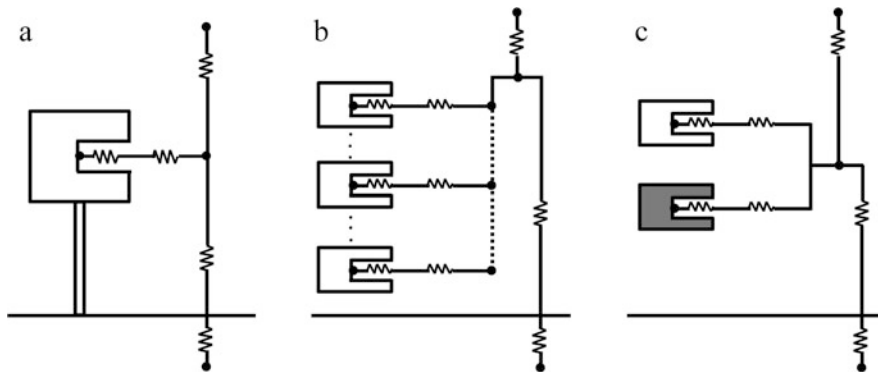


Fig. 10.9 Resistance network in three models of evaporation. (a) An improved two-source model; (b) a multilayer model; (c) a two-leaf model

flux, and an in-canopy aerodynamic diffusion resistance to the vapor evaporated from the soil (Shuttleworth and Wallace 1985). These two additional resistances are parameterized as functions of canopy foliage density, wind speed, and eddy diffusivity. This version overcomes the problem at the large L limit: the in-canopy aerodynamic resistance to soil evaporation increases with increasing leaf area index L , so that soil evaporation E_g vanishes as L approaches large values.

In a multilayer framework (Fig. 10.9b), the plant canopy is divided into multiple layers, each having a leaf area ΔL (Baldocchi and Harley 1995). The energy balance principle is applied to each layer, and the sensible and latent heat fluxes are determined layer by layer. Let $r_{s,i}$ and $r_{b,i}$ be the stomatal and the leaf boundary layer resistance for foliage layer i . The diffusion of water vapor originated from layer i encounters three resistances, a mean stomatal resistance $r_{s,i}/(\Delta L)$, a mean leaf boundary layer resistance $r_{b,i}/(\Delta L)$, and the usual aerodynamic resistance r_a . Since the bulk canopy resistance is no longer needed, the multilayer model is more rigorous than the big-leaf and the two-source models. A prerequisite for a successful multilayer model is accurate description of the transmission of solar radiation through the canopy because the solar radiation flux is required for the energy balance calculation for each foliage layer and because the stomatal resistance is strongly dependent on solar radiation. The total ecosystem water vapor and sensible heat flux are the sums of contributions from all the foliage layers and from the soil. Another model output is the vertical distribution of foliage temperature. (Some multilayer models can also predict air humidity and air temperature profile in the canopy.)

A hybrid between the two-source model and the multilayer model is called the two-leaf model (Fig. 10.9c; Wang and Leuning 1998). We conceptualize that the canopy be composed of two big leaves, a sunlit leaf and a shaded leaf. Partition of the foliage layer into sunlit and shaded groups is based on Beer's law of beam radiation transmission, taking into account of the geometry of solar angle and leaf angular distribution. The two-leaf model is computationally simple and achieves accuracies that are comparable to those of the multilayer model. This success is

attributed to the observed pattern that leaves in the same group have similar leaf temperature T_l and stomatal resistance r_s but have very different T_l and r_s from leaves in the other group.

10.6 One-Source Model of Surface Temperature

Models of the surface fluxes of heat and water vapor, the focus of our discussion so far, serve several functions. They permit calculation of the lower boundary conditions for atmospheric models, provide insights into ecosystem processes, and form an important component of the local hydrological cycle. In this section, we turn our attention away from this traditional focus to prediction of the surface temperature. The question we wish to investigate is this: how will the surface temperature change if one type of land use is replaced by another? Deforestation, or replacement of a forest by open land such as bare soil and grass, and urbanization, or replacement of natural land with an engineered landscape, are two classic examples of land use change.

Local radiative feedback and energy redistribution are two key mechanisms that govern how the surface temperature T_s responds to changes in land cover. To elucidate the first mechanism, let us consider a world without an atmosphere. Here, energy transfer involves only radiation processes, and the surface energy balance equation is simply that of the radiation balance:

$$(R_n =) S + L_{\downarrow} - \sigma T_s^4 = 0, \quad (10.32)$$

where

$$S = (1 - \alpha)K_{\downarrow} \quad (10.33)$$

is the net shortwave radiation flux and α is surface albedo. For simplicity, the surface is assumed to be a blackbody and consist of one source. Now let us suppose that the surface is suddenly replaced by a new type with a different albedo, causing S to increase to $S + \Delta S$. The surface will warm up, and the outgoing longwave radiation will increase accordingly, in a process termed the *longwave radiation feedback*, until a new state of energy balance is established:

$$S + \Delta S + L_{\downarrow} - \sigma(T_s + \Delta T_s)^4 = 0, \quad (10.34)$$

where $T_s + \Delta T_s$ is the surface temperature in this new state. Manipulating Eqs. 10.32, 10.33, and 10.34 yields the solution for the temperature perturbation ΔT_s :

$$\Delta T_s = \lambda_0 \Delta S, \quad (10.35)$$

where

$$\lambda_0 = 1/(4\sigma T_s^3) \simeq 1/(4\sigma T_a^3), \quad (10.36)$$

is the temperature sensitivity resulting from the longwave radiation feedback and is approximately $0.2 \text{ K W}^{-1} \text{ m}^2$. Parameter λ_0 , termed the *local climate sensitivity*, is a weak function of temperature, so it can be formulated using either the surface temperature or the air temperature (Eq. 10.36). Equation 10.35 predicts that the surface temperature will increase by about 1 K for a 5 W m^2 increase in the net shortwave radiation.

Equation 10.35 implies that a darker surface should always be warmer than a brighter surface when exposed to the same amount of incoming shortwave radiation. However, the opposite can occur in the real world. For example, it has been observed that despite having much lower albedo, a needle-leaf plantation forest in Israel is actually 5 K cooler in the daytime than an adjacent shrub land. The paradoxical situation exists because the temperature of a surface in the real world is also influenced by *energy redistribution* via convection and evaporation. Prediction of the surface temperature perturbation must consider convection, which dissipates sensible heat from the surface to the atmospheric boundary layer, and evaporation, which removes latent heat from the surface and deposits it above the atmospheric boundary layer by cloud condensation (Fig. 10.10).

The proper framework for developing a surface temperature model is the complete energy balance equation:

$$(1 - \alpha)K_{\downarrow} + L_{\downarrow} - \sigma T_s^4 = H + \lambda E + G. \quad (10.37)$$

Here the sensible heat flux is given by Eq. 10.23 and the latent heat flux is given by

$$\lambda E = H/\beta, \quad (10.38)$$

where β is Bowen ratio. Linearizing the outgoing longwave radiation as

$$\sigma T_s^4 \simeq \sigma T_a^4 + 4\sigma T_a^3(T_s - T_a)$$

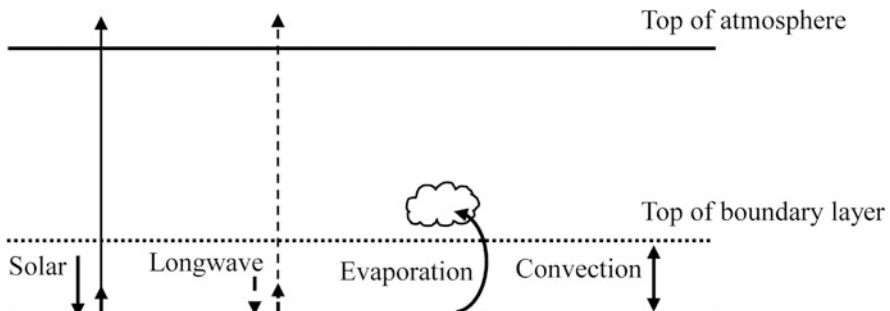


Fig. 10.10 Radiation processes versus energy redistribution via evaporation and convection

and making use of Eqs. 10.23 and 10.38, we obtain a solution for T_s from Eq. 10.37,

$$T_s = T_a + \frac{\lambda_0}{1+f}(R_n^* - G), \quad (10.39)$$

where

$$R_n^* = (1 - \alpha)K_{\downarrow} + L_{\downarrow} - \sigma T_a^4 \quad (10.40)$$

is apparent net radiation,

$$f = \frac{\rho_d c_p \lambda_0}{r_T} \left(1 + \frac{1}{\beta} \right) \quad (10.41)$$

is a dimensionless *energy redistribution factor*, and

$$r_T = r_a + r_m \quad (10.42)$$

is the total resistance to sensible heat diffusion.

In Eq. 10.39, T_a is air temperature at the first grid height of the atmospheric model in a modeling study or at the blending height in a site-pair analysis (Fig. 10.12). Blending height is a height scale in a heterogeneous landscape, above which the flow is fully “blended” so that the influences of individual land patches are no longer discernible.

The temperature perturbation caused by land use change is found by differentiating Eq. 10.39, as

$$\Delta T_s \simeq \frac{\lambda_0}{1+f}(\Delta S) + \frac{\lambda_0}{(1+f)^2}R_n^*(\Delta f_1) + \frac{\lambda_0}{(1+f)^2}R_n^*(\Delta f_2), \quad (10.43)$$

where

$$\Delta f_1 = f \frac{\Delta r_T}{r_T}, \quad (10.44)$$

$$\Delta f_2 = \frac{\rho_d c_p \lambda_0}{r_T} \left(\frac{\Delta \beta}{\beta^2} \right), \quad (10.45)$$

and the soil heat flux term is omitted (Lee et al. 2011). We have used the fact that T_a , L_{\downarrow} , and other atmospheric forcing variables remain unchanged because the land use change in question occurs at a scale that is too small to influence the overlaying atmosphere.

Equation 10.43 expresses explicitly the controls of three key biophysical factors, albedo, surface roughness, and evaporation, on ΔT_s . The first, second, and third terms on the right side of Eq. 10.43 represent radiative forcing associated

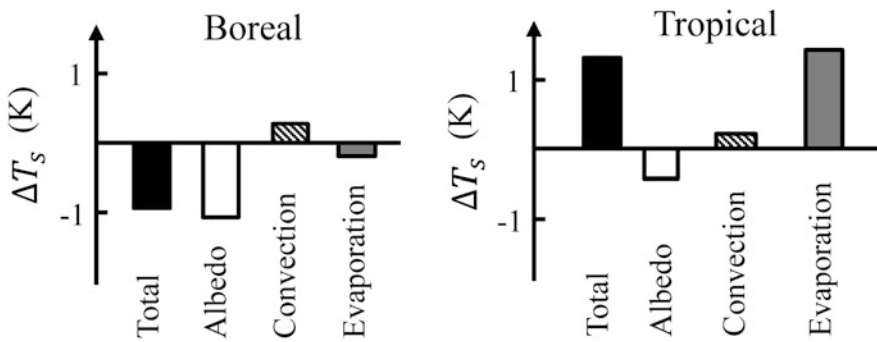


Fig. 10.11 Contributions of three biophysical factors to surface temperature change brought by deforestation (left panel, boreal climate; right panel, tropical climate) (Data source: Lee et al. 2011)

with albedo change, energy redistribution associated with roughness change, and energy redistribution associated with Bowen ratio change or change in evaporation, respectively. Because the inverse of the total resistance r_T is a measure of efficiency of energy dissipation by convective motion, the second term can also be interpreted as contribution of changes in convection efficiency to ΔT_s . Figure 10.11 is an illustration on how these biophysical factors contribute to the surface temperature change brought by deforestation.

Comparing the first term on the right side of Eq. 10.43 with the radiative feedback solution (Eq. 10.35), we find that energy redistribution always damps the climate sensitivity, keeping in mind that f is generally positive. In other words, the actual temperature perturbation associated with land use change is smaller in magnitude than that predicted from the radiative feedback mechanism alone.

Evaluation of Eq. 10.43 can be performed with a site-pair strategy or space-for-time substitution (Fig. 10.12). In experimental research, the change terms on the right side of the equation are determined by measurements at a pair of adjacent sites under the same atmospheric conditions and representing the two types of land use in question. In modeling studies, the site pair consists of two subgrid tiles in the same model grid.

Equation 10.43 applies to natural surfaces only. In the case of urbanization, ΔT_s is either temporal change in the surface temperature resulting from replacement of a natural surface by an urban landscape or difference in the surface temperature between urban and the adjacent rural land in the site-pair analysis. In other words, the temperature perturbation is equivalent to the *urban heat island intensity*. Anthropogenic heat release (Q_A) is an added energy input to the energy balance and should increase the surface temperature of the urban land. Buildings and other artificial materials can store more radiation energy in the daytime than can natural vegetation and soil; release of the stored heat (Q_S) at night contributes to nighttime warming. For urban studies, Eq. 10.43 is amended to:

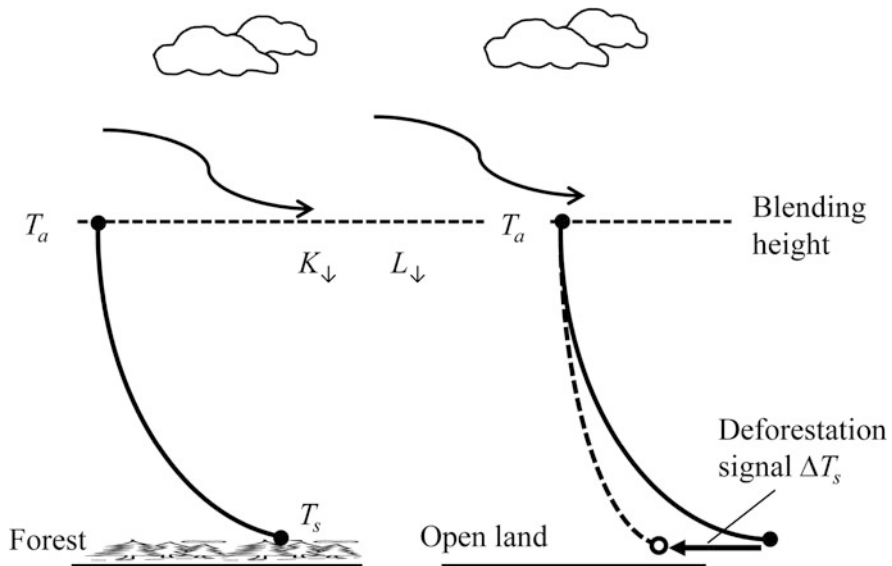


Fig. 10.12 A site-pair strategy for quantifying biophysical contributions of deforestation to the surface temperature change. Atmospheric forcing variables are identical between the paired sites or subgrid land tiles

$$\begin{aligned}\Delta T_s \simeq & \frac{\lambda_0}{1+f} (\Delta S) + \frac{\lambda_0}{(1+f)^2} (R_n^* - Q_S + Q_A) (\Delta f_1) \\ & + \frac{\lambda_0}{(1+f)^2} (R_n^* - Q_S + Q_A) (\Delta f_2) \\ & + \frac{-\lambda_0}{1+f} (\Delta Q_S) + \frac{\lambda_0}{1+f} Q_A.\end{aligned}\quad (10.46)$$

Equation 10.46 is the basis for attribution analysis of the urban heat island. The terms on the right side of the equation represent contributions to the urban heat island from changes in albedo (Term 1), convection efficiency (Term 2), evaporation (Term 3), and heat storage (Term 4) and from anthropogenic heat release (Term 5).

We note that other solutions for the surface temperature exist in the literature. For example, a solution can be derived from the Penman-Monteith big-leaf framework (Eq. 10.47, Problem 10.11). The Penman-Monteith solution requires that the surface net radiation R_n be given as an input variable. But because R_n itself depends on T_s (Eqs. 2.44 and 2.45), this solution is an implicit function, and as such it is not suitable for factor attribution analysis.

10.7 Problems

10.1 Calculate the leaf-scale sensible and latent heat flux using the following data: boundary layer resistance = 16 s m^{-1} , stomatal resistance = 50 s m^{-1} , leaf temperature = 16.3°C , air temperature = 14.6°C , and water vapor mixing ratio = 17.8 g kg^{-1} .

10.2 What is the vapor pressure deficit if air temperature is 12.1°C and relative humidity is 48.5%?

10.3 When exposed to solar radiation, thermometers can significantly overestimate air temperature. Determine measurement error for thermometers of $20 \mu\text{m}$ in diameter (fine-wire thermocouples) and 0.5 cm in diameter (mercury thermometers). Do the calculation for two levels of wind speed (0.1 and 10 m s^{-1}) and with the thermometers in the shade (net radiation 2 W m^{-2}) and exposed to the Sun (net radiation 50 W m^{-2}). Can you suggest preventive measures to minimize the bias error? (Hint: These thermometers satisfy the energy balance equation for non-evaporating leaves.)

10.4 Humans are homeotherms whose deep body temperature is regulated at about 37°C . In order to dissipate metabolic heat generated internally, they must keep the skin temperature lower than 35°C . Otherwise their deep body temperature will increase, leading to heatstroke or even death. Calculate the skin temperature of a naked and perspiring human body in hot and humid conditions (air temperature 38.3°C and relative humidity 54.5%). Now repeat the calculation by increasing the air temperature by 2 and 4°C to simulate heat stress and human health effects caused by the urban heat island and by global warming, respectively. Under which scenario(s) is the threshold temperature of 35°C exceeded? (Hint: The perspiring human body can be considered as a wet bulb.)

10.5 Derive the Penman-Monteith Eq. 10.17 from Eqs. 10.13, 10.14, and 10.15.

10.6 The available energy is 293.4 W m^{-2} , the vapor pressure deficit is 7.1 hPa , the aerodynamic resistance is 44 s m^{-1} , and the air temperature is 15.2°C . Find the evaporation rate of a dry surface (canopy resistance 109 s m^{-1}) and a wet surface (canopy resistance 0 s m^{-1}) using the Penman-Monteith equation.

10.7 Using the Penman-Monteith equation, explain why evaporation can take place even without any available energy (i.e., $R_n - G = 0$). Where does the energy that supports the evaporation come from? When this occurs, is the surface air layer statically stable or unstable?

10.8 (a) Determine the canopy resistance r_c of a well-watered soybean crop by inverting the Penman-Monteith equation. The latent heat flux λE is 365.0 W m^{-2} , the available energy flux $R_n - G$ is 388.8 W m^{-2} , the vapor pressure deficit D is 26.6 hPa , the air temperature T_a is 30.1°C , and the aerodynamic resistance r_a is 92 s m^{-1} . (b) Repeat the calculation for a temperate evergreen forest under drought stress ($\lambda E = 119.8 \text{ W m}^{-2}$, $R_n - G = 487.9 \text{ W m}^{-2}$, $D = 7.6 \text{ hPa}$, $T_a = 17.4^\circ\text{C}$, and $r_a = 13 \text{ s m}^{-1}$).

10.9 Calculate the reference evaporation rate using a wind speed of 3.5 m s^{-1} at the height of 2.0 m , an air temperature of 17.2°C , a relative humidity of 43.2% , and an available energy flux ($R_n - G$) of 201 W m^{-2} .

10.10* Using the Priestley-Taylor equation 10.20 and the surface energy balance equation 10.13, determine the Bowen ratio for a range of air temperature values ($1\text{--}20^\circ\text{C}$). Present your result in a graph. According to your result, how should the Bowen ratio of lake systems vary with latitude? If two lakes have the same temperature but are located at different altitudes (one on the Tibetan Plateau and the other at the sea level), which lake is expected to have higher Bowen ratio?

10.11 (a) Confirm that the following expression is the big-leaf model solution for the surface temperature:

$$T_s = T_a + \frac{r_a + r_c}{\rho_d c_p} \cdot \frac{\gamma(R_n - G) - \rho_d c_p D / (r_a + r_c)}{\Delta + \gamma(r_a + r_c) / r_a}. \quad (10.47)$$

(b) Green oases are irrigated farmlands whose surface temperature is lower than that of the surrounding dry landscape. Explain why an inversion typically prevails in the surface layer over a green oasis. (c) It is hypothesized that by using white and highly reflective materials as building roofs, a city will turn into a cold island whereby the urban land is cooler than the surrounding rural land. Do you expect unstable lapse conditions or stable inversion over this “white oasis”. Why?

10.12 Figure 10.13 is a comparison of the sensible heat flux calculated with Eq. 10.14 against that measured with eddy covariance over a soybean crop. Explain why the calculated flux is biased high at midday in the early growing season (leaf area index 1.0) and why the bias diminishes as the canopy becomes fully closed in the later part of the growing season (leaf area index 7.6).

10.13 The incoming longwave radiation flux is 437.3 W m^{-2} and the outgoing longwave radiation flux is 494.5 W m^{-2} . Calculate the surface temperature assuming (1) that the surface is a blackbody and (2) that the surface has an emissivity value of 0.97.

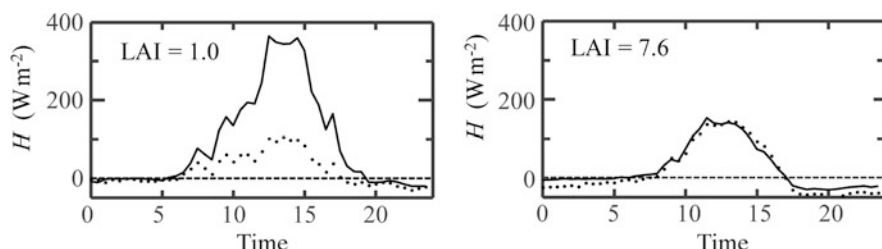


Fig. 10.13 Comparison of observed (dots) and calculated sensible heat flux (lines) for a soybean field. The calculation is made with Eq. 10.14 using the surface temperature measured with an infrared thermometer (Data source: Lee et al. 2009)

Table 10.1 Diagnostic variables of the surface energy balance at midday in the summer for urban and rural land in the Eastern United States: K_{\downarrow} , incoming solar radiation; L_{\downarrow} , incoming longwave radiation; α , surface albedo; r_T , total heat resistance; β , Bowen ratio; Q_S , heat storage; Q_A , anthropogenic heat flux; T_a , air temperature at the blending height

Surface	K_{\downarrow} W m^{-2}	L_{\downarrow} W m^{-2}	α	r_T s m^{-1}	β	Q_S W m^{-2}	Q_A W m^{-2}	T_a K
Urban	709	418	0.18	62	2.3	125	57	299.3
Rural	709	418	0.11	35	1.7	88	0	299.3

10.14 (a) Show that the local climate sensitivity λ_0 has dimensions of $\text{K W}^{-1} \text{m}^2$.
 (b) Determine its value for a temperature of 273 and 293 K.

10.15 A typical energy redistribution factor is 6 at midday and 2 at midnight. Estimate the anthropogenic heat contribution to the urban heat island if the anthropogenic heat flux is 40 W m^{-2} .

10.16* Using the diagnostic data in Table 10.1, estimate the contributions to the urban heat island intensity from changes in surface albedo, convection efficiency, Bowen ratio (or evaporation), and heat storage and from anthropogenic heat release.

10.17* In response to high human mortality in a heat wave event in 1995, the city of Chicago has been promoting the use of reflective roof materials for urban heat mitigation. According to a satellite study, this practice increased the citywide albedo by about 0.02 from 1995 to 2010. Estimate the surface temperature reduction caused by the albedo change. (Hint: Use the data provided in Table 10.1 for your calculation.)

10.18 Using the two-source model, compute the soil evaporation and the plant transpiration of an ecosystem with leaf area index of 4. The canopy resistance r_c is 50 s m^{-1} and the ground resistance r_g is 500 s m^{-1} . The ground heat flux is approximated as $G = 0.2R_{n,g}$. The meteorological conditions are aerodynamic resistance $r_a = 42 \text{ s m}^{-1}$, net radiation $R_n = 400 \text{ W m}^{-2}$, vapor pressure deficit $D = 20 \text{ hPa}$, and air temperature $T_a = 25^\circ\text{C}$.

10.19* Using the two-source model, compute the fraction of total evaporation contributed by plants (E_c/E) as a function of leaf area index L for ecosystems with moist (ground resistance r_g of 500 s m^{-1}) and dry soil (r_g of 2000 s m^{-1}). The mean stomatal resistance r_s is 200 s m^{-1} . The canopy resistance r_c is parameterized by Eq. 10.18, and the ground heat flux is approximated as $G = 0.2R_{n,g}$. The meteorological conditions are the same as in Problem 10.18.

10.20* Atmospheric modelers do not use equations of the Penman-Monteith type to compute the surface flux boundary conditions because the surface net radiation R_n is a predicted variable, not a forcing variable. Instead, they must first solve the surface temperature T_s and then use the resistance formulae to compute the fluxes. Derive an analytical expression for T_s using Eqs. 10.14, 10.15, and 10.37. Assume in your derivation that the ground heat flux is negligible.

References

- Baldocchi DD, Harley PC (1995) Scaling carbon dioxide and water vapour exchange from leaf to canopy in a deciduous forest. II. Model testing and application. *Plant Cell Environ* 18:1157–1173
- Ball JT, Woodrow IE, Berry JA (1987) A model predicting stomatal conductance and its contribution to the control of photosynthesis under different environmental conditions. In: Biggens J (ed) *Progress in photosynthesis research*. Martinus Nijhoff Publishers, Dordrecht
- Collatz GJ, Ball JT, Grivet G, Berry JA (1991) Regulation of stomatal conductance and transpiration: a physiological model of canopy processes. *Agric For Meteorol* 54:107–136
- Kelliher FM, Leuning R, Raupach MR, Schulze ED (1995) Maximum conductances for evaporation from global vegetation types. *Agric For Meteorol* 73:1–16
- Kustas W, Anderson M (2009) Advances in thermal infrared remote sensing for land surface modeling. *Agric For Meteorol* 149:2071–2081
- Lee X, Griffis TJ, Baker JM, Billmark KA, Kim K, Welp LR (2009) Canopy-scale kinetic fractionation of atmospheric carbon dioxide and water vapor isotopes. *Global Biogeochem Cycles* 23:GB1002
- Lee X, Goulden ML, Hollinger DY, Barr A, Black TA, Bohrer G, Bracho R, Drake B, Goldstein A, Gu L, Katul G, Kolb T, Law B, Margolis H, Meyers T, Monson R, Munger W, Oren R, Paw UKT, Richardson AD, Schmid HP, Staebler R, Wofsy S, Zhao L (2011) Observed increase in local cooling effect of deforestation at higher latitudes. *Nature* 479:384–387
- Norman JM, Kustas WP, Humes KS (1995) Two-source approach for estimating soil and vegetation energy fluxes in observations of directional radiometric surface temperature. *Agric For Meteorol* 77:263–293
- Oleson KW, Dai Y, Bonan G, Bosilovich M, Dickinson R, Dirmeyer P, Hoffman F, Houser P, Levis S, Niu GY, Thornton P, Vertenstein M, Yang ZL, Zeng X (2004) Technical description of the community land model (CLM). National Center for Atmospheric Research, Boulder
- Schultz NM, Lee X, Lawrence PJ, Lawrence DM, Zhao L (2016) Assessing the use of sub-grid land model output to study impacts of land cover change. *J Geophys Res Atmos* 121:6133–6147
- Shuttleworth WJ, Wallace JS (1985) Evaporation from sparse crops – an energy combination theory. *Q J R Meteorol Soc* 111:839–855
- Wang YP, Leuning R (1998) A two-leaf model for canopy, conductance, photosynthesis and partitioning of available energy I: model description and comparison with a multi-layered model. *Agric For Meteorol* 91:89–111
- Zhao L, Lee X, Suyker AE, Wen X (2016) Influence of leaf area index on the radiometric resistance to heat transfer. *Bound-Layer Meteorol* 105:105–123

Chapter 11

Budgets of Heat, Water Vapor, and Trace Gases in the Atmospheric Boundary Layer

11.1 Introduction

This chapter is an application of the energy and mass conservation principles to the whole atmospheric boundary layer (ABL). We are interested in the diurnal evolution of temperature and concentrations of water vapor, carbon dioxide, and other trace gases in the ABL and in the mechanisms that drive their temporal changes. A complete budget analysis requires that we quantify the time rate of change of these scalar quantities, dynamically couple their surface-air exchanges to varying forcing conditions in the ABL, and determine their transport between the ABL and the free atmosphere.

By examining how the boundary layer communicates with the free atmosphere, we gain an opportunity to understand how large-scale parameters that are external to the boundary layer shape the overall characteristics of the boundary layer. One such external parameter, which we have already encountered, is the pressure gradient force associated with synoptic weather patterns. The balance of this force against the Coriolis force results in the geostrophic wind (Eqs. 6.2 and 6.3). The work done by the force on the moving air is the source of mean flow kinetic energy in the boundary layer (Fig. 4.4). For the purpose of budget analyses, two other external parameters are also important: large-scale horizontal flow divergence and vertical gradients of these scalars in the free atmosphere. The mean vertical motion arising from flow convergence and divergence can promote or hinder the development of the boundary layer. The vertical gradients in the free atmosphere control the scalar transport at the top of the boundary layer.

Our budget analysis emphasizes column-mean quantities. Let Φ be a scalar quantity. Its column mean is given by

$$\overline{\Phi}_m = \frac{1}{z_i} \int_0^{z_i} \overline{\Phi} dz, \quad (11.1)$$

where z_i is the height of the boundary layer and subscript m is used to denote this column mean operation.

Column integration was also a strategy used in Chap. 8 for analyzing the mass and heat budgets of an eddy covariance control volume. A major difference is that the top face of the control volume is fixed at the eddy covariance instrument height, whereas the top of the ABL is evolving with time. The time rate of change of $\bar{\Phi}_m$ is influenced not only by the transport of Φ into and out of the ABL but also by the fact that the thickness of the ABL or the volume of the diffusion media is changing with time. Determination of z_i , either via field observation or through mathematical solution of the mass conservation of air, is a prerequisite for the budget analysis.

The ABL budget theory is relevant to several practical matters. First, the height of the boundary layer is a critical parameter for the prediction of local air pollution dispersion. Second, no method can measure directly the surface CO₂ flux at the landscape scale (10–100 km), but the flux can be inferred from the ABL CO₂ budget if all other terms of the budget are known. Third, models of surface-air exchanges, such as the Penman-Monteith model, use atmospheric variables in the ABL as inputs, as if these variables were unaffected by the exchanges. In reality, dynamic feedbacks exist between the ABL and the land surface, so that these forcing variables themselves are evolving with time and must be solved from a set of governing equations. The ABL budget equations can serve this purpose. Fourth, the mass flux into fair-weather cumulus clouds is compensated by air subsidence in the ABL. Knowledge of the ABL time evolution is helpful for cumulus cloud parameterization.

11.2 The Slab Approximation of the Convective Boundary Layer

In the slab approximation of the convective boundary layer, first proposed by D. K. Lilly (1968), all variables are horizontally homogeneous, and therefore there is no horizontal advection. The effect of large-scale flow convergence and divergence is manifested in a non-zero mean vertical velocity. No turbulence exists in the free atmosphere. In the ABL, turbulence is strong enough to maintain well-mixed conditions (Fig. 11.1). The surface layer occupies only a very small portion of the ABL, so it has negligible influence on the column mean potential temperature and the gas mixing ratios. The capping inversion that separates the ABL from the free atmosphere is infinitesimally thin, and the inversion strength is given by the potential temperature jump across the inversion layer. These simplifications are collectively referred to as the *slab approximation* because the profile shape has the appearance of a block of slab.

By definition, the column mean quantities are

$$\bar{\theta}_m = \frac{1}{z_i} \int_0^{z_i} \bar{\theta} dz, \quad \bar{s}_{v,m} = \frac{1}{z_i} \int_0^{z_i} \bar{s}_v dz, \quad \bar{s}_{c,m} = \frac{1}{z_i} \int_0^{z_i} \bar{s}_c dz. \quad (11.2)$$

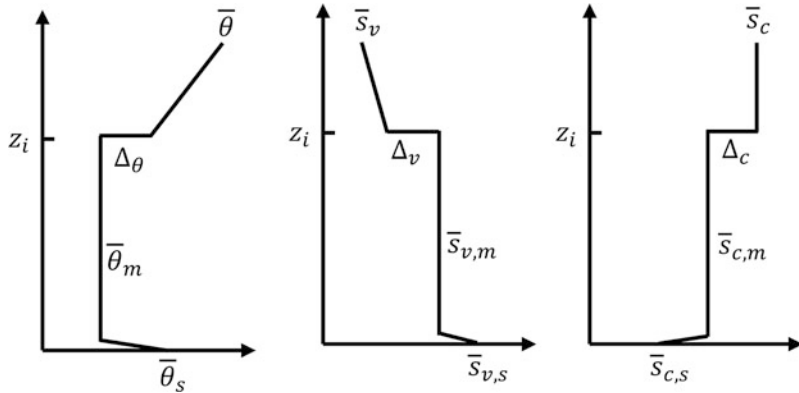


Fig. 11.1 The slab approximation of the daytime convective boundary layer on land, showing the profiles of potential temperature and water vapor and carbon dioxide mixing ratios

The inversion jumps are given as

$$\Delta_\theta = \bar{\theta}_+ - \bar{\theta}_m, \quad \Delta_v = \bar{s}_v,+ - \bar{s}_{v,m}, \quad \Delta_c = \bar{s}_c,+ - \bar{s}_{c,m}, \quad (11.3)$$

for temperature, water vapor, and carbon dioxide, respectively, where subscript + denotes values in the free atmosphere just above the capping inversion.

The slab approximation yields simplified energy and mass conservation equations. In Chap. 6, we showed that different forces dominate the momentum conservation equations in the surface layer, the mixed layer, and the free atmosphere. Similarly, the importance of the terms in the energy and mass conservation Eqs. 3.26, 3.27, and 3.28 depends on vertical position. Let us analyze the situation for each layer.

In the free atmosphere, all the Reynolds covariances vanish, and the energy and mass conservation equations are reduced to a balance between the time rate of change and vertical advection:

$$\frac{\partial \bar{\theta}}{\partial t} + \bar{w} \gamma_\theta = 0, \quad (11.4)$$

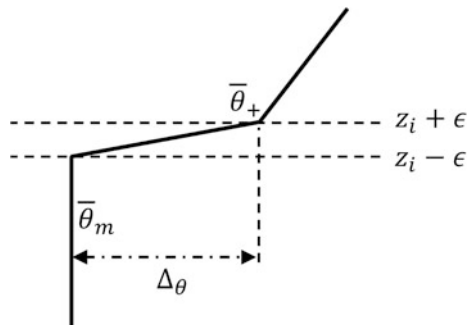
$$\frac{\partial \bar{s}_v}{\partial t} + \bar{w} \gamma_v = 0, \quad (11.5)$$

$$\frac{\partial \bar{s}_c}{\partial t} + \bar{w} \gamma_c = 0, \quad (11.6)$$

where

$$\gamma_\theta = \frac{\partial \bar{\theta}}{\partial z}, \quad \gamma_v = \frac{\partial \bar{s}_v}{\partial z}, \quad \gamma_c = \frac{\partial \bar{s}_c}{\partial z}, \quad (11.7)$$

Fig. 11.2 A schematic of potential temperature discontinuity at the capping inversion



are the vertical gradient of potential temperature, water vapor mixing ratio, and CO₂ mixing ratio in the free atmosphere.

Because γ_θ is positive, Eq. 11.4 indicates that the potential temperature above the boundary layer will increase with time if there is subsidence motion ($\bar{w} < 0$), a phenomenon known as *subsidence warming*.

At the capping inversion, the conservation equations require special treatment because the scalar quantities are discontinuous. Mathematically, the discontinuity is handled by first specifying a height range $\{z_i - \epsilon, z_i + \epsilon\}$ for the capping inversion layer, where ϵ is a small height interval and then taking the limit $\epsilon \rightarrow 0$ (Fig. 11.2). At height $z_i + \epsilon$, which is slightly above the ABL, there is vertical advection but no turbulent flux. At height $z_i - \epsilon$, which is slightly below the ABL top, there is turbulent flux but no vertical advection. The conservation of heat is expressed as

$$\frac{\partial \bar{\theta}}{\partial t} + \bar{w} \frac{\partial \bar{\theta}}{\partial z} = - \frac{\partial \overline{w' \theta'}}{\partial z}. \quad (11.8)$$

Similar equations can be written for other scalars. We will come back to Eq. 11.8 in the next section and will show how to implement the two boundary conditions.

In the mixed layer, vertical advection can be omitted because the vertical temperature and the mixing ratio gradients are negligible. The conservation equations are given as

$$\frac{\partial \bar{\theta}}{\partial t} = - \frac{\partial \overline{w' \theta'}}{\partial z} + \frac{1}{\rho_d c_p} \frac{\partial R_n}{\partial z} - \frac{\lambda}{\rho_d c_p} E_c, \quad (11.9)$$

$$\frac{\partial \bar{s}_v}{\partial t} = - \frac{\partial \overline{w' s'_v}}{\partial z} + \frac{E_c}{\rho_d}, \quad (11.10)$$

$$\frac{\partial \bar{s}_c}{\partial t} = - \frac{\partial \overline{w' s'_c}}{\partial z}. \quad (11.11)$$

To acknowledge the possibility of cloud presence in the ABL, we have included E_c , the rate of evaporation of liquid water in dimensions of $\text{kg m}^{-3} \text{ s}^{-1}$, as a source term for water vapor. In the presence of cloud, the radiative flux divergence, $\partial R_n / \partial z$, is not negligible and is a source of heat. Likewise, the latent heat consumed by evaporation of cloud droplets represents a heat sink in the energy conservation equation.

The surface layer is assumed to be thin so changes in this layer do not affect the ABL budget analysis. Large temperature, humidity, and CO₂ gradients exist between the surface and the mixed layer due to imperfect mixing and the presence of sources and sinks at the surface. These gradients are used in the parameterization of the surface Reynolds flux of heat ($w'\theta'$)_s, water vapor ($w's'_v$)_s, and carbon dioxide ($w's'_c$)_s as

$$(\overline{w'\theta'})_s = \frac{\bar{\theta}_s - \bar{\theta}_m}{r_a}, \quad (11.12)$$

$$(\overline{w's'_v})_s = \frac{\bar{s}_{v,s} - \bar{s}_{v,m}}{r_a} = \frac{s_v^*(\bar{\theta}_s) - \bar{s}_{v,m}}{r_a + r_c}, \quad (11.13)$$

$$(\overline{w's'_c})_s = \frac{\bar{s}_{c,s} - \bar{s}_{c,m}}{r_a}, \quad (11.14)$$

where $\bar{\theta}_s$, $\bar{s}_{v,s}$, and $\bar{s}_{c,s}$ are potential temperature and water vapor and CO₂ mixing ratios at the surface. These expressions serve as the lower boundary conditions for the ABL budget equations and permit full interactions between the surface sources and the state of the ABL.

11.3 Boundary-Layer Growth and Entrainment

Boundary-Layer Growth

Conceptually, the mechanisms responsible for ABL growth are rather straightforward. The ABL will expand upward if new air is added to the ABL column by horizontal flow convergence or by entrainment from the free atmosphere and will contract if air is removed from the column by flow divergence. Flow convergence and divergence do not change the ABL column mean quantities because the air advected horizontally is assumed to have the same properties of the air in the local ABL domain. In contrast, entrainment typically increases the potential temperature, reduces the water vapor mixing ratio, and in the growing season increases the CO₂ mixing ratio in the ABL.

A governing equation for the ABL height z_i can be obtained by manipulating the energy conservation equation for the capping inversion layer. The derivation involves two steps, integrating Eq. 11.8 with respect to z and taking the limit $\epsilon \rightarrow 0$.

Integration of the time change term of Eq. 11.8 gives

$$\int_{z_i-\epsilon}^{z_i+\epsilon} \frac{\partial \bar{\theta}}{\partial t} dz = \frac{\partial}{\partial t} \int_{z_i-\epsilon}^{z_i+\epsilon} \bar{\theta} dz - [\bar{\theta}(z_i + \epsilon) - \bar{\theta}(z_i - \epsilon)] \frac{\partial z_i}{\partial t}, \quad (11.15)$$

where we have used the Leibniz integral rule for differentiation:

$$\frac{\partial}{\partial t} \int_{x_1(t)}^{x_2(t)} y(z, t) dz = \int_{x_1(t)}^{x_2(t)} \frac{\partial y}{\partial t} dz + y(x_2(t), t) \frac{\partial x_2}{\partial t} - y(x_1(t), t) \frac{\partial x_1}{\partial t}. \quad (11.16)$$

We note that

$$\bar{\theta}(z_i - \epsilon) = \bar{\theta}_m.$$

In the limit $\epsilon \rightarrow 0$,

$$\int_{z_i-\epsilon}^{z_i+\epsilon} \bar{\theta} dz \rightarrow 0, \quad \bar{\theta}(z_i + \epsilon) \rightarrow \bar{\theta}_+$$

So we obtain

$$\lim_{\epsilon \rightarrow 0} \int_{z_i-\epsilon}^{z_i+\epsilon} \frac{\partial \bar{\theta}}{\partial t} dz = -\Delta_\theta \frac{\partial z_i}{\partial t}. \quad (11.17)$$

Integration of the second term on the left side of Eq. 11.8 yields

$$\int_{z_i-\epsilon}^{z_i+\epsilon} \bar{w} \frac{\partial \bar{\theta}}{\partial z} dz = [\bar{\theta}(z_i + \epsilon) - \bar{\theta}(z_i - \epsilon)] \bar{w}. \quad (11.18)$$

The limit of this integral is

$$\lim_{\epsilon \rightarrow 0} \int_{z_i-\epsilon}^{z_i+\epsilon} \bar{w} \frac{\partial \bar{\theta}}{\partial z} dz = \Delta_\theta \bar{w}. \quad (11.19)$$

Integrating the term on the right side of Eq. 11.8 and taking the limit, we have

$$\lim_{\epsilon \rightarrow 0} \left\{ - \int_{z_i-\epsilon}^{z_i+\epsilon} \frac{\partial \bar{w}' \bar{\theta}'}{\partial z} dz \right\} = \lim_{\epsilon \rightarrow 0} (\bar{w}' \bar{\theta}')_{z_i-\epsilon} = (\bar{w}' \bar{\theta}')_{z_i}. \quad (11.20)$$

Here $(\bar{w}' \bar{\theta}')_{z_i}$ is the heat flux just below the capping inversion and is negative, representing a downward transport of heat from the free atmosphere to the ABL.

Combining Eqs. 11.17, 11.19, and 11.20 with Eq. 11.8, we obtain a prognostic equation for z_i :

$$\frac{\partial z_i}{\partial t} = \bar{w} - \frac{(\bar{w}' \bar{\theta}')_{z_i}}{\Delta_\theta}. \quad (11.21)$$

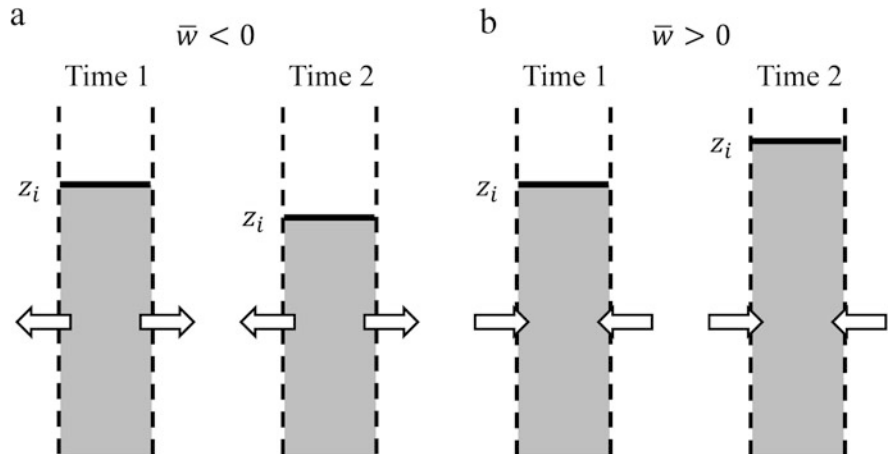


Fig. 11.3 Change of boundary-layer height due to flow divergence (a) and convergence (b)

Equation 11.21 is the outcome that the eddy heat flux just below the capping inversion layer is exactly balanced by the downward heat transport associated with vertical advection and air entrainment just above the inversion layer. It confirms the statement we made earlier that flow convergence ($\bar{w} > 0$ or ascending motion) and entrainment cause the ABL to deepen and flow divergence ($\bar{w} < 0$ or subsidence) causes it to contract. These processes are illustrated graphically in Figs. 11.3 and 11.4b.

Having the dimensions of velocity, the term

$$w_e = -\frac{(w'\theta')_{z_i}}{\Delta_\theta}, \quad (11.22)$$

is called the *entrainment velocity*. This velocity can be determined experimentally using two methods. If measurements of the entrainment flux and the inversion jump are available, w_e can be obtained from Eq. 11.22. If z_i is measured continuously and the large-scale subsidence velocity is given, w_e can be obtained from

$$w_e = \frac{\partial z_i}{\partial t} - \bar{w} \quad (11.23)$$

according to Eq. 11.21. In the absence of flow convergence or divergence, the entrainment velocity is equal to the rate of ABL growth.

Solution of Eq. 11.21 requires that the mean vertical velocity \bar{w} be prescribed and that the entrainment velocity be either measured or parameterized. If data on flow divergence is available, \bar{w} is found by integrating the divergence rate vertically from the surface to height z_i (Eq. 3.18).

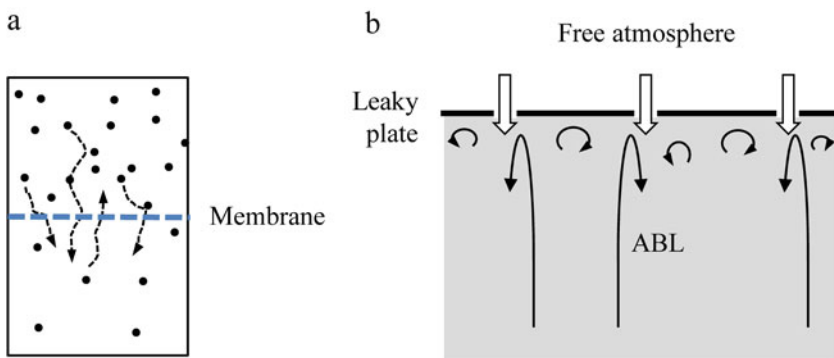


Fig. 11.4 Physical models for turbulent diffusion and entrainment: (a) a diffusion membrane and (b) a leaky and weightless plate

The Entrainment Process

Entrainment refers to the process whereby strands of air from the free atmosphere are mixed into the ABL. Entrainment is different from pure turbulent diffusion in one important aspect. Turbulent diffusion results in a net transport of the diffusant, such as heat and CO₂, usually in the direction from high temperature and concentration to low temperature and concentration, but there is no net transport of air or the diffusion media itself. In contrast, entrainment causes a downward transport of air across the capping inversion layer. A good physical model for turbulent diffusion is the cell membrane, which permits transport of salt from the side of high salt concentration to the other side of low concentration but does not permit bulk water movement through it (Fig. 11.4a). The entrainment process can be understood by representing the inversion layer as a leaky and weightless plate (Fig. 11.4b). This conceptualized plate is perforated with small openings. Each opening is controlled by a one-way check valve, so air can travel downward but not upward. As air bleeds through these openings, the plate will float upward because we assume that the air in the ABL is incompressible. The free atmospheric air that entered the ABL is quickly blended with the ABL air by the eddy motion confined below the plate, and its heat and other constituents are immediately released into the ABL.

Obviously, the leaky plate analog is an idealization of the actual entrainment process. In the real atmosphere, the “instigator” responsible for the net downward transport of the free atmospheric air is the eddy motion below the inversion layer. Although eddies of all sizes are involved, it is large thermal plumes that are the most effective in causing entrainment and in deepening the ABL. The process consists mainly of three stages (Fig. 11.5; Sullivan et al. 1998). The first stage is folding of the inversion interface. Having high buoyancy, the thermal plume is able to push the interface upward and cause it to bend over. In the second stage, the bending

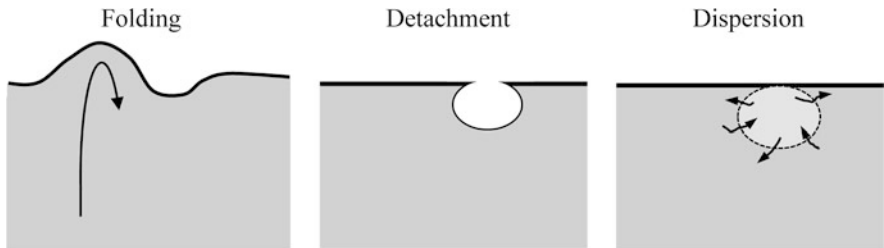


Fig. 11.5 Entrainment triggered by a large thermal plume according to the large-eddy simulation study of Sullivan et al. (1998)

is so severe that a pocket of the free atmospheric air becomes detached from the interface and is trapped in the ABL. In stage three, the detached air pocket is quickly dispersed in the old ABL air by actions of smaller-scale turbulent eddies, and the heat contained in the pocket is released into the ABL, contributing to the increase in the ABL potential temperature.

The Role of Boundary-Layer Clouds: Cumulus Clouds

The influence of cloud on ABL development depends on cloud type. The formation of shallow cumulus clouds causes subsidence motion, whereas the presence of stratocumulus clouds promotes turbulence near the capping inversion with the consequence of enhanced entrainment.

Covering a few percents of the sky, *shallow cumulus clouds* resemble the shape of cauliflower, having uneven upper boundaries but a flat and uniform cloud base. They are formed in fair weather conditions at a humidity exceeding 70–80%. The cooling mechanism responsible for their formation is adiabatic cooling of vigorous convective thermals. As these thermals rise vertically, they will cool adiabatically at a dry adiabatic lapse rate of 9.8 K km^{-1} , until the dew point temperature is reached, at which point condensation occurs and puffy clouds appear. The *lifting condensation level*, that is, the height at which condensation first occurs, is tens of meters to several hundred meters above the ABL top. The latent heat released by condensation increases the buoyancy of these thermals, causing them to rise even further. The release of latent heat is one reason for why cloud-forming thermals can penetrate into the free atmosphere but dry thermals usually cannot. This type of cumulus clouds is sometimes referred as active cumulus because they pump air out of the ABL (Fig. 11.6; Stull 1988).

Mass conservation requires that air should move downward in spaces in between the clouds to compensate for the in-cloud upward venting of air from the ABL (Stull 1988). Let σ_c be the fraction of sky covered by the clouds, $\bar{w}_c (> 0)$ be the mean vertical velocity in the clouds, and $\bar{w}_f (< 0)$ be the mean vertical velocity in regions outside the clouds. Mass conservation requires

$$\sigma_c \bar{w}_c + (1 - \sigma_c) \bar{w}_f = 0 \quad (11.24)$$

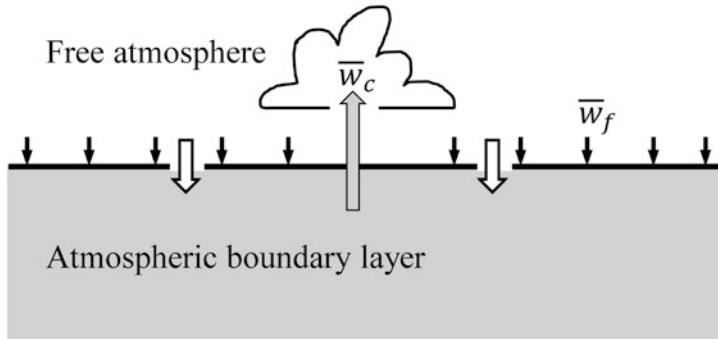


Fig. 11.6 Venting of air out of the atmospheric boundary layer into a cumulus cloud (gray arrow) is compensated by slow subsidence motion in the cloud-free region (solid black arrows)

Here \bar{w}_f describes the mean subsidence of air outside the clouds. Because σ_c is small, \bar{w}_f is much smaller in magnitude than \bar{w}_c .

The time rate of change of the ABL height is now given by,

$$\frac{\partial z_i}{\partial t} = \bar{w} - \sigma_c \bar{w}_c - (1 - \sigma_c) \frac{(\bar{w}' \theta')_{z_i}}{\Delta_\theta} \quad (11.25)$$

$$= \bar{w} + (1 - \sigma_c) \bar{w}_f - (1 - \sigma_c) \frac{(\bar{w}' \theta')_{z_i}}{\Delta_\theta} \quad (11.26)$$

$$\simeq \bar{w} + \bar{w}_f - \frac{(\bar{w}' \theta')_{z_i}}{\Delta_\theta}, \quad (11.27)$$

where the approximation leading to Eq. 11.27 is based on the fact that $\sigma_c \ll 1$. The first term on the right side of Eq. 11.27 is the vertical velocity arising from large-scale flows which affect both the cloud and cloud-free portions of the ABL. The second term is subsidence that counterbalances the air that feeds into the clouds and acts to retard the ABL growth. The third term represents entrainment in the cloud-free portion of the ABL.

The formation of cumulus clouds imposes dynamic constraints on the ABL (Stull 1988). The clouds owe their existence to vigorous convective motions which can only occur if there is strong solar heating of the surface. For convection to continue, there cannot be too many clouds in the sky, or else the surface will not receive enough solar radiation to support energetic thermals. Fewer and weaker thermals will slow down the entrainment process. Because these clouds pump air out of the ABL, they act to reduce the ABL vertical extent. But if the ABL becomes too shallow, rising thermals will not have enough time to reach the dew point temperature, and clouds are less likely to form. These negative feedbacks have a tendency to force the cloudy ABL into a quasi-steady state, whereby in the absence of large-scale flow convergence, the mass flux into the clouds from the ABL is

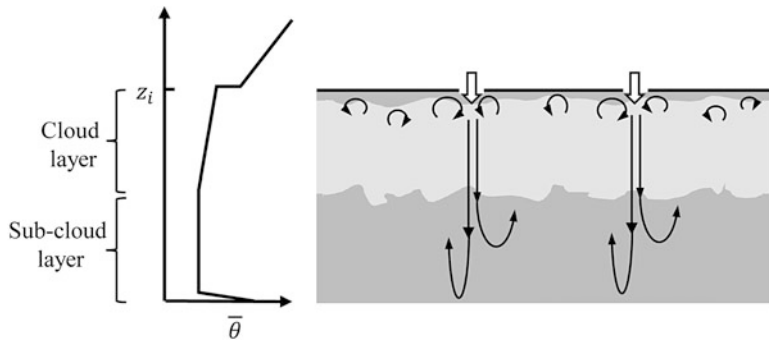


Fig. 11.7 A boundary layer topped by a deck of stratocumulous clouds: *left*, profile of potential temperature; *right*, top-down mixing caused by radiative cooling of the cloud top

balanced by the air that entrains from the free atmosphere into the ABL. The result is that the growth of the ABL is temporarily halted. Thus we have

$$\frac{\partial z_i}{\partial t} = 0, \quad \bar{w}_f = \frac{(\bar{w}'\theta')_{z_i}}{\Delta_\theta} = -w_e, \quad \bar{w}_c = \frac{1 - \sigma_c}{\sigma_c} w_e. \quad (11.28)$$

The Role of Boundary-Layer Clouds: Stratocumulus Clouds

Unlike active cumulus clouds, *stratocumulus clouds* are found within the ABL. The ABL now consists of a cloud layer in the upper part and a sub-cloud layer between the surface and the cloud base (Fig. 11.7). Stratocumulus clouds are 200–400 m thick and can extend unbroken for several hundreds of kilometers horizontally. Impeded by a strong capping inversion, these clouds tend to have a flat top, but may show a lumpy cloud base due to turbulent motions. Conditions that favor stratocumulus formation include strong stability of the lower troposphere, large-scale subsidence motion, and a continuous supply of surface moisture. Strong stability and subsidence motion prevent the clouds from developing vertically beyond the ABL. The supply of moisture from the surface is essential for sustaining the clouds because without it entrainment of dry air from the free atmosphere would cause the clouds to dissipate. These conditions are common over the cool regions of the tropical and subtropical oceans.

In the presence of stratocumulus, entrainment is maintained by a top-down mixing mechanism. Because the sky is overcast, the surface sensible heat flux, on the order of 10 W m^{-2} , is too weak to generate convective eddies. Instead, a major source of turbulent motion is located near the cloud top. Cloud droplets are very efficient at absorbing and emitting longwave radiation, but in the top 10–30 m of the cloud layer, the emission is stronger than the absorption. The net longwave radiative

cooling at the cloud top generates static instability, meaning that the temperature at the cloud top is lower than in the middle and lower portion of the cloud layer and convective overturning occurs. Because the turbulent motion takes place very close to the capping inversion, it can bring, in an intermittent fashion, filaments of dry and warm air from the free atmosphere to the cloud layer. Mixing of the dry air with the saturated air in the clouds causes some cloud droplets to evaporate, which further enhances local cooling. Some of the air pockets become so cool and dense that the negative buoyancy force can pull them all the way down to the surface (Fig. 11.7).

The convective overturning is most pronounced at night. During the day, absorption of solar radiation by the cloud layer partially offsets the longwave radiative cooling and weakens the downward heat transport. For this reason, the cloud-topped ABL is shallower during the day than at night, although this diurnal variation is still much smaller than that of a cloud-free ABL over land.

Field observations and large-eddy simulation studies show that the top-down convective motion is strong enough to mix thoroughly the cloud layer and the sub-cloud layer, as long as the ABL is not too deep ($z_i < \sim 800$ m; Wood 2012). Although we expect the mixing ratio of an inert gas, such as carbon dioxide, to be constant with height throughout the ABL, the potential temperature $\bar{\theta}$ and the vapor mixing ratio \bar{s}_v are constant only in the sub-cloud layer. In the cloud layer, neither $\bar{\theta}$ nor \bar{s}_v is a conserved quantity due to phase changes and radiative cooling. However, the total water mixing ratio and the equivalent potential temperature are found to be conserved quantities. The total water mixing ratio is the total amount of water (liquid plus vapor) contained in an air volume having a unit mass of dry air. The equivalent potential temperature is the temperature an air parcel would have if it were raised pseudo-adiabatically until all the vapor has been converted to the liquid form and has precipitated out and then brought down adiabatically to the sea level.

Stratocumulus clouds can persist for days without breaking up (Wood 2012). The relatively steady nature of the cloud layer and the lack of ABL growth suggest that the mean entrainment should be balanced by large-scale subsidence. Let D be the large-scale divergence rate

$$D = -\frac{\partial \bar{u}}{\partial x} - \frac{\partial \bar{v}}{\partial y}. \quad (11.29)$$

By the continuity requirement, the large-scale mean vertical velocity at the top of the boundary layer is

$$\bar{w} = Dz_i. \quad (11.30)$$

The entrainment velocity can be approximated by

$$w_e = -Dz_i. \quad (11.31)$$

11.4 Heat Budget in the Convective Boundary Layer

Let us first consider a cloud-free convective boundary layer where the radiation flux divergence and water phase changes can be omitted. The heat budget equation is found by integrating Eq. 11.9 with respect to height:

$$z_i \frac{\partial \bar{\theta}_m}{\partial t} = (\bar{w}'\bar{\theta}')_s - (\bar{w}'\bar{\theta}')_{z_i}. \quad (11.32)$$

Not surprisingly, warming of the ABL air column is controlled by the sum of the heat flux from the surface and that from the free atmosphere. At the same amount of heat input, the warming rate is high in the morning when the ABL is shallow and is reduced in the afternoon when the ABL becomes deep.

So far we have obtained three equations (Eqs. 11.12, 11.21, and 11.32) for the heat budget analysis, but there are five unknowns in these equations: $\bar{\theta}_m$, $(w'\theta')_s$, $(w'\theta')_{z_i}$, z_i , and Δ_θ . (The large-scale mean vertical velocity \bar{w} is a prescribed parameter.) To overcome the closure problem, we need two more equations.

The first additional equation, a prognostic equation for the temperature inversion jump or the inversion strength Δ_θ , can be derived from Eqs. 11.3 and 11.4. Let z_f be a reference height in the free atmosphere. The potential temperature at the bottom of the free atmosphere can be expressed as

$$\bar{\theta}_+ = \gamma_\theta(z_i - z_f) + \bar{\theta}(z_f), \quad (11.33)$$

(Vilá-Guerau de Arellano et al. 2016). Differentiating Eq. 11.33 with respect to time and making use of Eq. 11.4, we obtain

$$\frac{\partial \theta_+}{\partial t} = \gamma_\theta \left(\frac{\partial z_i}{\partial t} - \bar{w} \right). \quad (11.34)$$

The next step of this derivation involves differentiating Δ_θ in Eq. 11.3, yielding the prognostic equation for Δ_θ ,

$$\frac{\partial \Delta_\theta}{\partial t} = \gamma_\theta \left(\frac{\partial z_i}{\partial t} - \bar{w} \right) - \frac{\partial \bar{\theta}_m}{\partial t}. \quad (11.35)$$

A typical value of Δ_θ is 2 K over land at midday.

According to Eq. 11.35, three factors can change the inversion strength (Fig. 11.8). If everything else remains the same, deepening of the ABL will raise the base of the free atmosphere. As a result, the temperature at the base θ_+ will increase, leading to a stronger capping inversion. The capping inversion can also be strengthened by subsidence warming of the free atmosphere. However, warming of the ABL air column will weaken the inversion.

The second addition to the system of heat budget equations is based on a closure assumption for the entrainment heat flux $(w'\theta')_{z_i}$. In the state of free convection,

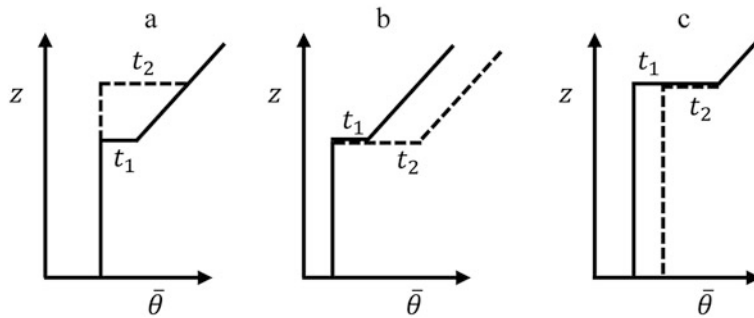


Fig. 11.8 Change to the strength of the capping inversion from time t_1 to time t_2 due to deepening of the boundary layer (**a**), large-scale subsidence (**b**), and warming of the ABL air column (**c**)

buoyancy production linked to the surface heat flux is the only source of turbulent kinetic energy. Consideration of the TKE budget near the capping inversion leads to the following entrainment relation for heat:

$$(\overline{w'\theta'})_{z_i} = -A_T(\overline{w'\theta'})_s, \quad (11.36)$$

where the entrainment ratio A_T is approximately 0.2 at the free convection limit. Field observations and large-eddy simulation studies show that the actual entrainment ratio is slightly higher than this, typically falling in the range of 0.2–0.4, as a result of the additional contribution of shear-generated turbulence.

Equations 11.12, 11.21, 11.32, 11.35, and 11.36 form a closed set of equations for the heat budget analysis.

One application of the heat budget equations is prediction of the ABL height z_i . If we impose the restriction that the initial ABL height is zero and omit large-scale subsidence, we obtain from these equations (with $A_T = 0.2$) a model for z_i and Δ_θ :

$$z_i \simeq \left[\frac{2.8}{\gamma_\theta} \int_0^t (\overline{w'\theta'})_s dt' \right]^{1/2}, \quad (11.37)$$

$$\Delta_\theta \simeq 0.14\gamma_\theta z_i, \quad (11.38)$$

where the integration starts at about the time of sunrise when the surface heat flux first becomes positive for the day (Tennekes 1973). Equation 11.37 underestimates the ABL height in the first 1–2 h after sunrise because the initial ABL height is set to zero, but describes the asymptotic behavior of z_i in the later hours of the day reasonably well (Fig. 11.9).

If we assume that the product $z_i \Delta_\theta$ is invariant with time and once again omit large-scale subsidence, we obtain another formulation for z_i :

$$z_i = \left\{ [z_i(0)]^2 + \frac{2}{\gamma_\theta} \int_0^t (\overline{w'\theta'})_s dt' \right\}^{1/2}, \quad (11.39)$$

(Tennekes 1973).

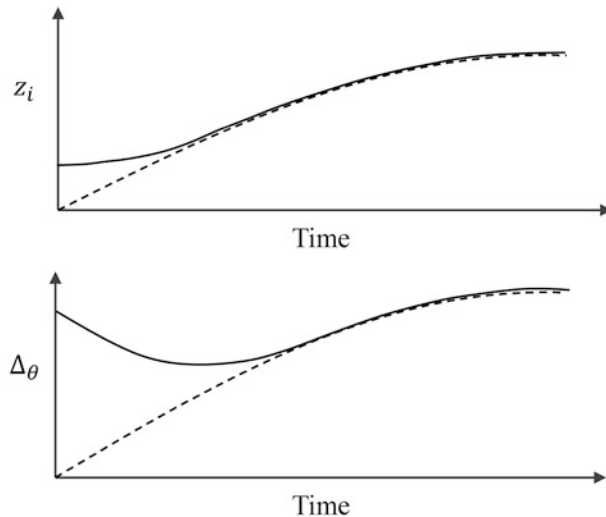


Fig. 11.9 Daytime evolution of the boundary-layer height z_i and the capping inversion strength Δ_θ : Solid lines, actual changes; dashed lines, asymptotic approximations given by Eqs. 11.37 and 11.38. The initial time coincides approximately with sunrise

Equations 11.37 and 11.39 are models of the ABL height. In the real world, z_i is determined by observation of the potential temperature profile (Problems 6.2, 11.15, and 11.16).

The above discussion is applicable to a cloud-free boundary layer. If the boundary layer is topped by stratocumulus clouds, several modifications are required of the governing equations. Equations 11.12, 11.21, and 11.35 are still valid, but Eq. 11.32 should be modified to account for the radiation flux divergence in the cloud layer and the latent heat associated with phase changes of water. Because turbulence is initiated at the ABL top and because the surface heat flux is small, Eq. 11.36 is no longer an appropriate parameterization for the entrainment flux.

11.5 Carbon Dioxide Budget in the Convective Boundary Layer

The carbon dioxide budget in the convective boundary layer is governed by the integral form of Eq. 11.11:

$$z_i \frac{\partial \bar{s}_{c,m}}{\partial t} = (\bar{w}' s'_c)_s - (\bar{w}' s'_c)_{z_i}, \quad (11.40)$$

where $(\overline{w's'_c})_{z_i}$ is the entrainment flux of CO₂ at the capping inversion. In contrast to the heat budget Eq. 11.32 where the two heat fluxes are in opposite directions, the entrainment CO₂ flux and the surface CO₂ flux $(\overline{w's'_c})_s$ generally have the same sign. Both are negative or directed toward the surface in the growing season and positive or directed away from the surface in the nongrowing season. Equation 11.40 holds for both cloud-free and cloud-topped boundary layers.

Another difference between CO₂ and heat is that CO₂ is a passive scalar but heat is not. As explained earlier, thermals linked to the surface heat flux are the main instigator causing entrainment of the free atmospheric air into the ABL. For this reason, the entrainment heat flux can be parameterized as being proportional to the surface heat flux (Eq. 11.36). The same parameterization would not work for the CO₂ entrainment flux because the surface CO₂ flux has no direct consequence on the entrainment process aloft. But provided that z_i is predicted by the set of equations that govern the heat budget, $(\overline{w's'_c})_{z_i}$ can be obtained from

$$(\overline{w's'_c})_{z_i} = -\Delta_c \left(\frac{\partial z_i}{\partial t} - \bar{w} \right), \quad (11.41)$$

where Δ_c is the CO₂ jump across the capping inversion (Fig. 11.1 and Eq. 11.3). Equation 11.41 has been derived from the CO₂ conservation equation for the capping inversion layer using the same strategy that yields Eq. 11.21 (Problem 11.22).

The CO₂ inversion jump Δ_c obeys

$$\frac{\partial \Delta_c}{\partial t} = \gamma_c \left(\frac{\partial z_i}{\partial t} - \bar{w} \right) - \frac{\partial \bar{s}_{c,m}}{\partial t}. \quad (11.42)$$

This prognostic equation has been derived using the same method deployed for the derivation of Eq. 11.35 (Problem 11.23).

Therefore, a complete modeling study of the ABL CO₂ budget requires that we solve four unknowns [$\bar{s}_{c,m}$, $(\overline{w's'_c})_s$, $(\overline{w's'_c})_{z_i}$, and Δ_c] from four equations (Eqs. 11.14, 11.40, 11.41, and 11.42). The CO₂ mixing ratio at the surface $\bar{s}_{c,s}$ and the ABL height z_i are input variables given by a biochemical parameterization of photosynthesis and by modeling of the ABL heat budget, respectively.

Experimental data on Δ_c are scanty. The few snapshot CO₂ profile observations reported in the literature indicate that the midday Δ_c is on the order of 15 mg kg⁻¹ (or molar mixing ratio about 10 ppm) over land in the growing season. Little is known experimentally of temporal variations of Δ_c , but some inferences can be made from the above governing equations. Because there is no CO₂ source or sink in the free atmosphere, the CO₂ mixing ratio gradient γ_c is zero. Taking advantage of this new constraint, we simplify Eq. 11.42 to:

$$\frac{\partial \Delta_c}{\partial t} = -\frac{\partial \bar{s}_{c,m}}{\partial t}. \quad (11.43)$$

Even though the temporal variation of the column mean CO₂ mixing ratio is controlled by the net balance between the surface and the entrainment flux, the temporal variation of the CO₂ inversion jump is only dependent on variations of the CO₂ concentration in the ABL. Assuming that the large-scale mean velocity is zero and eliminating $\bar{s}_{c,m}$ and $(\bar{w}'s'_c)_{z_i}$ from Eqs. 11.40, 11.41, and 11.43, we obtain

$$\frac{\partial(z_i\Delta_c)}{\partial t} = -(\bar{w}'s'_c)_s. \quad (11.44)$$

Time integration of Eq. 11.44 yields

$$z_i(t)\Delta_c(t) - z_i(0)\Delta_c(0) = - \int_0^t (\bar{w}'s'_c)_s dt \quad (11.45)$$

A graphic interpretation of Eq. 11.45 is given in Fig. 11.10. The area enclosed by the CO₂ mixing ratio profiles at time 0 and time t is equal to the cumulative surface CO₂ flux between the two times. If the ABL height is constant, which is an approximate situation for late afternoon hours, the increase in Δ_c over time is totally attributed to the cumulative removal of CO₂ due to photosynthetic uptake (Fig. 11.10 left panel). More generally, the change in Δ_c is influenced both by variations in the ABL height and by the surface CO₂ uptake (Fig. 11.10 right panel).

A consequence of the slab approximation of the convective ABL is *entrainment similarity*, which states that the entrainment flux of a scalar is proportional to the inversion jump of the scalar and that the same proportionality coefficient holds regardless of whether the scalar is passive or active. According to Eqs. 11.21, 11.22, and 11.41, this coefficient is represented by the entrainment velocity w_e , and the mathematical expression of entrainment similarity between heat and carbon dioxide is

$$w_e = -\frac{(\bar{w}'\theta')_{z_i}}{\Delta_\theta} = -\frac{(\bar{w}'s'_c)_{z_i}}{\Delta_c}. \quad (11.46)$$

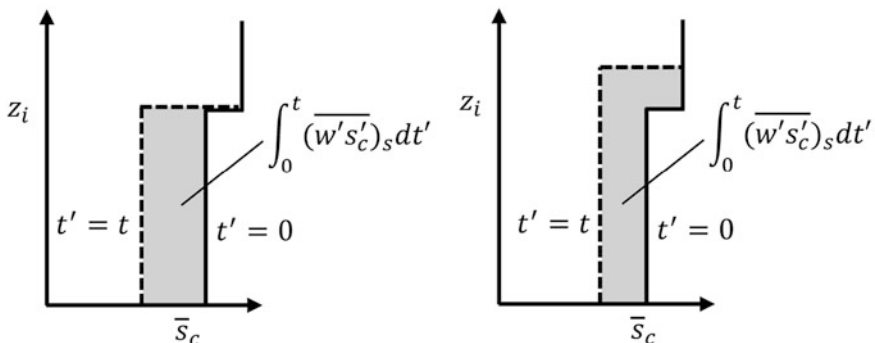


Fig. 11.10 Time evolution of the CO₂ inversion jump under the condition of a constant ABL height (left) or of a time-varying ABL height (right)

Entrainment similarity is the theoretical basis for the experimental technique that deploys a chemical tracer, such as ozone or dimethyl sulfide, for the determination of w_e (Faloona et al. 2005). Instead of measuring the heat flux and the potential temperature, we measure the tracer flux below the capping inversion and the tracer concentration difference between the ABL and the free atmosphere. The entrainment velocity w_e is calculated as the ratio of these two quantities.

Another experimental technique, referred to as the *ABL budget technique*, aims to infer the surface flux from boundary-layer measurements (Cleugh et al. 2004). Combining Eqs. 11.40 and 11.41, we obtain an expression for the surface flux:

$$(\overline{w's'_c})_s = z_i \frac{\partial \bar{s}_{c,m}}{\partial t} - \Delta_c \left(\frac{\partial z_i}{\partial t} - \bar{w} \right). \quad (11.47)$$

The large-scale mean vertical velocity \bar{w} is estimated with flow data at the synoptic scale. Because field campaigns of this kind are typically conducted in fair weather conditions associated with a high-pressure system, we expect subsidence motion or negative \bar{w} at the top of the ABL. Other quantities on the right side of Eq. 11.47 are determined with measurements of the CO₂ profile and the boundary-layer height at a sub-day resolution (Problem 11.16). Large eddies in the convective boundary layer effectively smooth out the influences of small-scale heterogeneity of the surface, so the measured concentration profile can be regarded as a “natural integrator” of the surface source contributions in a landscape that extends 10–100 km upwind. In theory, the ABL budget should be equal to the aggregation of the fluxes from individual patches as obtained using the eddy covariance approach, but such measurements are cost prohibitive.

11.6 Water Vapor Budget in the Convective Boundary Layer

We present here without derivation equations for the water vapor budget of a cloud-free convective boundary layer:

$$z_i \frac{\partial \bar{s}_{v,m}}{\partial t} = (\overline{w's'_v})_s - (\overline{w's'_v})_{z_i}, \quad (11.48)$$

$$(\overline{w's'_v})_{z_i} = -\Delta_v \left(\frac{\partial z_i}{\partial t} - \bar{w} \right), \quad (11.49)$$

$$\frac{\partial \Delta_v}{\partial t} = \gamma_v \left(\frac{\partial z_i}{\partial t} - \bar{w} \right) - \frac{\partial \bar{s}_{v,m}}{\partial t}, \quad (11.50)$$

where $(\overline{w's'_v})_{z_i}$ is the entrainment water vapor flux and Δ_v is the water vapor jump across the capping inversion layer. The unknowns to be solved from these equations and Eq. 11.13 are $\bar{s}_{v,m}$, $(\overline{w's'_v})_s$, $(\overline{w's'_v})_{z_i}$, and Δ_v . Once again, the ABL height z_i is

an input variable provided by the heat budget analysis. The surface temperature and the surface vapor mixing ratio are solved from the surface energy balance equation. In this calculation, the surface and the boundary-layer processes are fully coupled: calculation of the surface heat and water vapor fluxes uses the column mean quantities $\bar{\theta}_m$ and $\bar{s}_{v,m}$ as inputs, and the calculated fluxes are used to determine time changes in these quantities and the boundary-layer height (McNaughton and Spriggs 1986).

If clouds are present in the boundary layer, Eq. 11.48 should be amended to account for phase changes of water.

The fully coupled calculation is a prognostic application. In *prognostic mode*, the unknown variables are solved numerically from their governing equations. Measurements of these variables at sunrise are required to initialize the model. At the subsequent time steps, these variables are predicted by integrating the budget equations forward in time.

The ABL budget equations are also used in *diagnostic mode*, mostly by experimentalists, to understand one specific aspect of the ABL. In a diagnostic application, a subset of the equations is deployed to estimate one variable from measurements made of the other variables. For example, by measuring the inversion strength and the entrainment heat flux, we can estimate the ABL growth rate using one equation (Eq. 11.21). Another case in point is the ABL budget technique for quantifying the surface water vapor flux at the landscape scale. The diagnostic equation is obtained by elimination of the entrainment water vapor flux from two of the governing equations (Eqs. 11.48 and 11.49):

$$(\overline{w's'_v})_s = z_i \frac{\partial \bar{s}_{v,m}}{\partial t} - \Delta_v \left(\frac{\partial z_i}{\partial t} - \bar{w} \right). \quad (11.51)$$

Similar to estimation of the landscape-scale CO₂ flux (Eq. 11.47), in this diagnostic analysis, the surface water vapor flux is the target variable to be estimated, and z_i , $\bar{s}_{v,m}$ and Δ_v are measured variables (Problem 11.15).

11.7 Trace Gases in the Nighttime Stable Boundary Layer

The boundary layer over land is generally stable at night. Mixing is maintained by shear-generated turbulence which is strongest near the ground and is very weak at the top of the Ekman layer. That buoyancy acts to suppress turbulent motion has two consequences. First, the slab model is no longer appropriate because eddy mixing is not vigorous enough to sustain a constant profile of potential temperature (Fig. 6.3). Gaseous mixing ratios are expected to show steep vertical gradients too: if the ground surface is a source of these gases, they will accumulate near the ground rather than diffusing uniformly in the boundary layer. Second, turbulent exchange is negligible at the top of the boundary layer and can be omitted from the budget analysis.

Let s_y be the mixing ratio of trace gas y . The ABL budget of the trace gas is governed by

$$z_i \frac{\partial \bar{s}_{y,m}}{\partial t} = \langle \bar{w}' s'_y \rangle_s \quad (11.52)$$

where $\bar{s}_{y,m}$ is the column mean mixing ratio of trace gas y , $\langle \bar{w}' s'_y \rangle_s$ is the surface flux of gas y , and z_i is taken as the height of the Ekman layer. Dimensional analysis of the momentum equations yields the so-called Zilitinkevich relation for z_i in stable conditions:

$$z_i \simeq 0.4(u_* L/f)^{1/2}, \quad (11.53)$$

where u_* is the surface friction velocity, L is the Obukhov length, and f is the Coriolis parameter.

Equation 11.52 can be used in diagnostic mode to infer the surface flux from measurement of the time change of the column mean concentration. An advantage of this *nocturnal ABL budget technique* over the daytime convective ABL technique is that the nocturnal ABL is shallow, with a depth of about 200 m. Profile measurements can be made on a tall tower or with a tethered sonde, at more frequent time steps than would be possible with radiosonde measurements in a deep convective ABL.

A major source of uncertainty of the nocturnal ABL technique lies in determination of the boundary-layer height. (The Zilitinkevich relation is accurate to about 50%.) To avoid the need for z_i , we introduce an additional trace gas x , which is measured simultaneously with gas y and whose surface flux $\langle \bar{w}' s'_x \rangle_s$ is known either via eddy covariance measurement or through a predictive model parameterization. Integration of their budget equations over time yields

$$\bar{s}_{x,m}(t) = \bar{s}_{x,m}(0) + \frac{t}{z_i} \langle \bar{w}' s'_x \rangle_s, \quad (11.54)$$

$$\bar{s}_{y,m}(t) = \bar{s}_{y,m}(0) + \frac{t}{z_i} \langle \bar{w}' s'_y \rangle_s, \quad (11.55)$$

where

$$\langle \bar{w}' s'_x \rangle_s = \frac{1}{t} \int_0^t \langle \bar{w}' s'_x \rangle_s dt', \quad \langle \bar{w}' s'_y \rangle_s = \frac{1}{t} \int_0^t \langle \bar{w}' s'_y \rangle_s dt',$$

are the mean surface fluxes between time 0 and time t . Eliminating z_i from Eqs. 11.54 and 11.55, we obtain,

$$\bar{s}_{y,m}(t) = \bar{s}_{y,m}(0) + \frac{\langle \bar{w}' s'_y \rangle_s}{\langle \bar{w}' s'_x \rangle_s} [\bar{s}_{x,m}(t) - \bar{s}_{x,m}(0)]. \quad (11.56)$$

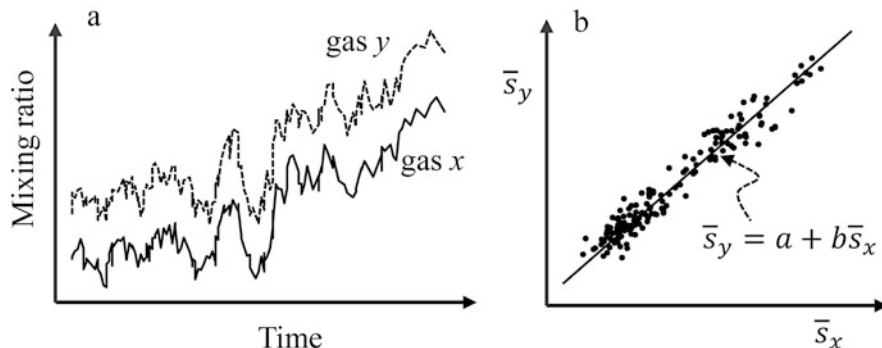


Fig. 11.11 Relationship between two trace gases in the stable boundary layer at night. (a) Time series of the gas mixing ratios at a single height; (b) correlation between the two mixing ratios

Therefore, the column mean mixing ratio of trace gas y is linearly correlated with that of trace gas x , and the slope of this linear relation is identical to their flux ratio. The actual flux of y is then calculated as the product of the slope value and the flux of trace gas x . In this application, gas x serves as a tracer, and gas y is the measurement target.

In practice, this *tracer correlation method* is often relaxed to

$$\bar{s}_y = a + b\bar{s}_x, \quad (11.57)$$

where \bar{s}_y and \bar{s}_x are the mixing ratios of trace gas y and x measured at a single level near the ground surface (Fig. 11.11). The slope parameter b , determined by linear regression, represents the flux ratio of trace gas y to x .

11.8 The Equilibrium Boundary Layer

Equilibrium Boundary Layer Over Oceans

Historically, the concept of *equilibrium boundary layer* is a description of steady-state conditions over the ocean that persist for a period longer than 24 h (Betts 1989). Several perspectives on this equilibrium state are satisfied simultaneously. In compliance with the mass conservation of air, the mean entrainment velocity is balanced by the large-scale subsidence velocity so that the ABL height is maintained constant over time. Likewise, the supply of water vapor via surface evaporation is equal to the rate of removal of water vapor by entrainment at the top of the ABL. There can be phase changes of water in the ABL, but no precipitation is produced as a result. In terms of energy conservation, a balance exists between the surface and the entrainment heat fluxes and the rates of radiative and evaporative cooling, so the column mean potential temperature is constant over time.

Oceanic regions most conducive to the equilibrium state are in the subsidence branches of the Hadley cell and the Walker circulation. The ABLs in these regions are a source of moisture to the free atmosphere, feeding precipitating clouds in the ascending branches of the circulations.

The slab model is an appropriate framework for investigating the equilibrium boundary layer. Because all the time change terms can be omitted, the model equations become simplified algebraic expressions linking the ocean surface temperature, the ABL state variables, and conditions in the troposphere. Researchers use the model to study the interactions between ABL processes and parameters external to the ABL, including tropospheric wind, moisture status, lapse rate, and subsidence.

Equilibrium Boundary Layer Over Land

The equilibrium boundary layer concept has been extended to describe the mean state of the ABL over land over periods of several weeks (Betts et al. 2004; Helliker et al. 2004). There are obviously large sub-day variations, but these variations are smoothed out by averaging over the 24 h cycle. In the growing season, the surface is a source of carbon dioxide at night and a sink during the day (Fig. 11.12). At the top of the ABL, the flux occurs only in the daytime convective phase. The nocturnal boundary layer is just a CO₂ accumulation phase with virtually no transport to the free atmosphere. However, the 24 h mean surface flux is in balance with the mean flux at the top of the boundary layer.

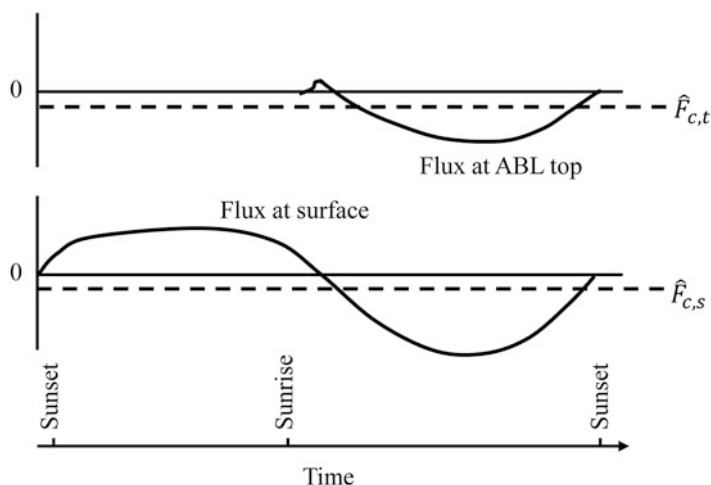


Fig. 11.12 A composite diurnal variation of the growing-season CO₂ flux at the surface and at the top of the ABL. The *dashed lines* indicate 24-h means

In the absence of horizontal advection, this mean state for CO₂ is expressed as

$$\hat{F}_{c,s} = \hat{F}_{c,t} \quad (11.58)$$

where $\hat{F}_{c,s}$ is the mean surface CO₂ flux and $\hat{F}_{c,t}$ is the mean CO₂ flux at the top of the boundary layer. Because the slab model is not valid at night, we cannot obtain an expression for $\hat{F}_{c,t}$ by simply performing time averaging operation on the slab model Eq. 11.47. However, the entrainment flux formulation of the slab model (Eq. 11.46) inspires us to propose the following parameterization for $\hat{F}_{c,t}$

$$\hat{F}_{c,t} = W\rho_d(\hat{s}_{c,+} - \hat{s}_{c,m}), \quad (11.59)$$

where $W(< 0)$ is a “mixing velocity” and $\hat{s}_{c,+}$ and $\hat{s}_{c,m}$ are long-term (weeks) mean CO₂ mixing ratios in the free atmosphere and in the boundary layer, respectively. It is understood that $\hat{F}_{c,s}$ here is a landscape-scale quantity since $\hat{s}_{c,m}$ is influenced by surface sources that extend 10–100 km upwind.

We have shown that in the convective boundary layer, the entrainment CO₂ flux is equal to the product of the entrainment velocity and the concentration difference across the capping inversion layer. Similarly, the long-term mean ABL flux to the free atmosphere is proportional to the mean concentration difference between the free atmosphere and the ABL, and the proportionality coefficient W also has the dimensions of velocity.

Combination of Eqs. 11.58 and 11.59 yields

$$\hat{F}_{c,s} = W\rho_d(\hat{s}_{c,+} - \hat{s}_{c,m}). \quad (11.60)$$

Equation 11.60 is the basis for the *equilibrium ABL technique* for inferring monthly to annual mean CO₂ flux of a landscape from atmospheric concentration measurements.

Application of Eq. 11.60 requires an independent method for determining W . There is evidence showing that in continental regions subject to persistent subsidence motion, such as the central US, the mixing velocity W is approximately equal to the long-term mean vertical velocity observed above the mean ABL. However, in regions influenced by large-scale ascending motion, such as eastern China during the monsoon season, W cannot be substituted by the mean vertical velocity of the atmosphere. More generally, water vapor is used as a convenient tracer gas to help constrain W . In the mean state, the surface evapotranspiration $\hat{F}_{v,s}$ is balanced by the water vapor flux to the free atmosphere, as

$$\hat{F}_{v,s} = W\rho_d(\hat{s}_{v,+} - \hat{s}_{v,m}), \quad (11.61)$$

where $\hat{s}_{v,+}$ and $\hat{s}_{v,m}$ are long-term mean water vapor mixing ratios in the free atmosphere and in the boundary layer, respectively. Since estimates of $\hat{F}_{v,s}$ are readily available, either via field measurement or land-surface model calculation, Eq. 11.61 can be used to find W (Problem 11.20). For best results, $\hat{s}_{v,m}$ and $\hat{s}_{c,m}$ should be observed at a level above the mean nocturnal surface inversion layer.

11.9 Problems

11.1 Under what conditions is the entrainment velocity equal to the time rate of change of the boundary-layer height? Assuming that these conditions are satisfied, estimate the entrainment velocity using the profile data shown in Fig. 6.11.

11.2 The entrainment ozone flux in a marine boundary layer topped by stratocumulus clouds is $-8.1 \text{ ppb cm s}^{-1}$, and the ozone concentration jump across the capping inversion is approximately 15 ppb (Faloona et al. 2005). What is the entrainment velocity?

11.3 For a heat flux of -0.03 K m s^{-1} below the capping inversion, an inversion strength of 1.7 K , a horizontal flow divergence rate of $2 \times 10^{-6} \text{ s}^{-1}$, and a boundary-layer height of 650 m , find the rate of boundary-layer growth.

11.4 The atmospheric boundary layer is in a quasi-steady state. Estimate the mean vertical velocity in cumulus clouds \bar{w}_c if the cumulus cloud fraction is 0.04, the entrainment velocity is 0.02 m s^{-1} , and there is no large-scale subsidence motion.

11.5 A reasonable estimate of the mean vertical velocity \bar{w}_c in shallow cumulus clouds formed in fair weather conditions can be obtained from the convective velocity scale w_* , as

$$\bar{w}_c \simeq w_* = \left[\frac{g}{\theta_s} (\overline{w' \theta'})_s z_i \right]^{1/3}, \quad (11.62)$$

(Vilá-Guerau de Arellano et al. 2016). The surface heat flux $(\overline{w' \theta'})_s$ is 0.31 K m s^{-1} , the entrainment flux is given by the closure Eq. 11.36 (with $A_T = 0.2$), the inversion temperature jump Δ_θ is 1.5 K , the boundary-layer height z_i is 950 m , the large-scale subsidence is negligible, and the boundary layer is in a quasi-steady state. Determine the fraction of the sky occupied by clouds.

11.6 Air temperature in the free atmosphere is generally lower than that in the boundary layer. Why do we say that entrainment of the free atmospheric air into the boundary layer will cause warming of the boundary layer?

11.7 The surface heat flux is given by

$$(\overline{w' \theta'})_s(t) = 0.1 \sin(\pi t / 12) \quad (0 < t < 12) \quad (11.63)$$

where $(\overline{w' \theta'})_s$ is in K m s^{-1} and t is time in hours since sunrise. The boundary-layer height is 0 m at sunrise. The large-scale flow divergence rate is zero. The potential temperature gradient in the free atmosphere γ_θ is 3.3 K km^{-1} . Estimate the boundary-layer height and the inversion temperature jump at hourly intervals from $t = 1$ to 10 h .

11.8 Repeat the calculation of Problem 11.7. But this time the boundary-layer height z_i and the temperature inversion jump Δ_θ are 200 m and 2.3 K at sunrise, and the product $z_i \Delta_\theta$ is invariant with time.

11.9 The surface heat flux is given by Eq. 11.63. The entrainment heat flux is given by the entrainment parameterization Eq. 11.36 with $A_T = 0.2$. The initial column mean potential temperature is 281.1 K. Using the boundary-layer height obtained in Problem 11.8, predict the column mean potential temperature at hourly intervals from $t = 1$ to 10 h.

11.10* The surface heat flux is given by Eq. 11.63. The initial z_i is 200 m, the initial Δ_θ is 2.3 K, and γ_θ is 3.3 K km^{-1} . Solve numerically the boundary-layer height z_i and the inversion strength Δ_θ for $t = 1$ to 10 h from Eqs. 11.21, 11.32, 11.35, and 11.36. The large-scale mean vertical velocity \bar{w} is zero. Compare these numerical solutions with the results obtained in Problems 11.7 and 11.8.

11.11* Repeat the calculation of Problem 11.10 but with a large-scale mean vertical velocity of $-0.5 \times 10^{-2} \text{ m s}^{-1}$. How does large-scale flow subsidence affect the ABL growth and the capping inversion strength?

11.12 For an entrainment velocity of 0.41 cm s^{-1} , a CO₂ concentration jump across the capping inversion of 20 mg kg^{-1} , and a zero subsidence velocity, find the entrainment CO₂ flux.

11.13 The surface CO₂ flux is given by

$$\overline{(w' s'_c)}_s(t) = -1.2 \sin(t\pi/12) \quad (0 < t < 12) \quad (11.64)$$

where $\overline{(w' s'_c)}_s$ is in $\text{mg kg}^{-1} \text{ m s}^{-1}$ and t is time in hours since sunrise. The initial CO₂ concentration jump across the capping inversion is -5 mg kg^{-1} . Using Eq. 11.45 and the boundary height obtained in Problem 11.8, estimate the concentration jump Δ_c at hourly intervals from $t = 1$ to 10 h.

11.14 The entrainment heat flux is -0.03 K m s^{-1} , and the temperature, water vapor, and CO₂ inversion jumps are 1.6 K, -2.0 g kg^{-1} , and 12.3 mg kg^{-1} , respectively, in a convective boundary layer. Find the entrainment water vapor and CO₂ fluxes.

11.15 Using the profile data shown in Fig. 11.13a and the ABL technique (Eq. 11.51), estimate the landscape water vapor flux and the latent heat flux between 10:00 and 14:00 local time. (Hint: There is no large-scale flow convergence or divergence.)

11.16 Using the profile data shown in Fig. 11.13b and the ABL technique (Eq. 11.47), estimate the surface carbon dioxide flux between 10:00 and 14:00 local time. (Hint: There is no large-scale flow convergence or divergence.)

11.17 For an Obukhov length of 20.5 m, a surface friction velocity of 0.22 m s^{-1} , find the boundary-layer height.

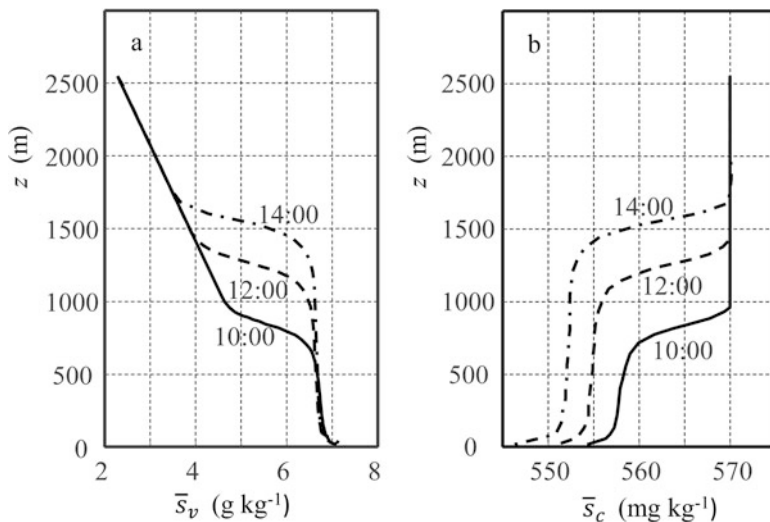
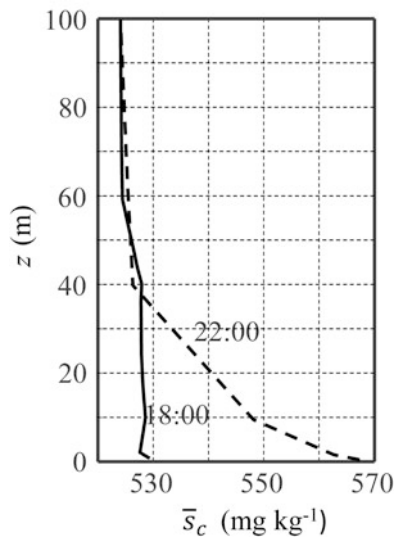


Fig. 11.13 Profiles of water vapor (a) and carbon dioxide mixing ratio (b) in a cloud-free convective boundary layer. Time marks are local time (Data source: Huang et al. 2011)

Fig. 11.14 Tethersonde profiles of CO_2 mixing ratio in a nocturnal boundary layer over a pasture land (Data source: Denmead et al. 1996)



11.18 Using the profiles of CO_2 mixing ratio shown in Fig. 11.14 and the nocturnal ABL technique (Eq. 11.52), find the surface CO_2 flux in $\mu\text{mol m}^{-2} \text{s}^{-1}$. Is the surface a source or sink of atmospheric CO_2 ?

11.19 Using the tracer correlation method and the data provided in Fig. 11.15, find the surface nitrous oxide flux.

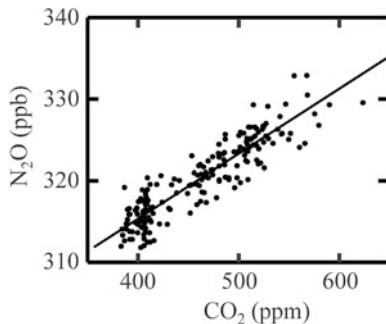


Fig. 11.15 Correlation between nitrous oxide and carbon dioxide molar mixing ratios observed in the stable boundary layer above a paddock grazed by sheep. The *solid line* represents the best-fit regression equation $y = 284 + 0.080x$. The surface CO_2 flux is $0.20 \text{ mg m}^{-2} \text{ s}^{-1}$ during the measurement period (Data source: Kelliher et al. 2002)

Table 11.1 Monthly mean carbon dioxide and water vapor mixing ratios above ($\hat{s}_{c,+}$ and $\hat{s}_{v,+}$) and in the atmospheric boundary layer ($\hat{s}_{c,m}$ and $\hat{s}_{v,m}$), and monthly mean land surface evapotranspiration rate (ET) in Wisconsin, USA (Data source: Helliker et al. 2004)

Month	$\hat{s}_{c,+}$ mg kg^{-1}	$\hat{s}_{c,m}$ mg kg^{-1}	$\hat{s}_{v,+}$ g kg^{-1}	$\hat{s}_{v,m}$ g kg^{-1}	ET $\text{mmol m}^{-2} \text{ s}^{-1}$
Jan	564.2	571.0	0.8	1.7	0.1
Feb	564.9	571.6	0.9	2.8	0.1
Mar	566.0	573.3	1.0	3.5	0.3
Apr	568.0	571.3	1.1	3.1	0.6
May	567.2	565.1	1.6	7.2	1.4
Jun	562.5	554.6	1.9	8.7	2.0
Jul	556.4	542.5	2.0	10.8	2.4
Aug	552.0	543.5	1.8	10.8	2.0
Sep	551.7	555.4	1.7	7.4	1.5
Oct	556.6	564.2	1.1	5.1	0.6
Nov	562.4	570.2	1.0	3.2	0.2
Dec	565.5	569.8	0.7	1.5	0.1

11.20 Using the equilibrium ABL technique and the data provided in Table 11.1, find the monthly mean landscape CO_2 flux.

11.21* The surface CO_2 flux is given by Eq. 11.64, the initial CO_2 inversion jump Δ_c is -5 mg kg^{-1} , and the initial column mean CO_2 concentration $\bar{s}_{c,m}$ is 575 mg kg^{-1} . Other constraints are given in Problem 11.10. Solve numerically Δ_c , $\bar{s}_{c,m}$, and the entrainment CO_2 flux $(w's'_c)_{z_i}$ for $t = 1$ to 10 h .

11.22 Derive Eq. 11.41 from the CO_2 conservation equation for the capping inversion layer using the same strategy that yields Eq. 11.21.

11.23 Derive Eq. 11.42 using the same method deployed for the derivation of Eq. 11.35.

References

- Betts AK (1989) Climatic equilibrium of the atmospheric convective boundary layer over a tropical ocean. *J Atmos Sci* 46:2621–2641
- Betts AK, Helliker B, Berry J (2004) Coupling between CO₂, water vapor, temperature, and radon and their fluxes in an idealized equilibrium boundary layer over land. *J Geophys Res* 109:D18103
- Cleugh HA, Raupach MR, Briggs PR, Coppin PA (2004) Regional-scale heat and water vapor fluxes in an agricultural landscape: an evaluation of CBL budget methods at OASIS. *Bound-Layer Meteorol* 110:99–137
- Denmead OT, Raupach MR, Dunin FX, Cleugh HA, Leuning R (1996) Boundary layer budgets for regional estimates of scalar fluxes. *Glob Chang Biol* 2:255–264
- Faloona I, Lenschow DH, Campos T, Stevens B, van Zanten M, Blomquist B, Thornton D, Bandy A (2005) Observations of entrainment in Eastern Pacific marine statocumulus using three conserved scalars. *J Atmos Sci* 62:3268–3285
- Helliker BR, Berry JA, Betts AK, Bakwin PS, Davis KJ, Denning AS, Ehleringer JR, Miller JB, Butler MP, Ricciuto DM (2004) Estimates of net CO₂ flux by application of equilibrium boundary layer concepts to CO₂ and water vapor measurements from a tall tower. *J Geophys Res* 109:D20106
- Huang J, Lee X, Patton EG (2011) Entrainment and budget of heat, water vapor and carbon dioxide in a convective boundary layer driven by time-varying solar radiation. *J Geophys Res -Atmos* 116:D06308
- Kelliher FM, Reisinger AR, Martin RJ, Harvey MJ, Price SJ, Sherlock RR (2002) Measuring nitrous oxide emission rate from grazed pasture using Fourier-transform infrared spectroscopy in the nocturnal boundary layer. *Agric For Meteorol* 111:29–38
- Lilly DK (1968) Models of cloud-topped mixed layers under a strong inversion. *Q J R Meteorol Soc* 94:292–309
- McNaughton KG, Spriggs TW (1986) A mixed-layer model for regional evaporation. *Bound-Layer Meteorol* 34:243–262
- Stull RH (1988) An introduction to boundary layer meteorology. Kluwer Academic Publishers, Dordrecht, 666pp
- Sullivan PP, Moeng CH, Stevens B, Lenschow DH, Mayor SD (1998) Structure of the entrainment zone capping the convective atmospheric boundary layer. *J Atmos Sci* 55:3042–3064
- Tennekes H (1973) A model for the dynamics of the inversion above a convective boundary layer. *J Atmos Sci* 30:558–567
- Vilá-Guerau de Arellano J, van Heerwaarden CC, van Stratum BJH, van den Dries K (2016) Atmospheric boundary layer: integrating air chemistry and land interactions. Cambridge University Press, New York, 265pp
- Wood R (2012) Review: statocumulus clouds. *Mon Weather Rev* 140:2373–2423

Symbols and Constants

overbar:	Reynolds averaging
prime ':	deviation from Reynolds mean value
[]:	canopy volume averaging
double primes ":	deviation from volume mean value
∇^2 :	Laplace operator
∇ :	gradient operator
∇_H :	horizontal gradient operator
A_i :	surface of plant element i
A_T :	entrainment ratio for sensible heat flux (dimensionless)
a :	plant area density ($\text{m}^2 \text{ m}^{-3}$)
a_H :	fractional contribution of horizontal advection (dimensionless)
C_D :	transfer coefficient for momentum or drag coefficient (dimensionless)
C_H :	transfer coefficient for sensible heat or Stanton number (dimensionless)
C_E :	transfer coefficient for water vapor or Dalton number (dimensionless)
C_d :	canopy drag coefficient (dimensionless)
C_h :	canopy heat exchange coefficient (dimensionless)
C_l :	leaf heat exchange coefficient ($\text{m s}^{-1/2}$)
c :	mass density of an inert tracer (kg m^{-3})
c_1 :	tracer concentration resulting from a unit line source (s m^{-2})
c_p :	specific heat of air at constant pressure ($= 1004 \text{ J kg}^{-1} \text{ K}^{-1}$)
c_v :	specific heat of air at constant volume ($= 718 \text{ J kg}^{-1} \text{ K}^{-1}$)
c_r :	wave speed (m s^{-1})
D :	saturation vapor pressure deficit (hPa)
D :	large-scale flow divergence rate (s^{-1})
d :	zero-plane displacement height (m)

d_l	leaf dimension (m)
E	water vapor flux or evaporation rate ($\text{g m}^{-2} \text{s}^{-1}$; $\text{mmol m}^{-2} \text{s}^{-1}$)
E_0	water vapor flux, measured at the land surface ($\text{g m}^{-2} \text{s}^{-1}$; $\text{mmol m}^{-2} \text{s}^{-1}$)
E_c	water vapor flux from a plant canopy ($\text{g m}^{-2} \text{s}^{-1}$; $\text{mmol m}^{-2} \text{s}^{-1}$)
E_c	rate of evaporation of cloud water ($\text{g m}^{-3} \text{s}^{-1}$)
E_g	soil evaporation or water vapor flux from the ground surface of an ecosystem ($\text{g m}^{-2} \text{s}^{-1}$; $\text{mmol m}^{-2} \text{s}^{-1}$)
E_l	water vapor flux at a leaf surface ($\text{g m}^{-2} \text{s}^{-1}$; $\text{mmol m}^{-2} \text{s}^{-1}$)
E	mean flow kinetic energy ($\text{m}^2 \text{s}^{-2}$)
E_T	total kinetic energy ($\text{m}^2 \text{s}^{-2}$)
e	turbulent kinetic energy ($\text{m}^2 \text{s}^{-2}$)
e_v	water vapor pressure (hPa)
e_v^*	saturation water vapor pressure (hPa)
F_c	eddy flux of CO_2 ($\text{mg m}^{-2} \text{s}^{-1}$; $\mu\text{mol m}^{-2} \text{s}^{-1}$)
F_h	eddy flux of sensible heat (W m^{-2})
F_m	eddy flux of momentum ($\text{m}^2 \text{s}^{-2}$)
F_v	eddy flux of water vapor ($\text{g m}^{-2} \text{s}^{-1}$; $\text{mmol m}^{-2} \text{s}^{-1}$)
$\hat{F}_{c,s}$	long-term mean CO_2 flux at the land surface ($\text{mg m}^{-2} \text{s}^{-1}$; $\mu\text{mol m}^{-2} \text{s}^{-1}$)
$\hat{F}_{v,s}$	long-term mean water vapor flux at the land surface ($\text{g m}^{-2} \text{s}^{-1}$; $\text{mmol m}^{-2} \text{s}^{-1}$)
$\hat{F}_{c,t}$	long-term mean CO_2 flux at the top of the boundary layer ($\text{mg m}^{-2} \text{s}^{-1}$; $\mu\text{mol m}^{-2} \text{s}^{-1}$)
$\hat{F}_{v,t}$	long-term mean water vapor flux at the top of the boundary layer ($\text{g m}^{-2} \text{s}^{-1}$; $\text{mmol m}^{-2} \text{s}^{-1}$)
f	energy redistribution factor (dimensionless)
f	Coriolis parameter ($\simeq 1 \times 10^{-4} \text{s}^{-1}$ at mid-latitudes in the northern hemisphere)
f_1	one-dimensional footprint function (m^{-1})
f_2	two-dimensional footprint function (m^{-2})
G	heat flux into the soil by conduction (W m^{-2})
G_0	heat flux into the soil by conduction, measured at the land surface (W m^{-2})
g	gravitational acceleration ($= 9.81 \text{ m s}^{-2}$)
H	sensible heat flux (W m^{-2})
H_0	sensible heat flux, measured at the land surface (W m^{-2})
H_c	sensible heat flux from a plant canopy (W m^{-2})
H_g	sensible heat flux from the ground surface of an ecosystem (W m^{-2})
H_l	sensible heat flux at a leaf surface (W m^{-2})
h	plant canopy height (m)
K_{\downarrow}	incoming solar radiation flux (W m^{-2})
K_{\uparrow}	reflected solar radiation flux (W m^{-2})

K_c, K_h, K_m, K_v :	eddy diffusivity for CO ₂ , heat, momentum, and water vapor, respectively (m ² s ⁻¹)
K_x, K_y, K_z :	eddy diffusivity for a passive tracer in the x , y , and z direction, respectively (m ² s ⁻¹)
k :	von Karman constant (= 0.4)
k :	wavenumber (rad m ⁻¹)
L :	Obukhov length (m)
L :	plant area index; leaf area index (dimensionless)
L_{\downarrow} :	incoming longwave radiation flux (W m ⁻²)
L_{\uparrow} :	outgoing longwave radiation flux (W m ⁻²)
l :	Prandtl's mixing length (m)
M_d :	molecular mass of dry air (= 0.029 kg mol ⁻¹)
M_c :	molecular mass of CO ₂ (= 0.044 kg mol ⁻¹)
M_v :	molecular mass of water vapor (= 0.018 kg mol ⁻¹)
m :	power law exponent for wind speed profile (dimensionless)
N :	Brunt-Västala frequency (Hz, s ⁻¹)
n :	power law exponent for eddy diffusivity profile (dimensionless)
n_x, n_y, n_z :	x , y , and z component of unit normal vector of a plant element surface
p :	three-dimensional probability of particle position (m ⁻³)
p_x, p_y, p_z :	particle probability distribution in the x , y , and z direction, respectively (m ⁻¹)
p :	air pressure (Pa)
p_c :	partial pressure of CO ₂ (Pa)
p_d :	partial pressure of dry air (Pa)
p_v :	partial pressure of water vapor (Pa)
p_0 :	background air pressure (Pa)
\tilde{p} :	pressure perturbation (Pa)
Q :	canopy averaging volume (m ³)
Q :	source strength (kg for instant point sources, kg s ⁻¹ for continuous point sources, kg m ⁻¹ s ⁻¹ for continuous line sources, and kg m ⁻² s ⁻¹ for area sources)
Q_A :	anthropogenic heat flux (W m ⁻²)
Q_s :	heat storage (W m ⁻²)
q :	specific humidity (g kg ⁻¹)
R :	universal gas constant (= 8.314 J mol ⁻¹ K ⁻¹)
R_c :	ideal gas constant for CO ₂ (= 189 J kg ⁻¹ K ⁻¹)
R_d :	ideal gas constant for dry air (= 287 J kg ⁻¹ K ⁻¹)
R_m :	ideal gas constant for moist air (J kg ⁻¹ K ⁻¹)
R_v :	ideal gas constant for water vapor (= 461 J kg ⁻¹ K ⁻¹)
R_f :	flux Richardson number (dimensionless)
R_i :	gradient Richardson number (dimensionless)
$R_{i,\min}$:	minimum gradient Richardson number (dimensionless)
R_L :	Lagrangian autocorrelation
R_n :	net radiation flux (W m ⁻²)

R_n^* :	apparent net radiation flux (W m^{-2})
$R_{n,c}$:	net radiation flux of a plant canopy (W m^{-2})
$R_{n,g}$:	net radiation flux of the ground surface in an ecosystem (W m^{-2})
$R_{n,0}$:	net radiation flux, measured at the land surface (W m^{-2})
$R_{n,l}$:	net radiation flux at a leaf surface (W m^{-2})
r :	shape factor for diffusivity and wind profiles (dimensionless)
$r_a, r_{a,h}$:	aerodynamic resistance to heat transfer (s m^{-1})
$r_{a,m}$:	aerodynamic resistance to momentum transfer (s m^{-1})
$r_{a,v}$:	aerodynamic resistance to water vapor transfer (s m^{-1})
r_c :	canopy resistance to water vapor transfer (s m^{-1})
r_e :	excess resistance to heat transfer (s m^{-1})
r_g :	ground or soil resistance to water vapor transfer (s m^{-1})
r_m :	radiometric resistance to heat transfer (s m^{-1})
r_T :	total resistance to heat transfer (s m^{-1})
r_b :	leaf boundary-layer resistance to heat transfer (s m^{-1})
r_s :	leaf stomatal resistance to water vapor transfer (s m^{-1})
S :	net shortwave radiation flux (W m^{-2})
S_c :	CO_2 source in free air ($\text{mg m}^{-3} \text{s}^{-1}$)
S_T :	heat source in free air (K s^{-1})
S_θ :	heat source in free air (K s^{-1})
S_v :	water vapor source in free air ($\text{g m}^{-3} \text{s}^{-1}$)
$S_{c,p}$:	plant canopy CO_2 source ($\text{mg m}^{-3} \text{s}^{-1}$)
$S_{T,p}$:	plant canopy heat source (K s^{-1})
$S_{v,p}$:	plant canopy water vapor source ($\text{g m}^{-3} \text{s}^{-1}$)
s :	shape factor for diffusivity and wind profiles (dimensionless)
s_c :	CO_2 mass mixing ratio ($\mu\text{g g}^{-1}$, mg kg^{-1})
s_v :	water vapor mass mixing ratio (g kg^{-1})
s_x, s_y :	mass mixing ratios of two arbitrary trace gases (kg kg^{-1})
$\bar{s}_{c,m}$:	column CO_2 mass mixing ratio in the boundary layer ($\mu\text{g g}^{-1}$, mg kg^{-1})
$\bar{s}_{v,m}$:	column mean water vapor mass mixing ratio in the boundary layer (g kg^{-1})
$\bar{s}_{c,+}$:	CO_2 mass mixing ratio at the base of the free atmosphere ($\mu\text{g g}^{-1}$, mg kg^{-1})
$\bar{s}_{v,+}$:	water vapor mass mixing ratio at the base of the free atmosphere (g kg^{-1})
$\hat{s}_{c,m}$:	long-term mean CO_2 mass mixing ratio in the boundary layer ($\mu\text{g g}^{-1}$, mg kg^{-1})
$\hat{s}_{v,m}$:	long-term mean water vapor mass mixing ratio in the boundary layer (g kg^{-1})
$\hat{s}_{c,+}$:	long-term mean CO_2 mass mixing ratio at the base of the free atmosphere ($\mu\text{g g}^{-1}$, mg kg^{-1})

$\hat{s}_{v,+}$:	long-term water vapor mass mixing ratio at the base of the free atmosphere (g kg^{-1})
$s_{v,o}$:	water vapor mass mixing ratio at a water surface (g kg^{-1})
$<\bar{s}_c>$:	column mean CO_2 mass mixing ratio below eddy covariance measurement height ($\mu\text{g g}^{-1}$; mg kg^{-1})
$<\bar{s}_v>$:	column mean water vapor mass mixing ratio below eddy covariance measurement height (g kg^{-1})
T :	temperature (K, $^{\circ}\text{C}$)
T_a :	air temperature (K, $^{\circ}\text{C}$)
T_g :	ground or soil temperature (K, $^{\circ}\text{C}$)
T_l :	leaf surface temperature (K, $^{\circ}\text{C}$)
T_s :	canopy or ecosystem surface temperature (K, $^{\circ}\text{C}$)
T_v :	virtual temperature (K)
T_w :	wet bulb temperature (K, $^{\circ}\text{C}$)
$<\bar{T}>$:	column mean temperature below eddy covariance measurement height (K, $^{\circ}\text{C}$)
T :	averaging length (s)
T :	wave period (s)
T_L :	Lagrangian integral time scale (s)
t :	time (s)
t_f :	sampling interval (s)
u, v, w :	velocity components in the x , y , and z direction, respectively (m s^{-1})
u_L, v_L, w_L :	Lagrangian particle velocity in the x , y , and z direction, respectively (m s^{-1})
u_0, w_0 :	background horizontal and vertical velocity, respectively, in linear instability analysis (m s^{-1})
u_0, v_0 :	initial x and y component velocity before the onset of inertial oscillation (m s^{-1})
u_e, v_e :	x and y component velocity in a new equilibrium state at night (m s^{-1})
u_g, v_g :	x and y component of the geostrophic wind (m s^{-1})
u_l :	wind speed outside a leaf boundary layer (m s^{-1})
u_p :	mean plume velocity (m s^{-1})
u_* :	friction velocity (m s^{-1})
\tilde{u}, \tilde{w} :	horizontal and vertical velocity perturbation, respectively (m s^{-1})
\mathbf{V} :	velocity vector
V :	magnitude of velocity vector (m s^{-1})
V_g :	geostrophic wind speed (m s^{-1})
W :	mixing velocity in an equilibrium boundary layer (m s^{-1})
w_e :	entrainment velocity (m s^{-1})
w_* :	convective velocity scale (m s^{-1})
\overline{w}_c :	ascending vertical velocity in cumulus clouds (m s^{-1})

\bar{w}_f :	subsidence vertical velocity outside cumulus clouds (m s^{-1})
X, Y, Z :	position of a Lagrangian particle (m)
x, y, z :	Cartesian coordinates (m)
x_m, y_m, z_m :	position coordinates of a flux measurement instrument (m)
z_1 :	tracer source height (m)
z_1 :	velocity and eddy diffusivity reference height (m)
z_g :	geometric mean height (m)
z_i :	boundary-layer height (m)
z_o :	momentum roughness (m)
$z_{o,h}$:	thermal roughness (m)
z_u :	height scale for footprint models (m)
α :	albedo (dimensionless)
α :	Priestley-Taylor coefficient ($\simeq 1.26$)
α_1, α_2 :	empirical coefficients in canopy wind profile models (dimensionless)
β :	fraction of solar radiation transmission through a surface water layer (dimensionless)
β :	Bowen ratio (dimensionless)
β :	angle between wind vector in the boundary layer and the geostrophic wind vector (degrees)
γ :	psychrometric constant ($= 0.66 \text{ hPa K}^{-1}$ at sea level)
γ_c :	vertical gradient of CO_2 mass mixing ratio in the free atmosphere ($\mu\text{g g}^{-1} \text{ m}^{-1}$)
γ_v :	vertical gradient of water vapor mass mixing ratio in the free atmosphere ($\text{g kg}^{-1} \text{ m}^{-1}$)
γ_θ :	vertical gradient of potential temperature in the free atmosphere (K m^{-1})
γ_m :	non-local closure correction factor for momentum transport (s^{-1})
Δ :	slope of saturation vapor pressure (hPa K^{-1})
Δ_c :	jump of CO_2 mass mixing ratio across the capping inversion layer ($\mu\text{g g}^{-1}$)
Δ_v :	jump of water vapor mass mixing ratio across the capping inversion layer (g kg^{-1})
Δ_θ :	jump of potential temperature across the capping inversion layer (K)
ϵ :	emissivity (dimensionless)
ϵ :	viscous dissipation of turbulent kinetic energy ($\text{m}^2 \text{ s}^{-3}$)
ζ :	Monin-Obukhov stability parameter (dimensionless)
θ :	potential temperature (K)
θ_o :	potential temperature at $z_{o,h}$ (K)
θ_0 :	background potential temperature (K)
$\bar{\theta}_+$:	potential temperature at the base of the free atmosphere (K)

$\bar{\theta}_m$:	column mean potential temperature in the boundary layer (K)
$\bar{\theta}$:	potential temperature perturbation (K)
θ_* :	potential temperature scale (K)
κ_c :	molecular diffusivity of CO ₂ in air ($= 1.53 \times 10^{-5} \text{ m}^2 \text{ s}^{-1}$ at 15 °C)
κ_T :	thermal diffusivity in air ($= 2.09 \times 10^{-5} \text{ m}^2 \text{ s}^{-1}$ at 15 °C)
κ_v :	molecular diffusivity of water vapor in air ($= 2.49 \times 10^{-5} \text{ m}^2 \text{ s}^{-1}$ at 15 °C)
λ :	latent heat of vaporization ($= 2466 \text{ J g}^{-1}$ at 15 °C)
λ :	wavelength (m)
λ_0 :	local climate sensitivity (K W ⁻¹ m ²)
μ :	ratio of molecular mass of dry air to that of water vapor ($= 1.61$)
ν :	kinematic viscosity ($= 1.48 \times 10^{-5} \text{ m}^2 \text{ s}^{-1}$ at 15 °C)
ρ :	air mass density (kg m ⁻³)
ρ_d :	dry air mass density (kg m ⁻³)
ρ_c :	CO ₂ mass density (mg m ⁻³)
ρ_v :	water vapor mass density (g m ⁻³)
σ :	Stefan-Boltzmann constant ($= 5.67 \times 10^{-8} \text{ W m}^{-2} \text{ K}^{-4}$)
$\sigma (= \sigma_r + i\sigma_i)$:	complex wave angular frequency (rad s ⁻¹)
σ_c :	cumulus cloud fraction (dimensionless)
$\sigma_x, \sigma_y, \sigma_z$:	standard deviations of particle position, also known as dispersion parameters (m)
σ_w :	standard deviation of vertical velocity (m s ⁻¹)
τ :	recursive filter time constant (s)
ϕ_e :	normalized turbulent kinetic energy (dimensionless)
ϕ_h :	stability function for heat (dimensionless)
ϕ_m :	stability function for momentum (dimensionless)
ϕ_ϵ :	normalized TKE dissipation rate (dimensionless)
χ_c :	molar mixing ratio of CO ₂ (ppm, $\mu\text{mol mol}^{-1}$)
χ_v :	molar mixing ratio of water vapor (mmol mol ⁻¹)
Ψ_h :	integral stability function for sensible heat (dimensionless)
Ψ_m :	integral stability function for momentum (dimensionless)
Ω :	Earth's angular rotation velocity ($= 7.27 \times 10^{-5} \text{ s}^{-1}$)

Index

A

ABL budget technique, 232–234
ascending motion, 221
adiabatic lapse rate, 68
adiabatic process, 19, 26, 68, 226
aerodynamic resistance, 49, 50, 55, 78
air quality model, 6, 130
air quality standard, 6, 146
albedo, 7, 22, 205, 212
amphistomatous, 151
anthropogenic heat, 7, 24, 208, 212
apparent net radiation, 207
area source, 139
atmospheric demand, 196
atmospheric layers, 2, 101, 102, 104, 105, 216
atmospheric stability, 60, 68, 131
autocorrelation, 126
available energy, 47
averaging length, 30, 31

B

baroclinic atmosphere, 110
Beer's law, 202
bias error, 164, 167, 171, 199, 210
big-leaf model, 195, 196, 211
biophysical factors, 207, 208
blackbody, 199
blending height, 54, 207
block averaging, 30
body force, 13, 14
boundary layer growth, 219, 224–226, 228
boundary layer height, 44, 219, 228
Boussinesq approximation, 91

Bowen ratio, 27, 47, 206

Bowen ratio method, 47
Brunt-Väisälä frequency, 94
buoyancy, 68, 70, 222, 223, 226
buoyancy production, 63, 66–68, 228
buoyancy-driven boundary layer, 63

C

canopy carbon dioxide source, 152
canopy drag, 88
canopy drag coefficient, 87, 91
canopy heat exchange coefficient, 92
canopy heat source, 152
canopy resistance, 196, 197
canopy volume averaging, 82, 150
canopy water vapor source, 152
canopy wind profile, 87, 88
capping inversion, 102, 130, 218, 227
carbon dioxide budget, 229
carbon dioxide profile, 39, 216, 231, 239
carbon dioxide source in canopy, 152
carbon dioxide source in free air, 17
cell membrane, 222
chamber, 154, 184
chemical state, 1
Chicago, 212
climate sensitivity, 206
clockwise rotation, 8
closed chamber, 154, 184, 185
closed-path, 48, 168, 169, 180, 184
closure parameterization, 40
closure problem, 40, 227
cloud evaporation, 219, 226
cloud fraction, 223

cloud venting, 223
 clouds, 18, 19, 37, 219, 223, 225, 229, 233
 clumping, 81
 coherent eddies, 96
 collapse of boundary layer, 75
 column mean, 216
 commutation property, 83, 85
 compression heat, 161
 conduction heat flux, 22
 conservation of energy, 18, 36
 constant-flux layer, 103
 continuity equation, 16
 continuum hypothesis, 15
 convection cells, 163
 convection efficiency, 7, 208, 209
 convective boundary layer, 2, 72, 101, 216
 convective instability, 91
 coordinate rotation, 11, 169
 coordinate system, 11, 58
 Coriolis force, 8, 14
 Coriolis parameter, 13, 14
 counter-gradient flux, 44
 counterclockwise rotation, 8, 108
 covariance, 31, 36, 37, 40, 45, 51
 cumulus clouds, 223

D

Dalton number, 51
 Dalton's law, 21, 179
 deforestation, 207
 density effects, 175
 desert, 177, 189
 diabatic process, 26
 diagnostic mode, 233
 dispersion of air pollutant, 6, 102
 dispersion parameters, 124, 130, 145
 dispersive flux, 86
 dissipation, 24, 67
 diurnal evolution, 105, 236
 drag coefficient, 51
 drainage flow, 162, 165
 drift velocity, 135, 177
 dry air, 176
 dry air flux, 177
 dynamic chamber, 155, 185

E

Earth's angular velocity, 14
 ecosystem health, 6, 130
 ecosystem metabolism, 5
 eddy covariance, 9, 46, 149
 eddy covariance control volume, 156

eddy diffusivity, 41, 122, 126, 137
 eddy flux, 45, 157
 eddy length scale, 43, 45
 eigen mode, 95
 Ekman layer, 103
 Ekman spiral extended, 110
 Ekman pumping, 8, 109
 Ekman spiral, 107
 emissivity, 23
 energy cascade, 59, 60
 energy imbalance, 161, 171
 energy redistribution, 7, 206
 energy redistribution factor, 207
 entrainment, 102, 222, 223, 225
 entrainment ratio, 228
 entrainment similarity, 231, 232
 entrainment velocity, 221
 equilibrium boundary layer, 106, 235, 236, 241
 equilibrium state, 111, 114
 equivalent potential temperature, 226
 error propagation, 181
 Eulerain frame, 133
 evapotranspiration, 7
 excess resistance, 56

F

far field, 127
 fetch, 167
 Fick's law, 128, 181
 first-order closure, 44
 flow divergence, 8, 34, 38, 53, 108, 159, 164, 221
 fluid parcel, 15, 156
 flux definition, 4
 flux Richardson number, 70
 flux-gradient method, 46
 flux-gradient relationship, 41, 141, 183
 footprint, 138
 footprint function, 139, 140, 167
 footprint model, 143, 144
 footprint rule, 142
 forced convection, 71
 forcing variables, 5
 forest, 27, 97, 104, 110, 183, 187
 forest edge, 162, 165
 form drag, 86
 forward problem, 122
 Fourier transformation, 31
 free atmosphere, 1, 101, 217
 free convection, 71
 frequency domain, 31
 friction velocity, 25, 42, 88, 136, 143

G

gas constants, 21
Gaussian distribution, 125
Gaussian plume model, 128
genetic contamination, 6
geometric mean height, 47
geostrophic relation, 107
geostrophic wind, 102, 107
global mass conservation, 122
gradient Richardson number, 71, 95
gradient wind solution, 110
gravitational force, 14
green oasis, 211
ground resistance, 201
ground temperature, 201
ground-level concentration, 130, 131

H

Hardley cell, 236
heat advection, 106
heat budget, 227
heat source in canopy, 152
heat source in free air, 18, 19
heat storage, 7, 24, 208, 212
heat stress, 210
heat stroke, 210
heatwave, 106, 116
high pressure, 8, 108, 162
high-frequency loss, 168
high-pass filter, 169
homogeneous turbulence, 125
horizontal advection, 38, 159, 166
horizontal flux, 159, 168
horizontal homogeneity, 38, 87
human health, 7, 130, 210
hydrostatic, 91
hydrostatic equilibrium, 14
hypostomatous, 84, 151

I

ideal gas law, 20, 179
ideal gas law approximation, 65
incoming longwave radiation, 22
incoming solar radiation, 22
incompressibility, 18, 26, 33, 35, 85, 91
incompressibility: strong form, 18, 34
incompressibility: weak form, 35, 36, 66
inertial oscillation, 111, 112
inflection point, 93
inflection point instability, 94
integral stability functions, 77

internal boundary layer, 167

internal energy, 18, 58, 60
internal force, 14
inverse problem, 122, 149
inversion, 70
inversion jumps, 218, 227, 230
inviscid, 91
irrigation, 7
iterative procedure, 47

K

kinematic viscosity, 13, 25
kinetic energy, 57
kinetic energy budget, 63, 89
kinetic energy production, 61, 63, 66–68, 70, 89
kinetic energy redistribution, 62, 67, 68
kinetic energy transfer, 59
kinetic energy transport, 63, 66, 89

L

Lagrangian frame, 18, 123
Lagrangian time scale, 126, 136
lake, 54–56, 162
land surface model, 50
land use, 205
landscape scale, 232, 233, 237
lapse rate, 102
large-eddy simulation, 33, 60, 63, 223
latent heat flux, 22
latent heat of vaporization, 24
leaf area index, 81, 197, 200, 202
leaf boundary layer, 152, 192
leaf boundary layer resistance, 192, 193
leaf dimension, 194
leaf heat exchange coefficient, 194
leaky plate analogy, 222
Leibniz integral rule, 220
lifting condensation level, 223
line averaging, 33
line source, 132, 136, 137, 141
linear detrending, 51
linear instability analysis, 92, 94
linear superposition, 121
local mass conservation, 122
logarithmic wind profile, 25, 43
longwave radiation, 22
longwave radiation feedback, 205
low frequency, 169
low level jet, 3, 114
low pressure, 8, 108, 162

M

mass conservation, 15, 122
 mass conservation of carbon dioxide, 17, 36
 mass conservation of dry air, 16
 mass conservation of water vapor, 17, 37
 mass density, 15
 mass flow controller, 186
 mass flux, 15
 mass mixing ratio, 15, 21
 mean flow kinetic energy, 52, 58, 60, 89
 mercury, 170
 methane, 27
 methane flux, 27, 55
 micrometeorological coordinate, 11
 mirror source, 130, 136
 mixed layer, 103, 116, 218
 mixing length, 8, 42
 mixing velocity, 237
 modified Bowen ratio method, 48
 molar mixing ratio, 21
 molecular diffusivity, 17, 18, 41
 momentum conservation, 12, 35
 momentum flux, 36
 momentum roughness, 25, 43, 53
 Monin-Obukhov stability parameter, 73
 mosaic scheme, 203
 multilayer model, 204

N

near field, 127, 137
 near-infrared waveband, 24
 net ecosystem exchange, 5, 153
 net radiation, 23
 nitrous oxide, 27, 170, 187, 240
 no-slip condition, 84, 88, 108
 nocturnal boundary layer, 3, 105, 115, 233
 non-local closure, 44
 number density, 125
 number sense, 10

O

Obukhov length, 73
 oceans, 50, 56, 187, 225, 235
 offline mode, 5
 ogive analysis, 31
 Ohm's law, 49, 192
 one-dimensional equations, 37
 online mode, 5, 50
 open-path, 180
 outgoing longwave radiation, 23
 overturning, 226

P

parameterization, 5
 partial pressure, 21, 26
 particle position, 124
 particle trajectory, 123
 Pasquill-Gifford, 146
 Penman-Monteith, 196
 persistence, 128
 photosynthesis, 2, 24, 84, 152, 176, 194, 231
 photosynthetic mode, 7
 physical state, 1
 physical units, 10
 plane mixing layer, 93
 plant area density, 81, 97
 plant area index, 81
 plant disease, 6
 plant seed, 6
 plume height, 134, 135
 plume velocity, 134, 135
 point source, 124, 128, 129, 135
 pollen, 6
 potential energy, 58, 66
 potential evaporation, 197
 potential temperature, 19
 potential temperature profile, 101, 116, 216
 potential temperature scale, 43
 power law, 133, 137
 Prandtl's theory, 8
 pressure discontinuity, 83
 pressure flux, 161
 pressure gradient, 3
 pressure gradient force, 8, 13
 pressure redistribution, 67, 68
 Priestley-Taylor equation, 197
 prognostic mode, 233
 psychrometric constant, 47, 195

R

R-C circuit, 32
 radiation flux, 22
 radiative cooling, 225, 226
 radiative forcing, 207
 radiometric resistance, 199
 Rayleigh's theorem, 94
 recursive filtering, 32
 reference evaporation, 198
 reflected solar radiation, 22
 remote sensing, 198
 residual layer, 105, 116
 respiration, 24, 172, 176
 return-to-isotropy, 68
 Reynolds averaging model, 59

Reynolds decomposition, 29

Reynolds rules, 9, 30, 51, 82

Rossby number, 118

roughness sublayer, 104

surface friction, 3, 8

surface integral, 85, 151

surface layer, 4, 39, 103, 219

surface temperature, 195, 198, 199, 203, 205, 211, 212

S

sampling interval, 31

saturation vapor pressure, 56

saturation vapor pressure slope, 193

scale gap, 59

sea breeze, 162

second-order closure, 44

secondary circulation, 8

self-heating, 188

sensible heat flux, 22

sensor separation, 168

separation of variables, 92

settling velocity, 6, 98

shear destruction, 63

shear instability, 91

shear production, 67, 68, 90

shear-driven boundary layer, 63

shortwave radiation, 22

sign convention, 23, 24, 153

significant digits, 10

similarity theory, 73

slab approximation, 216

Slattery's averaging theorem, 85, 150

smokestack, 129

soil evaporation, 201

solar radiation, 59

spatial averaging, 33

spatial covariance, 86

specific heat, 18, 19

spore, 6

stability functions, 43, 73, 74

standard atmosphere, 26, 102, 175

Stanton number, 51

stationary turbulence, 126

statistical independence, 123

statistical moments, 44

steady state, 224

Stefan-Boltzmann constant, 23

Stefan-Boltzmann law, 198

stoma, 84, 151, 192

stomatal resistance, 193, 194, 197

storage, 157

stratocumulus clouds, 225, 226, 229

sub-cloud layer, 225

subgrid, 54, 203, 208

subsidence, 221, 223, 226

subsidence warming, 218, 227

surface energy balance, 7, 22, 27, 161

T

Taylor expansion, 178, 193

Taylor-Golstein equation, 94

temperature profile, 39

temperature ramps, 96

tethersonde, 234, 239

thermal roughness, 43, 199

Tibetan Plateau, 106

tilt error, 11, 25, 169

top-down mixing, 225

total derivative, 13, 18

total kinetic energy, 52, 57

total water mixing ratio, 226

tracer correlation, 235, 240

transfer coefficients, 51, 56, 78

transition to turbulence, 91

transpiration, 200

transport phenomena, 8

tropical, 115, 119

turbulent kinetic energy, 45, 52, 58, 64, 66, 67

turbulent organized structures, 163

turbulent Prandtl number, 42, 79

turbulent Schmidt number, 42

two-leaf model, 204

two-source model, 201

U

unit line source, 141

upside-down boundary layer, 116

urban, 24

urban heat island, 7, 208

urban heat island attribution, 209

urban heat mitigation, 7

V

vapor pressure deficit, 194

variance, 31, 36

vertical advection, 159, 161, 217

vertical profiles, 3, 39, 43

vertical velocity, 161, 163, 164, 177, 221, 223, 237

virtual temperature, 22

viscous dissipation, 63, 67, 75

viscous drag, 87
viscous force, 14
viscous sublayer, 103
visible waveband, 24
volume averaging, 9, 33
von Karman constant, 25, 42, 74

W

wake production of turbulence, 90
Walker circulation, 236
water balance, 7
water column, 24
water resource management, 201
water use efficiency, 7, 201
water vapor budget, 232
water vapor pressure, 47
water vapor profile, 39, 216, 239
water vapor source in canopy, 152

water vapor source in free air, 18
wave equations, 91
wave growth, 93
wave perturbations, 91
wave properties, 92, 93
wet bulb temperature, 194, 210
wetland, 27
white oasis, 211
wind direction convention, 25
wind directional shear, 111, 119
wind profile, 39, 101
wind shear, 2

Z

zero-flux test, 177, 182, 185
zero-plane displacement, 44, 75, 98
Zilitinkevich relation, 234